

MICROSTRUCTURAL-BASED CHARACTERIZATION OF HYDROGENATION AND
DEHYDROGENATION MECHANISMS IN MG POWDERS

By

HUNG-YU TIEN

A DISSERTATION PRESENTED TO THE GRADUATE SCHOOL
OF THE UNIVERSITY OF FLORIDA IN PARTIAL FULFILLMENT
OF THE REQUIREMENTS FOR THE DEGREE OF
DOCTOR OF PHILOSOPHY

UNIVERSITY OF FLORIDA

2010

© 2010 Hung-Yu Tien

To my grandparents, dad, mom, sister and friends

ACKNOWLEDGEMENTS

In my 3 years PhD study, my advisor Dr. Ebrahimi is the most important person who helps me a lot not only in my research also in life. The attitude of learning is the major subject in her teaching. Her encourage and inspiration are the motivation for me to complete the degree. Without her painstaking teaching I would not reach this level. I would like to thank her help from my bottom of heart.

I would like to thank all of my committee members, Dr. Craciun, Dr. Jones, Dr. Manuel, and Dr. Lear for their precious advices toward my research. I also would like to thank Dr. Bourne for the valuable question in my qualify exam and the permission of using the polishing wheel in his lab. I am appreciated that Dr. Glicksman shares everything he knows to explain to me how to analyze my hydrogenation curves. Special thanks to Dr. Wu for proving the Theta Composer for the essential coating process. I am grateful to Dr. Dempere and Dr. Wayne for their suggestion in characterizing my samples in using EBSD and SEM in MAIC.

I would like to thank my group members Dr. Sankara Tartiparti, Dr. Yanli Wang, Dr. Orlando Rios, Dr. Mahesh Tanniru, Ian Liu, Sonalika Goyal, Mike Kesler, Glenn Bean Jr., Jon Besser, Ross, David Rule, Steven James, Diego, Christian for their sincere ideas on my research and presentation. To all my friends who help me whenever I face any difficulty, I would like to thank their concerns and accompanies. This project is funded by NSF under the contract number: DMR-0605406.

TABLE OF CONTENTS

	<u>page</u>
AKNOWLEDGEMENTS	4
LIST OF TABLES.....	8
LIST OF FIGURES.....	9
ABSTRACT	17
1 INTRODUCTION	20
2 BACKGROUND	27
2.1 The Structure of Magnesium and Magnesium Hydride	27
2.2 Thermodynamic Properties of Magnesium Hydride	27
2.2.1 Pressure-Composition-Temperature (PCT) of Magnesium	29
2.2.2 Alloying Effect.....	30
2.3 Kinetic Properties of Magnesium Hydride	31
2.3.1 Hydrogen Capacity of Magnesium Powders.....	31
2.3.2 Kinetics Model of Hydrogenation of Magnesium Powders.....	32
2.3.3 Effect of Catalyst	36
2.4 Microstructural Analysis of Hydrogenated Mg Powders.....	38
2.5 Effect of Shape and Size on Hydrogen Capacity of Metal Hydride	39
3 EXPERIMENTAL PROCEDURES	46
3.1 Material Fabrication	47
3.1.1 Addition of Catalyst by Theta Composer	47
3.1.2 Addition of Catalyst by Organometallic Nickel Solution	48
3.1.3 High Speed Orbital Ball Milling (HSOBM).....	49
3.2 Hydrogen Absorption	49
3.2.1 Hydrogenation Setup.....	49
3.2.2 Hydrogenation Procedure.....	51
3.3 Hydrogen Desorption.....	54
3.3.1 Dehydrogenation Setup.....	54
3.3.2 Dehydrogenation Procedure.....	54
3.3.3 Thermal Gravimetric Analyzer (TGA)	55
3.4 Analysis Methods and Characteristic Techniques.....	57
3.4.1 Particle Size Distribution.....	57
3.4.2 Scanning Electronic Microscope (SEM)	57
3.4.3 Optical Microscope (OM).....	58
4 CHARACTERIZATION OF POWDERS	64
4.1 Characteristics of the As-Received Mg powders	64

4.1.1	44 μ m Mg Powder	64
4.1.2	Characteristics of the 300 μ m Mg Powder.....	65
4.2	Characteristics of Mg Flakes.....	66
4.3	Characteristics of Ni-coated Mg Powders	67
4.3.1	Ni Coating Using Theta Composer	67
4.3.2	Ni Coating Using an Organometallic Solution.....	67
5	EVOLUTION OF MICROSTRUCTURE DURING THE HYDROGENATION PROCESS	78
5.1	Introductory Remarks.....	78
5.2	Microstructural Analysis	79
5.3	Effect of Particle Size on Hydrogen Capacity	84
5.4	Summary of Hydrogenation Process	86
5.5	Summary and Conclusions	87
6	KINETICS OF MG HYDRIDE FORMATION	104
6.1	Introductory Remarks.....	104
6.2	Analysis of Kinetics of Hydride Formation by the Johnson-Mehl-Avrami Relationship.....	104
6.2.1	Evaluation of Nucleation Number during Stage 2.....	106
6.2.2	Correlation of Grain Boundary and Nuclei of Magnesium Hydride	108
6.2.3	Effect of Hydrogenation Temperature.....	109
6.2.4	Microstructural Analysis of Powders Hydrogenated at Different Temperatures.....	111
6.3	Effect of Nucleation Rate on Hydrogen Capacity	112
6.3.1	Hydrogenation Procedures.....	112
6.3.2	Heating Procedure.....	117
6.4	Kinetics analysis by Johnson-Mehl-Avrami relation for Growth Mechanism of Magnesium Hydride.....	120
6.5	The Fraction of Magnesium Hydride at Impingement	123
6.6	Summary and Conclusions	125
7	EFFECT OF POWDER GEOMETRY and size ON THE HYDROGEN CAPACITY OF MAGNESIUM.....	151
7.1	Introductory Remarks.....	151
7.2	Effect of Particle Shape on Hydrogenation Behavior of Mg Powder	152
7.3	Effect of Particle Size on Hydrogen Capacity	156
7.4	Mathematical Modeling	157
7.5	Summary and Conclusions	160
8	DEHYDROGENATION MECHANISM OF MAGNESIUM HYDRIDE	168
8.1	Introductory Remarks.....	168
8.2	Desorption Study by Constant Heating Rate in TGA	169
8.3	Isothermal Dehydrogenation Study of MgH ₂	172

8.4 Summary and Conclusions	175
CONCLUSIONS AND FUTURE WORK.....	180
LIST OF REFERENCES	182
9 BIOGRAPHICAL SKETCH.....	188

LIST OF TABLES

<u>Table</u>		<u>page</u>
2-1	Dependence of n in the JMA equation.....	41
6-1	The result of the measurement of number of nucleation at different hydrogenation times	127
6-2	Hydrogen capacity at different hydrogenation temperatures	127
6-3	The slope of the three stages of hydrogenation as revealed by JMA analysis in Figure 6-29.	127
6-4	n and K values for Stage 2 and 3 at each temperatures.....	128
6-5	End time in minutes of each stage.....	128

LIST OF FIGURES

<u>Figure</u>	<u>page</u>
1-1 The schematic hydrogenation curve showing the hydrogen capacity and the hydrogenation kinetics.....	26
2-1 The crystal structure of hexagonal closed packed (HCP) Mg.....	41
2-2 The crystal structure of tetragonal magnesium hydride.....	41
2-3 Schematic illustration of the likely epitaxial growth mode of MgH ₂ on Mg on (001) Al ₂ O ₃ in the MgH ₂ (110)[001]//Mg(001)[100] relationship. For clearness, only the Mg atoms in MgH ₂ are shown. [42].....	42
2-4 Mg-H binary phase diagram at 1bar (0.1MPa) hydrogen pressure.....	42
2-5 Energy barriers for hydrogen absorption and desorption.....	43
2-6 PCT curves and Van't Hoff plot at different temperature (T ₁ >T ₂ >T ₃).....	43
2-7 The schematic growth of a product region.....	43
2-8 Cross-section of a magnesium particle at two different times and typical $\xi=f(t)$ curves for hydriding at A) $P \sim P_{eq}$ and B) $P \gg P_{eq}$	44
2-9 A schematic diagram for Core-Shell hydrogen absorption model.....	44
2-10 Potential energy curve for hydrogen binding to a metal surface which shows: (i) physisorption for both activated and non-activated processes; (ii) dissociation of hydrogen molecules and chemisorption; (iii) surface penetration and chemisorption; and (iv) diffusion of hydrogen atoms. [73].....	44
2-11 Microstructural analysis of hydrogenated magnesium powders after (a) first hydrogenation, (b) a series of long-term cycling test, (c) a few short-term cycling tests, and (d) a series of short-term cycling test.....	45
3-1 Glove box (Vacuum Atmosphere, model: Nexus).....	59
3-2 Monitoring the O ₂ and moisture level.....	59
3-3 Theta Composer Ni coating.....	59
3-4 Organometallic Ni coating. Black dot represent nano-Ni particles and white one is the magnesium powder. 110°C is the operating temperature. The arrows illustrate the cycling of toluene in the beaker.....	60
3-5 HSOBM milling.....	60

3-6	Schematic illustration of HSOBM milling	61
3-7	The relationship between applying voltage and milling speed.....	61
3-8	Mounting sample cut perpendicularly to the flake surface for thickness measurement.....	61
3-9	H/D system actual view	62
3-10	Schematic diagram of Hydrogenation/Dehydrogenation unit.....	62
3-11	The illustration of the calculation of pressure drops in Method I.....	63
4-1	The particle size distribution of the as-received 44 μ m magnesium powder as evaluated by laser diffraction technique	69
4-2	The SEM image of the as-received 44 μ m magnesium powder.	69
4-3	Cross-sectional optical image of the powders in the as-received 44 μ m magnesium powder.	70
4-4	The schematic illustration of polishing surfaces and calculation of aspect ratio for as-received 44 μ m magnesium powders.....	70
4-5	Particle size distributions of the as-received 44 μ m magnesium powder by statistic measurement in (a) number percent and (b) volume percent calculation.....	71
4-6	SEM images of the as-received 300 μ m magnesium powder.....	71
4-7	Cross-sectional optical image of the as-received 300 μ m magnesium powder. ...	72
4-8	Particle size distribution in the as-received 300 μ m magnesium powder based on (a) number percent and (b) volume percent calculation.	72
4-9	Magnesium flake thickness distribution after 100V and 20 seconds milling.	73
4-10	Magnesium flake thickness distribution after 100V and 1 minute milling.	73
4-11	Magnesium flake thickness distribution after 100V and 2 minutes milling.	73
4-12	Magnesium flake thickness distribution after 110V and 2 minutes milling.	74
4-13	Optical microscopic analysis at cross section of magnesium flake powders.	74
4-14	SEM images of as milled magnesium flake powders.....	74
4-15	Particle size distribution of Ni-coated 44 micron magnesium particles.	75

4-16	SEM images of Ni-coated the 44 micron magnesium powder after Ni coating with the Theta Composer.	75
4-17	The EDS Ni mapping of Ni-coated 44 micron magnesium particles.	75
4-18	The X-ray diffraction patterns.	76
4-19	SEM images of Ni-coated magnesium flake particles.....	76
4-20	The EDS Ni mapping of Ni-coated magnesium flake particles.	76
4-21	SEM image of Ni-coated 300 micron magnesium particles	77
5-1	Hydrogenation curve of magnesium powder sample at 210°C under 1MPa hydrogen pressure.....	89
5-2	Schematic illustration of Core-Shell model.	89
5-3	Hydrogenation curves of magnesium powder sample at 210°C under 1MPa hydrogen pressure at each interrupted times.	90
5-4	Microstructural analysis on the cross section of magnesium powder hydrogenated for 2.5 minutes.	91
5-5	Microstructural analysis on the cross section of magnesium powder hydrogenated for 7.5 minutes.	92
5-6	Optical microscopic images for the investigation of the location of nucleation of magnesium hydride.	93
5-7	Microstructural analysis on the cross section of powder hydrogenated for 15 minutes.	94
5-8	Microstructural analysis on the cross section of powder hydrogenated for 75 minutes.	95
5-9	Microstructural analysis on the cross section of powder hydrogenated for 300 minutes.	96
5-10	An example of different hydride fractions achieved by different sizes of particles.	97
5-11	An example of the measurement of phase fraction of magnesium hydride	98
5-12	Hydride fraction at different range of sizes and temperatures.	98
5-13	An illustration of hydride distribution and phase fraction for different size of particles at the same hydrogenation condition and time 15 minutes.	99

5-14	A comparison of hydrogenation curve with the data point estimated by the measurement of area phase fraction.	99
5-15	Step 1: Physisorption of hydrogen molecules.	100
5-16	Step 2: The dissociation of hydrogen molecules.	100
5-17	Step 3: The dissolving of hydrogen atoms.	101
5-18	Step 4: Chemisorption of hydrogen ions.	101
5-19	Step 5: Nucleation of magnesium hydrides.	102
5-20	Step 6: Growth of magnesium hydrides.	102
5-21	Step 7: The impingement of magnesium hydrides.	103
6-1	The JMA analysis of powders hydrogenated at 210°C under 1MPa.	129
6-2	The measurement of perimeter for powders hydrogenated for 2.5 minutes.	129
6-3	The measurement of perimeter for powders hydrogenated for 7.5 minutes.	130
6-4	The etched cross sectional surface of magnesium powder pre-heated at 210°C.	130
6-5	The hydrogenation curves of magnesium powders hydrogenated at 150, 180, 210, and 250°C.	131
6-6	The relationship between hydrogen capacity and hydrogenation temperatures.	131
6-7	The microstructural analysis of powders hydrogenated at (a)150°C, (b)180°C, (c)210°C, and (d)250°C under 1Mpa for 5 hours.	132
6-8	The schematic illustration of proposed model for the effect of nucleation rate on hydrogenation kinetics and hydrogen capacity.	133
6-9	Hydrogen absorption as a function of time for the two hydrogenation methods employed.	133
6-10	The evaluation of kinetics of hydride formation by Methods I and II on the JMA relationship.	134
6-11	A comparison of the hydrogenation curves for powders hydrogenated by Method I for 75 minutes and by Method II for 3 minutes.	134
6-12	SEM pictures comparing the hydride formation for powders hydrogenated by Method I for 75 minutes (a and b) and by Method II for 3 minutes (c and d);	

	(a) and (C) are cross sectional view and (b) and (d) are the external view of the powders.....	135
6-13	The surface coverage measurement.....	135
6-14	The distribution of the surface coverage of the particles hydrogenated by Method I and II.....	136
6-15	SEM pictures showing cross-sectional views of the particles with high hydride coverage after 75 minutes f hydrogenation by Method I (a and b) and with low hydride coverage after 3 minutes hydrogenation by Method II (c and d)....	136
6-16	Hydrogenation curves for 150°C, 210°C and the two-step heating. Point A denotes the time (15 minutes) at 210°C, which results in an equal amount of hydride as the powder hydrogenated at 150°C for 5 hours.	137
6-17	SEM (BSE mode) images showing the hydride distribution in the powder hydrogenated at (a and c) 210°C for 15 minutes, and (b and d) at 150°C for 300 minutes. (a) and (b) are cross-sectional images, while (c) and (d) are external surface images. magnesium hydride appears dark because of its lower density.....	138
6-18	SEM (BSE mode) cross-sectional images showing (a) hydride distribution in powders hydrogenated at 150°C for 2 minutes, (b) higher magnification of (a) showing internal nucleation of MgH ₂ , (c) hydride formation in powders hydrogenated by the two-step heating (150°C for 2 minutes and 210°C for 298 minutes), and (d) hydride formation in the powders hydrogenated at 150°C for 300 minutes.....	139
6-19	The JMA analysis of powder hydrogenated at 250°C (Sample 1).	140
6-20	The JMA analysis of powder hydrogenated at 250°C (Sample 2).	140
6-21	The JMA analysis of powder hydrogenated at 210°C (Sample 1).	141
6-22	The JMA analysis of powder hydrogenated at 210°C (Sample 2).	141
6-23	The JMA analysis of powder hydrogenated at 180°C (Sample 1).	142
6-24	The JMA analysis of powder hydrogenated at 180°C (Sample 2).	142
6-25	The JMA analysis of powder hydrogenated at 150°C (Sample 1).	143
6-26	The JMA analysis of powder hydrogenated at 150°C (Sample 2).	143
6-27	The relationship between n values and temperatures at Stage 2 and 3.	144
6-28	The location of transition region within the hydrogenation curves.	144

6-29	The activation energy calculated by Arrhenius plot.	145
6-30	The schematic illustration of the comparison of slopes at the beginning of Stage 3 at 150°C and 250°C.	145
6-31	The relationship between hydride fraction and reaction rate at 250°C.	146
6-32	The f^* calculation at 250°C.	146
6-33	The relationship between hydride fraction and reaction rate at 210°C.	147
6-34	The f^* calculation at 210°C.	147
6-35	The relationship between hydride fraction and reaction rate at 180°C.	148
6-36	The f^* calculation at 180°C.	148
6-37	The relationship between hydride fraction and reaction rate at 150°C.	149
6-38	The f^* calculation at 150°C.	149
6-39	A comparison between hydride fraction at impingement analyzed by two different methods (JMA analysis and relationship between hydride fraction and reaction rate).	150
7-1	External surface images at higher magnification of (a) as-received 300 μ m magnesium spherical and (b) magnesium flake particles.	161
7-2	The hydrogenation curves of different shapes of particles. The hydrogen capacity of magnesium flakes shows more than 5.5 H wt. % which is much higher than the as-received 300 μ m magnesium particles with 0.2 H wt. % capacity.	161
7-3	The SEM (BSE mode) images of hydrogenated as-received 300 μ m magnesium particles after hydrogenation at 300°C 1MPa for 15 hours.	162
7-4	The SEM (BSE mode) images for the hydride layer measurement at higher magnification of hydrogenated as-received 300 μ m magnesium particles after hydrogenation at 300°C 1MPa for 15 hours.	162
7-5	The SEM (BSE mode) images of hydrogenated magnesium flake particles after hydrogenation at 300°C 1MPa for 36 hours. (a) Thick flake particles (b) thin flake particles.	163
7-6	The schematics illustration of effect of shape change from sphere to flake on hydrogen capacity of magnesium particles with SEM (BSE mode) images for the comparison.	164

7-7	The hydrogenation curves of different sizes of particles. The hydrogen capacity of 44 μ m magnesium particles shows more than 6.5 H wt. % which is much higher than the 300 μ m magnesium spherical particles with 0.2 H wt. % capacity.	165
7-8	(a, c) The SEM (BSE mode) images of hydrogenated 44 μ m magnesium particles after hydrogenation at 300°C 1MPa for 10 hours compared with the images of (b, d) which show the cross section of hydrogenated as-received 300 μ m magnesium particles.....	166
7-9	(a) Prolate spheroid for AR 44 and 300 μ m (b) Disk spheroid for flake.	166
7-10	The experimental hydrogen capacity compared with theoretical calculation by using 11.8 μ m thick hydride layer at varying a/b aspect ratio.	167
8-1	(a) Hydrogenation curve of hcp-Mg at 210°C under 1MPa pressure. (b) Evaluation of different stages of hydrogenation of magnesium powders based on JMA relationship.	176
8-2	SEM (BSE mode) micrographs (a) of the saturated powder revealing the impingement of magnesium hydride grains/colonies and (b) of the partially hydrogenated powder showing the presence of the hcp-Mg phase on the surface.....	176
8-3	Dehydrogenation curves obtained using TGA of the partially and completely hydrogenated powders at 5°C/minute and under He flow, revealing the difference in the hydrogen release temperature between the samples.	177
8-4	SEM (BSE mode) micrographs of the partially dehydrogenated powder. (a) Lowering magnification of the particle showing the release of hydrogenation around the particle with MgH ₂ inside the particle. (b) Higher magnification image showing the extension of the hcp-Mg phase to the surface of the particle.....	177
8-5	(a) Hydrogenation/dehydrogenation curves. The hydrogenation condition is the same for all powder samples (At 210°C under 1 MPa for 5 hours). The dehydrogenation tests were done under 0.1 MPa at 290°C, 295°C, 300°C for 5 hours. The SEM/BSE image at point P is shown in Figure 1(b), in the vicinity near the powder surface of the partial dehydrogenated powders after 5 minutes releasing at 300 °C under 0.1MPa.	178
8-6	Hydrogenation/dehydrogenation curves. The hydrogenation tests are done at 210°C under 1MPa for 15 minutes and 5 hours. The dehydrogenation tests are done under 0.1 MPa at 290°C for 5 hours immediately after hydrogenation tests for both powder samples.	178
8-7	The SEM/BSE images of as-hydrogenated powder. In Figure 3(a), SEM/BSE images show the hydride distribution in the hydride powders hydrogenated at	

210 °C under 1 MPa for 5 hours. The Sample powder exhibits pseudo-saturation behavior. In Figure 3(b), the SEM/BSE images shows the hydride distribution in the hydride powders hydrogenated at 210°C under 1 MPa for 15 minutes and the sample powder shows unsaturated behavior. 179

8-8 Hydrogenation/dehydrogenation curves. The hydrogenation tests are done at 210°C under 1MPa for 15 minutes. The dehydrogenation tests are done under 0.1 MPa at 290°C for 5 hours at 275°C, 280°C, 290°C, and 300°C. 179

Abstract of Dissertation Presented to the Graduate School
of the University of Florida in Partial Fulfillment of the
Requirements for the Degree of Doctor of Philosophy

MICROSTRUCTURAL-BASED CHARACTERIZATION OF HYDROGENATION AND
DEHYDROGENATION MECHANISMS IN MG POWDERS

By

Hung-Yu Tien

December 2010

Chair: Fereshteh Ebrahimi

Major: Materials Science and Engineering

Metal hydrides display moderately high gravimetric and volumetric capacities and are being considered as potential solid-state hydrogen storage materials for on-board fuel-cell powered vehicles. Among them, magnesium hydride has been widely studied in the past few decades owing to its abundance, low density, reversibility, and reasonable ideal capacity of 7.6wt%. However, the hydrogen capacity of magnesium is usually below its theoretical value and varies with hydrogenation condition and powder size and shape. One of the main objectives of this dissertation was to develop a mechanistic understanding of the hydrogenation process in magnesium powders based on detailed microstructural analyses in order to shed light on the parameters that control the hydrogen capacity.

We have demonstrated that the hydrogenation of magnesium powders at 1Mpa pressure and in the temperature range of 150 to 300°C takes place in three stages. Stage 1 is the nucleation of the magnesium hydride, Stage 2 is the growth of magnesium hydride colonies up to their impingement, and Stage 3 is the further growth of the continuous hydride layer. The nucleation of the hydride was found to be limited to

the powder surface, except at 150°C, where internal hydride formation was observed. Quantitative metallography suggests that at high temperatures the magnesium hydride nucleates at the intersection of magnesium grain boundaries with the powder surface and consequently the number of hydride nuclei remains constant during Stage 2. The activation energy associated with Stage 2 was measured to be 32.4 kJ/ mole, which is close to the diffusion of hydrogen atom through the hcp-Mg metal. Stage 3, is believed to take place by the diffusion of hydrogen atoms through the hydride layer, which is quite slow and leads to the observation of a pseudo-saturation behavior that governs the hydrogen capacity.

Through different approaches it is elucidated that the reduced hydrogen capacity at low temperatures is associated with an increase in the hydride nucleation rate, which results in impingement of the hydride colonies at smaller hydride thickness values. The findings of this investigation also reveal that the powder size distribution, the average powder size and particle shape affect hydrogen capacity significantly. A broad particle size distribution was found to result in a gradual transition between Stage 2 and 3 and a less pronounced pseudo-saturation behavior. It is demonstrated that decreasing the size of the particles in the powder and increasing their aspect ratio drastically increase the hydrogen capacity. These phenomena are explained based on the nucleation and growth of the magnesium hydride.

Studies near the equilibrium conditions revealed that the nucleation of the hcp-Mg influences the kinetics of dehydrogenation process noticeably. The presence of metallic magnesium phase on the surface, owing to incomplete hydrogenation, was found to enhance the kinetics and reduce the dehydrogenation temperature by eliminating the

energy barrier required for the magnesium nucleation during hydrogen release process. The presence of metallic magnesium phase on the surface eliminates the energy barrier for the magnesium nucleation during hydrogen release process. This effect results in the lowering of the dehydrogenation temperature of magnesium hydride.

CHAPTER 1 INTRODUCTION

The energy supply for transportation has been mainly based on fossil fuels such as coal in the nineteenth century and gasoline and natural gas in the twentieth century. In twenty-first century, oil crisis gripped the world due to the political and religious conflicts in Middle-East which has 94% known oil fields [1]. It is also noted that to date no major crude oil field has been found since 1970s [2]. Hubbert peak theory points that the rate of petroleum production tends to decline because of resource depletion after the point of maximum production and discovery rate [3-5]. However, due to the release of the raising amount of carbon dioxide, the global warming and green house effects lead to a growing demand for the development of non-polluting new energy carriers for on-board automobile application. As for the environmental concern, zero levels of harmful emission should be a part of the energy cycles from all means of transportation [6-9].

Hydrogen fuel, which is the key to satisfying the energy requirement and reduction of carbon dioxide emission, has a potential to become such a new energy carrier for the operation of fuel cells. Furthermore, hydrogen is the focus for sustainable energy source due to its abundance, easy synthesis, and high efficiency [10]. The volumetric hydrogen capacity of hydrogen gas under 80Mpa is $40 \text{ kgH}_2/\text{m}^{-3}$ and that of liquid hydrogen is $71 \text{ kgH}_2/\text{m}^{-3}$. However, the safety issues and low volumetric density in compressed hydrogen storage and the technical issue of keeping the operating temperature below the boiling point of liquid hydrogen limit their application in automotive transportation.

Hydrogen storage materials in solid form play a crucial role in realization of fuel cells on-board of vehicles owing to their volumetric hydrogen capacity being in the

range of 80 to 160 kgH₂/ m³[11]. These materials, including metal and complex hydrides, are good potential storage methods due to their possibilities of high volumetric and gravimetric densities [12-16]. Because of the relatively low pressures involved in the metal hydride technologies, they do not suffer the drawback as compressed and liquid hydrogen.

Unlike the complex hydrides, most simple metallic hydrides, including magnesium hydride, have almost 100% reversible capacity, which is very important for the on-board automobile application. Among metal hydrides, light weight alkali metals such as lithium and magnesium hydrides, with good hydrogen capacity, have become the first priority for the renewable hydrogen storage application [17, 18]. Although LiH has an ideal 12.5 H wt. % storage capacity, under atmospheric pressure, its desorption temperature is above 450°C due to its high formation energy of -190 kJ/mole. On the other hand, magnesium hydride has a theoretical capacity of 7.6 H wt. % with an energy formation of -76kJ/ mole, which renders a lower hydrogen release temperature of about 300°C under atmosphere pressure [6]. However, as an efficient hydrogen storage material, this hydrogen release temperature is still too high for operation of the Proton Exchange Membrane Fuel Cells (PEMFC) [19-21]. But recently, there is a trend to increase the operating temperature of PEM fuel cell by using an electrolyte membrane of polybenzimidazole doped with phosphoric acid [22]. Moreover, nano-size magnesium hydride with a suitable catalyst could be used on-board in a proposed two-stage reservoir that enhances the kinetics of hydrogenation/dehydrogenation processes [23]. In addition to the required low hydrogenation and dehydrogenation temperatures, these process should take place within a reasonable time according the refueling rate and

cycle life targets set by Department of Energy (DOE) [24, 25]. Figure 1-1 shows a schematic hydrogenation curve that demonstrates the pseudo-saturation corresponding to the maximum capacity and the hydrogen absorption rate relating to the hydrogenation kinetics. The kinetics of hydrogenation processes have been improved by alloying, use of catalysts on the surface and microstructural modification of the metal by processes such as ball milling [26, 27]. While magnesium hydride has a reasonable ideal hydrogen capacity, this level cannot be achieved under all hydrogenation conditions [26, 28-31]. Many research groups have shown that the hydrogen capacity of Mg or Mg-based alloy powders depends on the hydrogenation temperature. In general, the hydrogen capacity decreases significantly with reducing the hydrogenation temperature [31-34].

In general, two models are proposed to explain the hydrogenation kinetics in magnesium and its alloys. It has been argued that hydrogen absorption behavior of magnesium is better described by a three-dimensional diffusion-controlled shrinking-core model [35, 36]. This mechanism assumes that a continuous layer of hydride forms immediately on the surface of magnesium powders upon hydrogenation. Hence, the kinetics of hydride formation is dependent on area of the interface at Mg/MgH₂ as well as the thickness of the hydride layer. With growth of the hydride layer, the area of the interface decreases and the hydride formation rate is reduced significantly owing the reduction of hydrogen flux from the gas phase to the interface of Mg/MgH₂. As the hydride layer thickens, the diffusion length increases which increase the time for hydrogen diffusion through the hydride layer. In resemblance with porous membranes [37], a large hydrogen concentration gradient within the magnesium hydride is assumed

to provide the necessary flux of hydrogen within the hydride. However, magnesium hydride is an ionic compound and according to the binary phase diagram of Mg–H, it has almost no solubility range [38]. Therefore, the assessment of the hydride as a porous layer is not suitable for explaining the hydrogenation behavior of magnesium. Nucleation and growth models have been suggested to describe the kinetics of magnesium hydride formation [29, 39, 40]. However, this approach does not imply a saturation level below the theoretical capacity because it is only developed for bulk materials and not for powders. It has been proposed that the hydride grains may impinge on each other before the entire magnesium particle is transformed [28-30]. According to this model, the capacity is defined as the point where the impingement is achieved.

In general, no microstructural analysis is reported to elucidate whether the growth mechanism is a thickening process of a continuous magnesium hydride layer or hydride forms as individual grains that eventually impinge on each other. Most of studies are calculated based on rate theories and there is a lack of microstructural evaluation of hydrogenation behavior of magnesium powders. Also, the role of nucleation and growth of phases during dehydrogenation of magnesium hydride has not yet been investigated.

The objective of this study is to investigate the microstructural evolution during the hydrogenation and dehydrogenation processes at different temperatures in order to develop a mechanistic understanding of the mechanisms that control the kinetics of formation of magnesium hydride and the maximum hydrogen capacity. Commercial magnesium powder was utilized in this investigation. Parameters such as hydrogenation

method, powders size and size distribution as well as powder shape were studied to confirm the hypotheses developed in this study.

Two different sizes of commercial magnesium particles with 44 and 300 μm average size were used. For catalysis of dissociation of hydrogen molecules on the surface of powders, the powders were coated by nanocrystalline nickel through two different techniques. The hydrogen pressure employed for hydrogenation was 1MPa and for dehydrogenation was 0.1MPa hydrogen pressure. The effects of temperature on hydrogenation and dehydrogenation behaviors of magnesium powders were investigated using detailed cross-sectional microscopy and quantitative metallography.

A brief review of relevant literature is presented in Chapter 2. The detailed experimental procedures are explained in Chapter 3. The results of this research are presented in five chapters. The characterizations of powders, including powder size, geometry, and also coating properties are given in Chapter 4. Chapter 5 describes the microstructural evolution during hydrogenation. Chapter 6 mainly focuses on the hydrogenation mechanism. The kinetics of magnesium hydride formation is discussed by the JMA (Johnson-Mehl-Avrami) analysis from the hydrogenation curves. For the first time a three stage hydrogenation process is described and its validity is proven by especially designed hydrogenation tests. Chapter 7 is about the geometry and size effect of magnesium powder on the hydrogen capacity. The results presented in this chapter confirm the hypothesis developed in Chapter 5 and show that decreasing the size and changing the shape of particles from spherical to flake increases the total hydrogen capacity significantly. Chapter 8 is the investigation of dehydrogenation mechanism of magnesium hydride. The dehydrogenation tests in this study reveal that

the presence of hcp-Mg phase on the surface plays a very important role for the enhancement of the dehydrogenation kinetics.

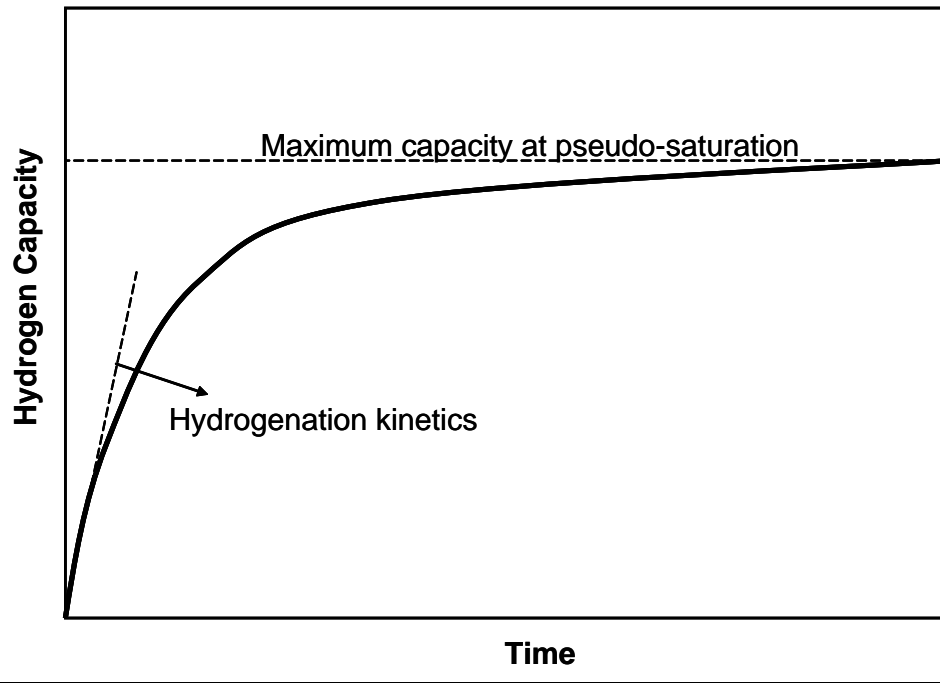


Figure 1-1. The schematic hydrogenation curve showing the hydrogen capacity and the hydrogenation kinetics.

CHAPTER 2 BACKGROUND

2.1 The Structure of Magnesium and Magnesium Hydride

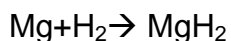
Magnesium is a hexagonal closed-packed structure with lattice constants $a=3.2\text{\AA}$ and $c= 5.2\text{\AA}$, as shown in Figure 2-1. In the occurrence of hydrogen gas, magnesium absorbs and reacts with hydrogen under standard conditions. At low concentration, hydrogen atoms dissolve in the magnesium matrix, while at high concentration the compound magnesium hydride precipitates from the solution. Magnesium hydride is a tetragonal structure (β) with ionic-like bonding between Mg and H, as shown in Figure 2-2. The magnesium cation is octahedrally surrounded by H anions: the H anion has a planar triangle of magnesium cations around it. The lattice parameters are $a= 4.5\text{\AA}$ and $c= 3.0\text{\AA}$ [41, 42]. Magnesium hydride forms epitaxially relative to magnesium in the thin film sample with a crystallographic orientation relationship to be $\text{MgH}_2(110)[001]//\text{Mg}(001)[100]$ on Al_2O_3 and $\text{MgH}_2(200)[00-1]//\text{Mg}(110)[-111]$ on LiGaO_2 [42]. In Figure 2-3, the schematic shows the probable epitaxial growth of magnesium hydride on a thin film of magnesium. In the ball milling, a part of the magnesium hydride (β) transforms to an orthorhombic structure (γ) which is stable at high pressure [31]. In this study magnesium hydride refers to a β phase crystal structure since no milling is performed by using hydrogenated magnesium powders.

2.2 Thermodynamic Properties of Magnesium Hydride

At a specific temperature and pressure, the driving force of the hydride reaction ($\text{Mg} + \text{H}_2 = \text{MgH}_2$) is Gibb's free energy which is composed of formation enthalpy and entropy.

$$\Delta G = \Delta H_f - T\Delta S_f \quad (2-1)$$

The enthalpy of magnesium hydride formation, ΔH_f , is negative (-76kJ/mole) and represents the heat released during the reaction. ΔS is mainly from the reduction of the gas phase to the chemisorbed hydrogen (-130J/moleK) [18, 26, 43-49]. A negative Gibb's free energy through formation of magnesium hydride indicates that this process is thermodynamically favorable while enthalpy formation is dominant. However, at high temperatures, entropy of formation plays an important role, and instead, ΔG of magnesium hydride formation becomes positive and dehydrogenation is thermodynamically favored. The binary Mg-H phase diagram is shown in Figure 2-4 [38]. During the magnesium and hydrogen reaction, at moderate pressure the hydride phase presenting in equilibrium with magnesium refers to magnesium hydride. The Mg-H phase diagram is shown in Figure 2-4, which indicates the stable phases. The reaction of magnesium hydride formation is shown as follows:



For the formation reaction to proceed, the hydrogenation temperature and pressure should be by some means below the equilibrium temperature at a given pressure to prevent the inversed reaction and confirm that each hydrogenation test was done at hydrogenation condition only. The equilibrium temperature of the hydride reaction is 287.7°C at 1 bar pressure [38]. It is required to apply enough thermal energy and fast kinetics to induce magnesium hydride to be decomposed above 300°C [26, 50, 51]. In practice, the dehydrogenation temperature is higher than this temperature in order to provide the driving force for the nucleation of new phases. Figure 2-5 shows the schematic diagram of the energy profile of hydrogen absorption and desorption processes. Even if the hydrogenation reaction is thermodynamically favorable due to

the negative Gibbs free energy, the reaction cannot take place with low thermal energy because the energy for hydrogen absorption needs to be overcome. Therefore, the catalysts are necessary to lower the energy barrier of hydrogen absorption. I will talk about the catalyst in a later section. The following section will explain the alloying effect for the reduction of formation enthalpy of magnesium hydride during dehydrogenation. In Figure 2-5, the destabilization of magnesium hydride not only reduces the formation enthalpy but also lowers the energy barrier of hydrogen desorption [43]. Baldi et al. reported that the thermodynamic properties were tuned by means of elastic clamping [52]. The pressure-composition-isotherms show that the magnesium film coated by Pd or Ni exhibits a hydrogen plateau pressure more than two orders higher than bulk magnesium at the same hydrogenation condition.

2.2.1 Pressure-Composition-Temperature (PCT) of Magnesium

Figure 2-6 shows an example of PCT curves of magnesium. First of all, hydrogen begins to dissolve in magnesium at interstitial sites and the solubility increases with increasing pressure. At low hydrogen concentration, the hydrogen solubility is proportional to the square root of hydrogen pressure [53]. When the concentration of hydrogen achieves the terminal solubility limit of magnesium at the plateau pressure, hydrides begin nucleating and hence growing. In the region of flat plateau, a solid solution of hydrogen in magnesium and MgH_2 phases coexist. Above the flat plateau, hydride transformation is complete and the slope is very sharp due to no solubility of H in MgH_2 .

The most important is the equilibrium plateau pressure during dissociation of hydrides. From Van't Hoff equation, $\ln P = \frac{\Delta H}{RT} - \frac{\Delta S}{R}$, P is equal to equilibrium pressure and T is constant in an isothermal process. The slope of the straight line

represents the stability of hydrides. Thus, the stability of hydride is measured from the relationship of plateau pressure and temperature, $\ln P/(1/T) = \Delta H/R$, which is the slope of the Vant't Hoff plot. Different temperature settings exhibit different equilibrium plateau pressures. With at least two PCT curves, we can obtain a line with a slope which corresponds to the formation enthalpy of hydrides over R.

2.2.2 Alloying Effect

Magnesium alanate, $Mg(AlH_4)_2$, with 9.3 wt% hydrogen capacity produced by chemical synthesis has been shown experimentally to release 7 wt% of hydrogen at around 135°C [54, 55]. However, theoretical calculations suggest that this alanate is metastable at room temperature and 1 bar pressure [44]. Complex hydrides are usually not reversible since the final products cannot be transformed back to the original complex hydrides; hence losing the ability for cycling. More recently, extensive research has been focused on destabilizing magnesium hydride, i.e. reducing its enthalpy of formation and/or increasing its entropy of formation. Song et al. assume that alloying elements will reduce the formation enthalpy based on the first principle calculation. If the alloying element is X, metal X thus dissolves in the magnesium lattice as a solid solution in the form as $(Mg, X)H_2$ [56]. Mechanical ball milling is one of the methods to alloy magnesium with other elements, i.e. Al [57], Ni [32, 48], Cd [32, 58], In [32], Si [18] and Sc [59, 60] which have been shown to be able to dissolve in magnesium at different solubility levels. However, the result shows that they do not change the thermodynamic properties of the formation enthalpy of magnesium hydride.

2.3 Kinetic Properties of Magnesium Hydride

2.3.1 Hydrogen Capacity of Magnesium Powders

The hydrogenation properties of commercial magnesium have been widely studied for a few decades due to its light weight, abundance, reasonable hydrogen capacity, etc. The studies go back about 50 years to the ground-breaking study of Stampfer et al. [61]. Magnesium has an ideal 7.6 H wt. % storage capability. However, it is difficult to fully hydrogenate magnesium powders. Later in the 1980s, detailed hydrogenation experiments at various temperatures and pressures were carried out by Vigeholm et al. on commercial magnesium powder [62, 63]. They concluded that any magnesium product with diameter less than 75 μ m will absorb hydrogen rapidly above 300°C under a hydrogen pressure beyond equilibrium pressure. The activation process was not required or needed only a few cycles of hydrogen absorption and desorption. The highest rate observed was around 350°C and absorption kinetics decreased with slightly increases in temperature due to the adverse effect. It was seen that the lower the hydrogen pressure, the closer the eventual reaction approached complete transformation from magnesium to single phase magnesium hydride [28]. In the initial absorption process at 400°C, it was observed that the lower the hydrogen pressure, the closer the reaction approached stoichiometric hydride 7.6 H wt. %. The hydride fraction shows 97.6% at 2MPa, 95.5% at 3.2Mpa, and only 81.5% at 4.8MPa. There is an adverse effect on hydrogen capacity as the temperature increases above 350°C owing to the competition of nucleation and growth taking place at 1.2MPa.

2.3.2 Kinetics Model of Hydrogenation of Magnesium Powders

2.3.2.1 Impingement Model

The dissociated hydrogen atoms penetrate the surface layer and diffuse inside the bulk magnesium when the hydrogen concentration reaches the solubility limit of hydrogen in magnesium; nucleation of magnesium hydride takes place [26, 30, 64]. In this system, the asymptotic hydrogen uptake as a function of time decreases with increasing hydrogen pressure [53]. The hydride nucleation reaction rate increases with increasing applied hydrogen pressure [26, 30, 65]. Theoretically, a hydrogen atom would diffuse along the interface of metal and hydride. If somewhere below the surface hydrogen accumulated, hydrides may nucleate inside the metal [26]. The kinetic energy barrier can be described by Arrhenius relationship equation that relates to the activation energy and is a temperature dependent reaction. The rate constant of most thermally activated processes is usually described well by the following equation [66-68]:

$$K = K_0 \exp(-Q/RT) \quad (2-2)$$

where K_0 is the prefactor and Q is the activation energy. The Arrhenius relationship implies that a plot of measured rate constants as a function of the reciprocal temperature results in a straight line with a slope Q/R [66]. The activation energy reported so far for hydrogenation is in the range of 66 to 308 kJ/mole.

An introductory description is given here for the nucleation and growth theory regarding the relationship between the fraction transformed and the time in isothermal transformation [69]. Consider first the individual transformed region. The size of the transformed region increases continuously as a linear function of time after $t=\tau$ (τ is called the induction period) as shown in Figure 2-7. The reduction of reaction rate is owing to the impingement of the individual transformed volumes. I^V is defined as the

nucleation rate per unit volume. It is supposed V_α is the un-reacted volume between $t=\tau$. At $t=\tau+d\tau$, some of the individual transformed regions nucleate in some arbitrary minimum size. The nucleation number of new β is in the time interval between $t=\tau$ and $t=\tau+d\tau$ is $I^\nu V_\alpha d\tau$. The extended transformed volume during this time period is $dV_{ex}=v_\beta I^\nu V_\alpha d\tau$. v_β is the volume of an individual transformed β phase. Thus the transformed extended volume of new β can be expressed as follows:

$$V_{ex}=(4\pi V_\alpha/3)\int_0^t I^\nu G^3(t-\tau)^3 d\tau \quad (2-3a)$$

G is the growth rate of new phase and 3D spherical growth is used in this case.

However, if V_{ex} is the extended volume of the new β phase the overlapped region should be taken into account. The actual V_β has a relationship with extended V_{ex} :

$$dV_\beta=(1-V_\beta/V_\alpha)dV_{ex} \quad (2-3b)$$

which can be re-written as $V_{ex}= -V_\alpha \ln(1-V_\beta/V_\alpha)$ and apply this equation to the previous one it can be summarized as following:

$$-\ln(1-f)=(4\pi V_\alpha/3)\int_0^t I^\nu G^3(t-\tau)^3 d\tau \quad (2-3c)$$

$f=V_\beta/V_\alpha$, is the volume fraction of hydride. If the nucleation rate, I^ν , and growth rate, G , are constant values, the relation can be shortened as:

$$f=1-\exp(-\pi I^\nu G^3 t^4/3) \quad (2-3d)$$

The Johnson-Mehl-Avrami equation is applied to describe reacted hydride fraction, f , as:

$$f=1-\exp(-Kt^n) \quad (2-3e)$$

where K is $(-\pi I^\nu G^3/3)$ which is related to the nucleation rate, growth rate and geometric factor; and n is the reaction order and is not temperature sensitive [39, 68, 70]. The way to investigate the hydrogenation kinetics is to analyze the hydrogenation curves and obtain K and n values. Furthermore, the activation energy and rate limiting step can be

realized based on the assumptions in the hydrogenation process. Table 2.1 shows the summary of the dependence of n on growth dimensionality, rate limiting process, and nucleation behavior as reported by Karty et al. [29, 70]. However, the listing in Table 2.1 does not exhaust all hydrogenation behaviors, but it does illustrate that in general the determination of reaction order does not provide a unique identification of the kinetics process except $n = 0.5$ or 4 . It is reported that the value of reaction order, n for hydrogen absorption of Mg_2Cu -catalyzed magnesium was equal to 0.5 and equal to 1 for hydrogen absorption for vapor-deposited magnesium [70]. Fernandez et al. reported that a nucleation and growth mechanism as illustrated by JMA equation with the reaction order $0.5-1$ for the absorption of hydrogen provides the best fit to the hydrogenation curves [68]. Fernandez et al. investigated the hydrogen absorption kinetics by using activated magnesium powders [71]. Their assumption for the hydrogenation mechanism was provided by Friedlmerier and Groll [30]. A nucleation and growth model was employed in the assumption of their model. Figure 2-8 shows the isothermal absorption divided into two cases based on the pressure dependence of the applied hydrogen pressure. Figure 2-8 (a) shows absorption for an applied pressure close to the equilibrium pressure; the rate limiting step is the chemical reaction which is proportional to the interface area of Mg/MgH_2 . The hydrogenation curve is sigmoidal. This situation is similar to solidification with very small under-cooling which results in very limited nuclei. The reaction of hydride formation eventually leads to a large fraction of a magnesium particle. An extremely slow diffusion of hydrogen is now the rate limiting step due to the very thick hydride layer [30]. In Figure 2-8 (b), under a large under-cooling, a large number of nuclei are formed around the surfaces as the applied

hydrogen pressure is much smaller than the equilibrium pressure. The transformation volume of magnesium hydride is much less than in the former case. The growth rate is much slower and a thin hydride layer is formed near the surface. The chemical reaction is excluded since no sigmoidal curve is observed. Although the initial kinetics is fast, the hydride fraction is relatively small.

2.3.2.2 Core-Shell Model

Martin et al. have given the following steps for the absorption of hydrogen: (1) physisorption of hydrogen molecules, (2) dissociation of hydrogen molecules and chemisorption, (3) surface penetration of hydrogen atoms, (4) diffusion of hydrogen through the hydride layer, (5) hydride formation at the Mg/MgH₂ interface [36]. Chou et al. suggested that only hydrogen diffusion in hydride phase is slow; the other steps all proceed very fast [35]. As seen in Figure 2-9, hydrogen first reaches the surface of the particle, is absorbed and then diffuses into hydride. When hydrogen arrives at the interface at Mg/MgH₂, a fast hydrogenation reaction takes place. The hydrogen layer becomes thicker and thicker as time increases. Finally, the hydrogenation reaction stops because the hydrogen is not able to diffuse through the thick hydride layer under that hydrogenation condition. A formula to describe the transformation fraction of absorbed hydrogen with time is shown as follows:

$$[1-(1-f)^{1/3}]^2 = -2D_H(C''-C')t/Rv \quad (2-4)$$

f: hydride volume fraction.

t: hydrogenation time.

D_H: diffusivity of hydrogen through magnesium hydride.

C'': hydrogen concentration at the interface of Mg/MgH₂.

C': hydrogen concentration in gas phase.

R: radius of the particle.

v: a coefficient that depends on substance and reaction.

The relation is particle size dependent and the hydride fraction decreases with an increase in size of particle. Therefore, unlike the nucleation and growth model, size should be taken into account in the Core-Shell model.

2.3.3 Effect of Catalyst

At the beginning of hydrogenation was the physisorption process; molecular hydrogen is first physisorbed on the surface of magnesium powders. The sticking coefficient of hydrogen and the surface properties are affected by oxide, CO and other impurities [72]. While the hydrogen molecule attaches to the surface of metals, the dissociation of hydrogen molecules takes place and the process is relative to the height of the energy barrier of hydrogen absorption [43, 73]. From Zaluzka et al. [26], ball milled magnesium powder is hydrogenated without catalyst at 300°C and 400°C. The curves show slow absorption rate of hydrogen due to the kinetics limitation. Fast hydrogenation demands the increase of kinetics by surface treatment.

In the standard condition, the potential energy of atomic 2H is much higher than that of the gas molecule H₂, as shown in Figure 2-10 [73]. When an interface is applied through a catalyst to modify the hydrogenation kinetics, the energy curve of atomic 2H is lowered and intersects with the curve of the potential energy of a gas hydrogen molecule at lower activation energy. This means the activation energy, E_a, is reduced. If E_a is less than zero, the interface becomes non-activated. When it has a non-activated interface, the potential energy of 2H decreases with increasing depth from the surface and becomes major chemical form. The potential energy of chemisorption is moderated for hydrogen to diffuse into metals.

A catalyst is mainly beneficial for dissociated absorption of a hydrogen molecule in hydrogenation [33, 74, 75]. With a catalyst of Pd, the kinetics of absorption significantly increases by lowering the activation energy of dissociation of H₂ [26, 76, 77]. Laing et al. found that Ti is the most rapid in hydrogenation while V as catalyst in dehydrogenation is the most rapid among Ti, V, Mn, Fe and Ni [27]. Gremaud et al. used Ti-catalyzed material for the study of the reversibility of magnesium alanate [78]. The drawback of Ti as catalyst is the formation of stable TiH₂ which does not allow the cycling ability [79]. The dehydrogenation can be complete at 235°C within 40 minutes using 5 at% V as catalyst but it does not change the thermodynamic properties of magnesium hydride [80]. From Charlot et al. [75], for dissociated absorption of a hydrogen molecule, transition metals produce a charge from TM-H to weaken H-H bonding and favor chemisorption. The lowering spin multiplicity might become important in chemisorption of hydrogen, and the sp orbital of Ni and the d orbital of Pd are mainly involved in the breaking of H-H bonds. Beside the transition metals, metal oxides and fluoride were considered as an alternative route in the investigation of catalyst for hydrogen storage materials [81, 82]. The catalytic effect may be attributed to the electronic exchange reaction with a hydrogen molecule which accelerates the kinetics of reaction. Oelerich et al. showed that oxides display good efficiency as metal atoms having multiple valence states [83]. It also benefits from the very high defect density introduced by metal oxides at the surface. Barkhordarian et al. reported that the desorption rate of Nb₂O₅ is the fastest among those metal oxides, Fe₃O₄, V₂O₅, Mn₂O₃, Cr₂O₃, TiO₂, Al₂O₃, SiO₂ [84]. The dehydrogenation is complete within 140 seconds at 300°C in vacuum, and it is much faster than pure V [80]. Friedrich et al. assumed at least large

part of the reported catalyst effects are due to the oxides present [85]. We cannot prevent oxides formation during such a long milling time, so the effect of metal oxides becomes important for hydrogen sorption and desorption processes. Oxides are much cheaper than pure metals for mass production, and we can add only small amounts to have a substantial effect. With 0.5 at% Nb₂O₅ addition, the desorption process completes in about 90 seconds at 300°C under vacuum which is the fastest hydrogen desorption rate so far [86].

2.4 Microstructural Analysis of Hydrogenated Mg Powders

A microstructural evaluation of hydrogenated magnesium powders in different phases of the cycling tests is supported by Figure 2-11 [87]. Figure 2-11(a) shows the polished cut image of a powder sample after first hydrogenation. The nearly spherical growing zones of magnesium hydride around the powder surface can be clearly seen and the penetration depth of hydride is not uniform. The nucleation and growth mechanism were validated by the individual growth of surrounding hydride grains near the powder surface. Figure 2-11(b) displays the cross sectional images of powders hydrogenated after a series of long term hydrogenations. The hydrogenation and dehydrogenation conditions are 350°C under 25 bars and the same temperature under 10bar, respectively. The cycling time for long term is 6 hours. The cross sectional images exhibit a continuous hydride layer with a relatively smaller fraction of hydride in the powders. Figure 2-11 (c) reveals the cross section of hydrogenated powder after a few short-term hydrogenations. Short-term means the cycling time is 2 hours. The hydride distribution is observed as a thinner layer than the hydrogenated powders after a series of long-term cycling. In Figure 2-11 (d), after a series of short term cycling, the

hydrogenated powder shows the thinnest hydride layer among all the cycling conditions. It can be concluded that the surface condition is very important to the hydrogenation behavior, and also the final hydrogen capacity. After a series of short-term cycling tests, it is suggested that a large number of nucleation sites form and they favor the nucleation of magnesium hydride.

2.5 Effect of Shape and Size on Hydrogen Capacity of Metal Hydride

The kinetics of hydrogenation and dehydrogenation of metal hydrides have been improved mechanically by increasing the surface to volume ratio, the grain boundaries, reducing the grain size and enhancing the hydrogen diffusion within the metal bulk which leads to the increase of hydride fraction [88]. The effect of size of magnesium particles on hydrogenation kinetics has been investigated by many groups, and mechanical ball milling has been used to reduce the particle size in nano-scale and also reduce the grain size of the particles. The hydrogen kinetics is relatively fast in the milled magnesium powder sample and also the hydrogen capacity of milled magnesium particles is higher than that of un-milled ones. However, the effect of shape of magnesium particles on hydrogen capacity has not yet been investigated in depth. Mint et al. concluded that the shape variation of the powder particles can be ignored [89]. Chernov et al. studied the influence of magnesium powder's shape on the kinetics of hydriding by using a more complicated model than the former study. Three different shapes of sphere, cylinder, and plate are considered for their computer simulation. The Core-Shell model has been used for their model development and assumption. The result reveals that the effect of change in powder geometry is not drastic [90]. Jeon et al. use the High Speed Orbital Ball Milling (HSOBM) to produce the magnesium flakes [88]. Their result shows that the hydrogen capacity of magnesium flakes is 4.57 H wt. %

by using TGA for the prediction of hydrogen absorption. Unfortunately, no hydrogenation data is obtained for the spherical magnesium particles. They have described that, for the magnesium flake, the flux area remains constant with respect to the hydrogen penetration depth but for the magnesium spherical particle the flux of hydrogen decreases dramatically with increasing hydride thickness. This is clearly the assumption from the Core-Shell model which suggests chemical reaction is the rate-controlling step during the hydride growth.

Table 2-1. Dependence of n in the JMA equation

Rate limiting step	Growth dimensionality	n	
		Constant nuclei number	Constant nucleation rate
Diffusion control	1	0.5	1.5
	2	1	2
	3	1.5	2.5
Interface control	1	1	2
	2	2	3
	3	3	4

*[70]

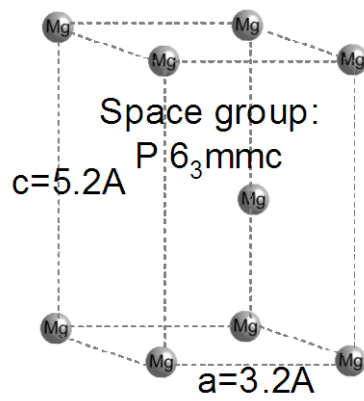


Figure 2-1. The crystal structure of hexagonal closed packed (HCP) Mg.

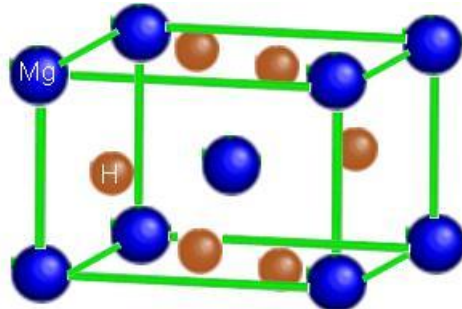


Figure 2-2. The crystal structure of tetragonal magnesium hydride.

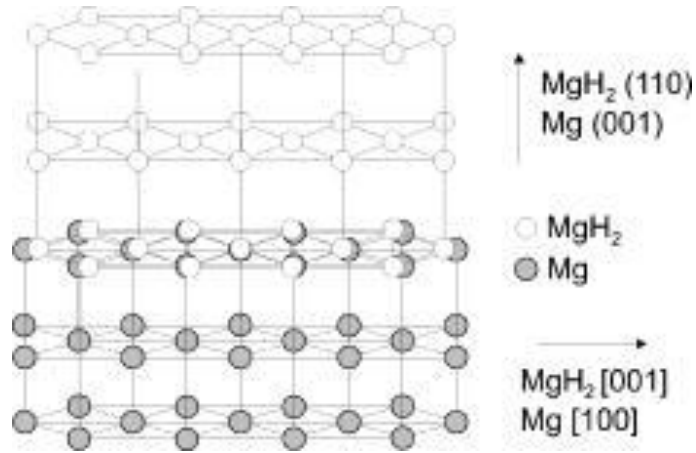


Figure 2-3. Schematic illustration of the likely epitaxial growth mode of MgH₂ on Mg on (001) Al₂O₃ in the MgH₂ (110)[001]/Mg(001)[100] relationship. For clearness, only the Mg atoms in MgH₂ are shown. [42]

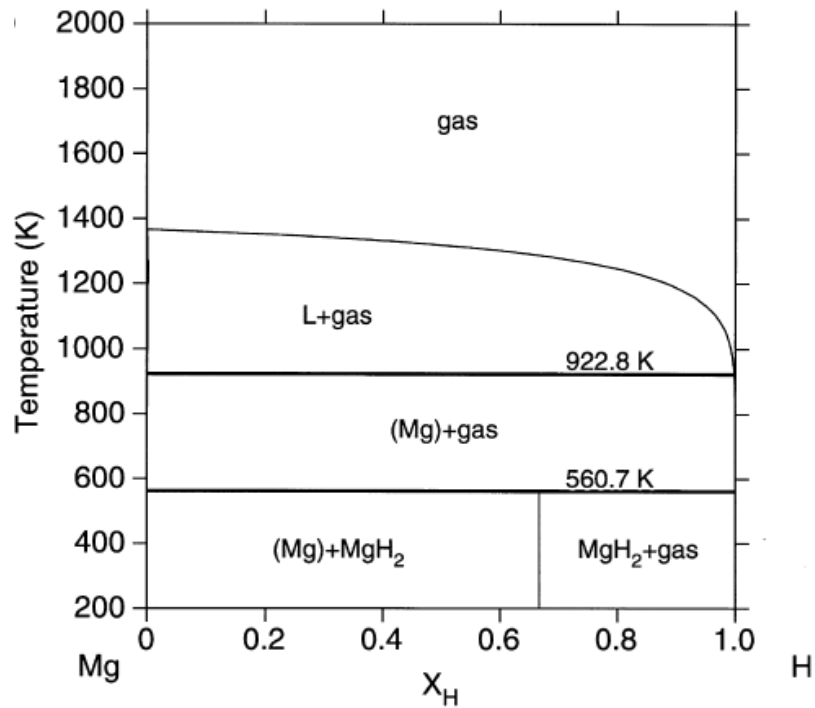


Figure 2-4. Mg-H binary phase diagram at 1bar (0.1MPa) hydrogen pressure.

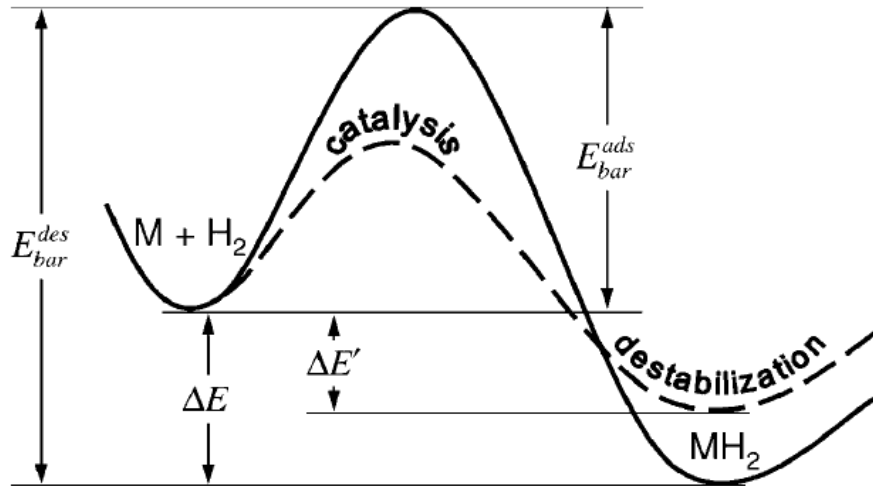


Figure 2-5. Energy barriers for hydrogen absorption and desorption.

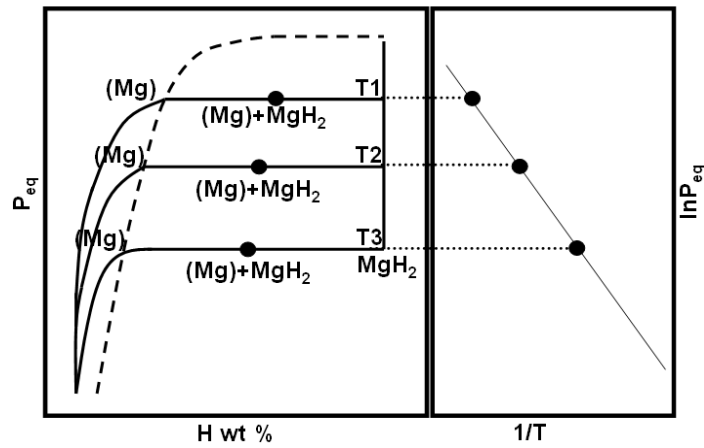


Figure 2-6. PCT curves and Van't Hoff plot at different temperature ($T_1 > T_2 > T_3$)

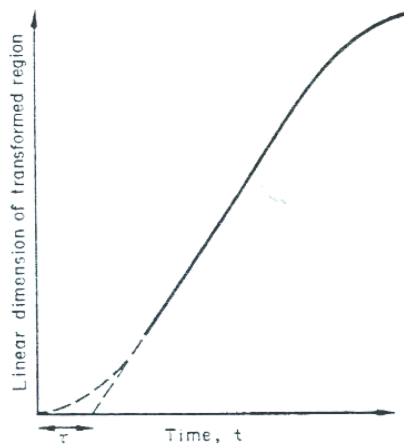


Figure 2-7. The schematic growth of a product region.

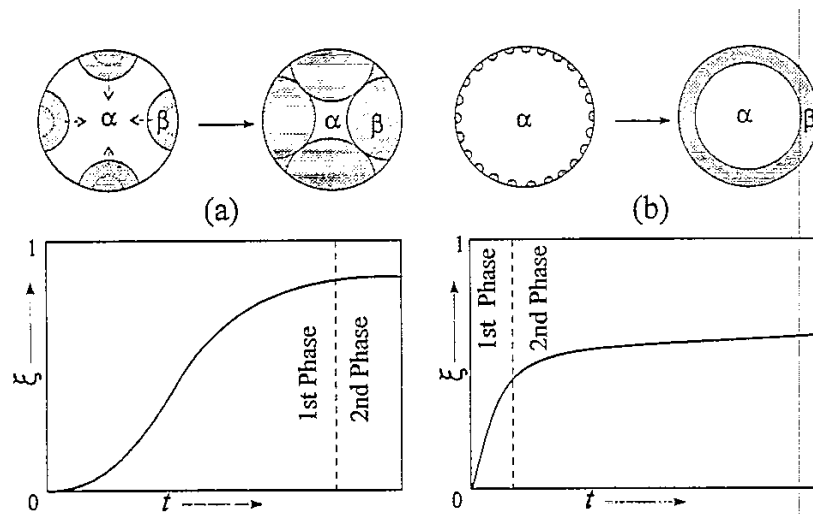


Figure 2-8. Cross-section of a magnesium particle at two different times and typical $\xi=f(t)$ curves for hydriding at A) $P \sim P_{eq}$ and B) $P \gg P_{eq}$.

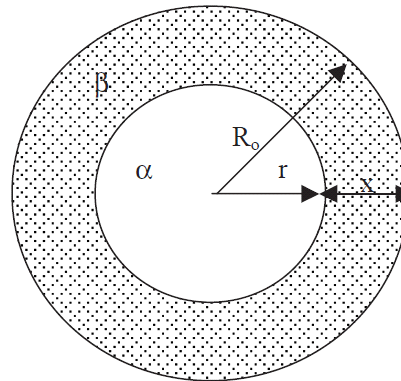


Figure 2-9. A schematic diagram for Core-Shell hydrogen absorption model.

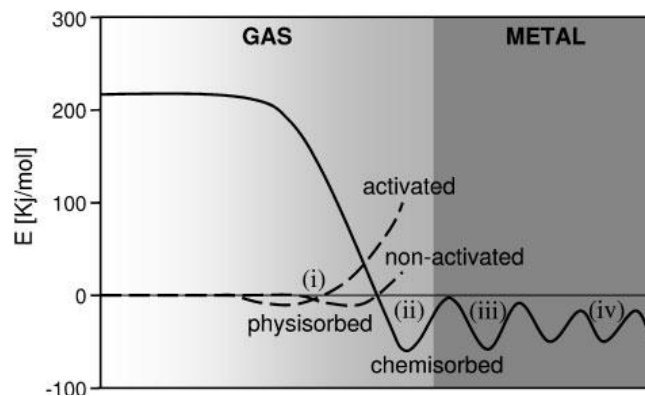


Figure 2-10. Potential energy curve for hydrogen binding to a metal surface which shows: (i) physisorption for both activated and non-activated processes; (ii) dissociation of hydrogen molecules and chemisorption; (iii) surface penetration and chemisorption; and (iv) diffusion of hydrogen atoms. [73]

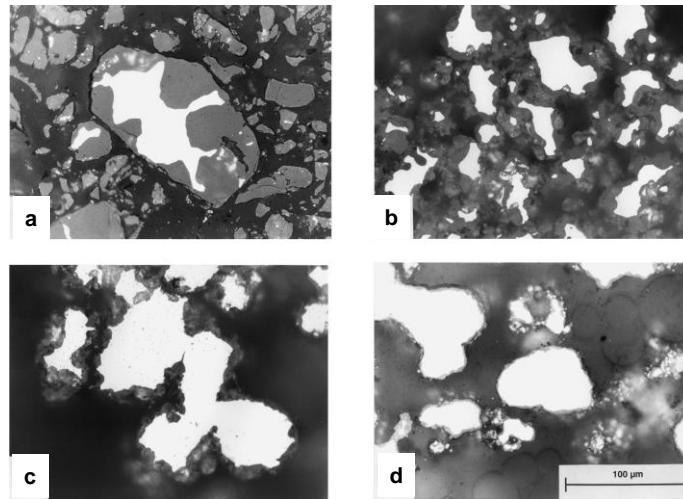


Figure 2-11. Microstructural analysis of hydrogenated magnesium powders after (a) first hydrogenation, (b) a series of long-term cycling test, (c) a few short-term cycling tests, and (d) a series of short-term cycling test.

CHAPTER 3 EXPERIMENTAL PROCEDURES

The ideal high hydrogen capacity 7.6 H wt. % of magnesium was considered the most promising material for on-broad hydrogen storage material. However, high desorption temperature and low kinetics are the major drawbacks of magnesium hydride. A fundamental model of magnesium hydride formation regarding thermodynamics and kinetics properties needs to be developed to enhance the efficiency of hydrogen absorption and desorption. Magnesium powders were extremely sensitive to oxygen and moisture; therefore, all the handling and coating were conducted in an argon filled glove box or argon atmosphere environment. The glove box was maintained at very low oxygen and moisture levels to avoid any contamination during handling of powders. Figure 3-1 shows the appearance of the glove box manufactured by Vacuum Atmosphere (Model: Nexus and Part Number: 100026). Figure 3-2 displays the screen which shows the oxygen and moisture level. The oxygen concentration is maintained below 0.5ppm at all times. Moisture level is kept below 2ppm (Dew point = -72°C). In this study, commercial $44\mu\text{m}$ and $300\mu\text{m}$ pure magnesium powders were used for various purposes of experiments, i.e. effect of size and shape. A catalyst was added to lower the energy barrier of the dissociation of hydrogen molecules to ensure that the continuous hydrogen source and other mechanisms interested were disclosed. The Ni coated magnesium powders were hydrogenated using a hydrogenation part of our house built Hydrogenation/Dehydrogenation unit. Desorption of hydrogenated powders was conducted using the isothermal dehydrogenation part of the Hydrogenation/Dehydrogenation unit. The other dehydrogenation test was done by using Thermal gravimetric analyzer (TGA) which

allows a constant heating rate during the hydrogen release. The microstructure of the magnesium powders at different stages of hydrogenation/dehydrogenation processes was analyzed using SEM/BSE mode to study the hydride distribution by phase contrast. The material processing procedures, analytical testing and the sample preparation for various characterization techniques applied in this research are explained in this chapter. Surface to volume is believed to influence the hydrogenation behavior. For the effect of shape, magnesium flake powders were made via HSOBM which applied shear force to the sphere particles and hence changed the shape of the magnesium powder from sphere to disk particles.

3.1 Material Fabrication

3.1.1 Addition of Catalyst by Theta Composer

To enhance the kinetics of hydrogen absorption and desorption magnesium powders they were coated with a catalyst. Many 3d transition elements are employed as catalysts for hydrogenation and dehydrogenation of magnesium powders. Ni is one of the effective catalysts that exhibit improved kinetics in these processes since a charge transfer from nickel to hydrogen weakens the bonding between H–H. Hence, the activation energy of hydrogen molecule dissociation is reduced. In this study, we employed a dry coating process using the Theta Composer. 10 gram Mg/nano-Ni mixture with 2 wt. % nickel nano-particles (Argonide 70nm) and pure magnesium powder (Alfa Aesar 44 μ m) in a batch was loaded in the Theta Composer chamber inside the glove box and entirely sealed. The Ni coating procedure was conducted under Ar atmosphere, which was at the same condition in the glove box. The nickel coating was conducted at the optimum condition of 4600 rpm rotor speed, 70 rpm vessel speed and 1 mm gap between vessel and rotor. The schematic of the Theta

Composer is illustrated in Figure 3-3. Only 44 μ m magnesium particles were employed by the Theta Composer Ni coating process. This material was used for the hydrogenation/dehydrogenation tests and JMA kinetics analysis in the Chapters 5, 6 and 8.

3.1.2 Addition of Catalyst by Organometallic Nickel Solution

For the limited amount produced in magnesium flakes by HSOBM, Organometallic solution was used for the Ni coating of a small amount of powder. This coating operation needs to be employed inside the glove box to avoid the exposure of magnesium powders to oxygen and moisture. An organometallic based Ni compound was used and the procedure was illustrated in the Patent: 4,554,152. The source of Ni is the dissociation of Bis-(1,5) cyclooctadiene Ni (Strem Chemicals, 98.3% purity). A schematic illustration of the Ni-coating setup is shown in Figure 3-4. The organometallic Ni and the magnesium powders were taken in 0.118:1 proportion and were refluxed in a flask with toluene at 110°C for 6 hours. In this study, 12 milling tests were done to collect 1.2g flakes for at least 4 hydrogenation tests including the consideration of reproducibility. The result will be shown in Chapter 7. For 1.2g magnesium flakes, 0.1416g organometallic Ni is used for high coating efficiency. A long jacket was attached to the top of the flask so that the toluene vapors are condensed on the walls and fall back into the flask, called refluxing. During the refluxing process, Ni nano particles break away from the organometallics compounds and attach onto the magnesium powder surface. After 6 hours, the Ni coated magnesium powders were collected by filter paper for the following hydrogenation tests. In Chapter 7, 3 powder samples were used by this coating method. 1.2 gram of magnesium 44 μ m, 300 μ m and flakes powders was coated by organometallics Ni in the same coating condition. Size

effect will be evaluated between 44 and 300 μ m magnesium particles and shape effect will be discussed between 300 μ m sphere and flakes powders.

3.1.3 High Speed Orbital Ball Milling (HSOBM)

Ball milling was the most common method in the mechanical processing of alloy powders with reduction of size and change in shape. Figure 3-5 shows the HSOBM. It has a sealed milling tube through which magnesium powders are loaded inside the glove box. The milling tube has been machined to the dimensions shown, threaded on one end, and sealed with an end cap. Figure 3-6 shows how the shear force is applied to the magnesium powder to change the shape of the particles from spheres to flakes. Under argon atmosphere, 0.1gram of Alfa Aesar magnesium powder and a 6 mm in diameter 52100 chrome-steel ball with Rockwell C hardness 63-65 (Norstone Inc) were loaded into a 316 stainless steel milling tube. The powder was then milled in the HSOBM using various combinations of starting powder size and milling speed/time. Milling speed in the HSOBM was controlled via a variable transformer and the speed was measured using an optical tachometer. The flake powders will be mounted and the mounting was cut perpendicularly to the polishing surface, as shown in Figure 3-7 for the thickness measurement of flakes or the hydride layer of hydrogenated flake powders. Figure 3-8 displays the relationship between the applied voltage and the milling speed in RPM, which is measured by a laser speed gun. The milling speed increases with increasing voltage.

3.2 Hydrogen Absorption

3.2.1 Hydrogenation Setup

Figure 3-9 displays the house-built Hydrogenation/Dehydrogenation unit. Figure 3-10 presents the schematic diagram of the Hydrogenation/Dehydrogenation unit with

electrical connections. All the tubing used to compose the system was from Swagelok and was fixed using corresponding pressure fittings and VCR connection to avoid any leakage. The hydrogenation setup is on the bottom side of the whole unit, which is referred to the high and low pressure regulator with the rest of the tubing including the reservoir chamber and specimen chamber. The hydrogen absorption measurement by time was based on the volumetric method (Siverst' type instrument). Basically, the left side of the regulator controls the hydrogen pressure at a desired constant value, which means the hydrogen pressure in the specimen chamber is kept the same during the experiment and the reservoir chamber acts as a source of hydrogen tank which keeps supplying the hydrogen gas through the regulator to the sample powder to keep the pressure constant at the specimen chamber. The high pressure regulator is not used in this study and its highest operating pressure is 3MPa. The low pressure regulator has 0.25% accuracy in the range from 0 to 1.5MPa and this regulator was used for all the hydrogenation tests in this study. A pressure transducer (PX880-1KGi) which can operate between 1-1000 psi was located at the middle of the hydrogenation step and it has very high accuracy of 0.2%. The pressure transducer is connected to a two-way valve. This two-way valve can be either pointed to the specimen chamber or to the reservoir chamber. Before the data recording starts, the pressure change in the specimen chamber was measured to ensure a constant pressure. After the hydrogenation starts, the two-way valve was pointed to the reservoir chamber to measure the dropping pressure by time. The analog signal from the voltage change was converted to a digital signal from the pressure transducer to an Omega A/D converter (DAQ 55) and simultaneously the pressure was also observed using the Omega

pressure indicator (DP25B-E). An Omega J-type thermocouple (TJ36-ICSS-180-6) inserted into the specimen chamber was located as close as possible onto the sample surface. The thermal couple was connected to two places. One was to a temperature controller (Glas-col heater) and the other was to the A/D converter for recording real time data. The temperature controller has the ability to use PID (Proportion; Integration; Derivative) 3 parameters to precisely control the temperature within $\pm 0.5^{\circ}\text{C}$ in an auto-tuning mode. Another thermocouple was attached on the surface of the reservoir chamber to indicate the temperature of the hydrogen gas and this was maintained at room temperature by using another temperature controlling system (See Figure 3-8). The reservoir chamber was wrapped by a copper tube which has in/out plug onto the system to circulate water. The temperature of the reservoir chamber was maintained at 24.5°C to avoid the noise signal generated from the room temperature change. The thermocouple attached on the reservoir chamber was also connected to the A/D converter. The pressure and temperature data were sent instantaneously from the A/D converter to the computer program LabView 8.0.

3.2.2 Hydrogenation Procedure

After the powder sample was loaded inside the glove box, the hydrogenation chamber was attached to the Hydrogenation/Dehydrogenation unit. Prior to hydrogenation of the magnesium powder, a leak test was conducted at a hydrogen pressure of 1MPa for one hour to check the system. The powder was loaded and sealed in a stainless steel hydrogenation chamber under the argon atmosphere in a glove box. The whole setup was connected to high purity Ar gas (Airgas, 99.99999 %), high purity hydrogen gas (Airgas, 99.99999%) tanks and gas was removed via a mechanical pump. The unit was flushed three times with argon and finally with hydrogen

to a pressure of 3 Pa. The chamber was heated using a wrapped heater rope (Omega FGR-030). Considering that the nucleation rate of the hydride phase at a given pressure is proportional to the driving force, we designed two methods for hydrogenation. In Method I, the specimen chamber was first pressurized with hydrogen to 1MPa and then the temperature was raised at an approximate rate of 12°C/min from room temperature to 210°C. During this procedure, the pressure sensor was directed toward the hydrogenation chamber and the valve located after the pressure regulator was closed such that no hydrogen would flow from the reservoir chamber to the specimen chamber. Upon heating, initially the gas expansion in the hydrogenation chamber resulted in an increase in the pressure and it reached a maximum value of 1.13MPa, at which point the pressure dropped upon further hydrogen absorption. The pressure saturated at the level of 0.85MPa after 75 min. The amount of hydrogen absorbed was estimated using the pressure decrease as calculated from the following equation:

$$dP = P - P_0$$

where P and P_0 are the pressure values inside the chamber at time t obtained during testing an empty chamber and during the hydrogenation test, respectively. Figure 3-11 shows the real time calculation of dP by subtracting the pressure change during the heating of an empty chamber test. Any effect of heat release owing to the exothermic nature of the hydrogenation reaction on the temperature change was ignored. However, this change is expected to be very small because the temperature registered as a function of time during hydrogenation test was similar to that recorded during the test with an empty chamber. The total number of moles of hydrogen atoms absorbed for Method I, n , was estimated assuming the ideal gas equation.

$$n = 2(V_1dP/RT_1 + V_2dP/RT_2)$$

where V_1 is the volume of the specimen chamber which is at the hydrogenation temperature of T_1 and V_2 is the volume of the tubing between the specimen chamber and the pressure sensor which is at the room temperature of T_2 , and R is the ideal gas constant. The second approach, Method II, consisted of first heating the specimen chamber under a low partial pressure of hydrogen (approximately 3 Pa) up to 210°C and then increasing the pressure to 1MPa. For this method, the reservoir was pressurized initially to 1MPa and the pressure regulator was kept open during the hydrogenation process. As the sample absorbed hydrogen, the pressure regulator allowed the flow of hydrogen from the reservoir to the specimen chamber such that the pressure remained constant in the specimen chamber throughout the test. The amount of hydrogen absorbed was calculated from the pressure drop measured in the reservoir chamber, which was at room temperature. Again, the ideal gas equation was employed to compute the amount of hydrogen absorbed from the measured pressure changes in the reservoir. The total number of moles of hydrogen atoms absorbed, n , for Method II was estimated assuming the ideal gas equation:

$$n = 2VdP/RT$$

V is the volume of reservoir, dP is the pressure drop during hydrogenation, and T is a constant hydrogenation temperature. Each test was repeated twice to ensure the consistency of the results. After hydrogenation, the samples were stored in the glove box under low oxygen pressure and moisture level. Method I was applied only in Chapter 6, the effect of change in the hydrogenation procedure. Other than that, Method II was mainly used in this study.

3.3 Hydrogen Desorption

3.3.1 Dehydrogenation Setup

Figure 3-10 presents the schematic diagram of the Hydrogenation/Dehydrogenation unit with electrical connections. All the tubing used to compose the system was from Swagelok and were fixed using the corresponding pressure fittings and VCR connection to avoid any leakages. The dehydrogenation setup is on the top side of the whole unit, which is referred to the back pressure regulator, with the rest of the tubing including reservoir chamber and specimen chamber. The hydrogen desorption measurement by time was also based on the volumetric method (Siverst' type instrument). Basically, the left side of the back pressure regulator controls the hydrogen pressure at a desired constant value, 0.1MPa, which means the hydrogen pressure in the specimen chamber is kept the same during the experiment. The excess hydrogen gas produced during dehydrogenation goes through the back pressure regulator to keep the pressure constant at the specimen chamber. The hydrogen pressure increases in the reservoir chamber can be calculated as the real time drawings of dehydrogenation curves. The heat transfer was considered in the setup while removing the hydrogen gas following the hydrogenation test. The gas temperature reached equilibrium at room temperature rapidly owing to a temperature control (NESLAB RTE 140) system which kept the reservoir chamber at 24.5°C.

3.3.2 Dehydrogenation Procedure

After the sample has been hydrogenated, a dehydrogenation test is performed immediately after the hydrogenation. Usually the dehydrogenation temperature is set higher than the hydrogenation temperature, i.e. 210°C at hydrogenation and 300°C at dehydrogenation. The trickiest part is the pressure setting during the heating process.

The pressure setting was managed close to the equilibrium pressure of the desired temperature to assure that neither hydrogenation nor dehydrogenation takes place during the heating process. The purpose is only to reduce any interference and keep the same condition of hydrogenated powders during the heating process. For example, the pressure setting for 300°C during the heating process is 0.07MPa lower than the equilibrium pressure of 300°C. This extremely small amount of hydride formation can be ignored in this short time which is always less than 10 minutes in this time period since the hydrogen pressure is very low. The dehydrogenation starts when the dehydrogenation temperature is reached. During the dehydrogenation experiments, 0.1MPa hydrogen pressure is kept constantly in the specimen chamber the whole time by using the back pressure regulator which allows the reverse flow of hydrogen gas from the specimen chamber to the reservoir chamber. The amount of hydrogen desorbed was calculated from the pressure change measured in the reservoir chamber, which was at room temperature and whose temperature was measured continuously over time. The total number of moles of hydrogen atoms desorbed was estimated assuming the ideal gas equation from the measured pressure increase in the reservoir chamber.

$$n = 2VdP/RT$$

V is the volume of reservoir, dP is the pressure increase during dehydrogenation, and T is a constant dehydrogenation temperature.

3.3.3 Thermal Gravimetric Analyzer (TGA)

In addition to the dehydrogenation study in the house-built Hydrogenation/Dehydrogenation system, the kinetics study of hydrogen release experiments was carried out in TGA (Setaram setsys). The two results of experiments

are not comparable because the heating procedure in TGA is not isothermal and the heating rate is set to be 5°C/minute. The sample powder was heated from room temperature to a maximum temperature. 350°C is usually the highest temperature used for the release of magnesium hydride in TGA. During the heating process the changes in the weight of the sample were observed as a function of time and temperature. The weight loss by the hydrogenated sample during the experiment confirmed the reaction was taking place in the material and the weight loss indicates the amount of hydrogen released. Unlike the in-situ test in the house-built system, the hydrogenated powder needs to be removed from the specimen chamber inside the glove box. The hydrogenated sample powders were brought out of the glove box using a vacuum container. The powder was removed from the vacuum chamber and was weighed precisely at 12 mg. After recording the initial weight, the sample was loaded into the TGA chamber. The weight loss during the experiment corresponds to the amount of hydrogen released from the material expressed in wt% and was calculated by using 12 mg as the initial weight of the sample. An empty crucible test was performed to remove the instrumental error from the measured weight loss. The same crucible was used in the same conditions. The weight loss observed during this experiment was subtracted from the weight loss in the previous experiment. The weight loss subtracted after the empty crucible run indicates the actual amount of hydrogen present in the powder. After the temperature had reached 350°C the furnace was cooled rapidly to room temperature at the rate of 100°C/minutes to keep the microstructure at that temperature. The corresponding SEM (BSE mode) microstructural analysis was carried out on the partially or fully dehydrogenated powder samples.

3.4 Analysis Methods and Characteristic Techniques

3.4.1 Particle Size Distribution

The particle size distribution after Ni coating was measured using a Coulter LS 13320 laser diffraction system. It is assumed that laser scattered from a spherical particle is a function of angle, size and shape of the particle; incident wavelength; and the refractive index of the material to light. The scattering behavior obeys the Mie model, which is the solution to Maxwell's equations for the interaction of spherical particles with electromagnetic plane waves. More than a hundred detector array allows equations to solve for the unknown numbers of particles for each size. A 780 nm laser diode, light source, is used for analysis in the size range from 400 nm to 2 mm. In this study, the experiment for micron-sized particles within this range was conducted using this laser diode. A tungsten halogen bulb and filters assembly sizes in the range 40 to 800 nm. Isopropyl alcohol was used for the proper mixing of the powders and also enhances the resolution of the measurement.

3.4.2 Scanning Electronic Microscope (SEM)

For the metallographic preparation of the samples, a small amount of powder was brought outside and embedded in an epoxy resin at room temperature. Due to the reactivity of magnesium, oil was used during the mechanical polishing processes and the samples were never exposed to water, otherwise the artificial contamination disturbs composition analysis at SEM (BSE mode). A thin layer of carbon coating was used to increase conductivity. Microstructural evaluations were conducted using a JEOL 6400 scanning electron microscope (SEM).

3.4.3 Optical Microscope (OM)

After the powder sample was polished, it was examined under an optical microscope (Leica DM2500M). The software attached for the image capture and various kinds of measurement is ProgRes CapturePro 2.7. The eyepiece is equipped with a digital camera (Jenoptik ProgRes C5) with a real time image displaying in the software. Magnesium looks brighter and magnesium hydride appears darker under OM. Magnesium is a conductor which reflects the incident visible light and magnesium hydride has a large band gap which absorbs the light relatively easily. Furthermore, the interface at the phase contrast between magnesium and magnesium hydride can be easily seen from the cross section images. The software was also used for the measurement of the hydride thickness and the geometry of the magnesium flakes, i.e. thickness.

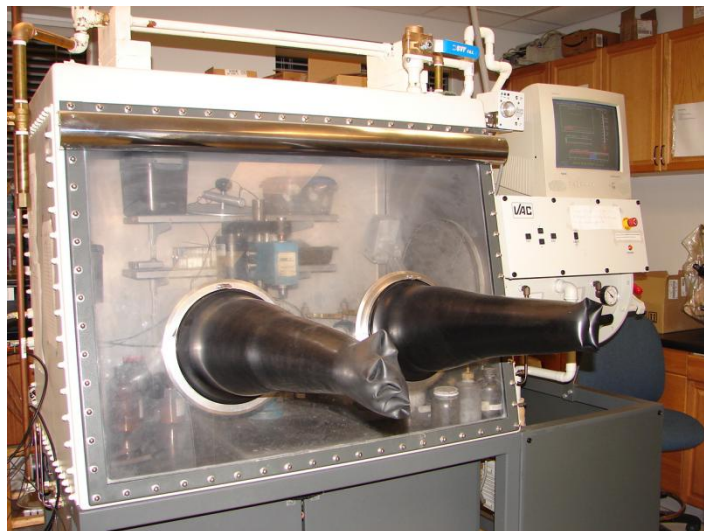


Figure 3-1. Glove box (Vacuum Atmosphere, model: Nexus)



Figure 3-2. Monitoring the O₂ and moisture level

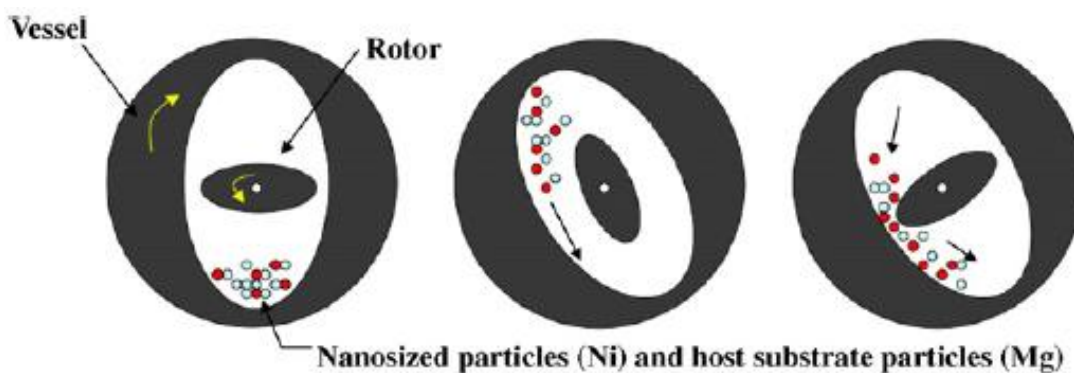


Figure 3-3. Theta Composer Ni coating

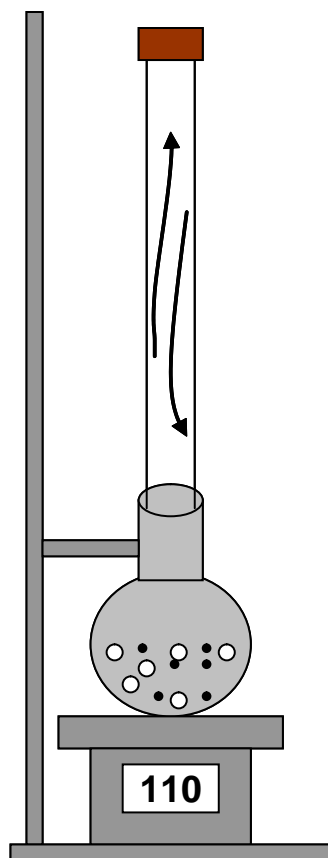


Figure 3-4. Organometallic Ni coating. Black dot represent nano-Ni particles and white one is the magnesium powder. 110°C is the operating temperature. The arrows illustrate the cycling of toluene in the beaker.

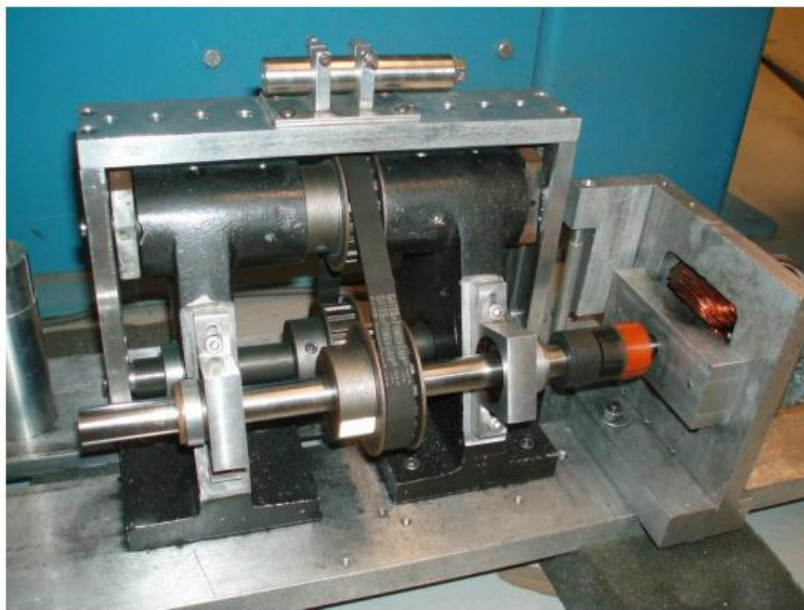


Figure 3-5. HSOBM milling

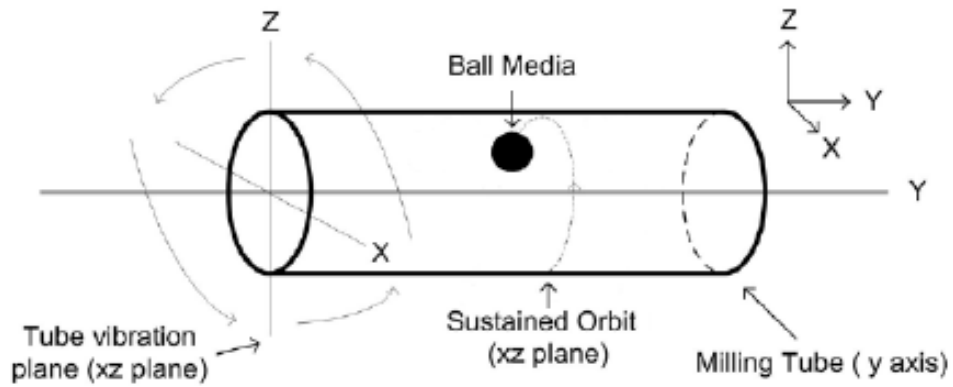


Figure 3-6. Schematic illustration of HSOBM milling

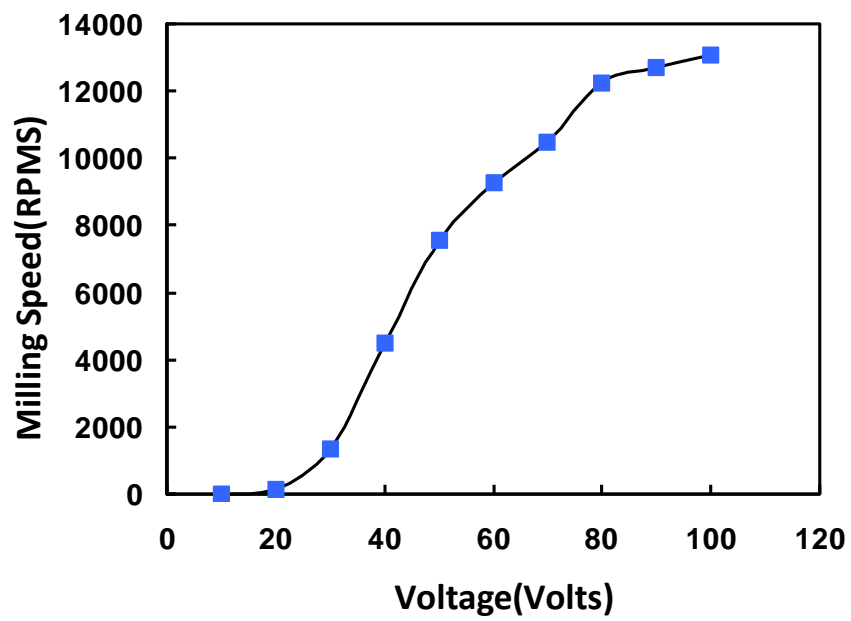


Figure 3-7. The relationship between applying voltage and milling speed.



Figure 3-8. Mounting sample cut perpendicularly to the flake surface for thickness measurement.

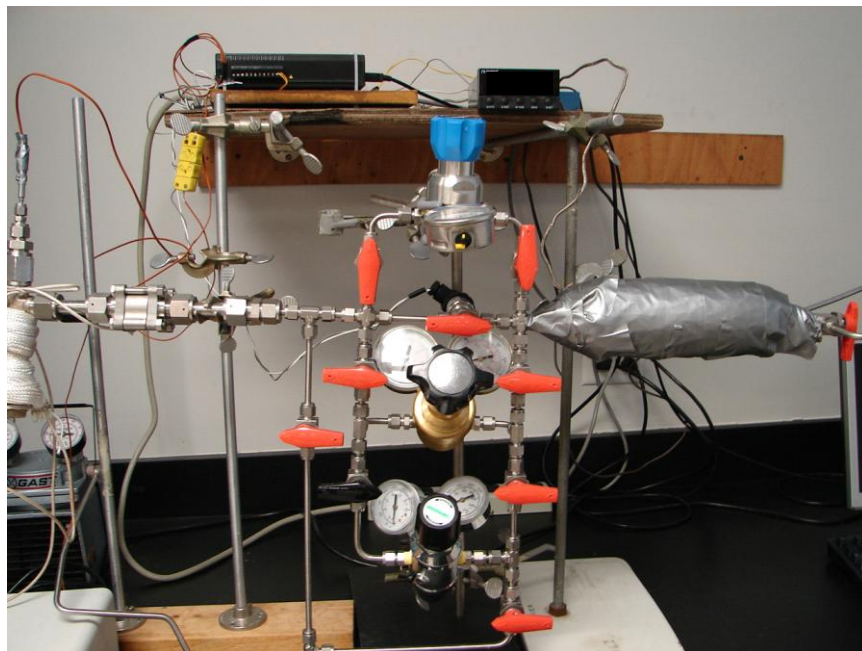


Figure 3-9. H/D system actual view

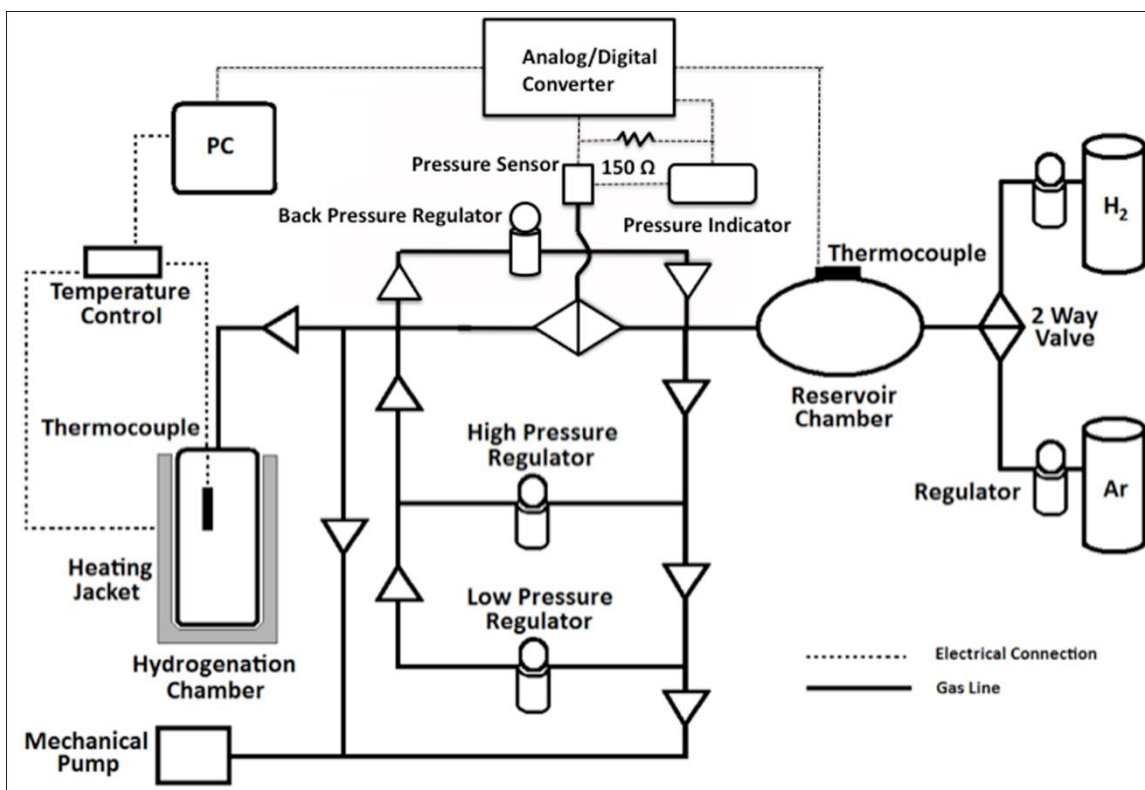


Figure 3-10. Schematic diagram of Hydrogenation/Dehydrogenation unit.

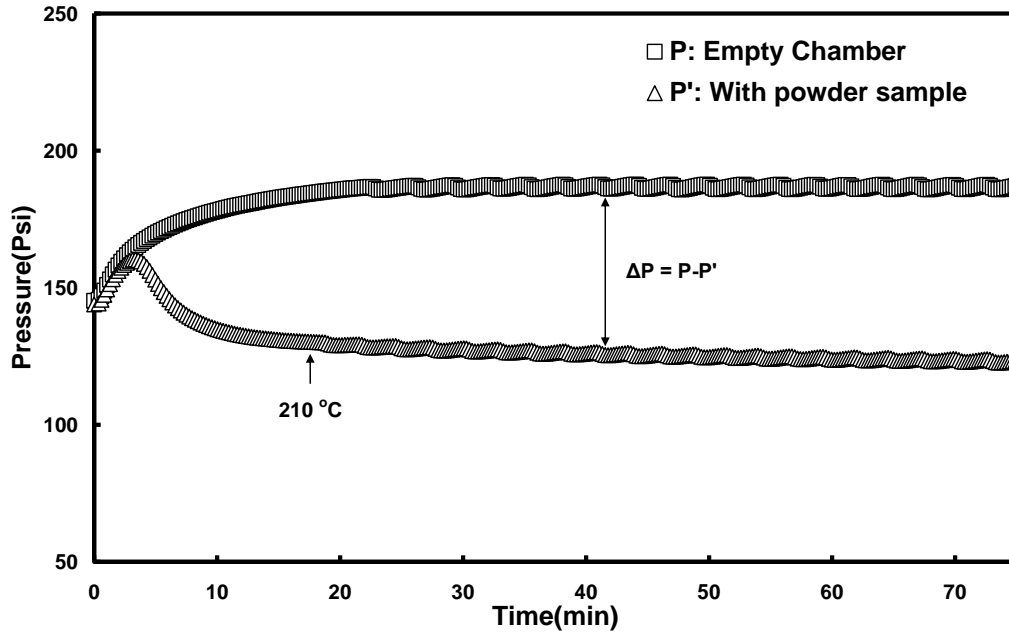


Figure 3-11. The illustration of the calculation of pressure drops in Method I.

CHAPTER 4 CHARACTERIZATION OF POWDERS

This chapter presents the characteristics of magnesium powders used in this research prior to hydrogenation processes. The powder morphology, phase distribution, and microstructure have been studied and described by using optical or scanning electron microscopes. The distribution of particle sizes in the powders has been analyzed via laser scattering and/or direct measurement from cross-sectional images obtained by metallography. Two different sizes of powders have been used, 44 and 300 μm average diameter. The 44 μm magnesium powder was used for most experiments in this study, i.e. the effect of temperature, study of hydrogenation mechanism and dehydrogenation study. The 300 μm magnesium powder was employed to investigate the effect of particle size and shape on the hydrogenation properties. A Ni coating (see Chapter 3) was the catalyst used to enhance the dissociation of hydrogen molecules on the surface of magnesium particles. The presence and distribution of the nano-size Ni particles were evaluated using the energy dispersive spectroscopy (EDS) technique in SEM.

4.1 Characteristics of the As-Received Mg powders

4.1.1 44 μm Mg Powder

Fig. 4-1 shows the particle size distribution of magnesium powder obtained by the Coulter LS 230 system. The average diameter based on the volumetric percentage was measured to be 44.29 μm , which is similar to the average size suggested by the Alfa Aesar Company for this powder in the as-received condition. Fig. 4-2 presents an SEM picture showing the size and the shape of the as-received 44 μm magnesium powder. The shape of the particles is not spherical and is more like a prolate spheroid. Figure 4-

3 shows the powder cross sectional images of as-received 44 μ m magnesium powders. In the schematic presented in Figure 4-4, possible cross sectional images are illustrated. The shape and the average size of the particles were characterized by measuring the aspect ratio a/b (a is the short axis and b is the long one) and the $(a+b)/2$ from the cross sectional images obtained from the polished samples. Obviously the cross section we see depends on how the particle has been cut. In general, the shape of the image does not represent the shape of the whole particle. Figure 4-5 exhibits the particle size distribution of the as-received 44 μ m magnesium powder based on the number frequency, Figure 4-5(a) and volume frequency, Figure 4-5(b). The average diameter from the measurement of number percent is 29 μ m and from that of volume percent is 32 μ m. The average particle size measured from cross-sectional images is smaller than the average size obtained by the laser technique. This difference may arise from the number of samplings. More samplings would help the accuracy of the particle size measurement.

4.1.2 Characteristics of the 300 μ m Mg Powder

Figure 4-6 presents the SEM picture showing the particle geometry of the as-received 300 μ m magnesium particles. Figure 4-7 shows the cross-sectional optical image of the as-received 300 μ m magnesium powder. Quantitative analysis of the shape of the particles in this powder using the optical images revealed that the aspect ratio is 0.67 although the powders look spherical in Figures 4-6 and 4-7. Figure 4-8 presents the particle size distribution of 300 μ m magnesium particles based on the number frequency, Figure 4-8(a), as well as volume fraction, Figure 4-8(b). The average particle sizes based on these analyses were 436.26 μ m and 438.57 μ m, respectively.

4.2 Characteristics of Mg Flakes

In order to investigate the effect of particle shape, as was described in section 4-3, flakes were produced using HSOBM. The evaluation of the particles produced under different conditions revealed that the thinnest cross-sections could be obtained at the highest voltage achievable in the HSOBM system. Figure 4-9 shows the thickness distribution for the particles milled for only 20 seconds at 100V. Particles with a very broad thickness distribution and an average thickness of 100 μ m were observed after the HSOBM milling. As the milling time was increased to 1 minute the distribution shifted to smaller thickness values, as shown in Figure 4-10. For the particles milled for 2 minutes, thickness was measured using more than 50 flakes and the thickness distribution is shown in Figure 4-11. The thickness of the flakes ranges from 14 to 68 μ m and the average thickness is 36 μ m. Figure 4-12 shows the thickness distribution for the powder milled at 110V for 2 minutes. The thickness distribution shifts more to the left by 110V compared with that by 100V milling. However, this milling test was done only once since the limitation of the vibration system is no more than 100V. So for safety it was not possible to produce thinner particles unless the design of the vibration system was changed or the loading increased. Figure 4-13 displays the cross-sectional optical images of the magnesium flakes. The thickness can be measured directly by this cross section image since the flake was cut at the center and perpendicular to the flat surface as described in Chapter 3 (Figure 3-5). Quantitative evaluations showed that the aspect ratio was reduced drastically from 0.67 to about 0.05 due to the milling process. Figure 4-14 presents the SEM image of the as-milled 300 μ m magnesium flakes. In comparison

to Figure 4-6, the particles show a definite change in the shape from semi-sphere to disk.

4.3 Characteristics of Ni-coated Mg Powders

4.3.1 Ni Coating Using Theta Composer

In order to enhance the dissociation of hydrogen molecules on the surface of magnesium powders, nano-size nickel particles were added as a catalyst. Most of the experiments in this study were done using this material, i.e., the 44 μ m magnesium powder coated with Ni using the Theta Composer. Figure 4-15 displays the particle size distribution after Ni coating with the Theta Composer. The average particle size was 43 μ m. A comparison of Figure 4-15 with Figure 4-1 indicates that Ni coating using the Theta composer does not modify the size of the magnesium particles. Figure 4-16 reveals the particle geometry of the Ni-coated 44 μ m magnesium powder, which looks very similar to Figure 4-2, indicating that no shape change took place after Ni coating with the Theta Composer. Figure 4-17 shows the Energy-dispersive X-ray spectroscopy (EDS) mapping of the Ni-coated 44 μ m magnesium powder, which demonstrates that the nano-size Ni particles are distributed uniformly over the surface of the magnesium powders. Figure 4-18 shows the XRD pattern of Ni-coated 44 μ m magnesium powder which indicates the presences of Ni and magnesium.

4.3.2 Ni Coating Using an Organometallic Solution

The amount of magnesium flakes produced using HSOBM was very small and each milling resulted in only 0.1g per batch. To obtain optimum milling condition and efficiency in the Theta Composer, at least 10g powder of magnesium and nano-Ni mixture is needed for each run. For consistency of coating, an organometallic Ni coating for a small amount of magnesium flakes was employed. Approximately 1 gram batches

of the as-received 300 μ m and the HSOBM treated magnesium flakes were coated under similar conditions. Figure 4-19 displays a low magnification an SEM picture of the Ni-coated flake powder. In Figure 4-20, EDS mappings indicate a homogeneous distribution of nano-size Ni particles on the magnesium flake powder surface. The size and the shape of the powders were found not to be affected by the organometallic Ni coating process. Figure 4-21 shows the organometallic Ni coated as-received 300 μ m magnesium particles which indicate no shape change after the coating process.

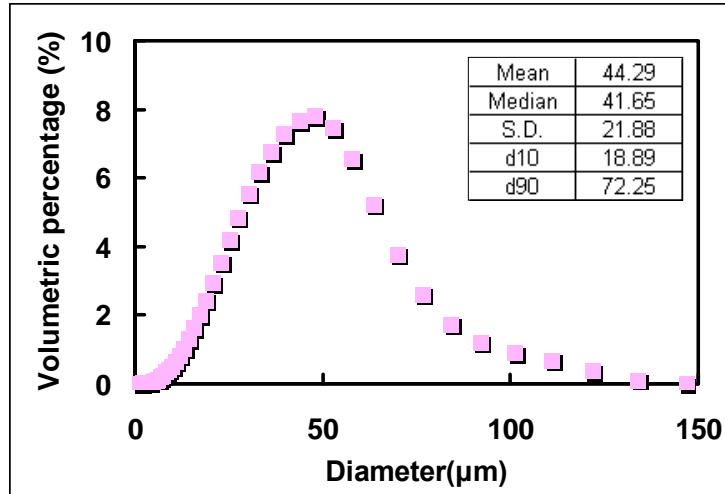


Figure 4-1. The particle size distribution of the as-received 44 μ m magnesium powder as evaluated by laser diffraction technique

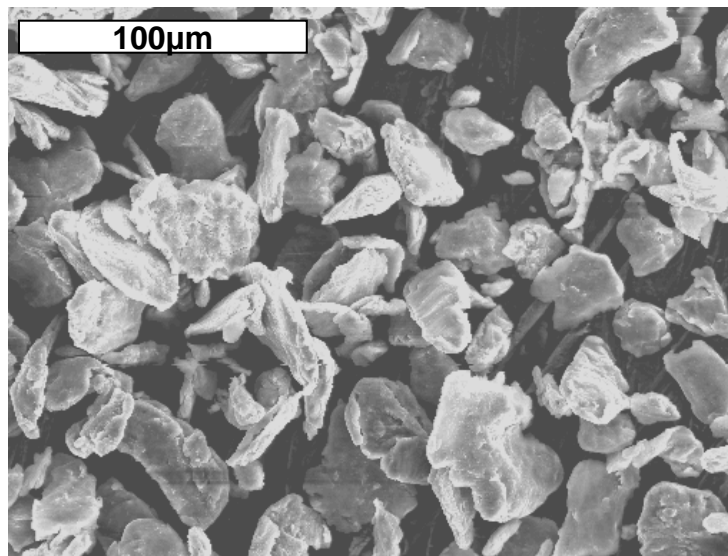


Figure 4-2. The SEM image of the as-received 44 μ m magnesium powder.

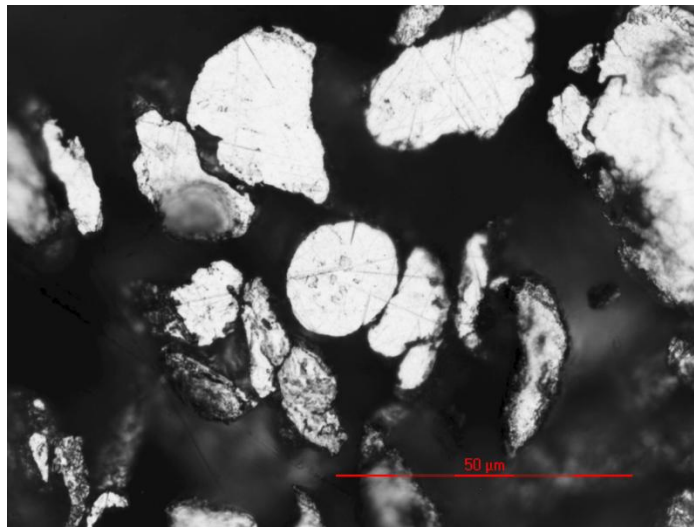


Figure 4-3. Cross-sectional optical image of the powders in the as-received 44 μm magnesium powder.

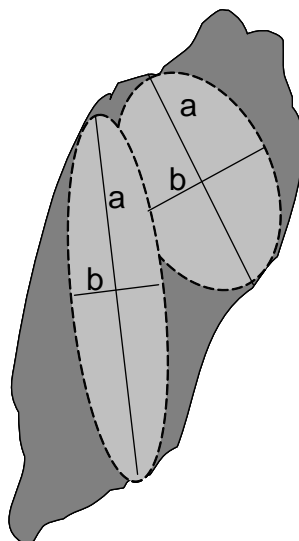


Figure 4-4. The schematic illustration of polishing surfaces and calculation of aspect ratio for as-received 44 μm magnesium powders.

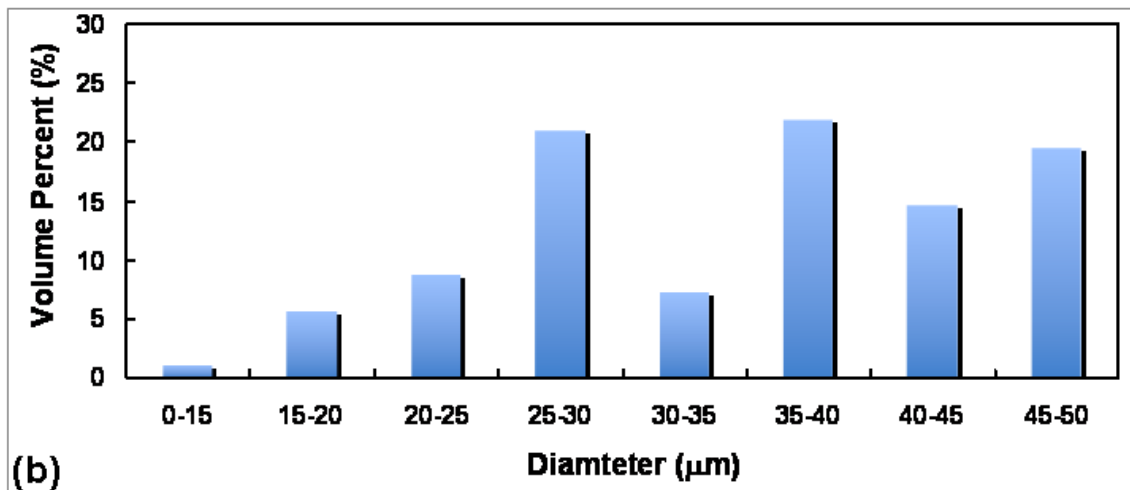
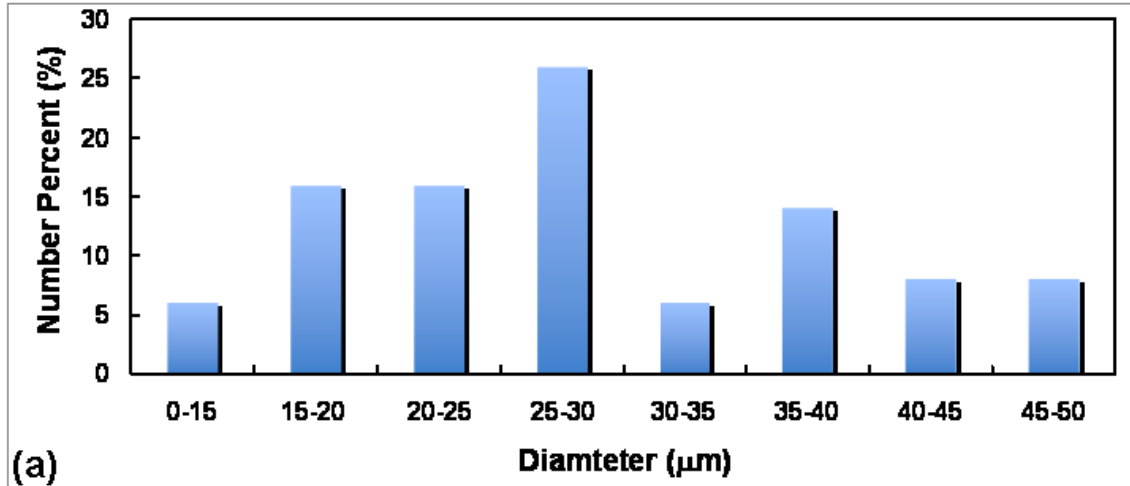


Figure 4-5. Particle size distributions of the as-received 44 μ m magnesium powder by statistic measurement in (a) number percent and (b) volume percent calculation.

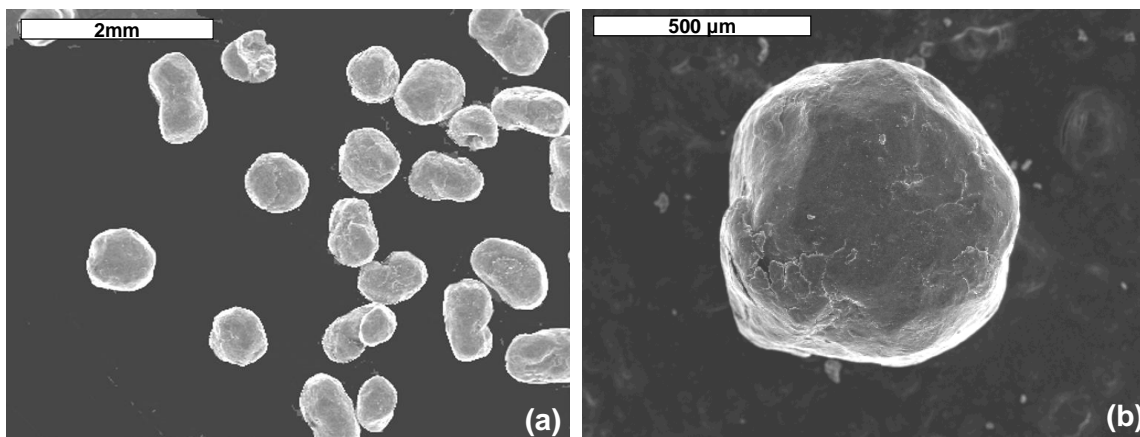


Figure 4-6. SEM images of the as-received 300 μ m magnesium powder.

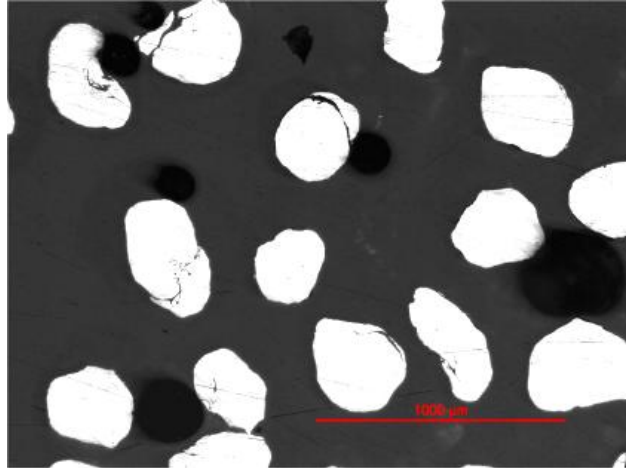


Figure 4-7. Cross-sectional optical image of the as-received 300µm magnesium powder.

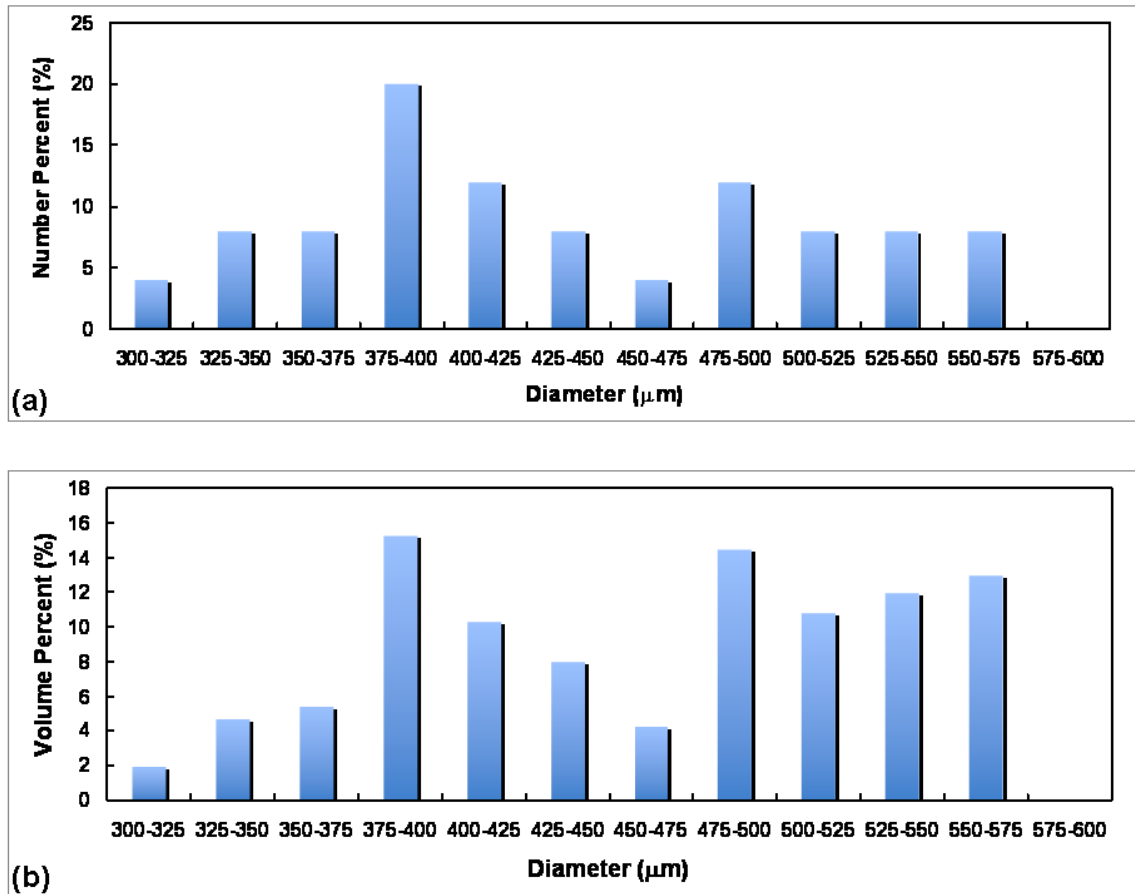


Figure 4-8. Particle size distribution in the as-received 300µm magnesium powder based on (a) number percent and (b) volume percent calculation.

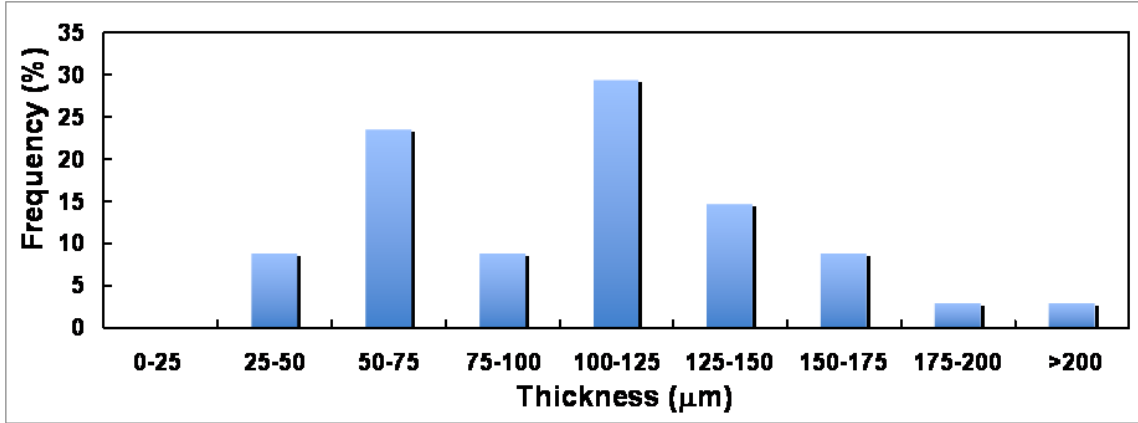


Figure 4-9. Magnesium flake thickness distribution after 100V and 20 seconds milling.

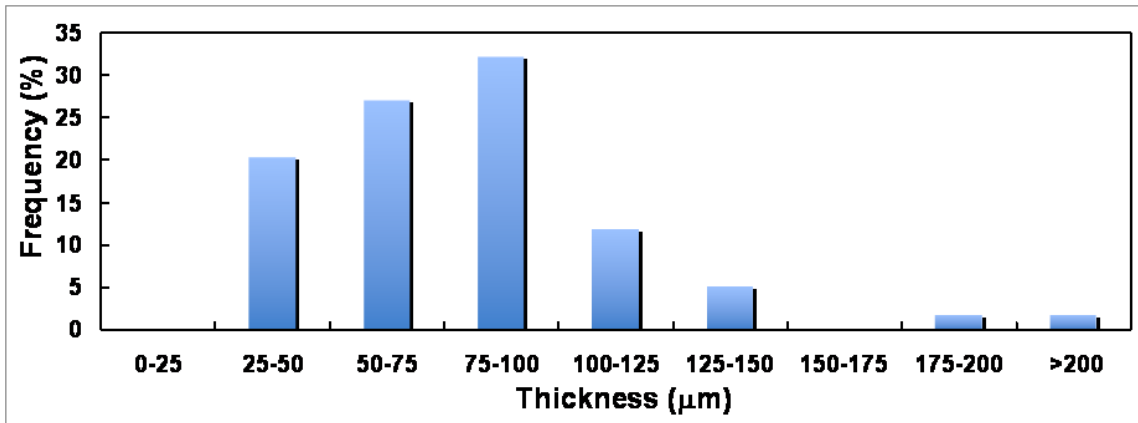


Figure 4-10. Magnesium flake thickness distribution after 100V and 1 minute milling.

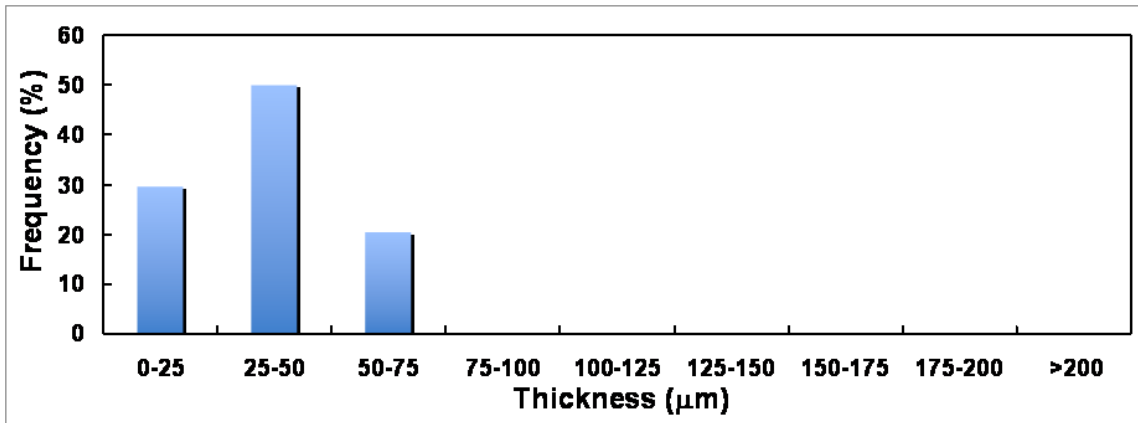


Figure 4-11. Magnesium flake thickness distribution after 100V and 2 minutes milling.

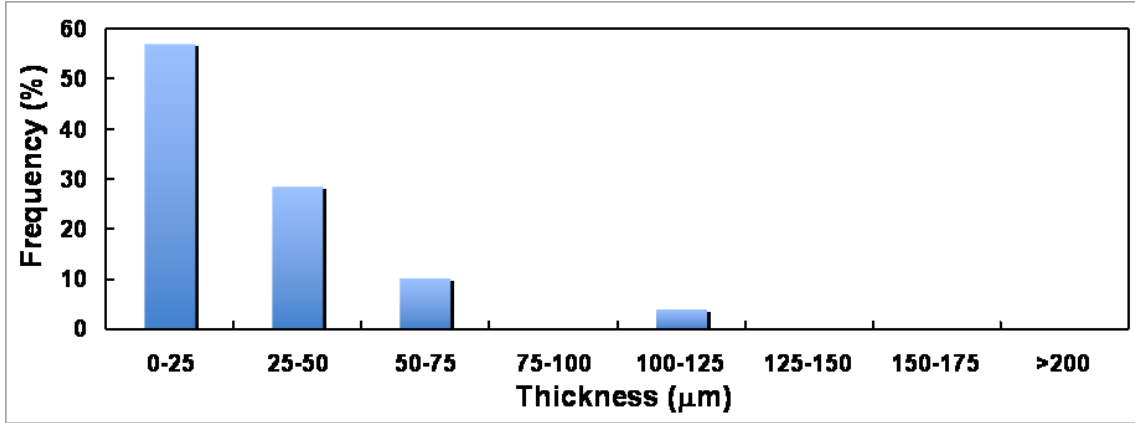


Figure 4-12. Magnesium flake thickness distribution after 110V and 2 minutes milling.

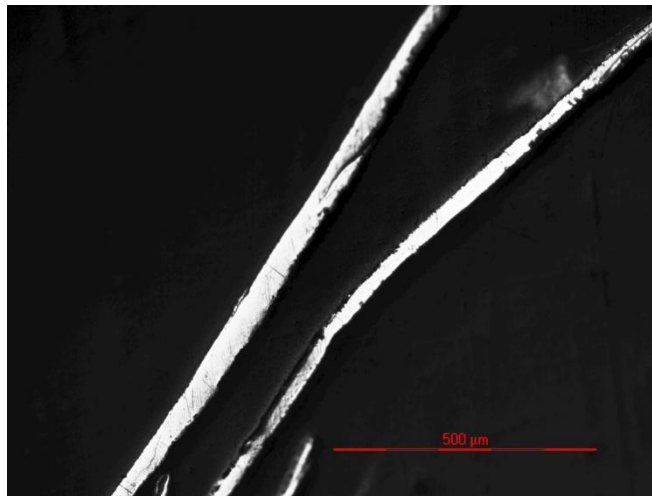


Figure 4-13. Optical microscopic analysis at cross section of magnesium flake powders.

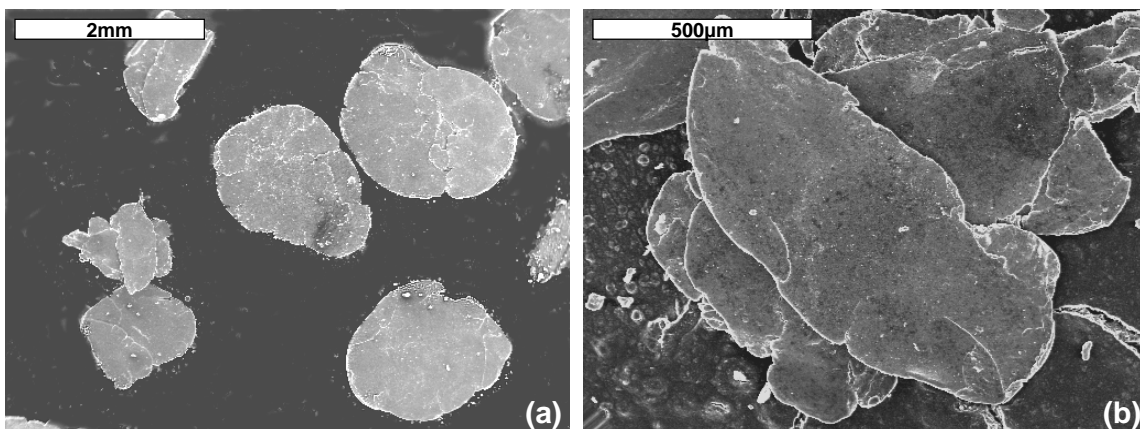


Figure 4-14. SEM images of as milled magnesium flake powders.

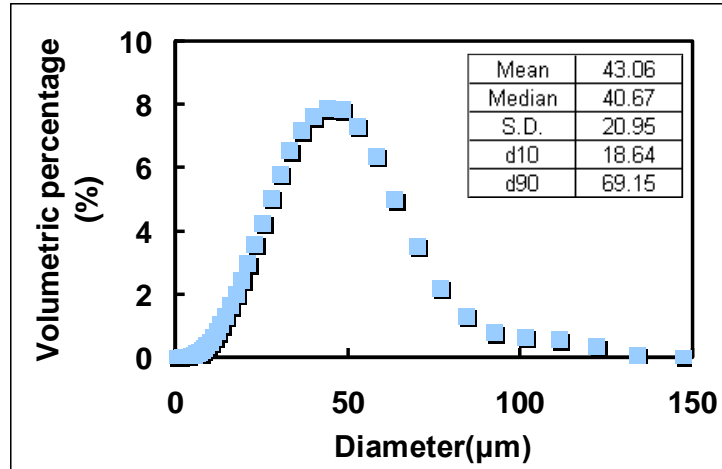


Figure 4-15. Particle size distribution of Ni-coated 44 micron magnesium particles.

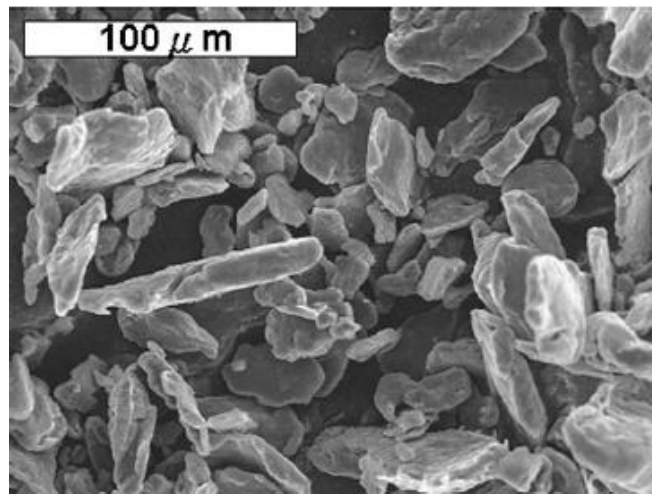


Figure 4-16. SEM images of Ni-coated the 44 micron magnesium powder after Ni coating with the Theta Composer.

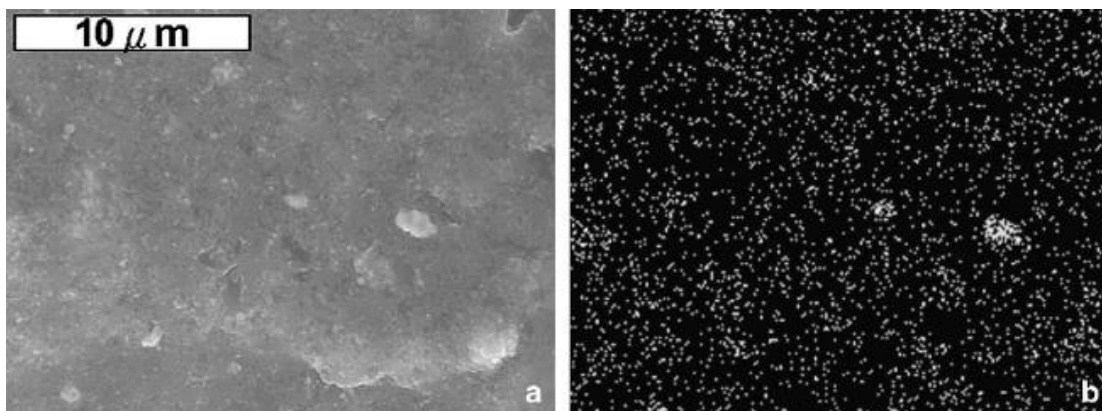


Figure 4-17 The EDS Ni mapping of Ni-coated 44 micron magnesium particles.

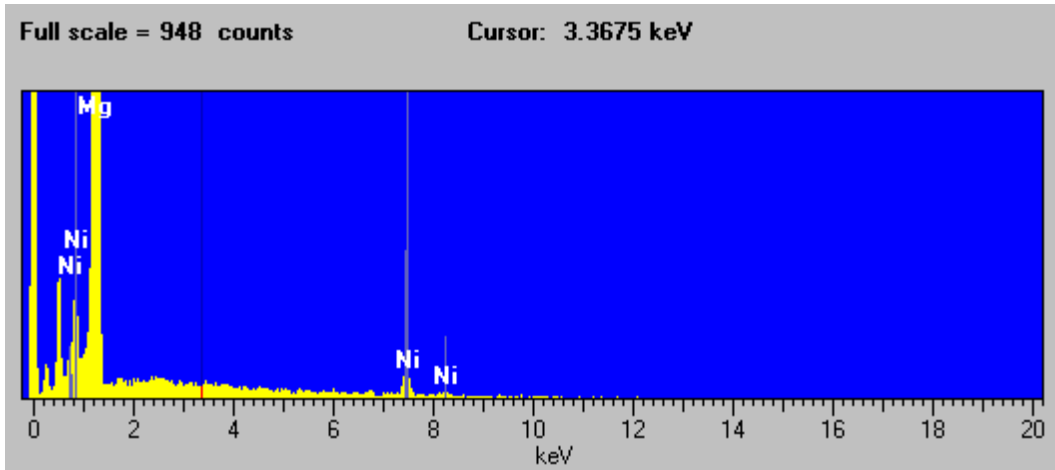


Figure 4-18. The X-ray diffraction patterns.

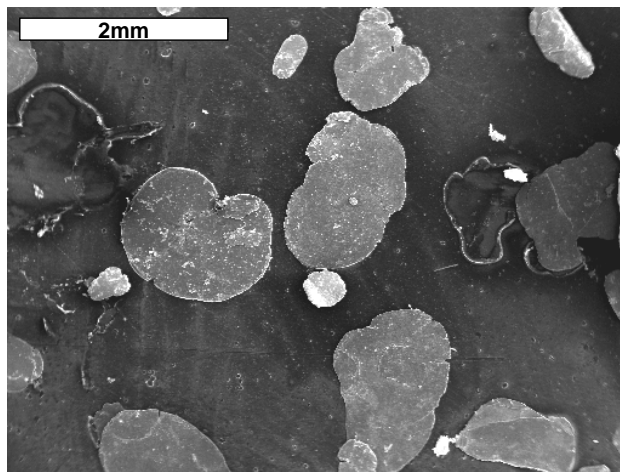


Figure 4-19. SEM images of Ni-coated magnesium flake particles.

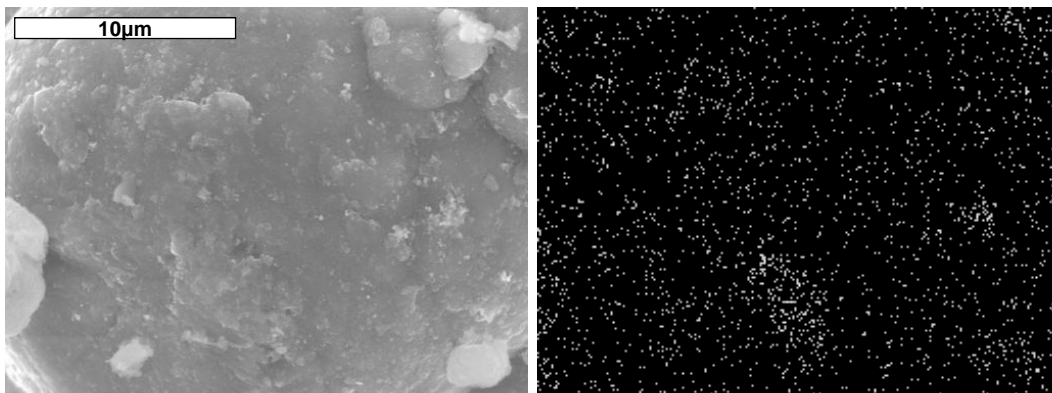


Figure 4-20. The EDS Ni mapping of Ni-coated magnesium flake particles.

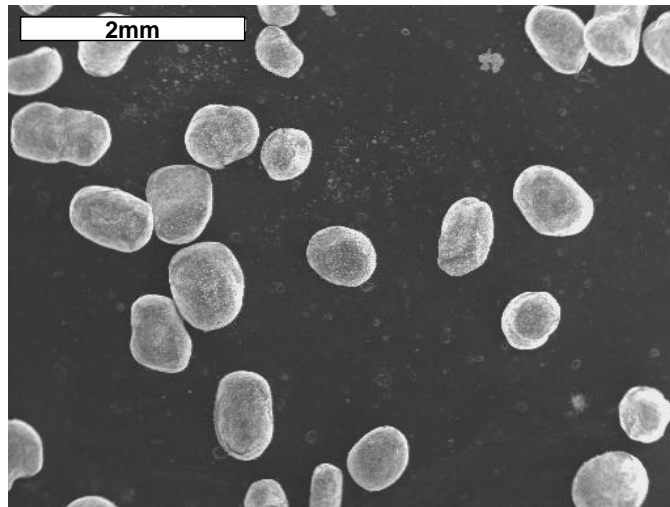


Figure 4-21. SEM image of Ni-coated 300 micron magnesium particles

CHAPTER 5 EVOLUTION OF MICROSTRUCTURE DURING THE HYDROGENATION PROCESS

5.1 Introductory Remarks

Previous studies have shown that the hydrogen capacity of magnesium powders depends on many parameters including temperature, pressure, processing such as ball milling, particle size and shape. In order to develop a mechanistic understanding of how these factors affect the hydrogen capacity, a microstructurally-based investigation of the hydrogenation process is needed. The objective of this study was to understand the development of magnesium hydride as a function of time in order to elucidate the mechanism that controls the hydrogen capacity for magnesium powders.

Figure 5-1 shows a typical hydrogenation curve under the conditions where magnesium hydride is in a stable phase and the Gibb's free energy for the reaction is a negative value. As can be seen in Figure 5-1, initially the reaction rate for the powder tested is relatively fast, and it becomes slower as the time increases. Eventually the reaction rate is reduced to such a low value that pseudo-saturation is reached. The amount of hydrogen content at this pseudo saturation level is defined as the hydrogen capacity. It can be noticed that the hydrogen capacity in this curve is below the theoretical value 7.6 H wt. %. As explained in Chapter 2, several models have been suggested to explain the shape of the hydrogenation curve and its dependency on parameters such as T, P, etc. The two significant models are the Core-Shell model and the impingement model. The Core-Shell model assumes that after the initial hydride layer is formed it grows thicker and thicker as hydrogenation time increases. As the hydride layer gets thicker, the flux of hydrogen through it becomes smaller, which results in a lowering of the reaction rate. The driving force for diffusion of hydrogen is

the concentration gradient of hydrogen in hydride, as shown in Figure 5-2. However, the diffusivity of hydrogen through magnesium hydride is very slow. The diffusion coefficient for hydrogen diffusing through magnesium hydride is $D = 1.507 \times 10^{-4} \text{ (m}^2\text{s}^{-1}) [\exp(-96,000 \text{ (J/mole)/RT})]$ [91]. In this model the high hydrogen flux rate needed to achieve the observed hydrogenation rates is achieved by assuming that the concentration of hydrogen, rather than its activity, at the interface between magnesium phase and hydrogen gas phase as well as at the interface between magnesium and magnesium hydride phase is equal. This assumption is invalid because the magnesium hydride phase is an ionic compound [41] and has a negligible solubility range for hydrogen [38]. The less referenced model is based on the nucleation and growth of the magnesium hydride phase and the pseudo-saturation level during the hydrogenation process is explained by the impingement of hydride colonies/grains. According to this model hydrogen atoms diffuse through the magnesium phase rather than the hydride phase. The reaction rate decreases with time because the area of the gas/Mg phase interface shrinks as the hydride phase grows. Consequently, the flux of hydrogen decreases with time resulting in a decreased reaction rate.

In this study the material used for hydrogenation was a 44 μm commercial magnesium powder, which was coated with Ni nanoparticles using the Theta Composer. The hydrogenation tests were conducted for different times at a constant temperature (210°C) and a constant pressure (1Mpa). The evolution of the hydride phase was investigated to shed light on the mechanism of the hydrogenation process.

5.2 Microstructural Analysis

Magnesium powder samples were hydrogenated at 210°C under 1MPa hydrogen pressure for 2.5, 7.5, 15, 75, 300 minutes. The microstructure of each hydrogenated

sample was evaluated and analyzed for the hydride evolution as a function of time. Figure 5-3 presents the curves obtained by hydrogenation for different times overlapped on the curve obtained after 5 hours of hydrogenation. There is an excellent repeatability of the hydrogenation rate and the curves match each other well. .

Figure 5-4 shows the cross-sectional images for the powder hydrogenated for 2.5 minutes. The hydride phase is imaged as the darker phase in the BSE mode owing to its lower average atomic number (Z-contrast mechanism) and the ionic structure and metallic magnesium phase appear bright. Invariably, it was found that the hydride phase nucleates and grows on the surface of the magnesium particles. Usually, it is assumed that the magnesium hydride nucleates on the surface of the particles because of the highest activity of hydrogen atoms on the surface and the fact that heterogeneous nucleation is associated with a lower energy barrier than the internal homogeneous nucleation. Of course, in the presence of second phase particles with very high interfacial energy the internal nucleation of the magnesium hydride is perceivable. Little work has been done to microstructurally evaluate the nucleation of the magnesium hydride. Antisari et al. reported that the nucleation site of magnesium hydride is heterogeneously defect preferred and the magnesium hydride nuclei were found at the interface of the catalyst Ni particles and magnesium phase [92]. Montone et al. demonstrated that, in particular, magnesium hydride nucleation in magnesium is assisted by crystal defects, while free surface is the only nucleation site [93]. Oguchi et al. suggested that the nucleation of magnesium hydride is a fast heterogeneous formation of hydride followed by a drastically slow growth of the magnesium hydride

phase [94]. The growth rate was initially 1.3nm/s and the average growth rate was 0.03nm/s.

As seen in Figure 5-4, the nucleation sites of the hydride units are well separated and do not touch or impinge on each other. The hydride units appear faceted and the interfaces between the hydride units and the magnesium phase seem to be relatively flat, which suggests that these units grow as single crystals into the magnesium matrix. Owing to the lack of further evidence, here each unit will be referred to as hydride colonies (meaning made of several grains)/grain (meaning single crystal). The metallic magnesium phase is still a large portion of the particles and large areas of the magnesium particles have not yet transformed to magnesium hydride. Assuming that the hydride forms as single crystals, the number of nodules of hydride represents the nuclei number of magnesium hydride and can be calculated from microstructural analysis. The total number of nodules was measured from at least 80 particles and the linear nucleation density was obtained by the number of nodules divided by the perimeter of the powder.

Figure 5-5 shows the SEM (BSE mode) cross-sectional images of particles from the powder hydrogenated for 7.5 minutes. The hydride grains/colonies are larger than the particles hydrogenated for 2.5 minutes but no drastic increase in the number of them was detected. Some hydrides seem to grow preferentially into the metallic magnesium phase rather than grow laterally, resulting in a hemisphere shape, as indicated by the arrows in Figures 5-5 (a, b, d). In Figure 5-5(c), a hydride grain/colony can be observed inside the partially hydrogenated magnesium particle which conflicts with the assumption that the hydride nucleates exclusively at the powder surface only. A

serial sectioning method using an optical microscope was employed to evaluate whether this patch of hydride was observed due to the three dimensional nature of the hydride units or indeed it was associated with an internal nucleation event. Figure 5-6 displays the optical microscopic images after several levels of polishing. In Figure 5-6(a), it is noticed that there is an isolated hydride grains/colonies located inside of the hydrogenated particle as marked by an arrow. To investigate whether the hydride touches the surface or not further polishing was done As evidenced in Figure 5-6(b), interestingly the hydride patch touched the powder surface. Figures 5-6(c, d) displays the images of further subsequent polishing. All of the images point out that the hydride patch found inside the particle in Figure 5-5(c) is due to the polishing issue and not due to the inside nucleation of magnesium hydride. As can be seen in Figure 5-5, some hydride grains/colonies have begun to impinge on each other but still a large fraction of the surface of the magnesium particles is free of hydrides and hydrogen atoms can diffuse fast through these areas.

The SEM (BSE mode) images of magnesium particles hydrogenated for 15 minutes are shown in Figure 5-7. In comparison to the powder hydrogenated for 7.5 minutes, the hydride colonies/grains have grown in size, and consequently a larger number of them have impinged on each other but the surface is still not completely covered by hydride. There is a large volume expansion (about 30% increase) associated with the transformation of magnesium to magnesium hydride. As a result, as evidenced in Figure 5-7, the hydride colonies/grains, which are brittle, crack under the volume expansion stresses. These stresses can play an important role in nucleation and growth of the magnesium hydride, especially in thin films [95, 96]. Also, it can be

noticed that some colonies/grains bulge out of the original magnesium particle surface to accommodate the volume change.

Figure 5-8 presents the microstructure of magnesium particles hydrogenated for 75 minutes. Here, the most important observation is the extent of the impingement behavior. In this powder, some of the particles have been covered completely by magnesium hydrides, and some of them still have metallic magnesium exposed on the surface. This observation shows that the complete impingement of the hydride colonies/particles does not take place in all particles simultaneously, suggesting that there will be a transition period where the mechanism of the hydride growth transitions from being controlled by the diffusion of hydrogen through the metallic magnesium to a through hydride diffusion mechanism (Core-Shell model).

For powders hydrogenated for 300 minutes, the transformation comes to an end and almost all of the magnesium particles are covered by a magnesium hydride layer, as shown in Figure 5-9. At this point only a small fraction of the metallic magnesium is left in the center of the particles and the growth rate of the hydride is exclusively controlled by the diffusion of hydrogen atoms through the hydride layer. Since the diffusivity of hydrogen through the ionic magnesium hydride is very slow [91], and at 210°C and 1MPa the thickness of the hydride layer at the point of impingement is relatively large, the hydride growth rate after impingement is very slow. Therefore, a pseudo-saturation of hydrogen absorption, referred to as hydrogen capacity, is achieved. It should be noted that, under different hydrogenation conditions, for example low hydrogenation temperature, this pseudo-saturation is not achieved. When the

thickness of the hydride at the impingement point is small, the flux of hydrogen through a thin hydride layer can still be significant.

5.3 Effect of Particle Size on Hydrogen Capacity

In Chapter 4, the particle size distribution of magnesium powders shows a relatively broad range in diameter. As demonstrated in Figure 5-10 the amount of metallic magnesium left in the center of the magnesium particles after hydrogenation at 210°C for 300 minutes depends on the size of the particle. As will be shown in the forthcoming chapters, the thickness of the hydride at the point of impingement depends only on temperature and pressure of hydrogenation for a given coated magnesium powder. Therefore, as illustrated in the schematic in Figure 5-10, the larger particles contain a larger fraction of unhydrogenated magnesium, hence resulting in a lower hydrogen capacity per particle.

To study the particle size distribution effect on the hydrogen capacity, the hydrogenated particles were divided into 3 groups according to their sizes, which range from 0 to 15, 15 to 30 and 30 to 60 μm . The size range for the three groups is chosen arbitrarily based on the observation at low magnification (1000X) of the SEM (BSE mode) images. The method of the calculation of the phase fraction is shown in Figure 5-11. The SEM (BSE mode) image was loaded into the Microsoft PowerPoint and grids were overwritten on the images for the phase fraction measurement. The volume fraction of the hydride phase was calculated based on the point count method [97]. As mentioned previously, the darker phase region is magnesium hydride and the brighter area was composed of the magnesium phase. In Figure 5-11, if the intersection located just right on the darker area, one intersection is counted for the magnesium hydride. The same treatment was used for the magnesium phase. For the intersection on the

interface of Mg/MgH₂, it was divided and counted as ½ for magnesium hydride and ½ for magnesium phase, respectively. The total number of intersections was summed for each phase. The area phase fraction can be obtained by dividing the number of intersections for each phase over total number of intersections. The area phase fraction is usually assumed to be a good measure of the volume fraction.

Figure 5-12 displays the area phase fraction of magnesium hydride for different size of particles. The hydrogen capacity varies with different sizes of magnesium powders. It is obvious that with an increase of the particle size the hydride area fraction decreases. The hydride fraction is 0.94 for the size of magnesium powders smaller than 15µm. It is expected that the hydrogen capacity will be close to one if all the sizes of magnesium powders are below 15µm. Figure 5-13 shows examples of microstructures corresponding to different sizes illustrating the effect of particle size distribution on the measured average hydrogen capacity. It is interesting to note that the thickness of the hydride layer is approximately the same in these particles, confirming the suggestion that the hydride thickness at the point of impingement is controlled by the nucleation and growth rates of the hydride, hence only dependent on temperature and pressure of hydrogenation for a given coated powder. Some small size particles in the 0-15µm span reach even 100% complete phase transformation because the hydride impingement thickness is larger or comparable to the half diameter of the particles. The medium 15-30µm magnesium particles show larger areas of metallic magnesium phase left in the particles compared to the 0-15µm particles. The large 30-60µm magnesium particles exhibit a much larger metallic magnesium area than the medium ones. The capacities of these three different sizes of hydrogenated particles contribute to the total hydrogen

capacity for the hydrogenation curve in Figure 5-1. Figure 5-14 displays the hydrogen capacity for different sizes of magnesium particles at different hydrogenation time periods. The data points of hydrogen capacity follow the same trend as the hydrogenation curve. Furthermore, the hydrogenation curve is located within the capacity ranges for different size of the magnesium particles which means the area phase fraction successfully estimates the hydrogen capacity.

5.4 Summary of Hydrogenation Process

The magnesium hydride formation has been treated as a simple layer growth which can be explained by the Core-Shell model. However, based on the microstructural analysis of the hydrogenated powders, it seems that the nucleation of magnesium hydride is one of the kinetics barriers during magnesium hydride formation; individual grains/colonies of magnesium hydride have been seen in the initial stage of hydrogenation. A schematic illustration was developed to describe the hydrogenation process; Figures 5-15 to 5-21 show the schematic diagrams at each step from the beginning to the saturation to understand step by step the magnesium hydride formation.

- Step 1: Physisorption of hydrogen molecules.
- Step 2: The dissociation of hydrogen molecules into two hydrogen atoms.
- Step 3: Dissolution of hydrogen atoms (Solubility of H atom in magnesium).
- Step 4: Chemisorption of hydrogen ions (Magnesium hydride formation).
- Step 5: Nucleation of magnesium hydride.
- Step 6: Growth of magnesium hydride.
- Step 7: Impingement of magnesium hydride.
- Step 8: Continuous thickening of magnesium hydride layer.

Step 1 for the hydride formation, the solid-gas reaction, is the physisorption of hydrogen gas molecules attached on the solid material magnesium powder surface by van der Waals force. Under the standard condition, there is an activation energy barrier

for the hydrogen molecule to break into two hydrogen atoms. In order to eliminate this process to act as a rate limiting step during hydrogenation, nano-Ni particles have been used to enhance the dissociation kinetics of hydrogen molecules. The image of EDS Ni mapping in Figure 3-5 exhibits a very homogeneous distribution of nano-Ni particles on the magnesium particle. Therefore, the dissociation of hydrogen molecules should not be an issue while considering the rate limiting steps. After the hydrogen molecules turn into hydrogen atoms at Step 2, the hydrogen atoms start to dissolve into the magnesium phase until reaching the solubility limit in the magnesium phase at a given temperature which is Step 3. At Step 4, magnesium hydride forms whereas the hydrogen concentration is oversaturated and the crystal structure transforms from hcp-Mg to tetragonal magnesium hydride with about 20% volume expansions. Ideally the increase of the volume due to the phase transformation would result in the defect structure, i.e. dislocation, cracks which induce the faster kinetics. In Step 5, if the number of nuclei is higher than the critical number of nuclei, the magnesium hydride nucleates somewhere on the powder surface. Step 6 is the growth process of magnesium hydride. Step 7 is when those individual hydride grains/colonies impinge on each other and form a complete hydride layer. The last step, Step 8, is the stage that the powder surface is completely covered by the magnesium hydride. It looks like a core shell in the cross section view. After this stage, the core shell model can be used to explain the very slow thickening process of magnesium hydride. Before this step, the nucleation and growth model has gained most agreement in describing magnesium hydride formation.

5.5 Summary and Conclusions

The hydrogenation study was performed using the hydrogenation part of a house-built Hydrogenation/Dehydrogenation unit. The hydrogenation behavior was studied

using the microstructural analysis at different time periods during the hydrogenation process. The major conclusions are the following:

1. Prior to impingement of magnesium hydrides, a nucleation and growth model can best explain the mechanism of magnesium hydride formation at hydrogenation temperature 210°C under 1MPa. However, the Core-Shell model should be applied after the magnesium hydride impinges on each other (at pseudo-saturation).
2. The pseudo-saturation is the hydrogen capacity at a given hydrogenation condition and time (6.1 H wt. % at 210°C, 1MPa for 5 hours).
3. With the decrease of the size of magnesium particles, the magnesium hydride fraction increases.
4. With the increase of the hydrogenation time, the hydride fraction increases.
5. The measurement of area phase fraction for each phase on 2-D is able to estimate the hydrogen capacity and hydrogenation curve.

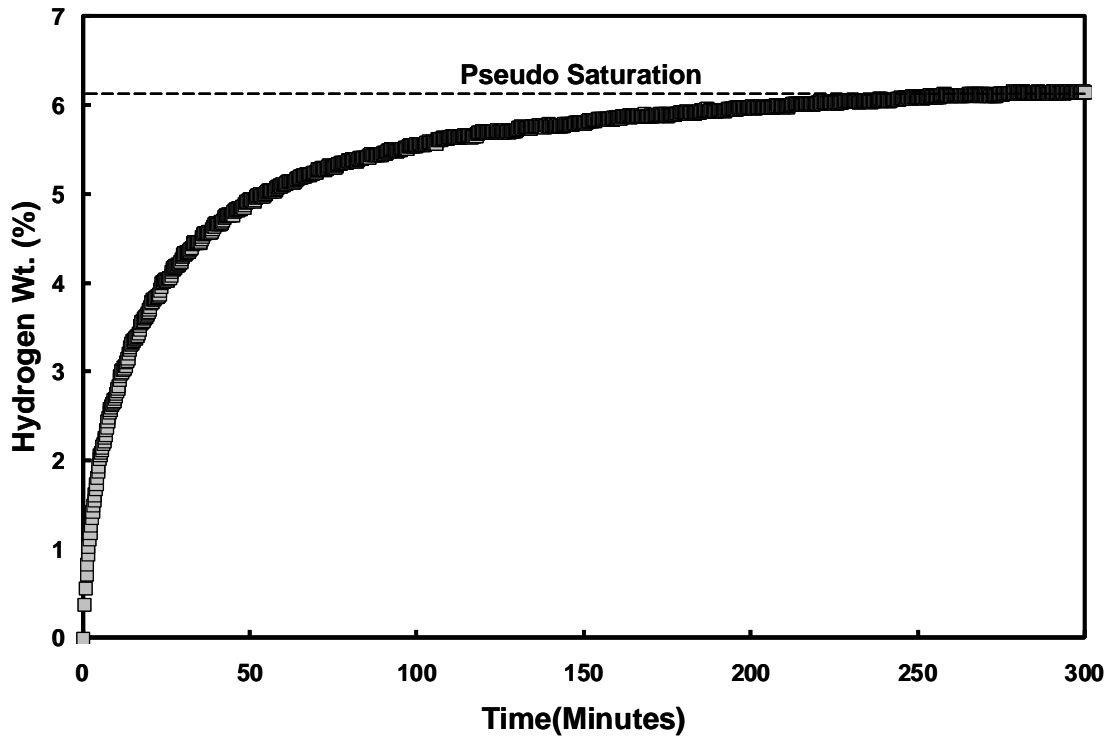


Figure 5-1. Hydrogenation curve of magnesium powder sample at 210°C under 1MPa hydrogen pressure.

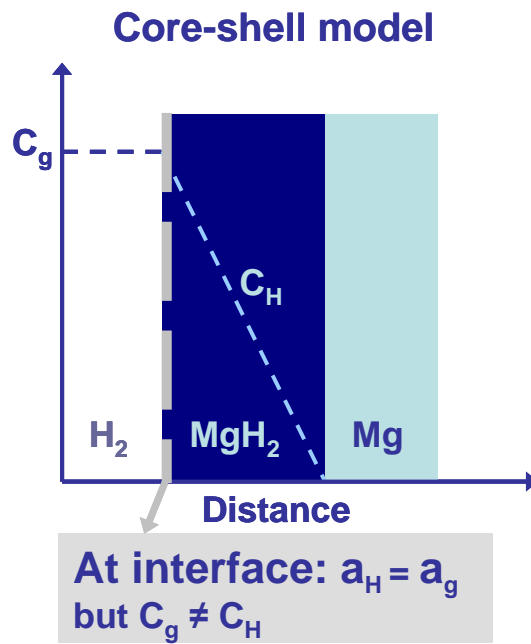


Figure 5-2. Schematic illustration of Core-Shell model.

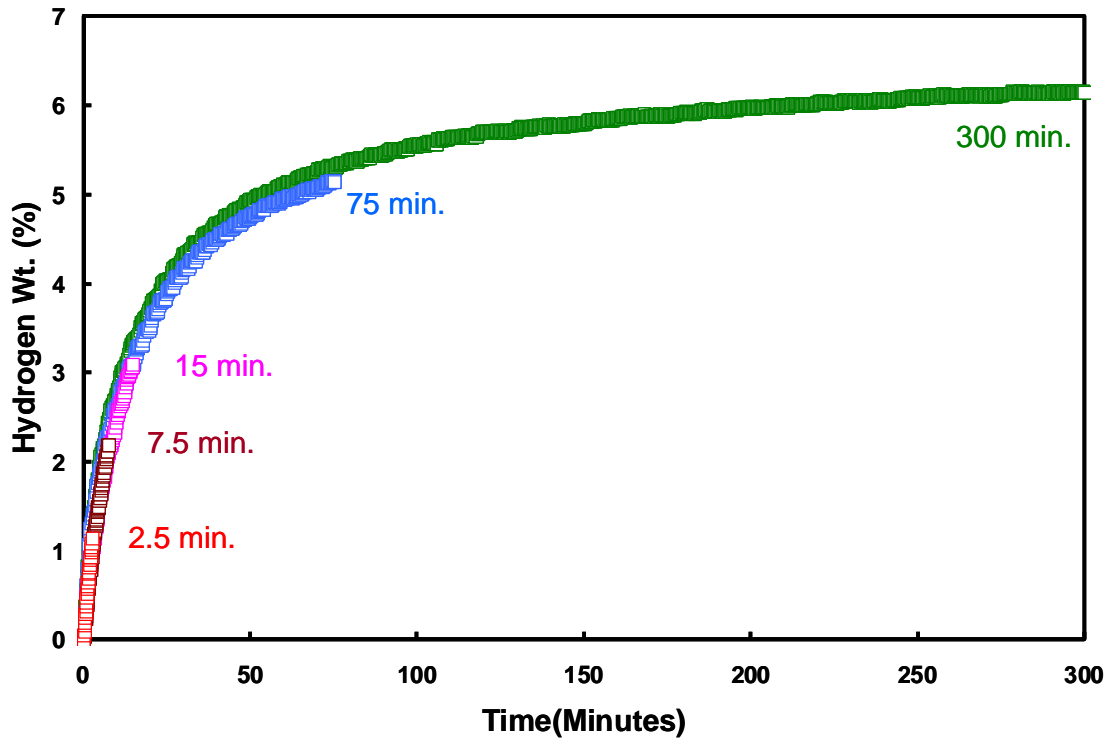


Figure 5-3. Hydrogenation curves of magnesium powder sample at 210°C under 1MPa hydrogen pressure at each interrupted times.

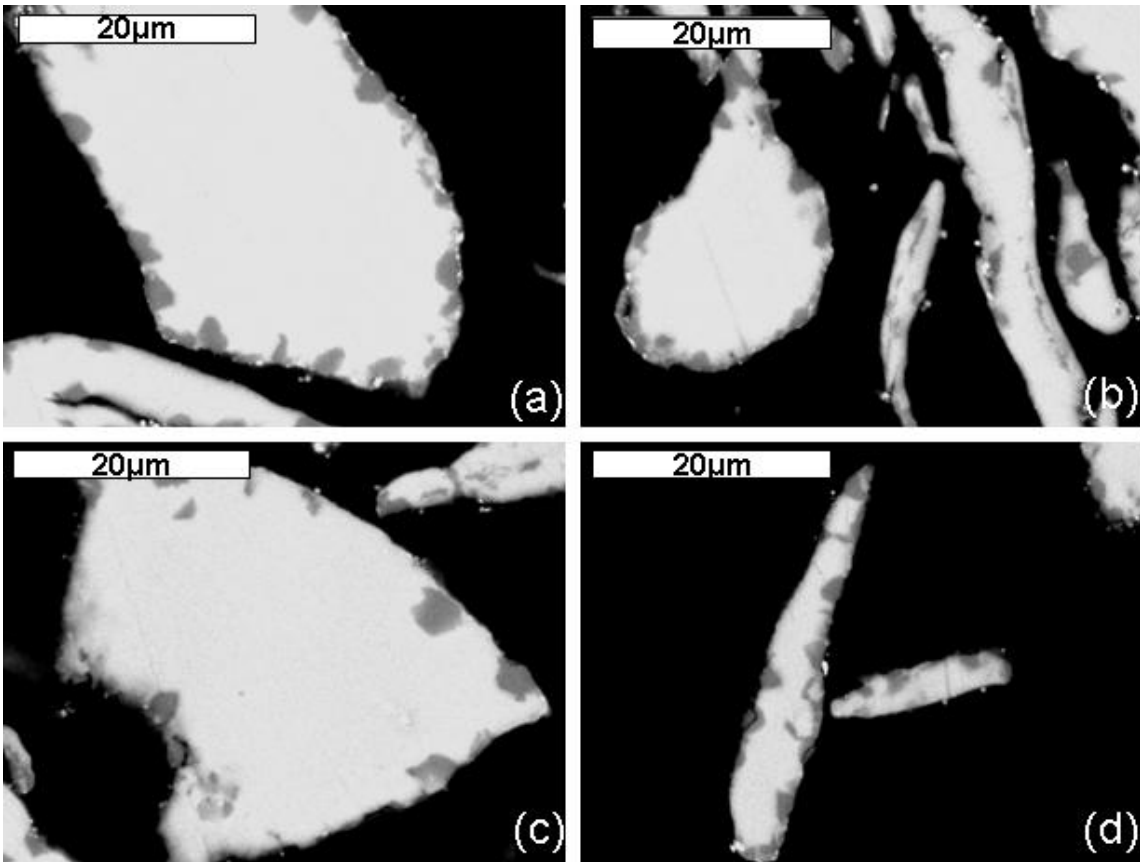


Figure 5-4. Microstructural analysis on the cross section of magnesium powder hydrogenated for 2.5 minutes.

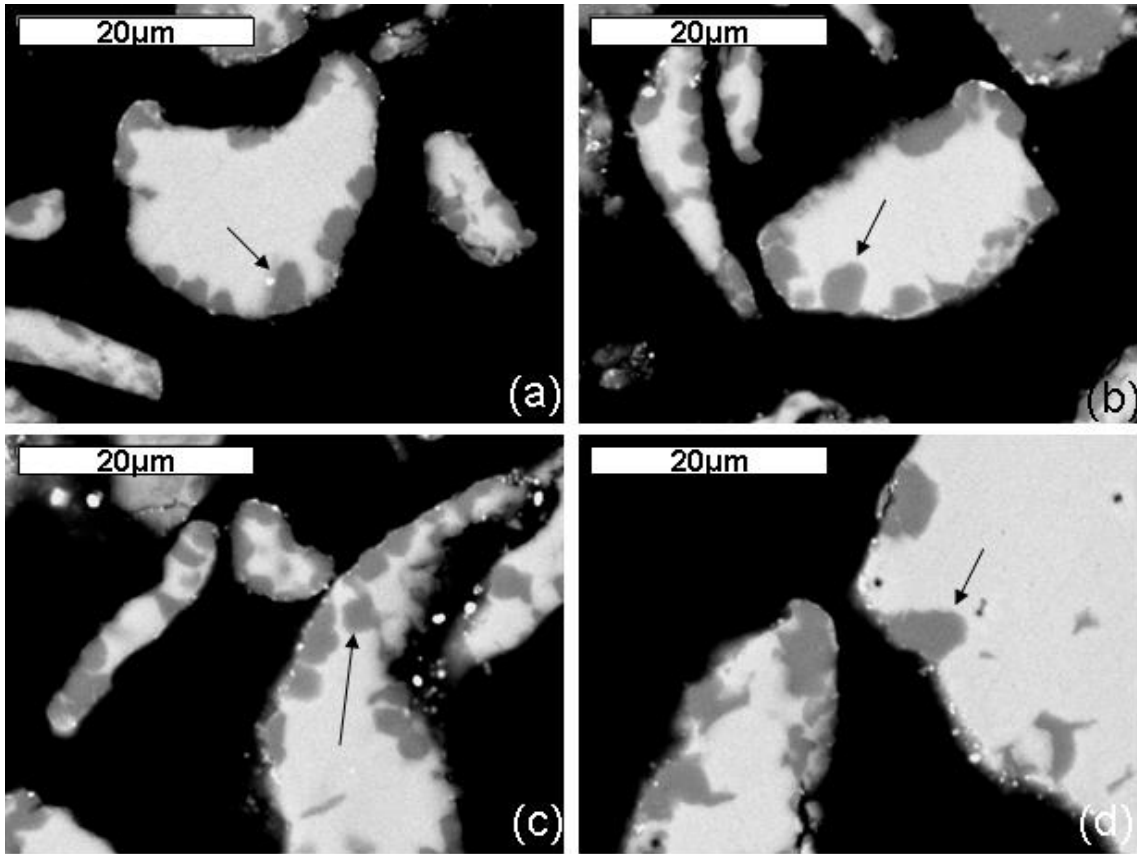


Figure 5-5. Microstructural analysis on the cross section of magnesium powder hydrogenated for 7.5 minutes.

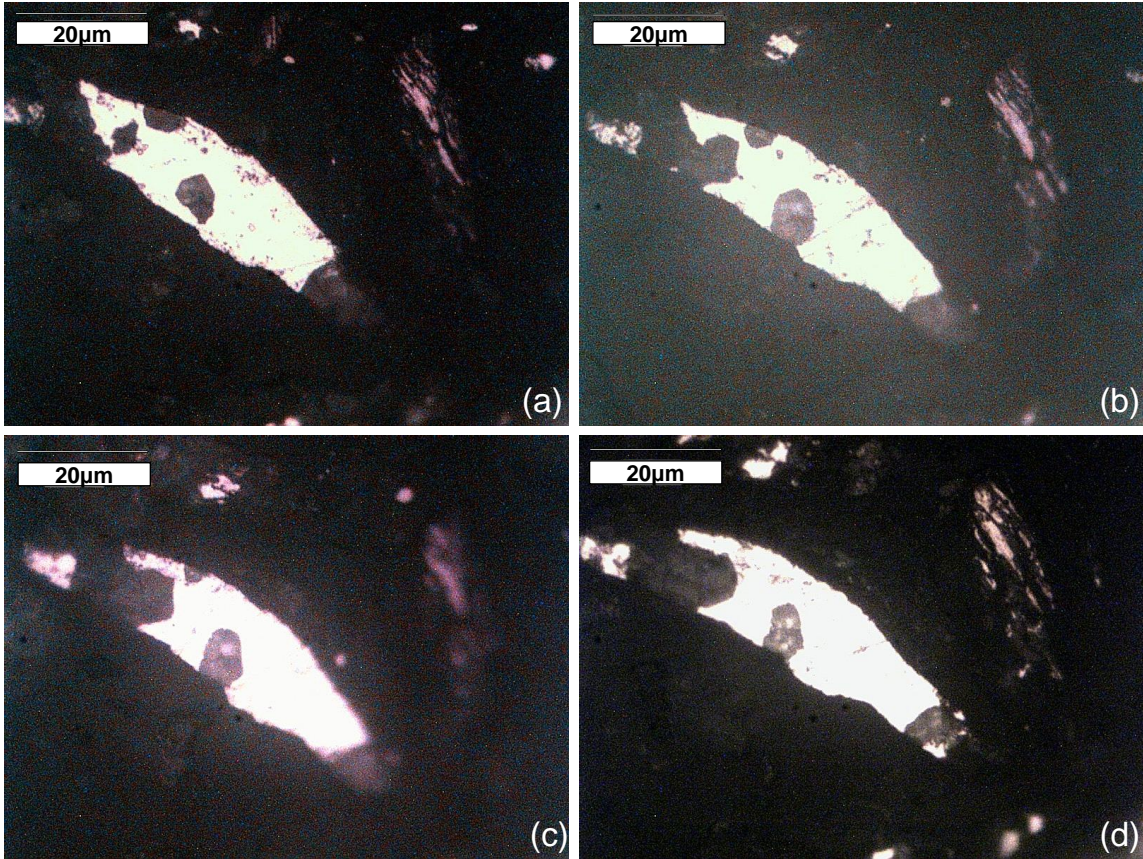


Figure 5-6. Optical microscopic images for the investigation of the location of nucleation of magnesium hydride.

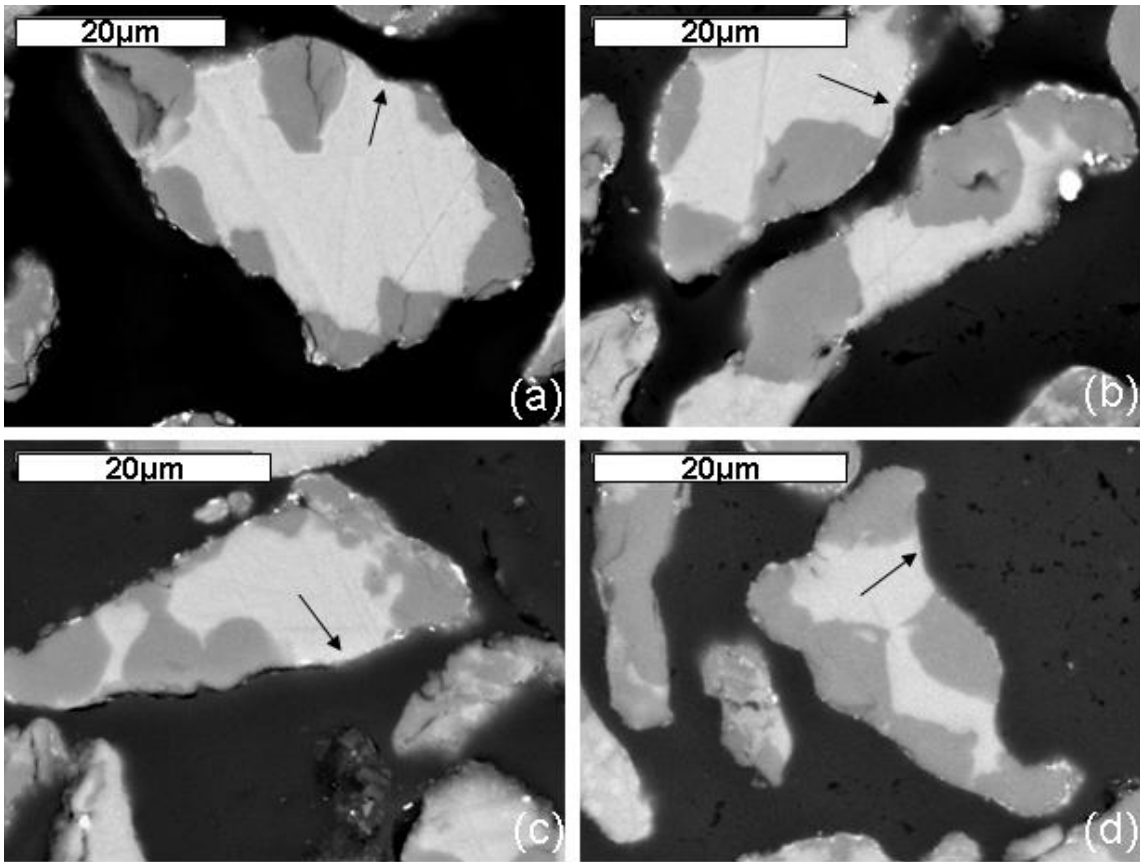


Figure 5-7. Microstructural analysis on the cross section of powder hydrogenated for 15 minutes.

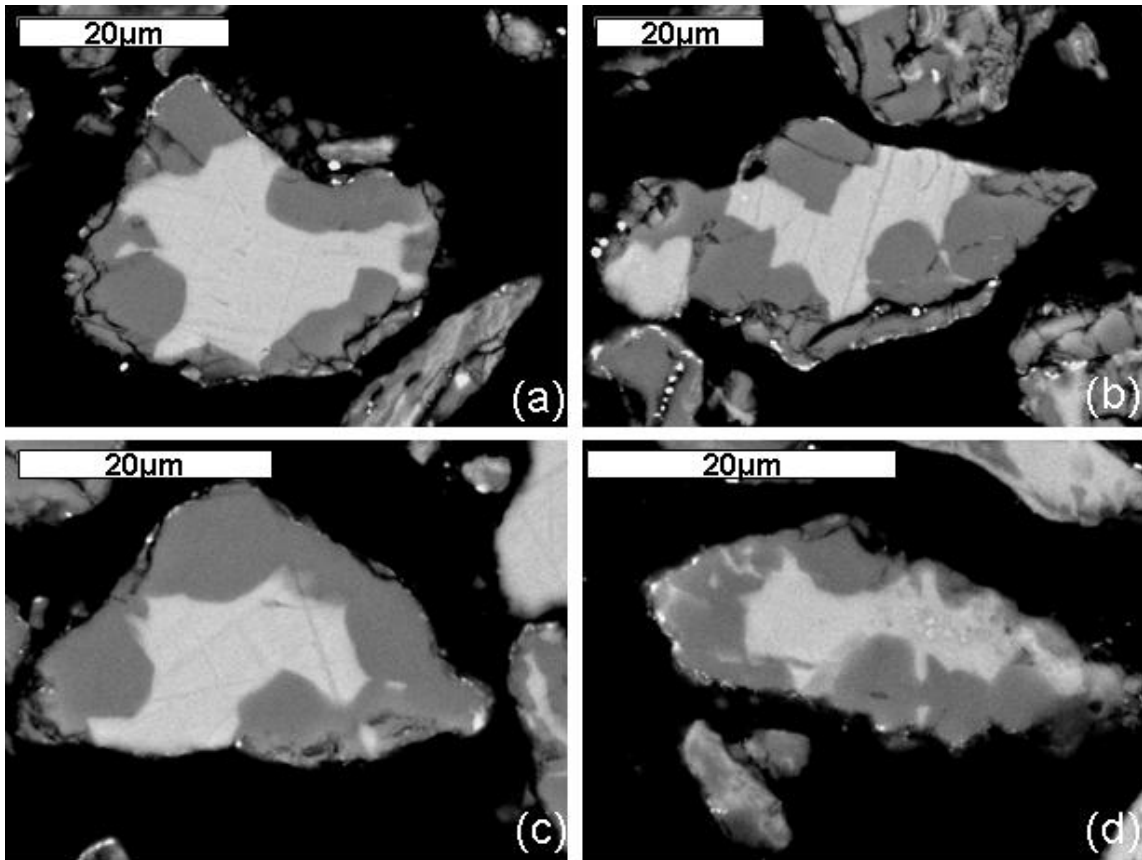


Figure 5-8. Microstructural analysis on the cross section of powder hydrogenated for 75 minutes.

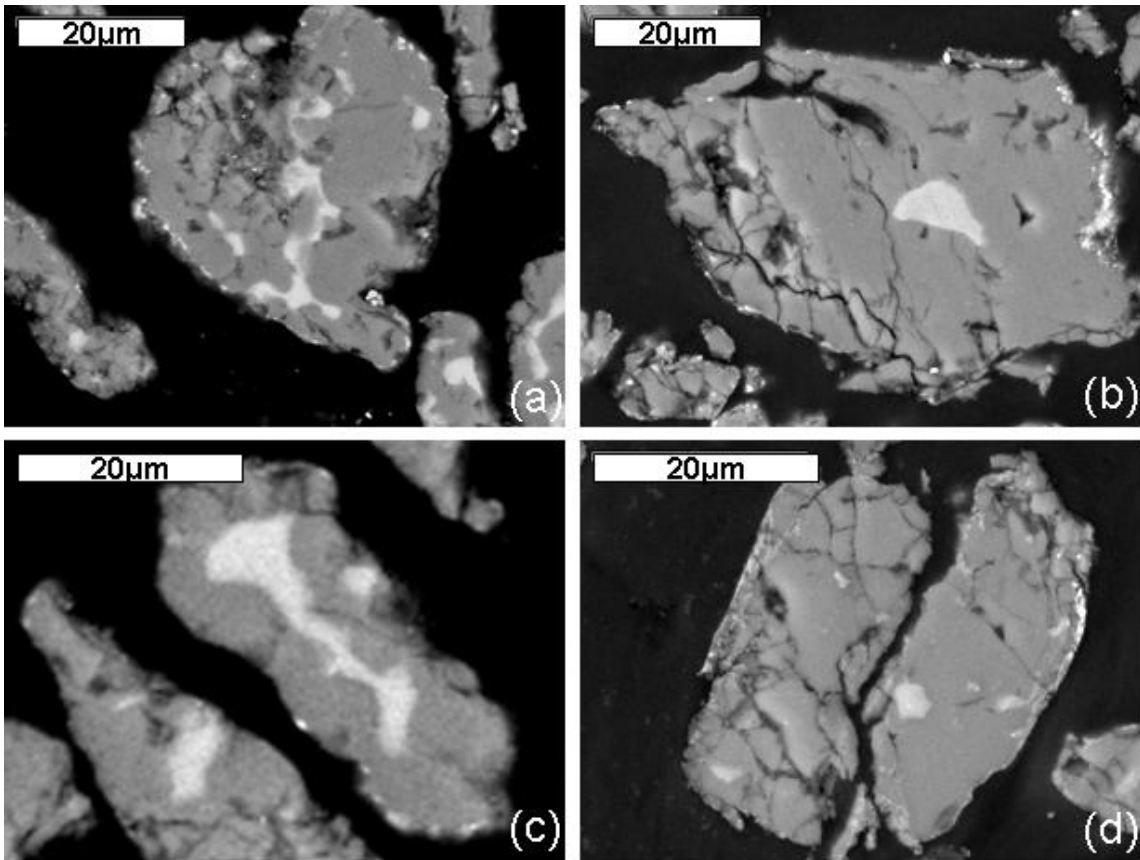


Figure 5-9. Microstructural analysis on the cross section of powder hydrogenated for 300 minutes.

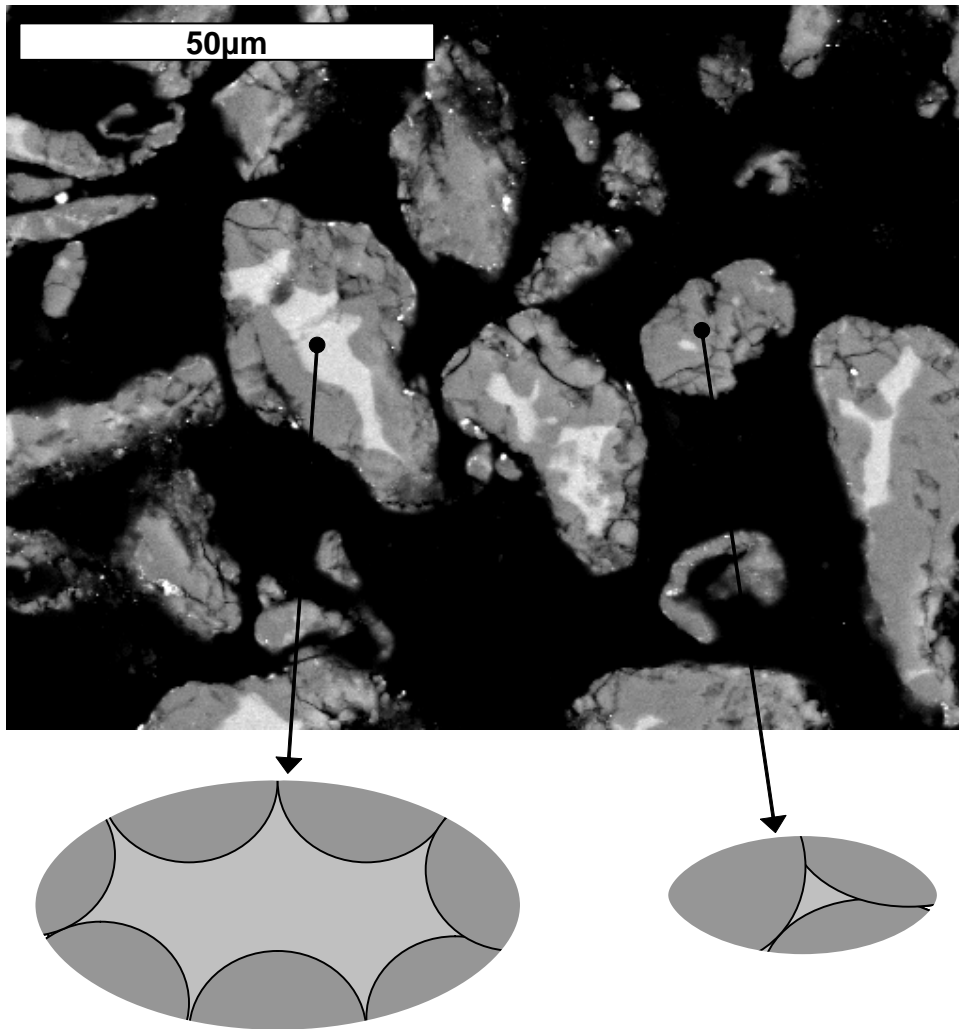


Figure 5-10. An example of different hydride fractions achieved by different sizes of particles.

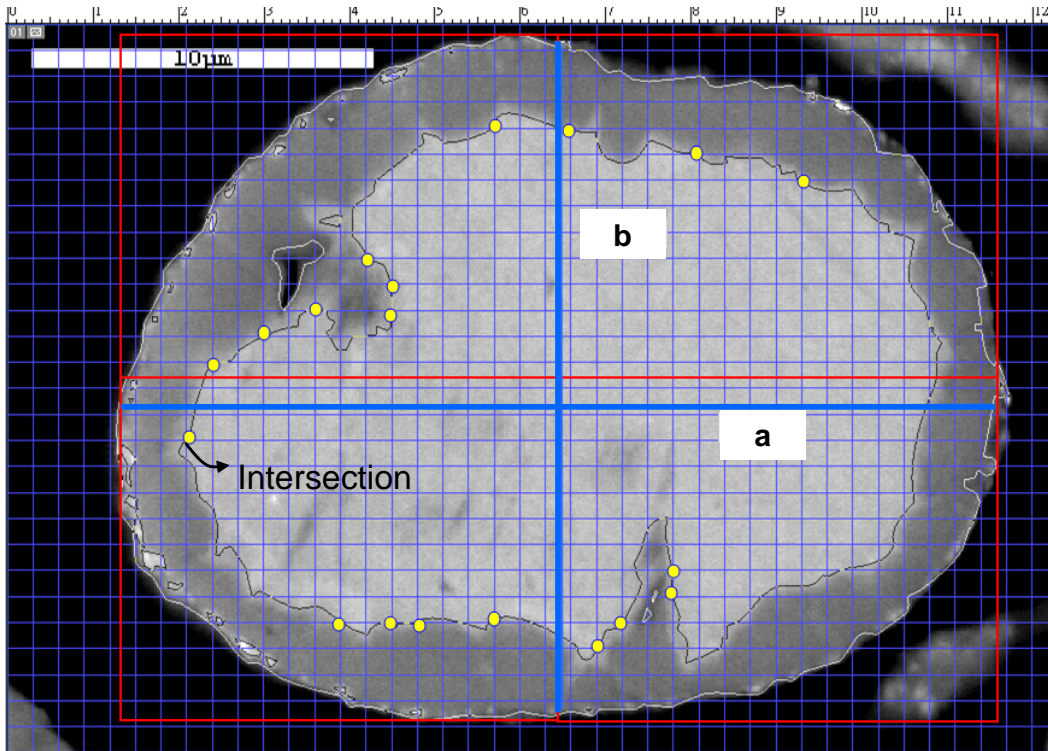


Figure 5-11. An example of the measurement of phase fraction of magnesium hydride

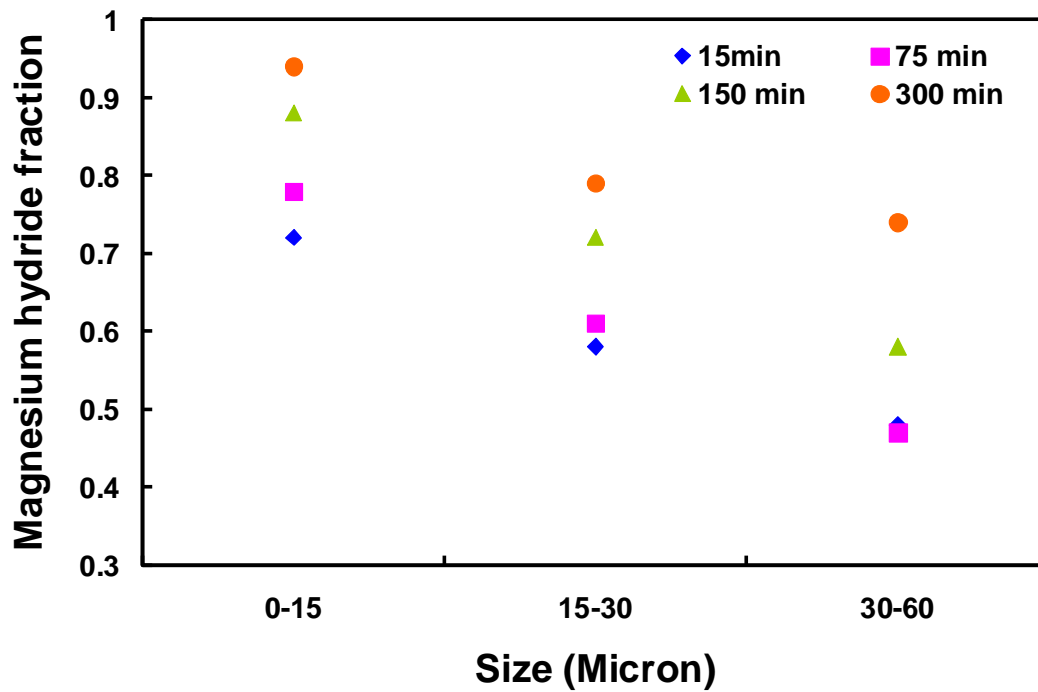


Figure 5-12. Hydride fraction at different range of sizes and temperatures.

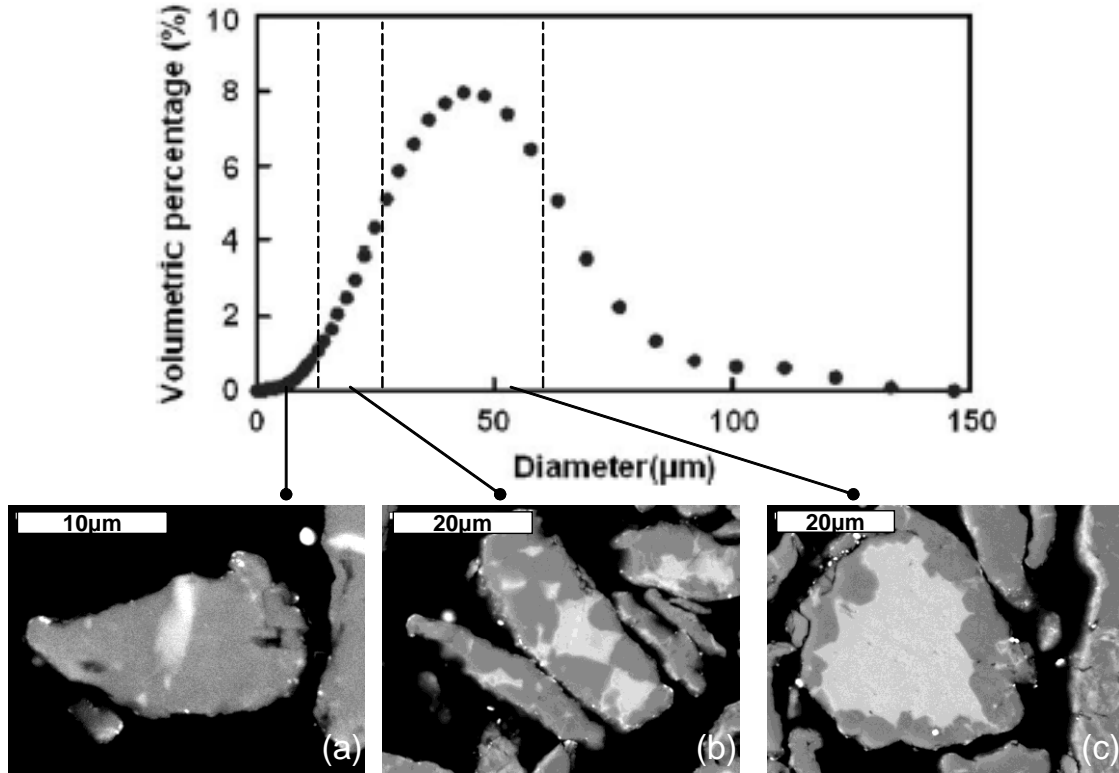


Figure 5-13. An illustration of hydride distribution and phase fraction for different size of particles at the same hydrogenation condition and time 15 minutes.

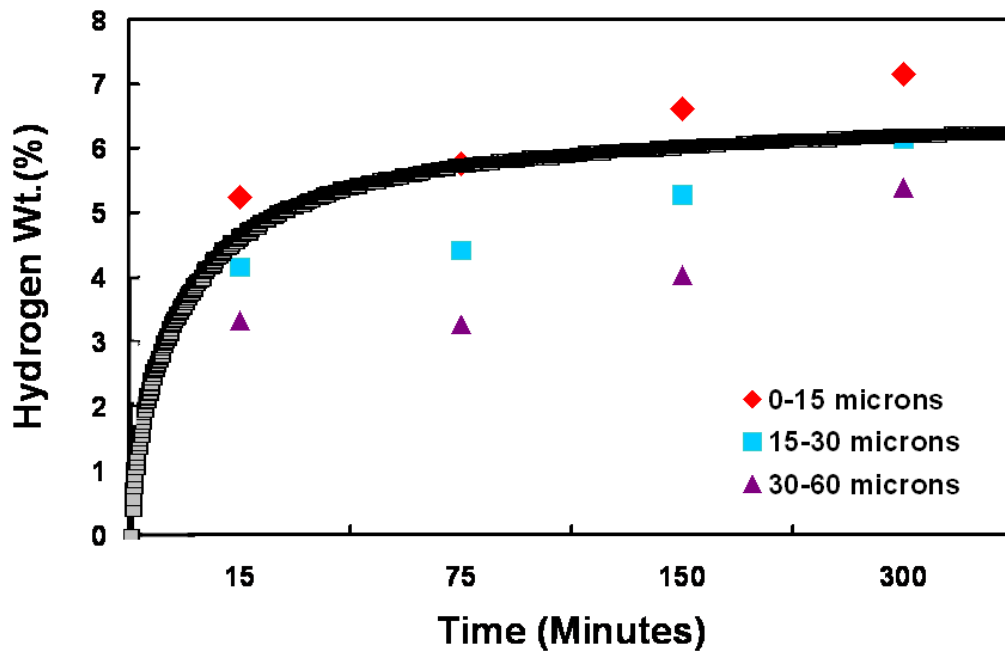


Figure 5-14. A comparison of hydrogenation curve with the data point estimated by the measurement of area phase fraction.

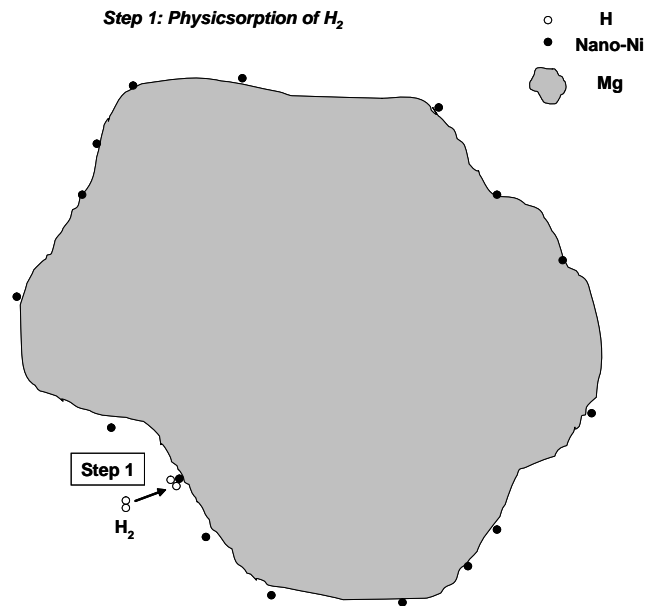


Figure 5-15. Step 1: Physisorption of hydrogen molecules.

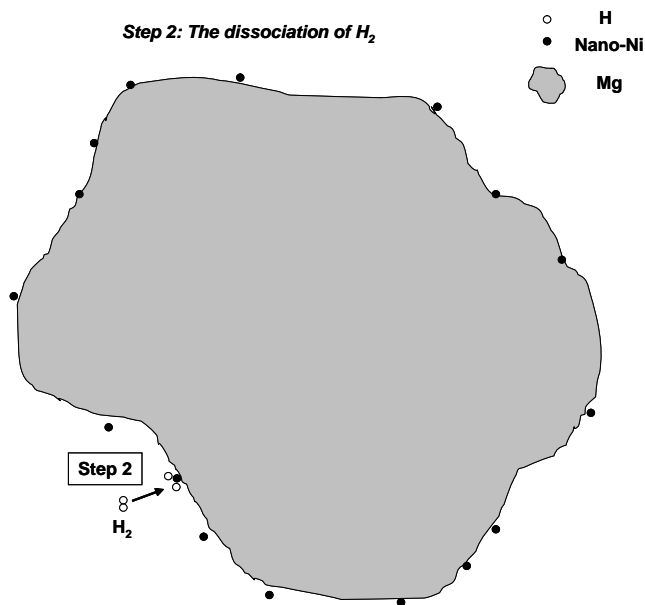


Figure 5-16. Step 2: The dissociation of hydrogen molecules.

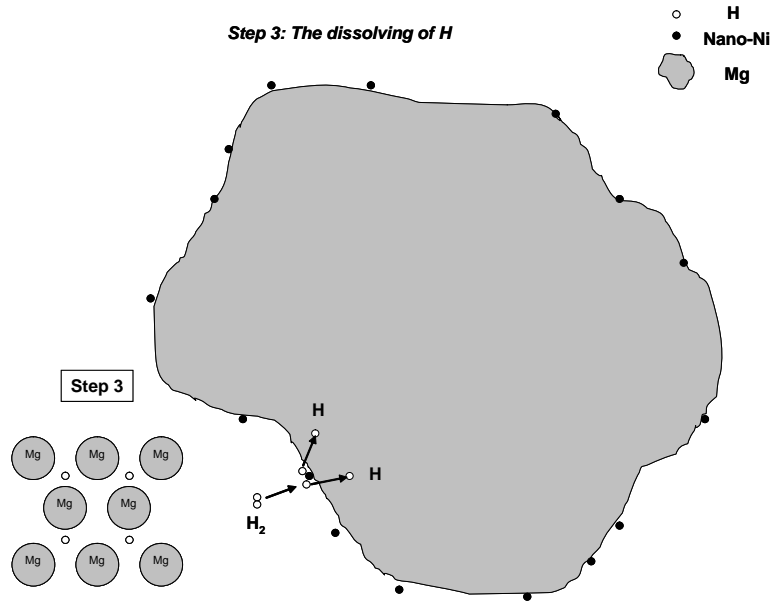


Figure 5-17. Step 3: The dissolving of hydrogen atoms.

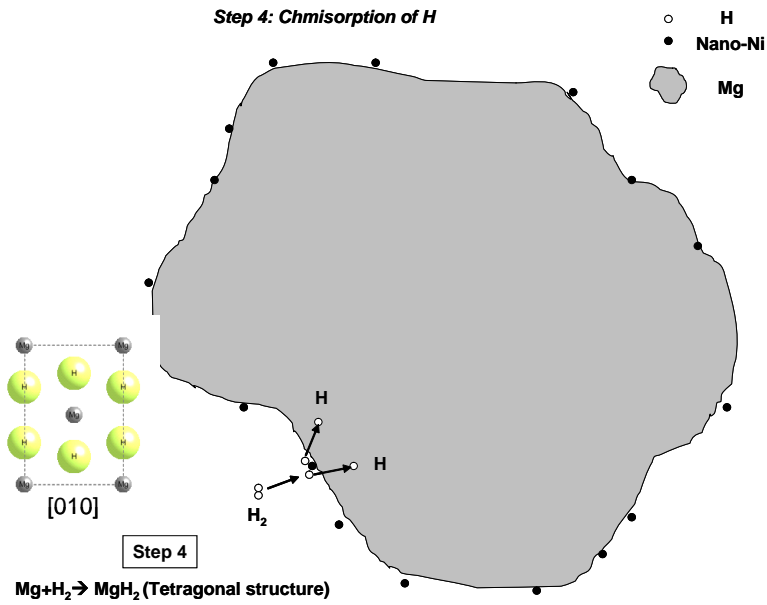


Figure 5-18. Step 4: Chemisorption of hydrogen ions.

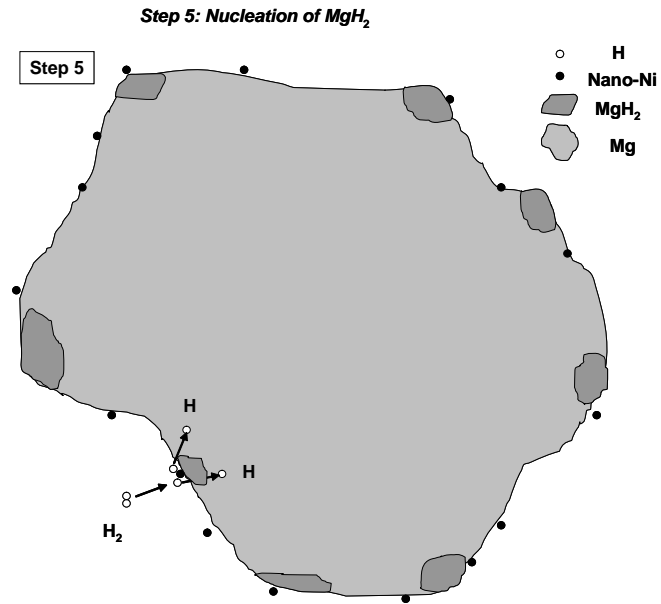


Figure 5-19. Step 5: Nucleation of magnesium hydrides.

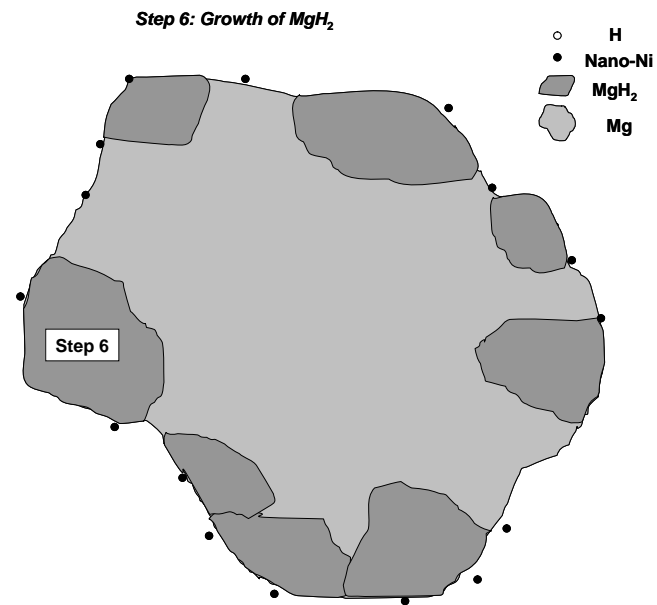


Figure 5-20. Step 6: Growth of magnesium hydrides.

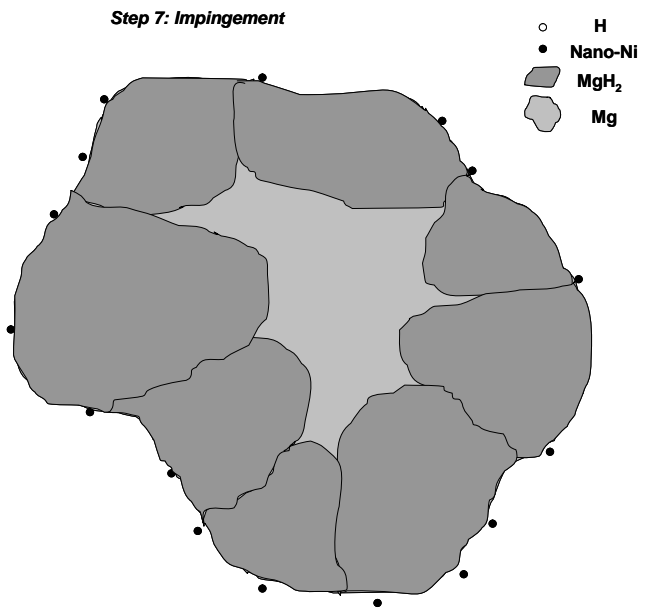


Figure 5-21. Step 7: The impingement of magnesium hydrides.

CHAPTER 6 KINETICS OF MG HYDRIDE FORMATION

6.1 Introductory Remarks

In Chapter 5, the microstructural evolution at different time periods of hydrogenation at a given temperature and pressure was presented and discussed. The results suggested that the hydrogen capacity is controlled by the impingement behavior of magnesium hydride grains/colonies and the magnesium hydride formation occurs by following up the nucleation and growth model. One of the limitations for practical application of magnesium hydride in hydrogen storage is its slow hydrogenation kinetics. In this chapter, to understand the kinetics of hydrogenation at different temperatures, the nucleation and growth processes are treated by the JMA (Johnson-Mehl-Avrami) model [69].

Magnesium powders were hydrogenated at different temperatures under the isothermal and isobaric hydrogenation conditions. The hydrogenation curves were measured and employed to identify the kinetic properties of the magnesium hydride formation. Different stages of hydride formation were identified based on the JMA analysis. In addition, the number of the hydride colonies/grains nuclei was measured at different temperatures in order to better understand the impingement phenomenon. The results of JMA analyses were employed to acquire the activation energy and identify the possible mechanism of hydride growth via constructing the Arrhenius's plot.

6.2 Analysis of Kinetics of Hydride Formation by the Johnson-Mehl-Avrami Relationship

Based on the microstructural analysis, the clearly distinguished individual grains/colonies shown in the cross section of hydrogenated magnesium powder strongly suggest that the formation behavior of magnesium hydride is best explained by a

nucleation and growth model. The details of the Johnson-Mehl-Avrami (JMA) model were discussed in Chapter 2. Using this model, the relation between the hydride fraction and the hydrogenation time at a given pressure can be expressed as:

$$f = 1 - \exp(-Kt^n) \quad (6-1)$$

f: Volume fraction of magnesium hydride.

K: Reaction constant = $K_0 \exp(-Q/RT)$, (Q: Activation energy, R: Ideal gas constant, and T: Isothermal temperature).

t: Hydrogenation time.

n: Reaction order.

n is supposedly independent of the hydrogenation temperature only if there is no change in the nucleation mechanism. The reaction constant, K, on the other hand, depends on the nucleation rate, growth rate and the geometry factor which are very sensitive to the hydrogenation temperature [29, 39, 69]. Equation (6-1) can be rewritten as:

$$(1-f) = \exp(-Kt^n) \quad (6-2a)$$

$$\ln(1-f) = -Kt^n \quad (6-2b)$$

$$\ln\{\ln[1/(1-f)]\} = \ln K + n \ln(t) \quad (6-2c)$$

A plot of $\ln\{\ln[1/(1-f)]\}$ vs $\ln t$ curve is shown in Figure 6-1, which is the JMA-analyzed curve of Figure 5-1. The curve can be clearly divided into three linear stages including a transition region between Stage 1 and Stage 3, which is contributed by different hydrogenation behaviors of the magnesium powders as discussed in Chapter 5. The time range for each stage was defined based on the best fit analysis. The range was selected when the R^2 for each stage was equal or larger than 0.995 (R^2 is defined as

the statistical measure of how well a regression line approximates real data points; an R^2 of 1 indicates a perfect fit). Based on the discussions presented in Chapter 5, Stage 1 is probably associated with the dissociation of hydrogen molecules and/or the nucleation of magnesium hydride. In my opinion, the energy barrier of the dissociation of hydrogen molecules is most probably reduced or eliminated in this case with the catalyst added to the magnesium powder surface. Stage 2 is suggested to be associated with the growth of magnesium hydride assuming that the nucleation rate of magnesium hydride does not depend on time and remains constant. If the nucleation rate of magnesium hydride is zero, which means all the nuclei have been consumed after Stage 1, the number of magnesium hydride nuclei will be a constant value through the whole test. In this case, the controlling step of Stage 2 is the growth of magnesium hydride. The transition region from the beginning to the end of the impingement process resides between Stages 2 and 3. At the end of the transition region, the impingement is complete and further growth of the hydride takes place by the diffusion of hydrogen through the hydride layer. As discussed previously this process is very slow and therefore Stage 3 is associated with a very slow kinetics of hydride formation, which is a continuous thickening process of the hydride layer.

6.2.1 Evaluation of Nucleation Number during Stage 2

A hydrogenation test was designed to disclose the nucleation behavior in the very initial hydrogenation stage. The nuclei numbers are compared at different hydrogenation times to study whether there is a continuous nucleation of the hydride or the number of the nuclei remains constant during Stage 2. The hydrogenation times of 2.5 and 7.5 minutes were selected for this analysis. The microstructural analysis of these samples was conducted in detail as was shown in Chapter 5.

The hydrogenation curves for 2.5 and 7.5 minutes, shown in Figure 5-1, exhibit an overlapping reproducibility in the hydrogenation curve. The powders hydrogenated for 2.5 and 7.5 minutes were imbedded in mounting and checked in the cross section under SEM (BSE mode). As discussed in Chapter 5, the nucleation of magnesium hydride takes place exclusively on the powder surface. Therefore, linear density is sufficient for the evaluation of the number density; otherwise area density should be utilized for the nucleation study. In this analysis it is assumed that the linear density indirectly represents the surface density and they will both show the same tendency in the calculation of nucleation number. Figure 6-2 shows an example of using the ProgRes CapturePro 2.7 software to measure the perimeter of path surrounding the area for the powder sample hydrogenated for 2.5 minutes. Since the magnification by SEM (BSE mode) is different from that by optical microscope, there is a ratio which must be applied to the calculation to obtain the real perimeter of the hydrogenated powder. The same magnification is used in SEM (BSE mode) for the convenience of the perimeter measurement by the software. More than 80 particles were included in this measurement. The nucleation linear density can be obtained by the following equation:

$$D_L = N_L / L \quad (6-3)$$

D_L : Linear density of nuclei.

N_L : Number of nuclei on the powder surface.

L : The total length of powder surface.

The linear density D_L calculated from equation (6-3) is 0.2316 (#/ μm). The same method was applied to the powder sample hydrogenated for 7.5 minutes. An example is shown in Figure 6-3 and about 100 particles were taken into account for this study. The

D_L obtained for 7.5 minutes is 0.2347 (#/ μm) which is very close to that for the 2.5 minutes hydrogenated powder. Table 6.1 shows the results of the measurement of number of nuclei at different hydrogenation times. The inversed values of the linear density represent the distance between two magnesium hydride nodules. According to these measurements, about every 4.3 μm there would be another hydride grain/colony showing up and the total numbers of the nodules on a single 44 μm particle, assuming a spherical shape, would be 32 (#/particle). Based on these results, we concluded that the nuclei number is a constant value during Stage 2 and only the growth of the hydride colonies/grains that form in Stage 1 take place during Stage 2.

6.2.2 Correlation of Grain Boundary and Nuclei of Magnesium Hydride

As shown in Chapter 5, the number of hydride nuclei at 210C was constant during Stage 2. One possible nucleation site for hydride is the intersection of magnesium grain boundaries with the powder surface. In order to correlate the number of intersection sites with the number of hydride nuclei, a magnesium powder sample was heated from room temperature to 210°C under very low hydrogen pressure (~3Pa) without introducing the hydrogen gas into the specimen chamber. The powder sample was prepared for metallography using an optical microscope. Acetic glycol was used as the etching agent to reveal magnesium grain boundaries. Figure 6-4 shows the optical microscopic image of the pre-heating magnesium powder sample. The grain size of magnesium is approximately 20 μm . The study in our lab for the magnesium grain size measurement under TEM demonstrates that the grain size of the as-received magnesium powder is approximately 2 μm [98]. This result indicates that the grain size has increased during the pre-heating process of the magnesium powder sample. Generally, the heterogeneous nucleation is easier than the homogeneous nucleation.

The intersection at the powder surface becomes the nucleation site owing to its low surface energy. The linear density of intersections of the grain boundaries with the powder surface per unit length is measured to be $0.08(\#/ \mu\text{m})$, which means about every $12.5\mu\text{m}$ an intersection at the powder surface is located. As reported in Table 6-1, the actual linear density of the hydride nuclei is about $4.3\mu\text{m}$, which is smaller than the linear intersection density. This difference may be attributed to the lack of enough statistics as well as the fact that linear density can be different than the actual areal density.

6.2.3 Effect of Hydrogenation Temperature

The objective of this chapter is to study the hydrogenation mechanism during magnesium hydride formation. A systematic approach including reproducibility has been considered to evaluate the hydrogenation curves of magnesium powders. The majority of previously reported hydrogenation curves for magnesium have been evaluated at relatively high temperatures [31, 34, 63]. In this study the kinetics of hydrogenation of magnesium is investigated at relatively low temperatures ($\leq 300^\circ\text{C}$). Four hydrogenation temperatures 150°C , 180°C , 210°C , and 250°C were used for the investigation of the effect of hydrogenation temperature. Figure 6-5 shows the hydrogenation curves at these temperatures under constant hydrogen pressure of 1MPa . Each test was conducted twice in order to ensure repeatability of the tests. These curves reveal that as the test temperature is decreased the hydrogen capacity is reduced. The initial hydrogenation rate, as identified by the slope of the curve in the early stages of hydrogenation, seems to decrease with decreasing temperature up to 180°C and then becomes quite fast at 150°C . This behavior can be explained by the opposite effect of

hydrogenation temperature on nucleation and growth of hydrides. As the hydrogenation temperature is reduced the hydride growth rate is expected to decrease. On the other hand, because of the increase in the driving force for the formation of the hydride phase at low temperatures, the number of hydride nuclei is much higher at low temperatures. Another interesting observation is that as the test temperature is decreased, there is less tendency to reach pseudo-saturation after 5 hours of hydrogenation. As the hydrogenation temperature is decreased, owing to the large number of hydride nucleation sites, the thickness at which impingement is achieved is reduced. Since the flux of hydrogen through a thinner hydride layer is larger, the hydrogenation rate after impingement will be faster at a lower hydrogenation temperature.

The hydrogen capacities at each temperature are shown in Table 6-2. Figure 6-6 presents the relationship between the hydrogen capacities and the hydrogenation temperatures. The trend reveals that the hydrogen capacity increases with increasing temperature. It is noticed that the hydrogen capacities vary from about 3.2 to 6.9 H wt.% in this temperature span and never reach the theoretical value 7.6 H wt. %. Powders hydrogenated at 250°C show the closest values, 6.5 and 6.9 H wt. %, to the theoretical values. However, the curves exhibit no further hydrogen absorption after approximately 150 minutes during the hydrogenation tests. Powders hydrogenated at 210°C show slightly lower hydrogen capacities than those at 250°C. The hydrogen capacities are 6.1 and 6.3 H wt. %. One of the hydrogenation tests was interrupted at 282 minutes due to an equipment issue but luckily the curve had already reached saturation stage. As the test temperature is dropped to 180°C, the hydrogenation capacities after 5 hours of

hydrogenation reduce to 5.4 and 5.8 H wt. %. At 150°C hydrogenation temperature the capacity drops further to 3.2 and 3.3 H wt. % in 300 minutes.

6.2.4 Microstructural Analysis of Powders Hydrogenated at Different Temperatures

A microstructure analysis of the powders hydrogenated at the four temperatures of 150°C, 180°C, 210°C, and 250°C after 300 minutes of hydrogenation was performed. It is observed that the hydride layer is composed of the impinged hydride grains/colonies for all temperatures, as shown in Figure 6-7. In Figure 6-7(a), the powder sample hydrogenated at 150°C shows a continuous magnesium hydride layer with a very small thickness about 2µm. This observation confirms that the impingement of the hydride grains/colonies takes place relatively fast and the growth of the hydride layer takes place by the diffusion of hydrogen through the hydride layer (Core-Shell model). Figure 6-7(b) shows the SEM (BSE mode) cross-sectional image of powders hydrogenated at 180°C for 5 hours. Larger hydride grains/colonies are identified here with a 4 to 8µm hydride layer thickness. The microstructure of powders hydrogenated at 210°C is shown in 6-7(c). Some of the cracks appeared inside the hydride phase and the hydride thickness varied from 4-15µm. When the powders were hydrogenated at 250°C, many particles were completely hydrogenated and as shown in Figure 6-7(d) only patches of the metallic magnesium, encapsulated by the hydride growth, were left.

Figure 6-8 illustrates the proposed effect of hydrogenation temperature on the microstructure of hydrogenated particles. The driving force for hydride nucleation is relatively low near the equilibrium temperature (Fig. 6-8 a) whereas the growth rate is maximized. Under this condition a large fraction of a magnesium particle is transformed to magnesium hydride before the impingement of the hydride colonies/crystals takes

place. On the other hand, a low hydrogenation temperature (Fig. 6-8b) is expected to render a fast nucleation rate, which causes the impingement of the hydride colonies to be achieved at a relatively smaller hydride thickness, i.e. at a lower volume fraction of hydride. The driving force is the temperature difference between equilibrium temperature and experimental temperature (hydrogenation temperature) $\Delta T = T_{eq} - T_h$. From the literature, the equilibrium temperature for 1MPa hydrogen pressure is 373°C [38]. At 150°C the nucleation rate is relatively high as compared to other temperatures, hence the impingement takes place shortly while the surface has been covered by a large number of hydride colonies/grains. We can expect that the lower the hydrogenation temperature, the higher the nucleation rate of magnesium hydride. With the temperature increasing the driving force decreases since the hydrogenation temperature becomes close to the equilibrium temperature. The nucleation rate, which is driving force, decreases with increasing temperature. It should be noted that the nucleation theory only applied up to the hydrogenation temperature below the equilibrium temperature because beyond or equal to the equilibrium temperature, a reversed reaction and desorption of hydrogen happens.

6.3 Effect of Nucleation Rate on Hydrogen Capacity

6.3.1 Hydrogenation Procedures

In this study the nucleation rate was changed by modifying the hydrogenation procedure. As described in Chapter 3, two methods may be used to hydrogenate a powder. In Method I the powder was first pressurized to 1MPa with hydrogen gas. Then, the specimen is heated to the desired temperature. In Method II, which has been used throughout this dissertation, the specimen chamber is heated to the desired temperature under vacuum, and the chamber is pressurized with hydrogen gas to

1MPa. Fig. 6-9 displays hydrogenation curves for the methods for the hydrogenation temperature of 210°C. A comparison of the hydrogenation curves by the two methods applied in this study revealed that the hydrogen capacity is strongly dependent on the sequence of pressurization and heating. It is clear that the apparent saturation level, i.e. the hydrogen capacity, is much higher for Method II (6.1 H wt. %) than that for Method I (1.5 H wt. %).

To elucidate the mechanism of magnesium hydride formation, we analyzed the hydrogenation curves using the Johnson–Mehl–Avrami (JMA) equation, The $\ln[\ln(1/1 - f)]$ is plotted as a function of $\ln(t)$ in Fig. 6-10, which demonstrates that the magnesium hydride develops in three stages as discussed in Chapter 5. The reaction rate in Stage 1, which takes place in a very short time (<2 min) is probably controlled by nucleation of magnesium hydride. It is believed that the hydride phase initially nucleates on the surface of the powders. The beginning of extensive growth of the hydride corresponds to the onset of Stage 2. As the hydride colonies/grains grow, the total effective cross-section area for hydrogen diffusion into the magnesium phase decreases. The end of Stage 2 corresponds to the beginning of impingement of the hydride colonies/grains, after which the growth of hydride is limited by the diffusion of hydrogen through the hydride and maximum capacity is reached for relatively high hydrogenation temperatures. As shown in Fig. 6-10, Method II exhibited a much longer growth period, i.e., Stage 2. Table 6-3 presents the n values representing the slope of the curves shown in Fig. 6-10 for the three stages of hydrogenation. The hydrogenation method affected the n values significantly, suggesting that the kinetics of hydrogenation is strongly dependent on the hydrogenation method.

In order to confirm that the difference in the hydrogenation behavior of the powders, as a result of the change in the heating and pressurizing schedule, is associated with the nucleation rate of hydride, a powder sample was hydrogenated by Method II to a hydride fraction equivalent to the saturation level of the powder hydrogenated by Method I. Fig. 6-11 compares the hydrogenation curve by Method II for 3 minutes with that of Method I. It should be noted that the time axis for Method I starts when the heating begins and consequently a lower initial apparent kinetics is observed. As indicated on the curve, in the sample hydrogenated by Method I, most of the hydride was formed prior to reaching 210°C. Fig. 6-12 shows SEM images of the hydrogenated powders with an equal amount of hydride. From the cross-section and surface images, it can be seen that the samples hydrogenated to the same level have very different distributions of hydride colonies/grains. For the powder hydrogenated by Method I, the hydride colonies/grains are relatively small (Fig. 6-12 a) and cover the entire surface of the particle (Fig. 6-12 b). In contrast, Method II resulted in few nucleation sites for magnesium hydride as seen in the cross-section micrograph (Fig. 6-12 c) and the observation of the metallic magnesium on the surface (Fig. 6-12 d). Also, the size of the hydride colonies/grains formed by Method II is somewhat larger compared to those observed in the powder hydrogenated by Method I. To quantify the nucleation behavior, we evaluated the apparent surface coverage fraction by magnesium hydride in both powders. As shown in Figure 6-13, the fraction of coverage was estimated from the SEM pictures of over 50 particles for each powder sample by:

$$\text{Surface Coverage} = \frac{\sum H_i}{(\sum H_i + \sum M_i)} \quad (6-4)$$

where H_i is the length of the particle perimeter covered by the hydride, M_i is the length of the particle perimeter remaining as metallic magnesium, and i denotes the particle number. Fig. 6-14 presents the fraction of particles as a function of their surface coverage. As it can be seen in this graph, Method I resulted in a large fraction of particles (0.55) with more than 90% coverage. On the other hand, the powders hydrogenated by Method II exhibited some powders with very low surface coverage (low number of nucleation sites) and a much smaller fraction of particles (0.26) with more than 90% coverage. Fig. 6-15 shows examples of high and low surface coverage in powders hydrogenated by Methods I and II, respectively. Considering the shape of the particles, the cross-section shape varied among the powders – from circular (Fig. 6-15 a and c) to elliptical (Fig. 6-15 b and d) shape as discussed in Chapter 4.

In summary, by varying the hydrogenation procedure at a given temperature, we have demonstrated that the hydrogen capacity of magnesium powder is inversely related to the nucleation rate of the hydride phase. Here, it is assumed that the magnesium hydride preferentially nucleates on the surface of magnesium particles. As the surface coverage with magnesium hydride increases with time, less area for hydrogen entry will be available, hence, due to a decrease in the growth rate, the hydrogen absorption rate reduces. When the hydride colonies/crystals impinge on each other, the diffusion of hydrogen will be limited through the hydride phase. Since the diffusivity of hydrogen through the hydride phase is at least three orders of magnitude smaller than through magnesium [91] the hydrogenation rate will be decreased significantly and a pseudo-saturation is reached. This pseudo-saturation level is considered as the hydrogen capacity, which is defined as the hydrogen content after a

long hydrogenation period at a given temperature and pressure. The effect of temperature on hydrogen capacity can be explained by the dependency of the hydride nucleation rate, which increases with undercooling, $\Delta T = T_{\text{eq}} - T_{\text{h}}$ (T_{e} is the equilibrium temperature for $\text{Mg} + \text{H}_2 \rightarrow \text{MgH}_2$ at a given pressure and T_{h} is the hydrogenation temperature).

The much smaller n value in Stage 1 for Method I in comparison to Method II can be attributed to the lower kinetics of hydrogen dissociation, which is a thermally activated process. Considering that during hydrogenation by Method I the temperature, hence the hydride growth rate, is lower, the larger slope of Stage 2 (Table 6.3) indicates that the hydride phase nucleated faster than during hydrogenation by Method II. The smaller size of hydride colonies/grains and the high surface coverage of particles elucidated by microstructural analysis confirmed the rapid nucleation of the magnesium hydride under Method I. The driving force for nucleation is proportional to the deviation from the equilibrium condition. At pressure of 1MPa, the equilibrium temperature for magnesium hydride formation is 373°C [38]. When the powder was heated after pressurization with hydrogen (Method I), the hydride formation began shortly after the heater was turned on. The large deviation from the equilibrium temperature provided a high driving force resulting in a fast nucleation rate. Consequently, the powder surface was covered with MgH_2 in a short time during hydrogenation by this method. After this point, further hydrogen absorption takes place by diffusion of hydrogen through the magnesium hydride layer. From the literature, the diffusion coefficient of hydrogen in magnesium hydride can be expressed as $D = 1.507 \times 10^{-4} (\text{m}^2\text{s}^{-1}) [\exp(-96\text{kJ/mole})/RT]$ [91]. At the hydrogenation temperature of 210°C, the approximate diffusion length is

quite small ($0.35\mu\text{m min}^{-1}$) resulting in a very slow hydrogen uptake. On the other hand, in Method II, hydride nucleated and grew at 210°C , which is consistent with the lower hydride nucleation rate observed based on the microstructural investigations. The slope of Stage 3 was slightly higher for Method II, suggesting that not all particles had been completely covered by a hydride layer. The results of this study reveal that for a given hydrogenation method the powders do not display similar level of hydride formation (Fig. 6-14). This phenomenon is probably associated with the differences in the surface condition of the powders as well as any variation in the Ni coating among particles. The hydrogen coverage distribution curves shown in Fig. 6-14 suggest that the saturation is achieved when approximately more than 80% of the powders have a surface coverage of 80% or more.

6.3.2 Heating Procedure

The objective of this study was to confirm that the pseudo-saturation observed in the hydrogenation curves at relatively high temperatures is associated with the impingement of the hydride grains/colonies rather than the thickening of a continuous hydride layer as in the Core-Shell model. In this investigation the nucleation rate was modified by applying two different temperatures during a single hydrogenation experiment. Initially, the powder sample was hydrogenated at a low temperature (150°C) to establish a high number of hydride nuclei. Then, the hydrogenation temperature was increased (210°C) to allow for faster growth rate. In addition, samples were hydrogenated in one step at 150°C and 210°C for comparison. Figure 6-16 presents the hydrogenation curves up to 5 h for temperatures of 150 and 210°C as well as the two-step hydrogenation ($150^{\circ}\text{C} + 210^{\circ}\text{C}$). As expected, the hydrogen capacity of magnesium powder hydrogenated at 210°C (6.1 wt. % H) was much higher than that

achieved at 150°C (3.2 wt. % H). In two-step hydrogenation, the first step was conducted at 150°C for 2 min and then the hydrogenation temperature was increased to 210°C. Based on the Core–Shell model, the two-step hydrogenation procedure should have resulted in hydrogen absorption kinetics close to the 210°C curve. However, interestingly, the two-step hydrogenated sample showed an even lower hydrogen capacity (2.4 wt. % H) than the sample hydrogenated at 150°C. This finding confirms that the Core–Shell model is not representative of hydrogenation process in magnesium powders. In order to prove the hydride nucleation concept illustrated in Figure 6-16, the microstructures of powders hydrogenated to identical quantity of hydride fraction at different temperatures were investigated. A magnesium powder sample was hydrogenated at 210°C for 15 min (point A on Fig. 6-16) to produce an equal amount of hydride as in the sample hydrogenated at 150°C for 5 h. Figure 6-17 presents SEM/BSE images of cross-sectioned (a and b) and whole (c and d) particles. Figures 6-17a and b clearly demonstrate the effect of temperature on the nucleation behavior of magnesium hydride. Only a few nucleation sites were activated at 210°C and the magnesium hydride phase did not cover the surface of the particles (Fig. 6-17a). In contrast, a continuous hydride layer with much smaller hydride colonies/crystals were found in the powder hydrogenated at 150°C. The external images (Fig. 6-17c and d) also confirm the presence of hydride-free areas on the particle surface in the 210°C hydrogenated powder, while complete coverage was achieved when powders were hydrogenated at 150°C. Figure 6-18(a) displays the cross-sectional image of powders hydrogenated at 150°C for only 2 min. As shown in the high-magnification picture

presented in Figure 6-18b, the nucleation of magnesium hydride was not limited to the surface and indeed many fairly small hydride particles were found near the surface.

The results presented above confirm that the hydrogen capacity is controlled by the impingement of hydride colonies/crystals. The equilibrium temperature at 1MPa for $\text{Mg} + \text{H}_2 \rightarrow \text{MgH}_2$ reaction is approximately 373°C. At 150°C ($\Delta T = 223^\circ\text{C}$), and the hydride nucleation rate is quite large and as demonstrated in Figures 6-18b and 6-18d the hydrogen capacity is reached at a small hydride thickness. The lower driving force for nucleation and the higher diffusion rate at 210°C ($\Delta T = 163^\circ\text{C}$) render a much smaller nucleation rate and faster growth rate, which result in extensive growth of hydrides grains/colonies before their impingement (Fig. 6-17a). Increasing the temperature to 210°C after establishing the nucleation sites by hydrogenating at 150°C for 2 min only expedited the growth of the hydride phase and their impingement. As shown in Figure 6-18b, the hydride nucleation at 150°C was not limited to the surface. The lower capacity of the two-step hydrogenated sample in comparison to the 150°C hydrogenated sample (Fig. 6-18d) can be attributed to the incomplete growth of the inner hydride nuclei in the former sample. In other words, the slower growth at 150°C allowed more growth of the inner hydride particles before the occurrence of the impingement. This observation suggests that when there is a large driving force for nucleation, as is the case at 150°C, hydride nucleation can take place at other defects such as grain boundaries and dislocations. Note that most of the hydride was found near the surface where the highest concentration of hydrogen is expected to exist based on the diffusion of hydrogen from the surface inward. After further hydrogenation at 210°C for 298 min, no new nucleation of the hydride phase took place and as shown

in Figure 6-18c the magnesium hydride particles grew and completely covered the magnesium particle. Hydrogenation at 150°C for 5h (2 + 298 min), as demonstrated in Figure 6-18d, resulted in a similar hydride layer. This observation further confirms that the Core-Shell model is not relevant to the microstructural evolution during the hydrogenation of magnesium.

6.4 Kinetics analysis by Johnson-Mehl-Avrami relation for Growth Mechanism of Magnesium Hydride

As mentioned in section 6-2, the magnesium hydride nucleates heterogeneously at the intersection between grain boundary and powder surface. After $t=\tau$, all the nucleation sites were consumed and follows the individual growth of each magnesium hydride nucleus. In this section, the objective is to investigate the growth mechanism of magnesium hydride formation. The JMA analysis for hydrogenation temperatures of 250, 210, 180 and 150°C are presented in Figures from 6-19 to 6-26. Except for the 150°C hydrogenation temperature, all curves show the three stages as discussed in Chapter 5.

The mechanism responsible for each stage can be identified by evaluating the activation energy. According to equation (2-2) the activation energy for Stage 2 can be calculated by considering the temperature dependency of the constant K , assuming that n is not temperature dependent. Table 6-4 summarizes the K , $\ln K$ and n values for Stage 2 and 3. It is noticed that the n values for Stage 2 decrease slightly with increasing temperature, as shown in Figure 6-27. The n values change from 0.5 to 0.68. However, n value is assumed to be unaffected by the temperature. In Table 2-1, it is noticed that for diffusion control growth, every 0.5 is taken as a unit. It is reasonable to use $n=0.5$ for this material. Karty et al. reported the n value for hydrogen absorption of

Mg₂Cu coated magnesium to be 0.5 [70]. Fernandez et al. demonstrated that the hydrogenation of magnesium is controlled by nucleation and growth and reported exponent values of $n = 0.5-1$ give the best fit to the experimental data [71]. The n values from both groups provided the same value as the n value calculated in this study. Based on Rudman et al.'s work, the n value of 0.5 suggests one dimensional diffusion control growth process [29, 70]. For the diffusion controlled growth process, it is shown:

$$G=(gt)^n=(gt)^{1/2} \quad (6-5)$$

where G is the total growth at time t , g is the growth rate, and n value is 0.5. Figure 6-27 also shows the n values in Stage 3, which are much smaller than the n values for Stage 3. It should be noted that Stage 3, which is associated with the thickening of a continuous hydride layer, cannot be evaluated by JMA analysis. Table 6-5 shows the starting point and end of each stage with the corresponding hydrogenation time. The end of the impingement is the end of the transition region. It should be born in mind that the impingement only occurs in the transition region. The transition region is located between the two arrows in each curve in Figure 6-28 at each temperature. The end of the transition region represents the end of impingement. After all the surface of the magnesium powders is surrounded by hydride layers, Stage 3 occurs. However, it is still unknown which phase hydrogen is diffusing through during the growth of hydride; it can be the metallic magnesium phase or magnesium hydride phase. The following section explains the calculation of the activation energy of the growth of magnesium hydride which was compared to the result obtained by other groups. The value of activation energy would give us an idea which phase hydrogen diffuses through.

The activation energy for Stage 2 was calculated by applying the Arrhenius plot. The K values for JMA analysis of powders hydrogenated at 150°C were excluded because these samples did not show a Stage 2. Only the K values of Stage 2 for hydrogenation temperatures of 180, 210, and 250°C were taken into account. Figure 6-29 presents the Arrhenius plot, where $\ln K$ is plotted versus $1/T$. We can see the slope equal to $-Q/R$ is -3899.9, so the activation energy calculated here is 32.4 kJ/ mole. The value of the activation energy is very close to the activation energy of the diffusion of hydrogen through the magnesium phase latest result reported in the literature, which is 24kJ/mole [67, 91]. The good correlation between the activation energy for diffusion of hydrogen in metallic magnesium and the activation energy for Stage 2 confirms that the magnesium hydride growth takes place by the diffusion of hydrogen through magnesium and not magnesium hydride. As the hydrogenation temperature is lowered to 150°C (Figures 6-25 and 6-26), it is noticed that the curve exhibits only two stages during the formation of magnesium hydride. As demonstrated in Figure 6-18(b), because of the driving force for nucleation of magnesium hydride at this temperature, lots of surface defects were activated near the powder surface, which acted as the nucleation sites for magnesium hydride on the surface as well as inside the powder particles. Consequently, the impingement of the hydride grains is achieved in a short time with a very thin hydride layer. It is suggested that the nucleation is not a rate-controlling step for 150°C in this case. Therefore, Stage 2, which is the growth of the hydride to impingement, is not detectable in the JMA analysis at 150°C. Because all the powders formed a thin hydride layer at the same time the transition region is also skipped. However, there are 3 possible mechanisms which may control the Stage 3: (1)

The dissociation of hydrogen molecules, (2) the diffusivity of hydrogen through hydride layer, (3) the diffusion length of hydrogen through the hydride layer. It is believed that the rate of the dissociation of hydrogen molecule into two hydrogen atoms increases with increasing temperature. The diffusivity of hydrogen through hydride layer is also increased with increasing temperature. Both two possible mechanisms are thermally activated which will lead to a faster reaction rate in Stage 3 at higher temperature. Figure 6-30 shows the possible slopes in the beginning of Stage 3 at 150°C and 250°C. If this figure is compared with Figure 6-28, it is noticed that the slope in Stage 3 at 150°C is higher than that at 250°C. Figure 6-7(a, d) shows the microstructural analysis of powders hydrogenated at 150°C and 250°C, respectively. The diffusion length of hydrogen through hydride layer is shorter at 150°C than that at 250°C, which leads to a higher slope and faster thickening process in the Stage 3. Meanwhile it also indicates that the rate limiting step in Stage 3 is controlled by the diffusion length of hydrogen through hydride layer.

6.5 The Fraction of Magnesium Hydride at Impingement

Friedlmeier et al. [30], based on experimental hydrogenation data, have shown empirically that for a given test temperature and pressure the df/dt (f =weight fraction of hydride formed at time t , t = time) varies linearly as a function of time. They have assumed that at relatively high temperature, from 273 to 355°C, the total hydrogen capacity can be approximated as the hydride fraction at impingement, f^* . However, as demonstrated in Figures 6-31 through 6-36, the results of hydrogenation of the magnesium powder at 1MPa and in the temperature range of 250-180°C, reveal that at low temperatures noticeable hydrogen is absorbed during Stage 3. This absorption is manifested as a drastic change in the slope of df/dt as a function of t . These figures

demonstrate that similar to the JMA results presented earlier, there is a transition from Stage 2 to Stage 3. Therefore, here, the value of f^* is estimated as the intersection of the two linear sections corresponding to these two stages.

The hydride fractions f^* for 250°C here are 0.55 and 0.59 for two independent tests. Figure 6-33 exhibits the curve of reaction rate, df/dt , vs the hydride fraction, f , for the hydrogenation tests completed at 210°C. In Figure 6-34, it is calculated that the f^* values are 0.52 and 0.56. It is noticed that the f^* for 210°C is smaller than those at 250°C but the difference is not very significant. For the curve analyzed for the relationship of reaction rate and hydride fraction, f , at 180°C in Figure 6-35, the f^* for both curves are measured to be 0.40 and 0.47, as shown in Figure 6-36. Those f^* values are clearly smaller than the f^* values of 210°C and also 250°C. Figure 6-37 reveals the reaction rate against the hydride fraction, f , for powder samples hydrogenated at 150°C. The f^* values for 150°C are both 0.17 as shown in Figure 6-38 and the f^* values are smallest among all tests.

The f^* represents the hydride fraction at impingement and the trend of f^* is shown to increase with increasing temperatures. Based on the theoretical assumption of this analysis, f^* should be comparable with the hydride fraction at the midpoint of the transition region from JMA analysis. Figure 6-39 compares the results from the JMA analysis with those calculated based on the linear relationship between the reaction rate and the weight fraction of hydride. There is a relatively good correlation between the two approaches and the latter method results in consistently lower values. The difference may be partially associated with the mathematical methodology to define f^* .

6.6 Summary and Conclusions

The hydrogenation mechanism for a commercially available 44 μ m Ni-coated magnesium powder at 1MPa and in the temperature range of 150 to 250°C was successfully evaluated and discussed in this chapter. The amount of hydrogen absorbed after 5 hours of hydrogenation was revealed to be temperature dependent and controlled by the amount of hydrogen absorbed to the point of the impingement of the hydride colonies/grains (Stage 2) and the amount of hydrogen consumed in the further growth of the continuous layer of hydride after impingement (Stage 3). As the hydrogenation temperature decreases, the contribution of Stage 3 becomes more significant and the tendency to reach a pseudo-saturation level of hydrogen absorption is decreased. JMA analysis was applied to calculate the activation energy for hydride growth in Stage 2. According to this calculation, the rate limiting step of magnesium hydride growth is the diffusion of hydrogen through the metallic magnesium.

For the study of nucleation rate on hydrogen capacity, we investigated the hydrogenation kinetics by two hydrogenation methods and two-stage heating procedures. The results of both studies have demonstrated that the hydrogen capacity of magnesium powder is influenced drastically by the nucleation rate of the hydride. At a high nucleation rate, limited hydride growth takes place before the impingement of the hydride colonies/grains, which retards further growth of the hydride owing to the drastic reduction of hydrogen flux because of the low diffusivity of hydrogen in the magnesium hydride. Based on the findings of this investigation, for a given particle geometry, there is an optimum hydrogenation condition that leads to the near theoretical hydrogen capacity with fast absorption rate. For example, at low hydrogenation temperatures, owing to a fast nucleation rate the capacity will be low. On the other hand, increasing

the hydrogenation temperature will enhance the growth rate but will decrease the nucleation rate, hence hydrogenation rate. Therefore, there is an optimum hydrogenation temperature, where a good capacity is reached in a relatively fast manner. The study of hydride fraction at impingement gives us an idea how f^* values vary with hydrogenation temperatures and shows the very different df/dt curves at 150°C compared with others which proves that it jumps from Stage 1 to Stage 3 in the JMA analysis.

In conclusion:

1. The study of nucleation number in the initial hydrogenation time period suggests that the nucleation is a constant number during the growth of magnesium hydride.
2. The impingement model is best explained in Stage 1 and 2 (Nucleation and growth of hydride), and after impingement the Core–Shell model can only explain the Stage 3 (Continuous thickening of hydride layer).
3. The microstructural analysis confirms that the hydrogenation of magnesium particles can be explained by nucleation, growth and impingement processes before impingement of hydride.
4. The reduction of hydrogen capacity by lowering the hydrogenation temperature can be attributed to the increased nucleation rate.
5. The growth of magnesium hydride in Stage 2 is controlled by the diffusion of hydrogen through the magnesium phase during hydrogenation.

The thickening of the hydride layer in Stage 3 is controlled by the diffusion of hydrogen through the magnesium hydride phase during hydrogenation.

Table 6-1. The result of the measurement of number of nucleation at different hydrogenation times

Hydrogenation Time (Minutes)	Total length	Total Number of nodules	Linear density (#/μm)	Distance between two nucleuses	Number of nucleation on 44μm powder surface
2.5	4796	1111	0.2316	4.32	32.02
7.5	4444	1043	0.2347	4.26	32.49

Table 6-2. Hydrogen capacity at different hydrogenation temperatures

Temp. Test	150		180		210		250	
	1	2	1	2	1	2	1	2
Hydrogen capacity	3.2	3.3	5.8	5.4	6.1	6.3	6.5	6.9

Table 6-3. The slope of the three stages of hydrogenation as revealed by JMA analysis in Figure 6-29.

Method	Stage 1	Stage 2	Stage 3
I	0.27	1.60	0.14
II	0.80	0.53	0.17

Table 6-4. n and K values for Stage 2 and 3 at each temperatures

	Stage 2			Stage 3		
	n	lnK	K	n	lnK	K
150-1	-	-	-	0.25	-1.92	0.15
150-2	-	-	-	0.34	-2.32	0.10
180-1	0.61	-2.47	0.08	0.24	-0.88	0.41
180-2	0.67	-3.28	0.04	0.29	-1.35	0.26
210-1	0.68	-2.42	0.09	0.17	-0.19	0.83
210-2	0.53	-1.87	0.15	0.17	-0.37	0.69
250-1	0.50	-1.44	0.24	0.09	0.25	1.28
250-2	0.55	-1.84	0.16	0.17	-0.28	0.76

Table 6-5. End time in minutes of each stage

	Stage 1		Stage 2		Transition	
	ln t ₁	t ₁	ln t ₂	t ₂	ln t _t	t _t
150-1	1.2	-	-	-0.09	0.9	1.2
150-2	0.8	-	-	0.32	1.4	0.8
180-1	1.1	3.87	47.9	5.15	172.5	1.1
180-2	1.1	3.89	49.1	5.16	174.7	1.1
210-1	1.6	3.77	43.3	5.23	187.5	1.6
210-2	1.8	3.77	43.5	5.33	207.5	1.8
250-1	1.6	3.67	39.3	5.00	148.6	1.6
250-2	1.8	3.79	44.2	5.1	165.6	1.8

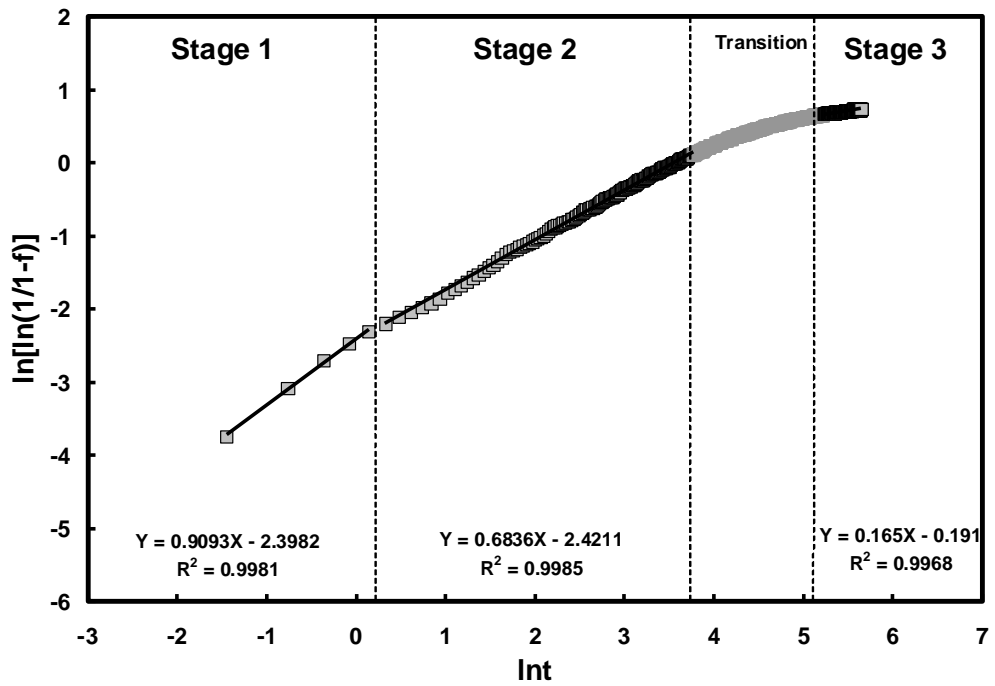


Figure 6-1. The JMA analysis of powders hydrogenated at 210°C under 1MPa.

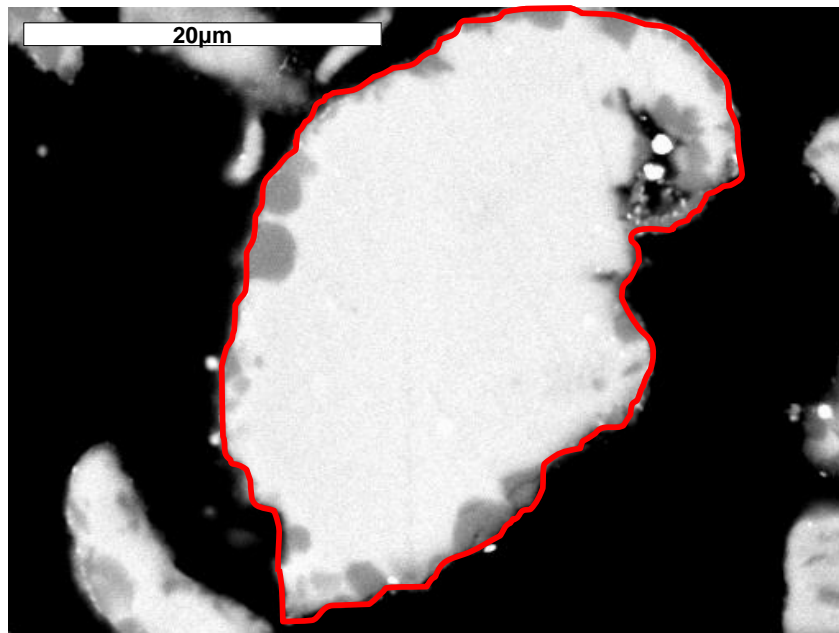


Figure 6-2. The measurement of perimeter for powders hydrogenated for 2.5 minutes.

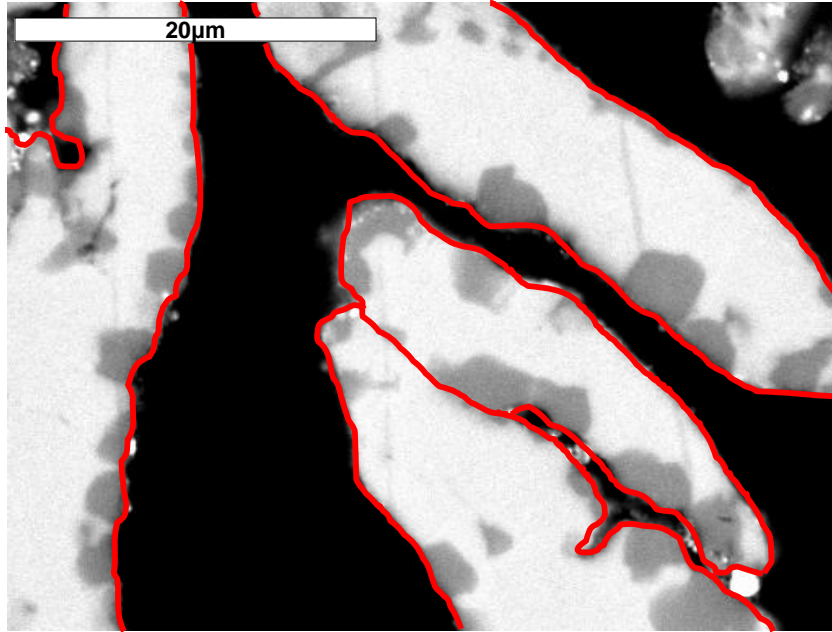


Figure 6-3. The measurement of perimeter for powders hydrogenated for 7.5 minutes.

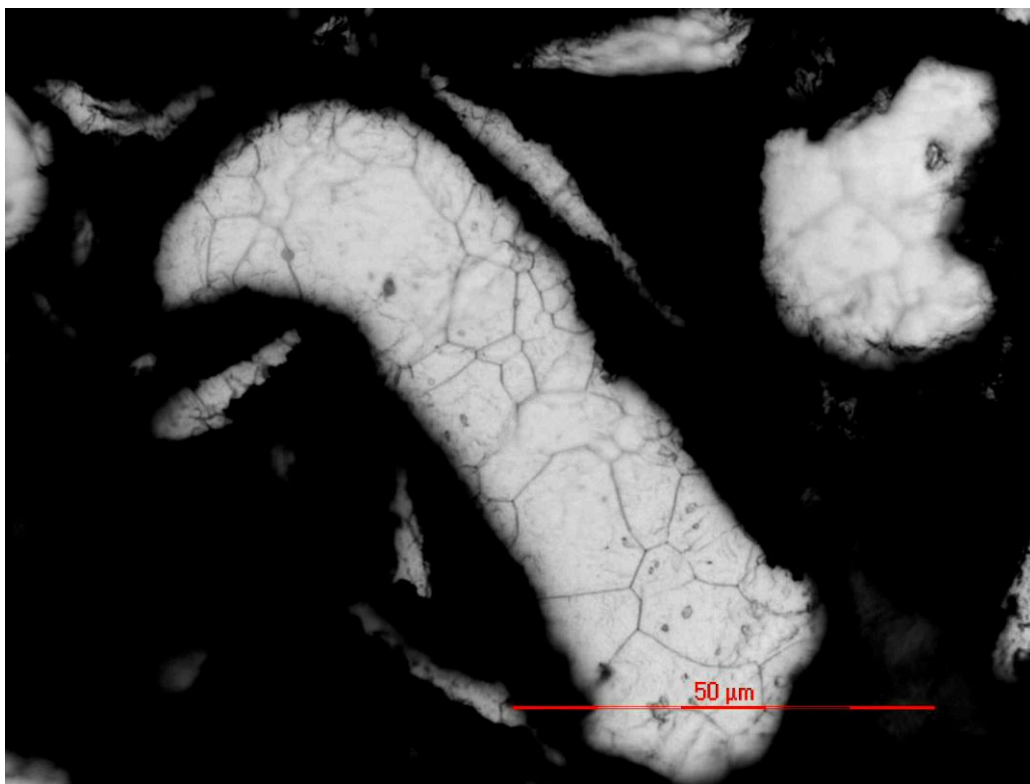


Figure 6-4. The etched cross sectional surface of magnesium powder pre-heated at 210°C.

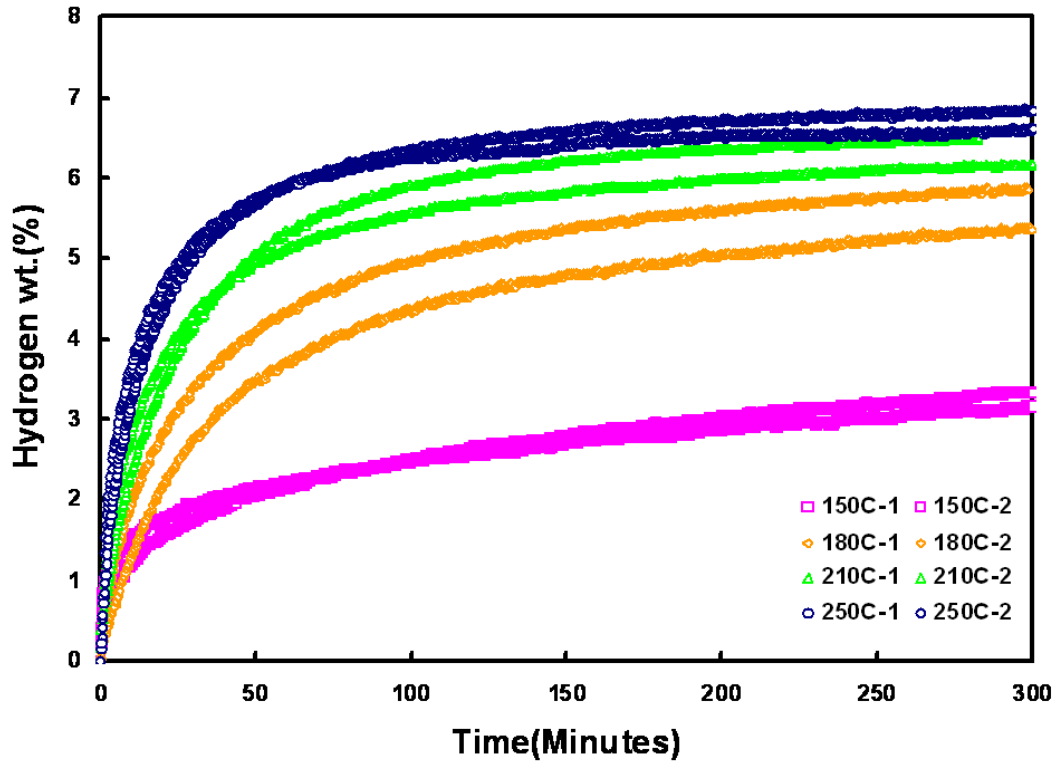


Figure 6-5. The hydrogenation curves of magnesium powders hydrogenated at 150, 180, 210, and 250°C.

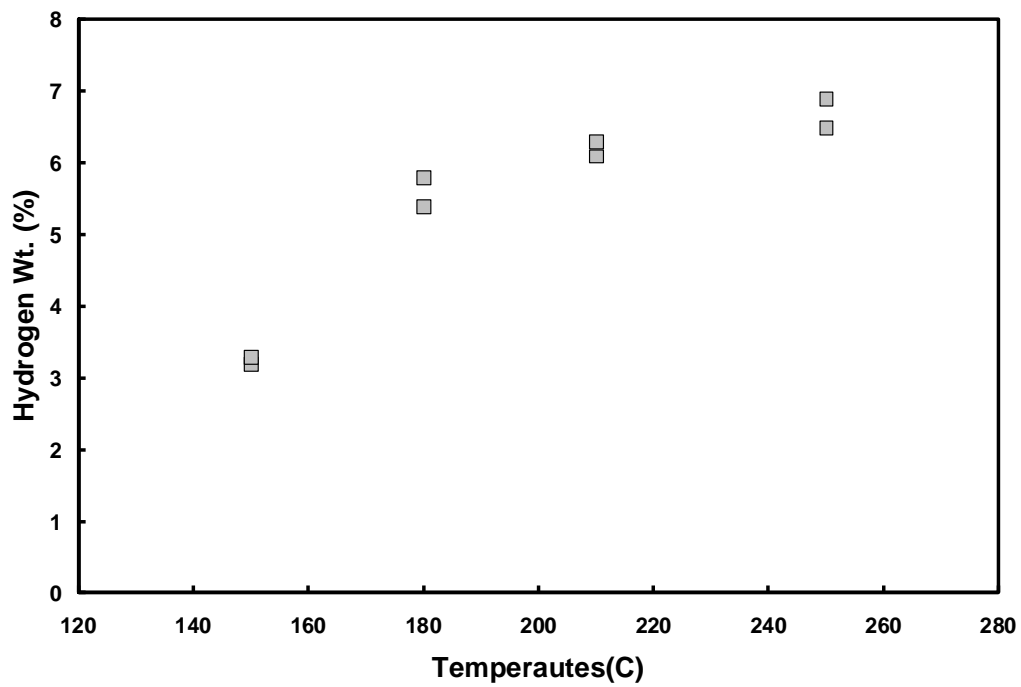


Figure 6-6. The relationship between hydrogen capacity and hydrogenation temperatures.

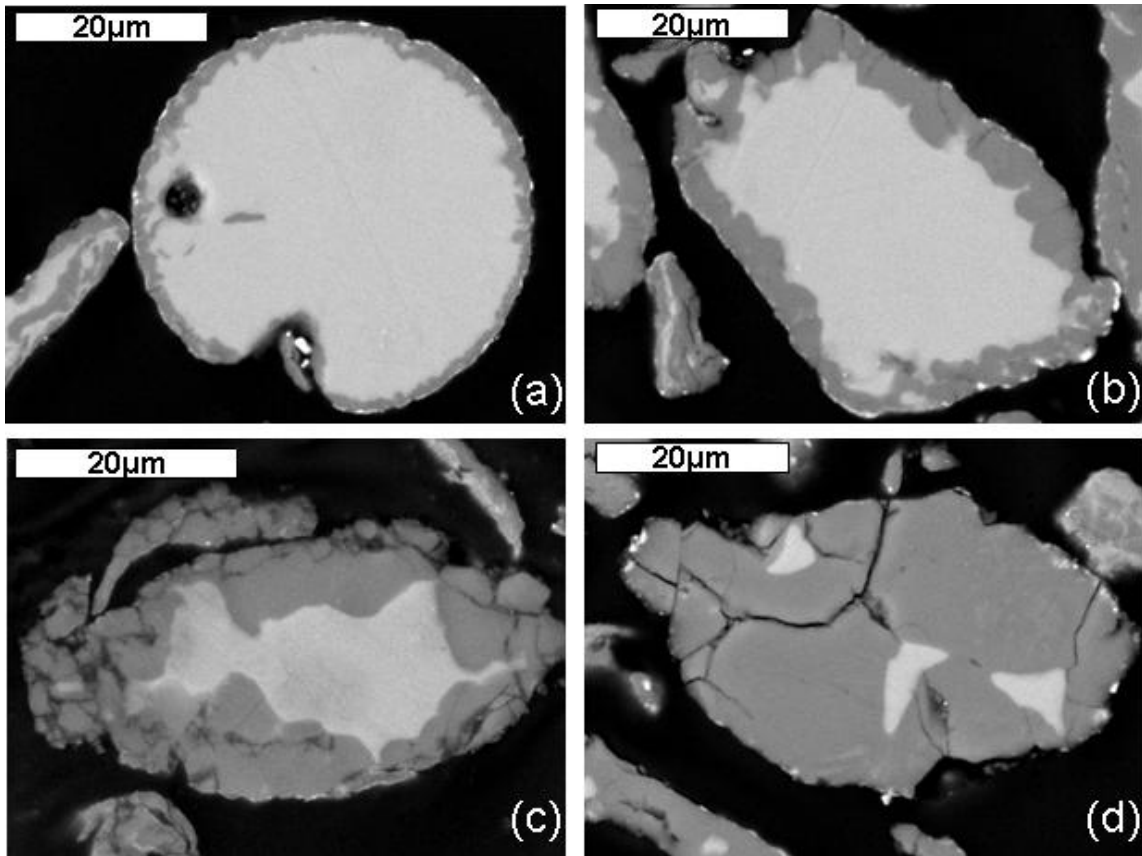


Figure 6-7. The microstructural analysis of powders hydrogenated at (a)150°C, (b)180°C, (c)210°C, and (d)250°C under 1Mpa for 5 hours.

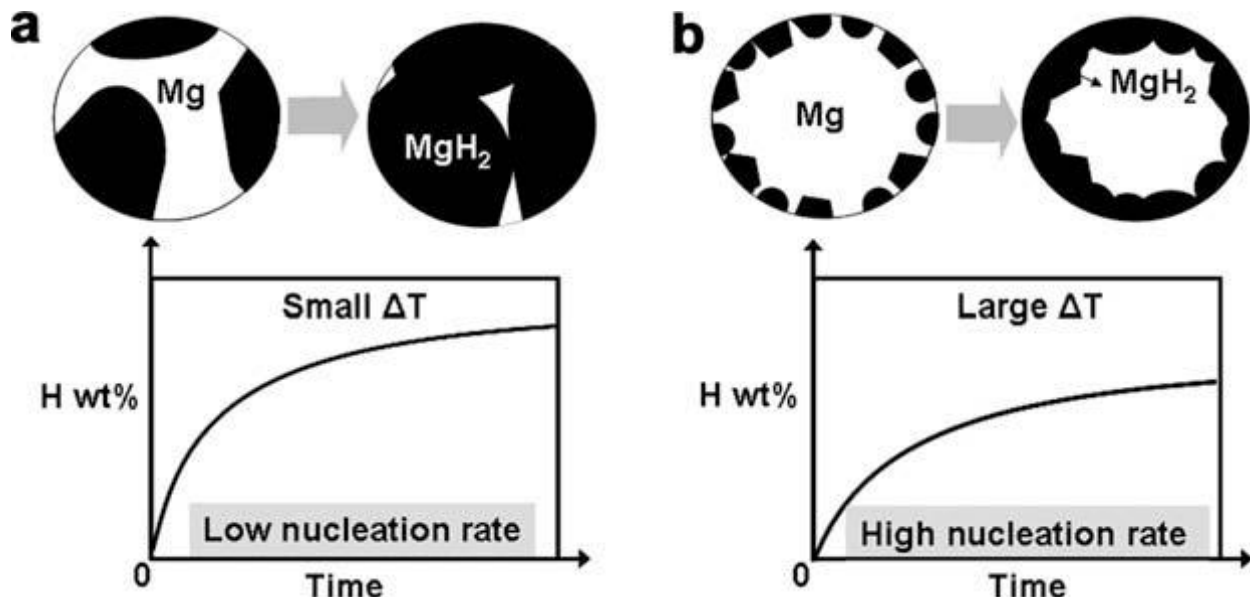


Figure 6-8. The schematic illustration of proposed model for the effect of nucleation rate on hydrogenation kinetics and hydrogen capacity.

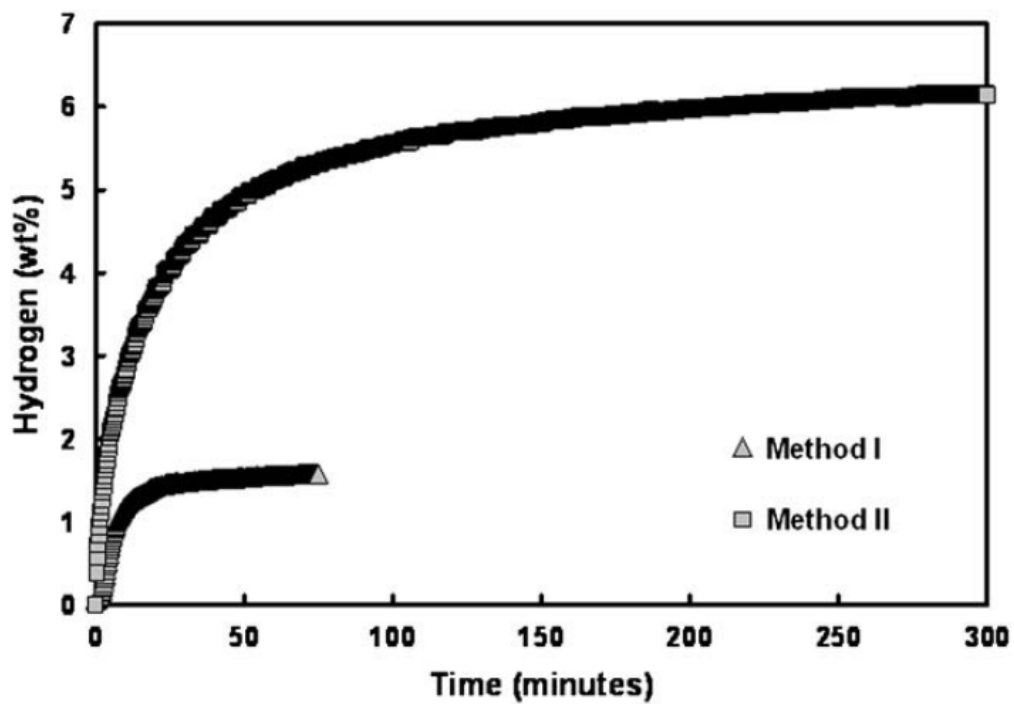


Figure 6-9. Hydrogen absorption as a function of time for the two hydrogenation methods employed.

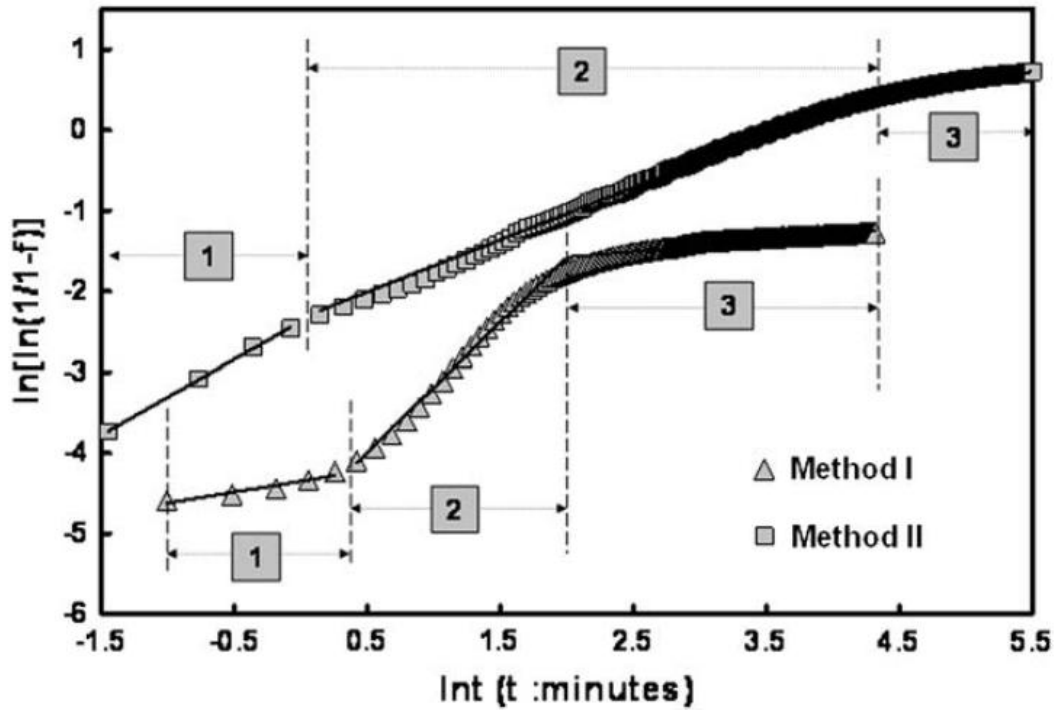


Figure 6-10. The evaluation of kinetics of hydride formation by Methods I and II on the JMA relationship.

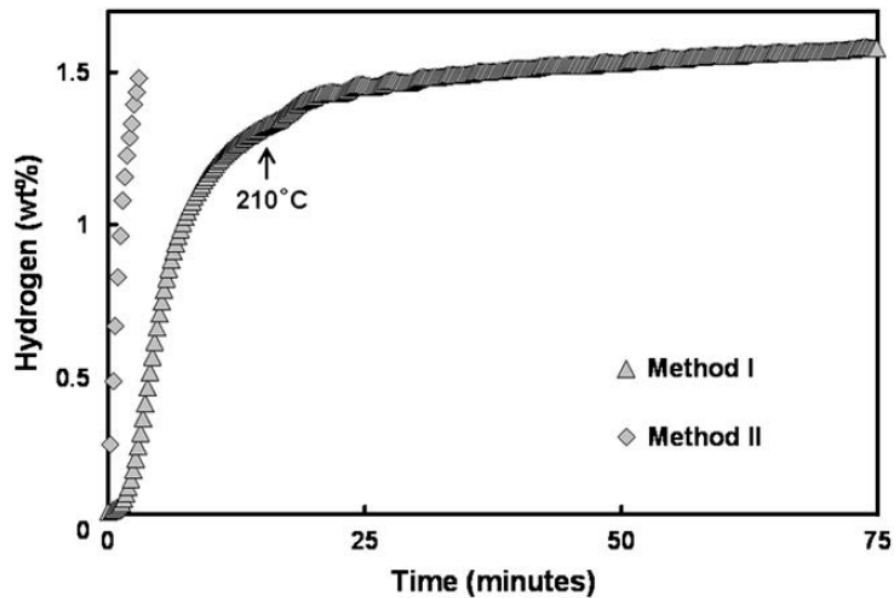


Figure 6-11. A comparison of the hydrogenation curves for powders hydrogenated by Method I for 75 minutes and by Method II for 3 minutes.

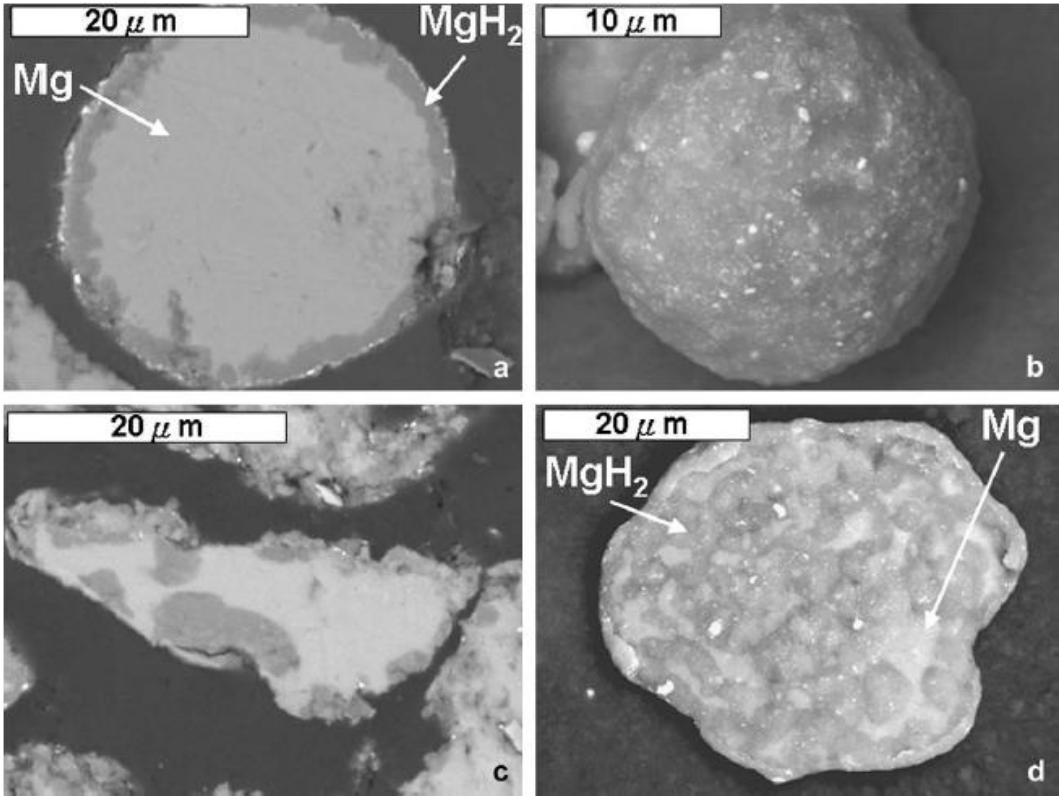


Figure 6-12. SEM pictures comparing the hydride formation for powders hydrogenated by Method I for 75 minutes (a and b) and by Method II for 3 minutes (c and d); (a) and (C) are cross sectional view and (b) and (d) are the external view of the powders.

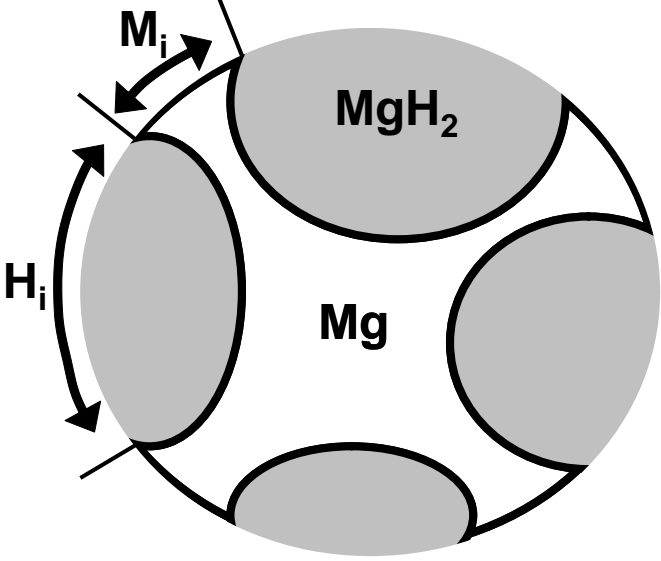


Figure 6-13. The surface coverage measurement.

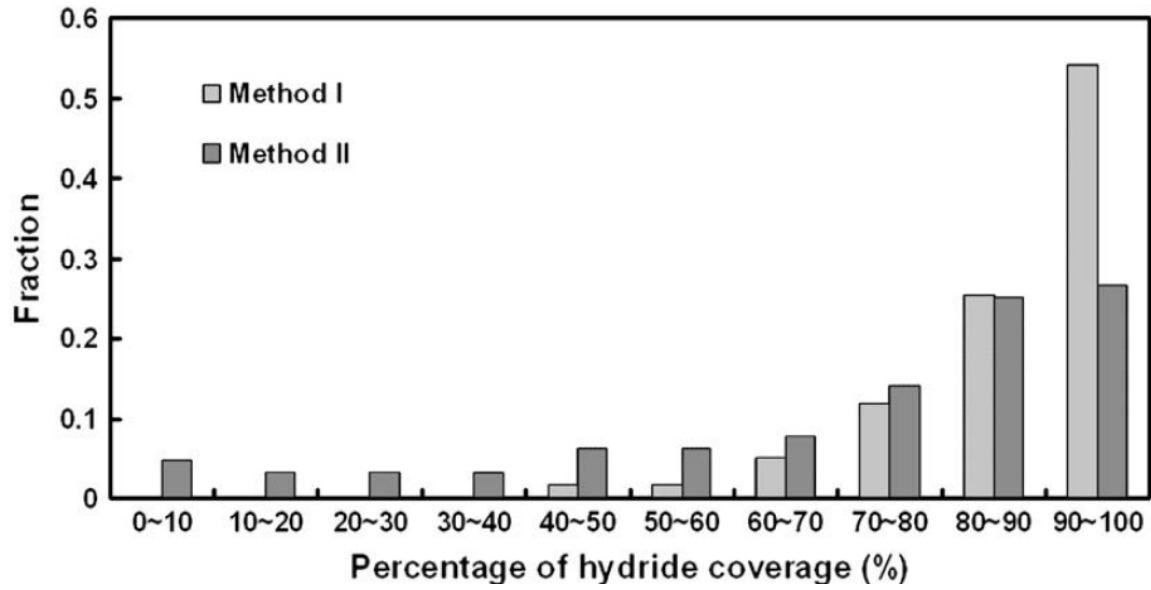


Figure 6-14. The distribution of the surface coverage of the particles hydrogenated by Method I and II.

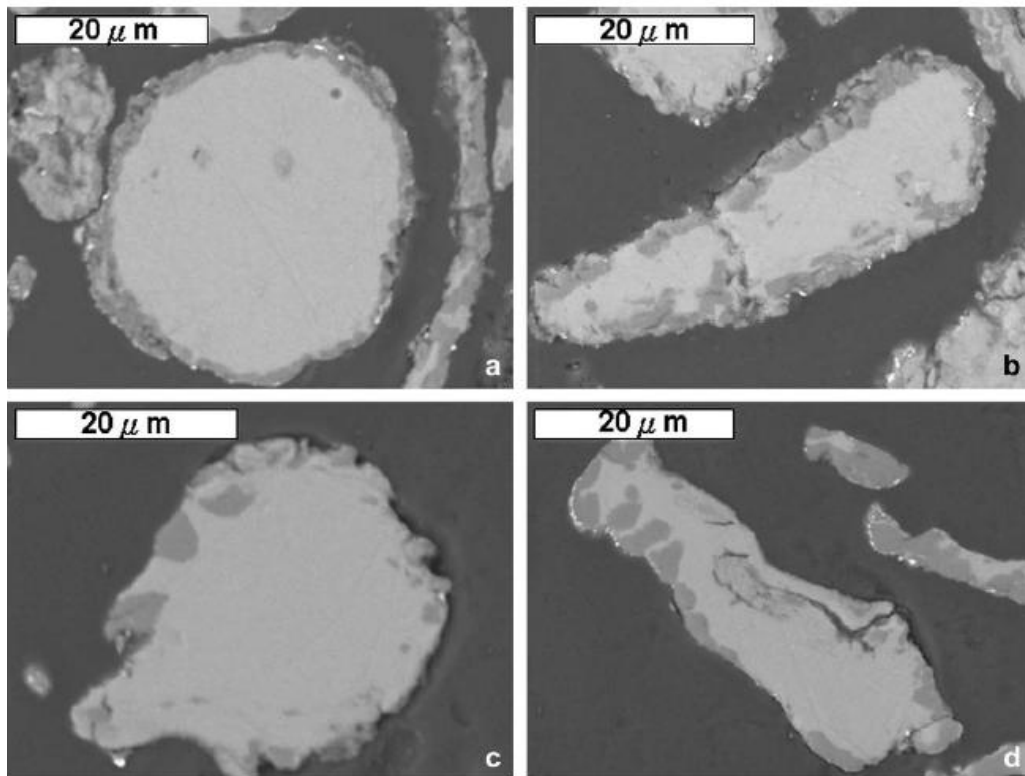


Figure 6-15. SEM pictures showing cross-sectional views of the particles with high hydride coverage after 75 minutes of hydrogenation by Method I (a and b) and with low hydride coverage after 3 minutes of hydrogenation by Method II (c and d).

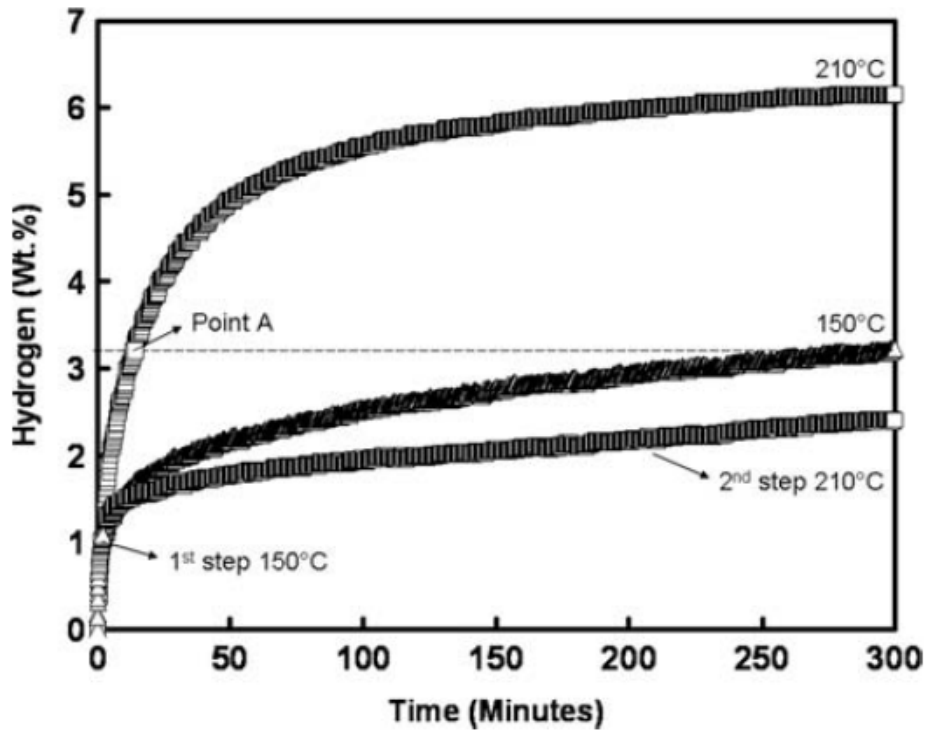


Figure 6-16. Hydrogenation curves for 150°C, 210°C and the two-step heating. Point A denotes the time (15 minutes) at 210°C, which results in an equal amount of hydride as the powder hydrogenated at 150°C for 5 hours.

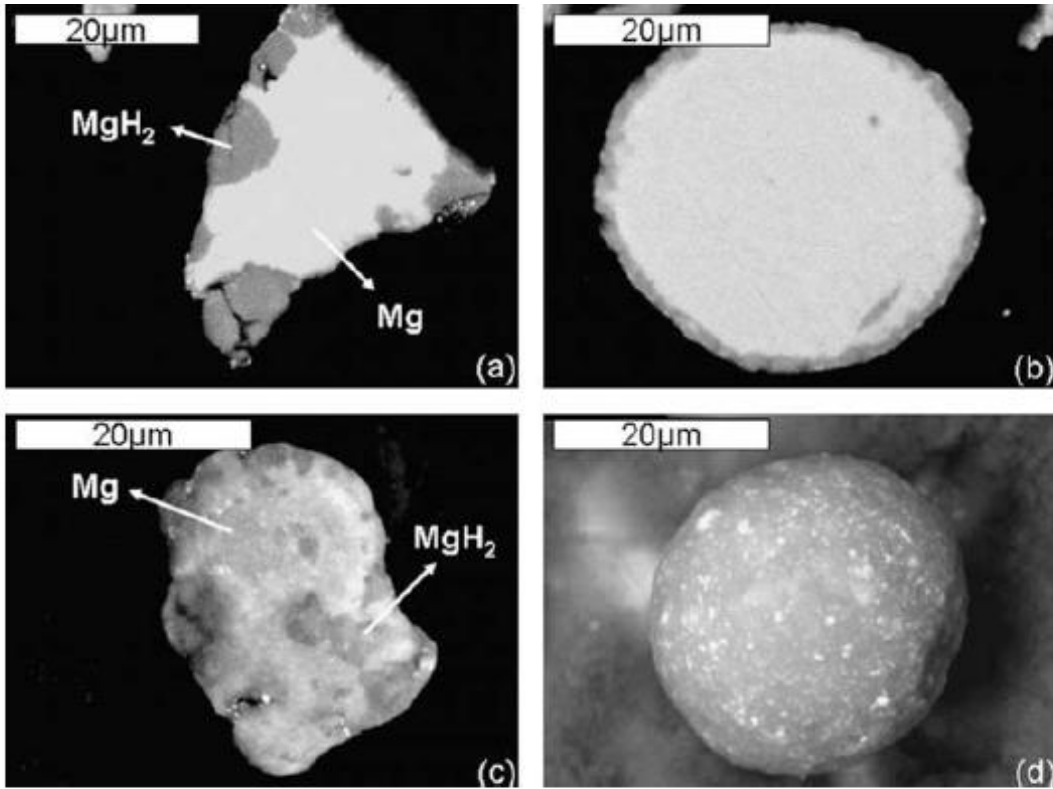


Figure 6-17. SEM (BSE mode) images showing the hydride distribution in the powder hydrogenated at (a and c) 210°C for 15 minutes, and (b and d) at 150°C for 300 minutes. (a) and (b) are cross-sectional images, while (c) and (d) are external surface images. magnesium hydride appears dark because of its lower density.

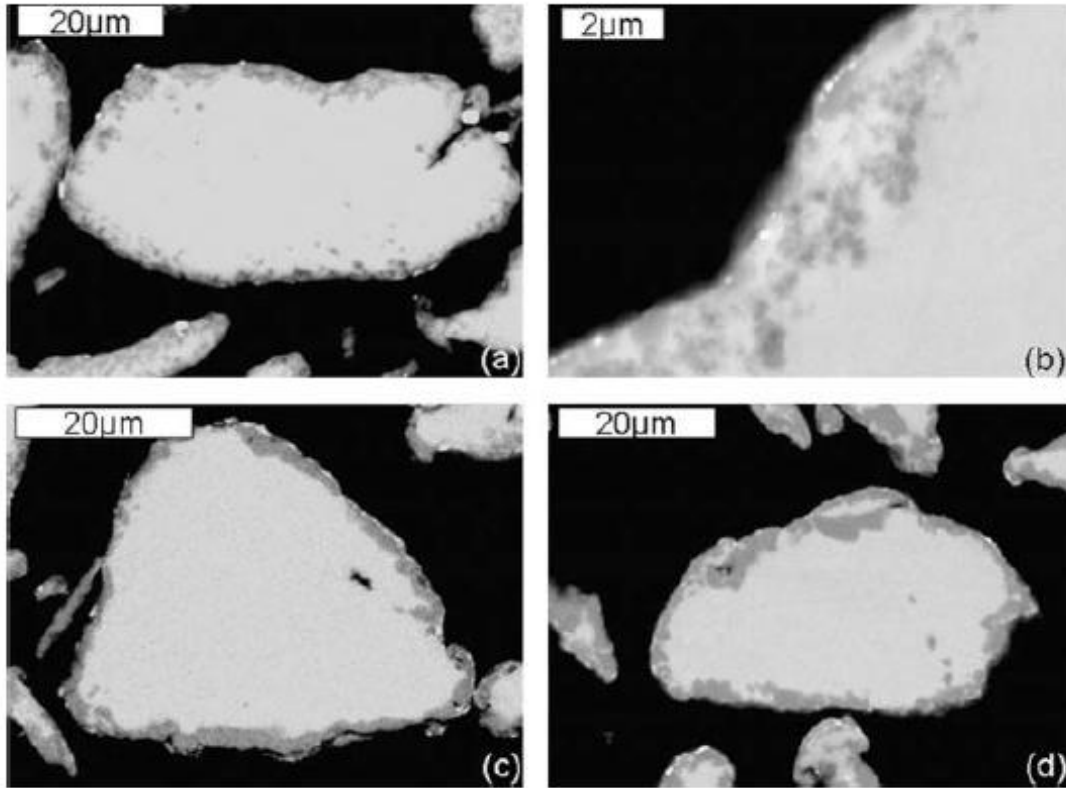


Figure 6-18. SEM (BSE mode) cross-sectional images showing (a) hydride distribution in powders hydrogenated at 150°C for 2 minutes, (b) higher magnification of (a) showing internal nucleation of MgH_2 , (c) hydride formation in powders hydrogenated by the two-step heating (150°C for 2 minutes and 210°C for 298 minutes), and (d) hydride formation in the powders hydrogenated at 150°C for 300 minutes.

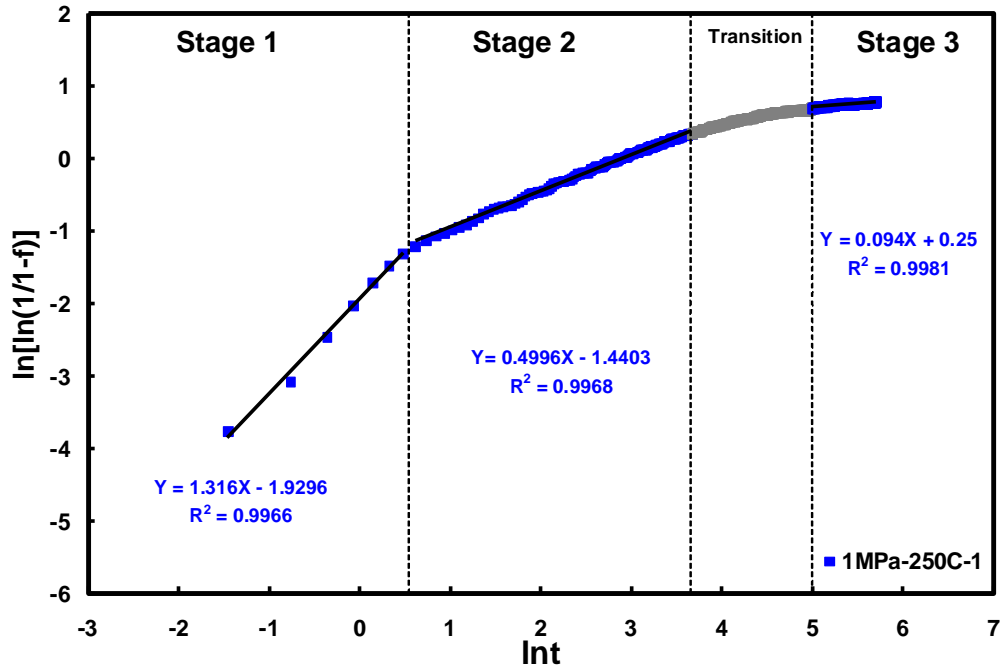


Figure 6-19. The JMA analysis of powder hydrogenated at 250°C (Sample 1).

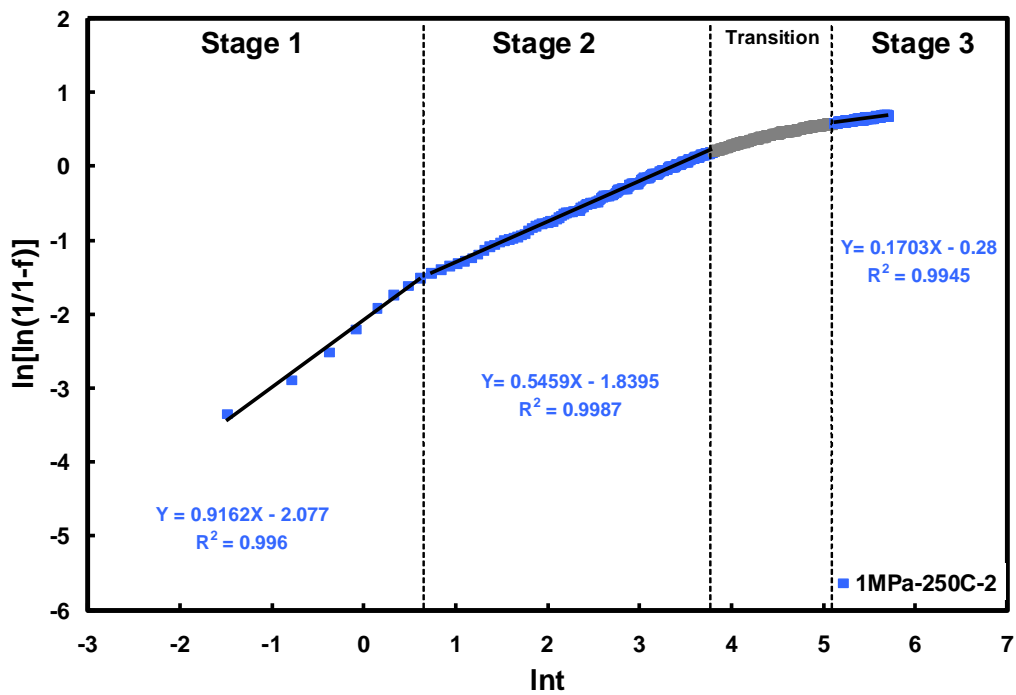


Figure 6-20. The JMA analysis of powder hydrogenated at 250°C (Sample 2).

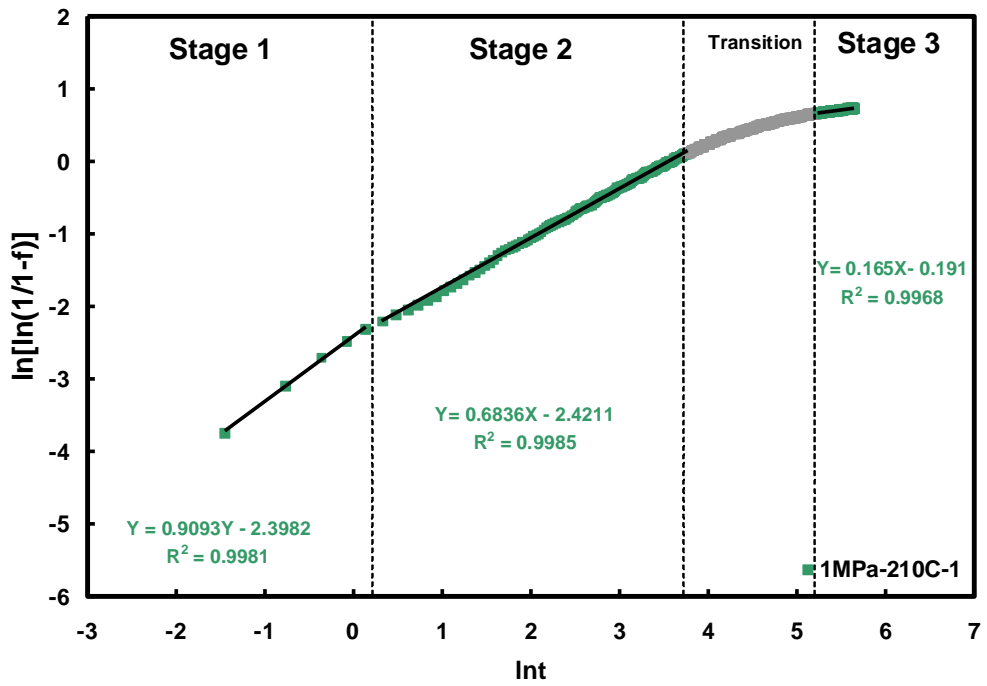


Figure 6-21. The JMA analysis of powder hydrogenated at 210°C (Sample 1).

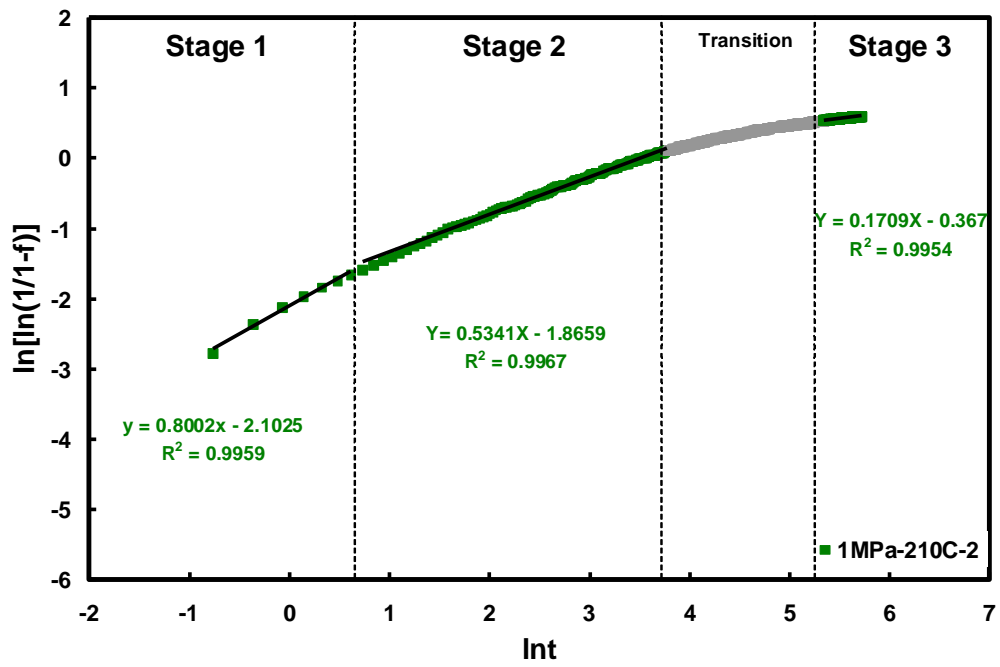


Figure 6-22. The JMA analysis of powder hydrogenated at 210°C (Sample 2).

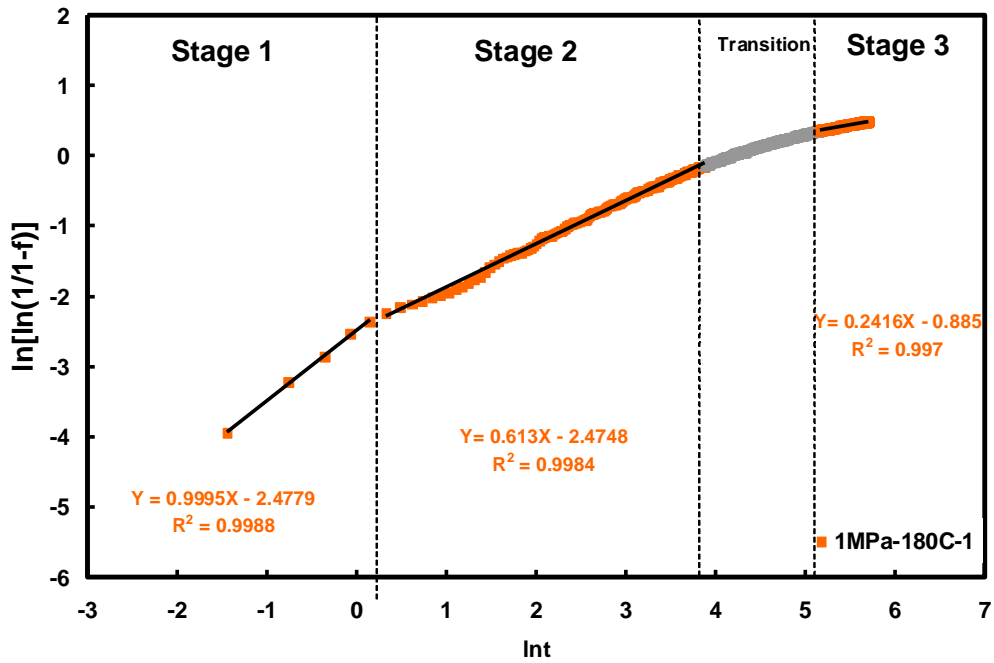


Figure 6-23. The JMA analysis of powder hydrogenated at 180°C (Sample 1).

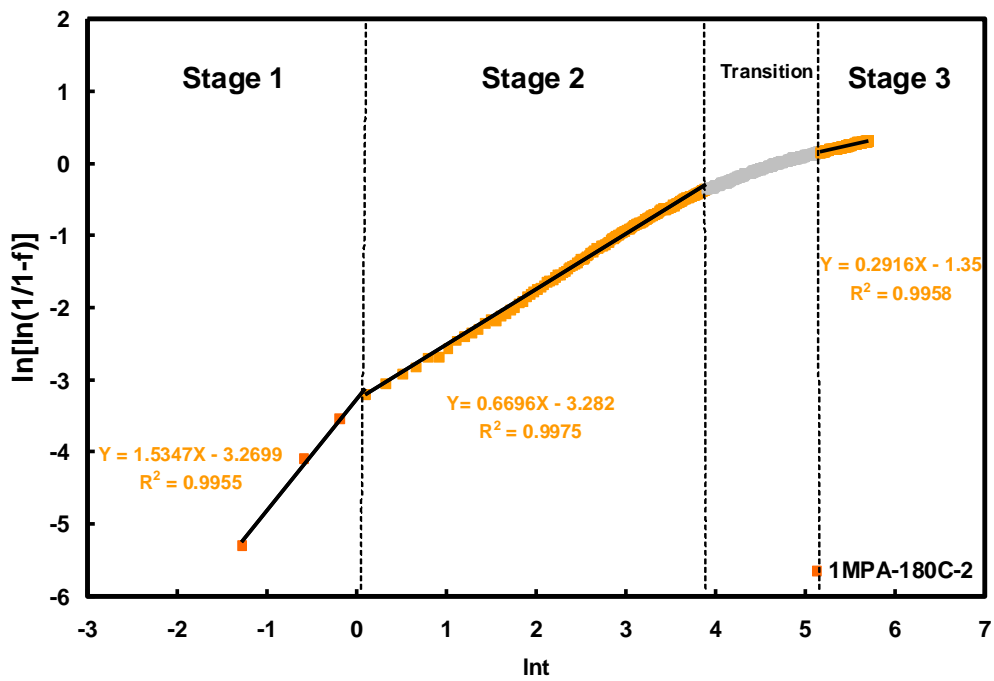


Figure 6-24. The JMA analysis of powder hydrogenated at 180°C (Sample 2).

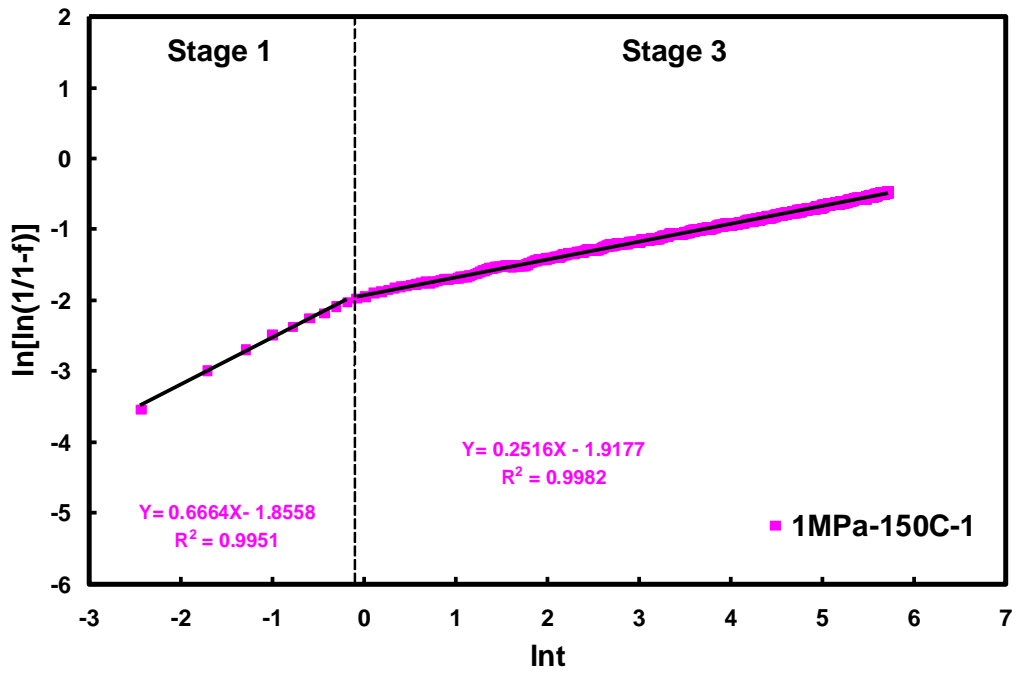


Figure 6-25. The JMA analysis of powder hydrogenated at 150°C (Sample 1).

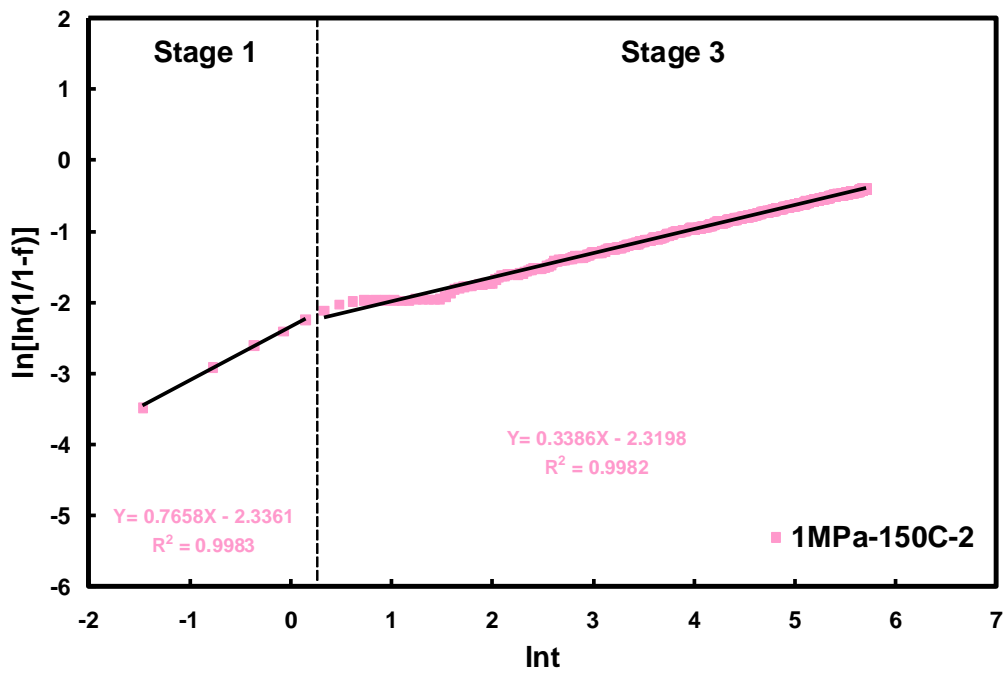


Figure 6-26. The JMA analysis of powder hydrogenated at 150°C (Sample 2).

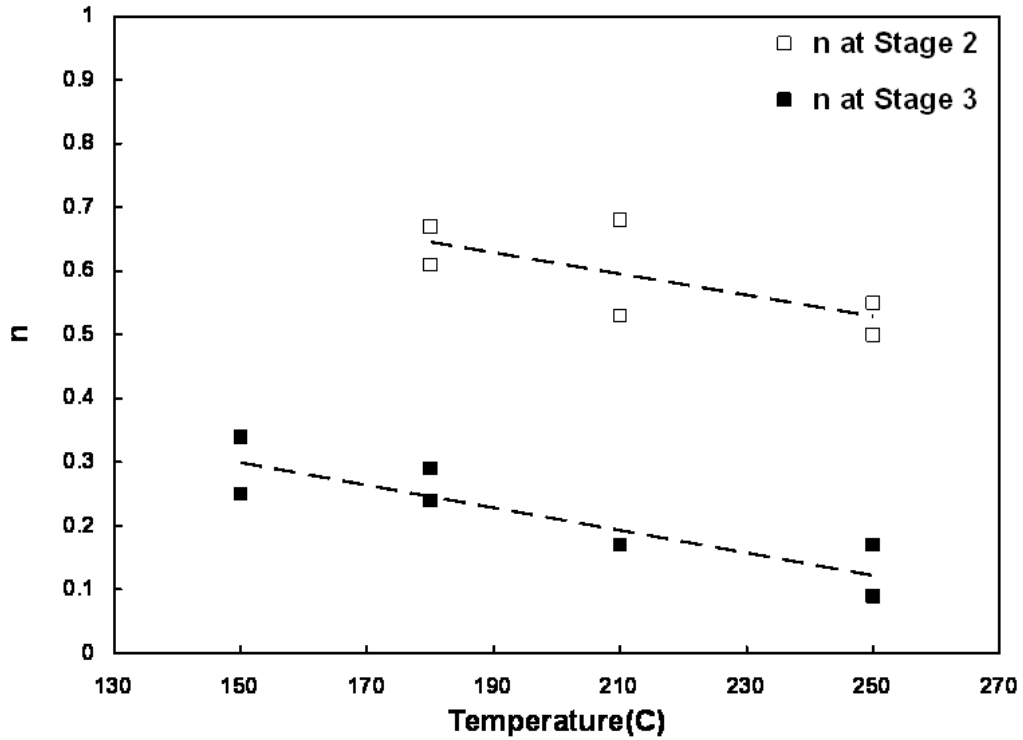


Figure 6-27. The relationship between n values and temperatures at Stage 2 and 3.

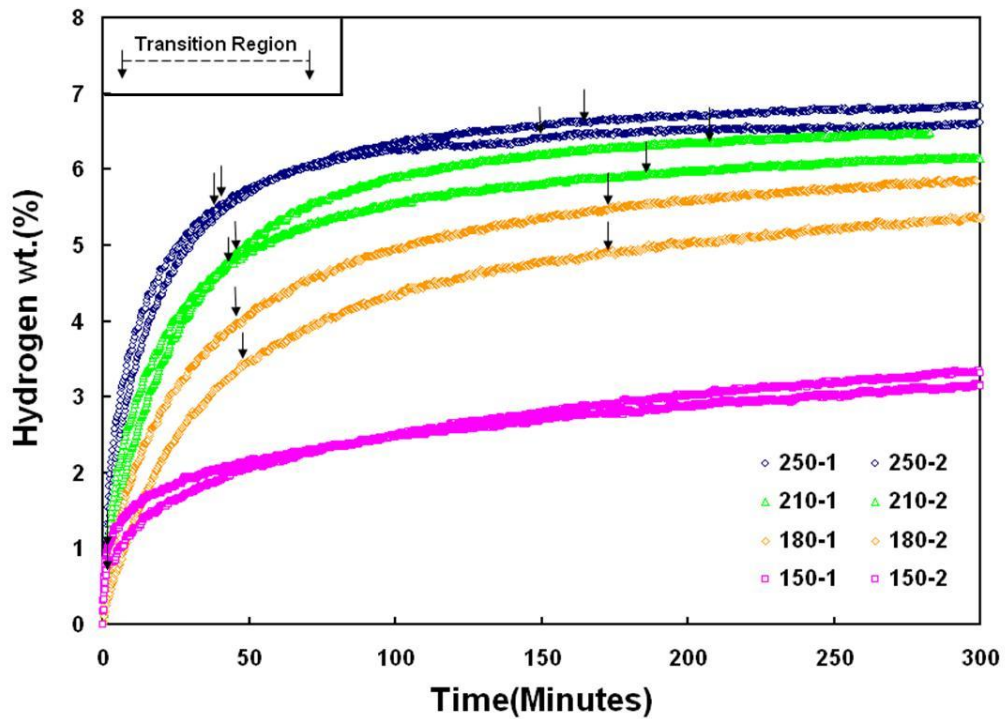


Figure 6-28. The location of transition region within the hydrogenation curves.

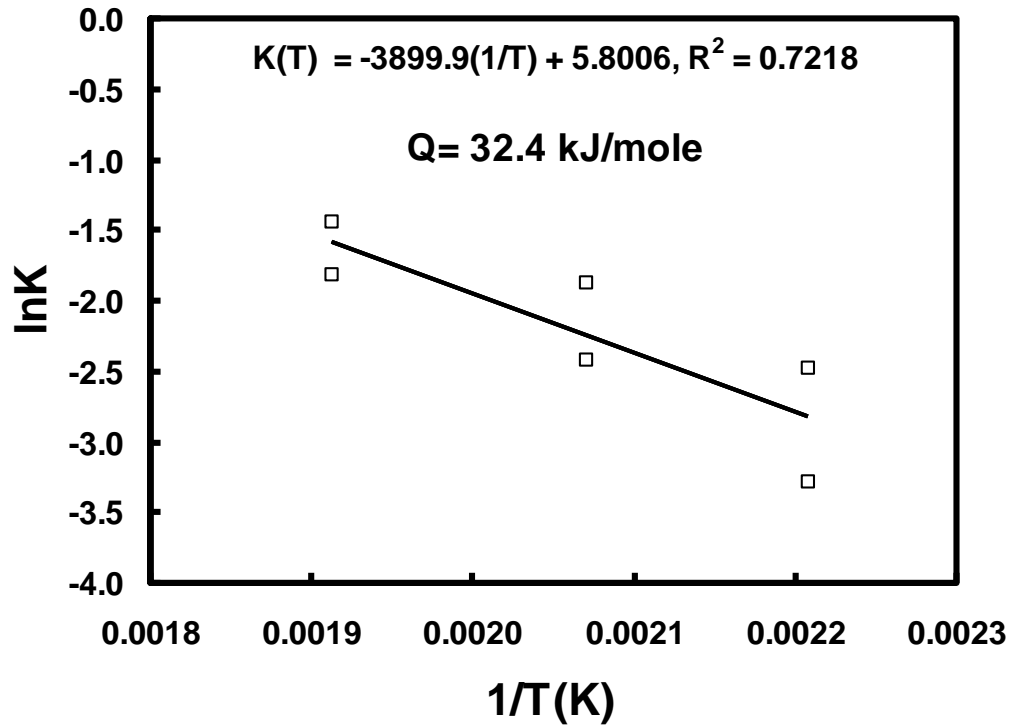


Figure 6-29. The activation energy calculated by Arrhenius plot.

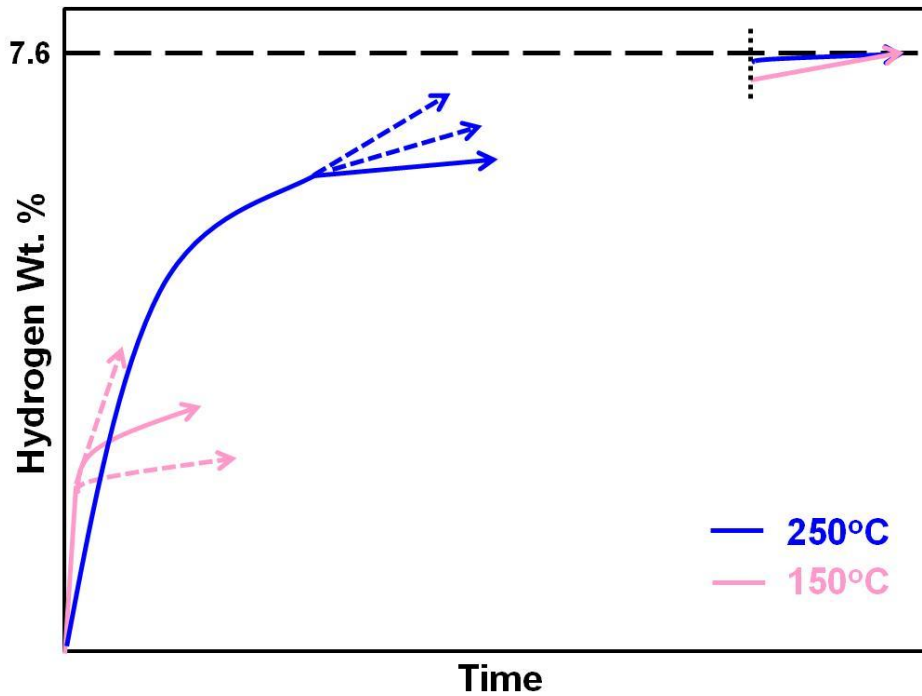


Figure 6-30. The schematic illustration of the comparison of slopes at the beginning of Stage 3 at 150°C and 250°C.

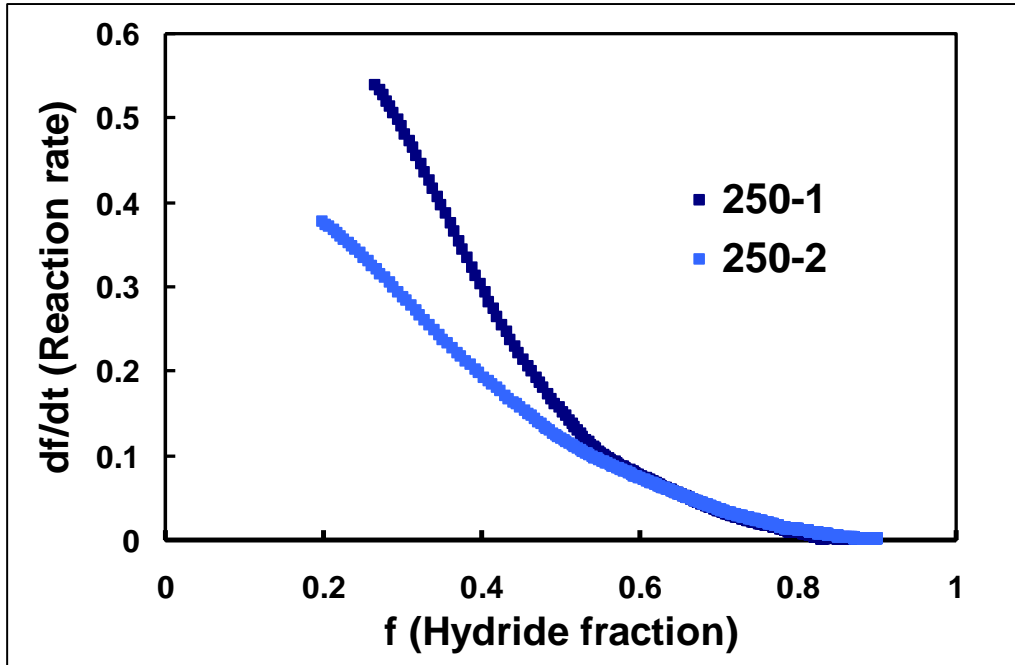


Figure 6-31. The relationship between hydride fraction and reaction rate at 250°C.

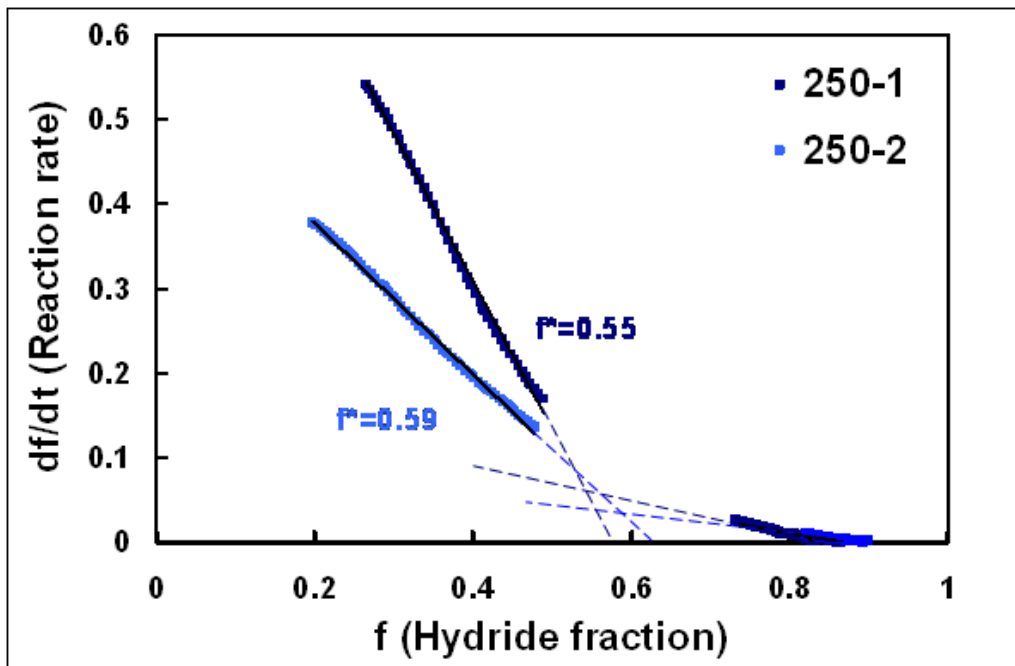


Figure 6-32. The f^* calculation at 250°C.

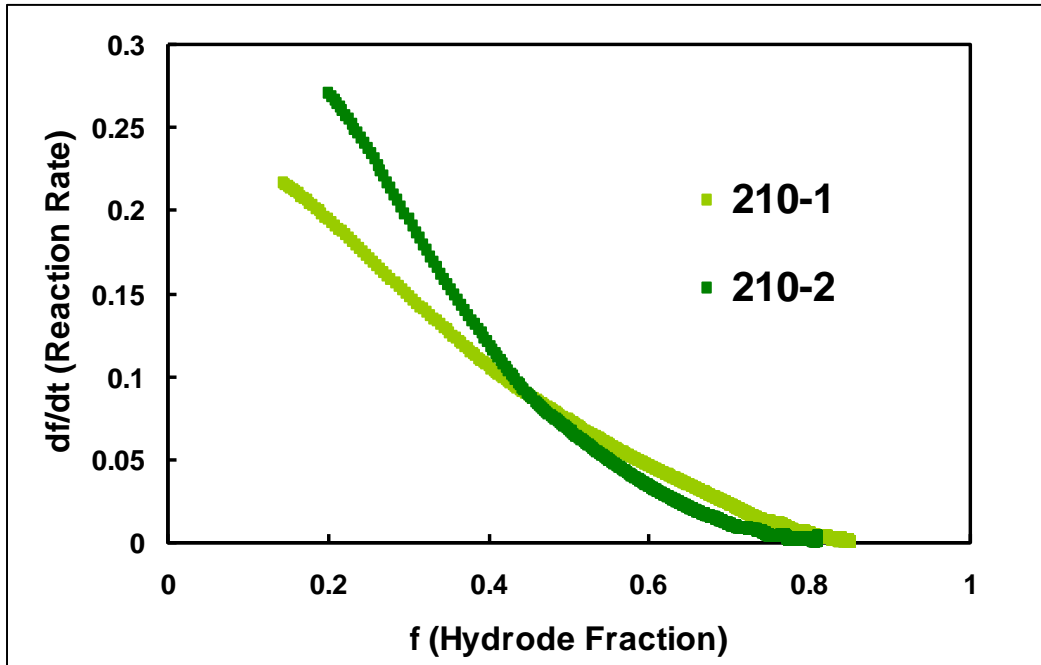


Figure 6-33. The relationship between hydride fraction and reaction rate at 210°C.

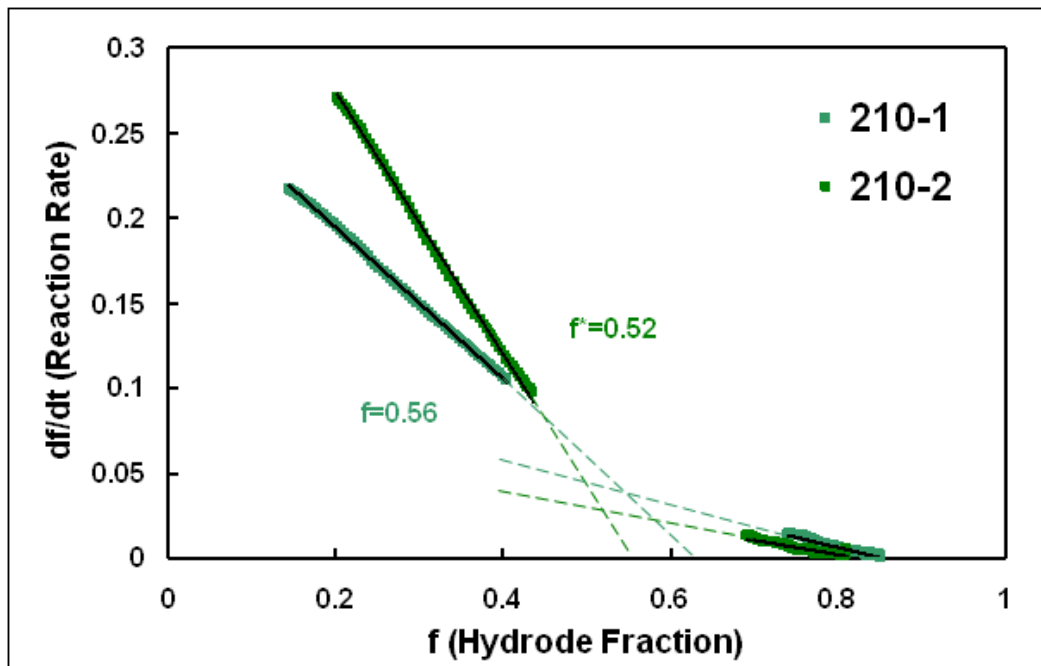


Figure 6-34. The f^* calculation at 210°C.

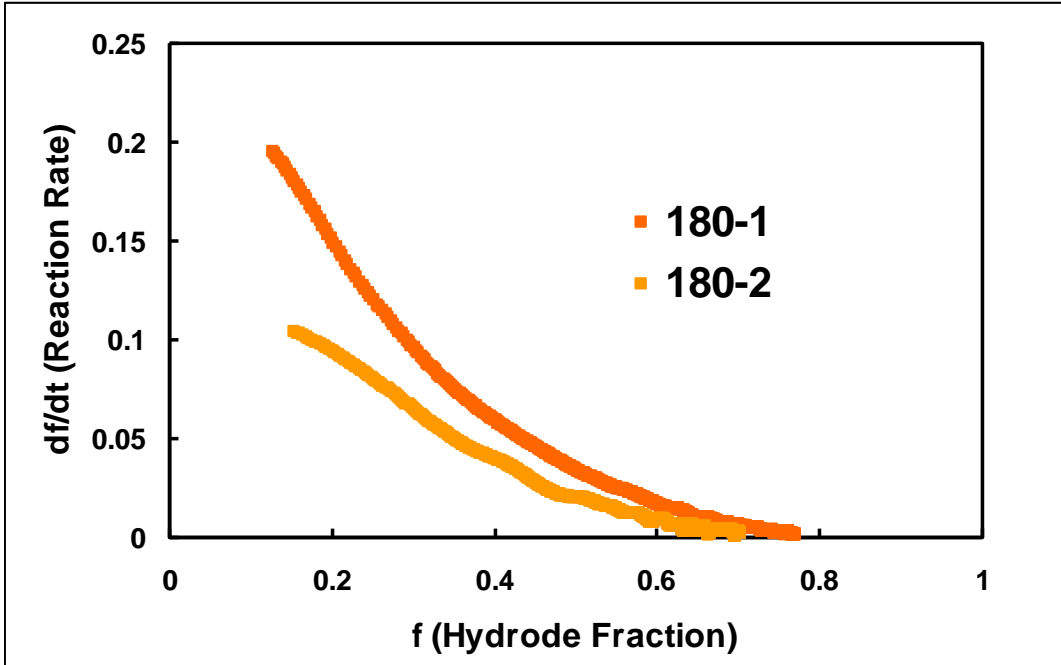


Figure 6-35. The relationship between hydride fraction and reaction rate at 180°C.

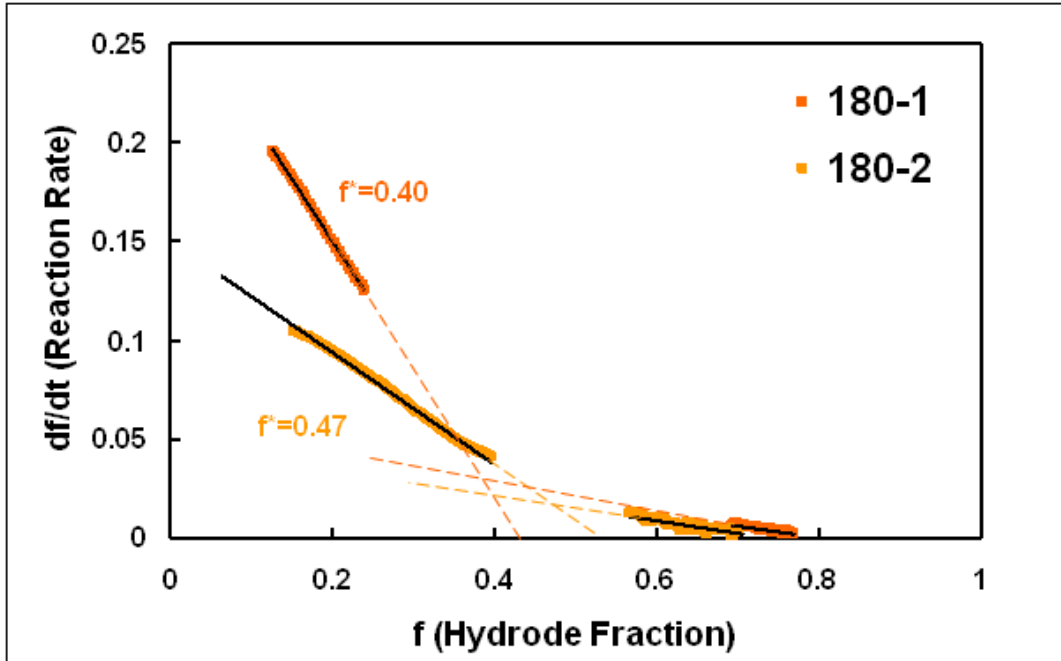


Figure 6-36. The f^* calculation at 180°C.

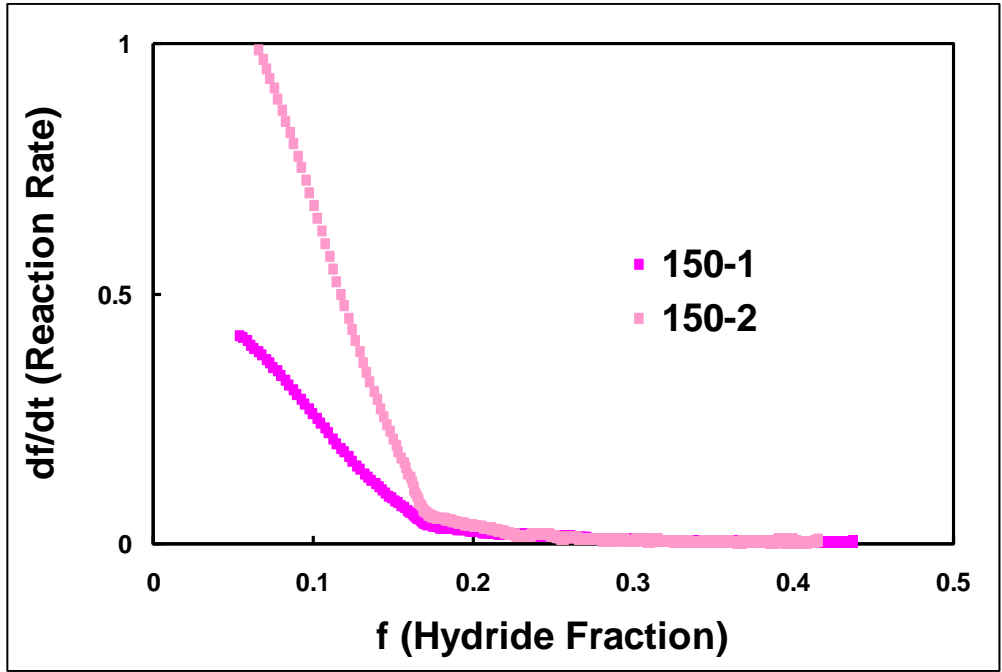


Figure 6-37. The relationship between hydride fraction and reaction rate at 150°C.

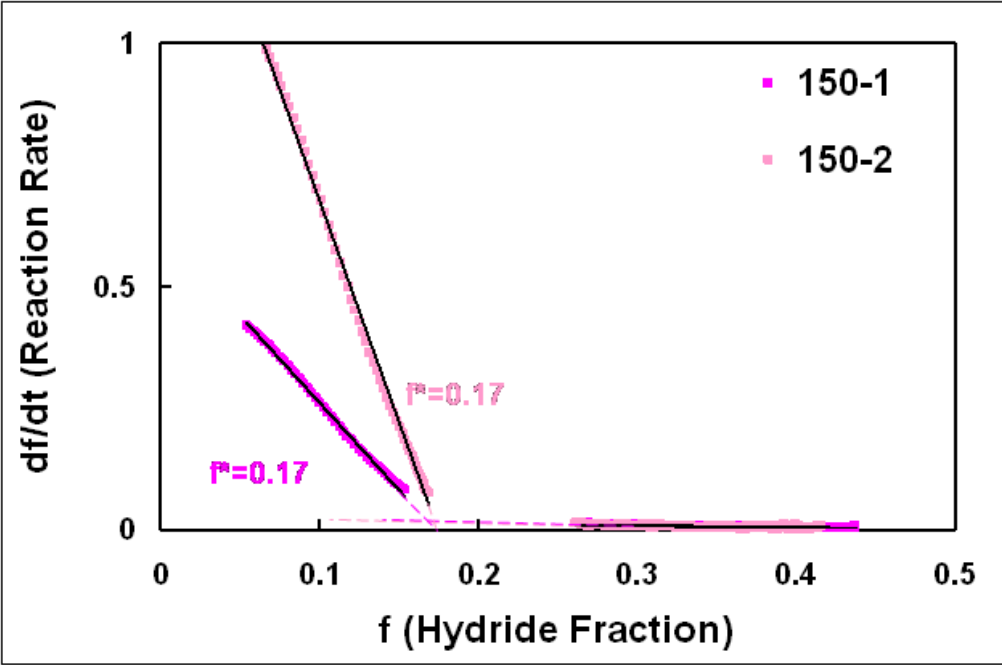


Figure 6-38. The f^* calculation at 150°C.

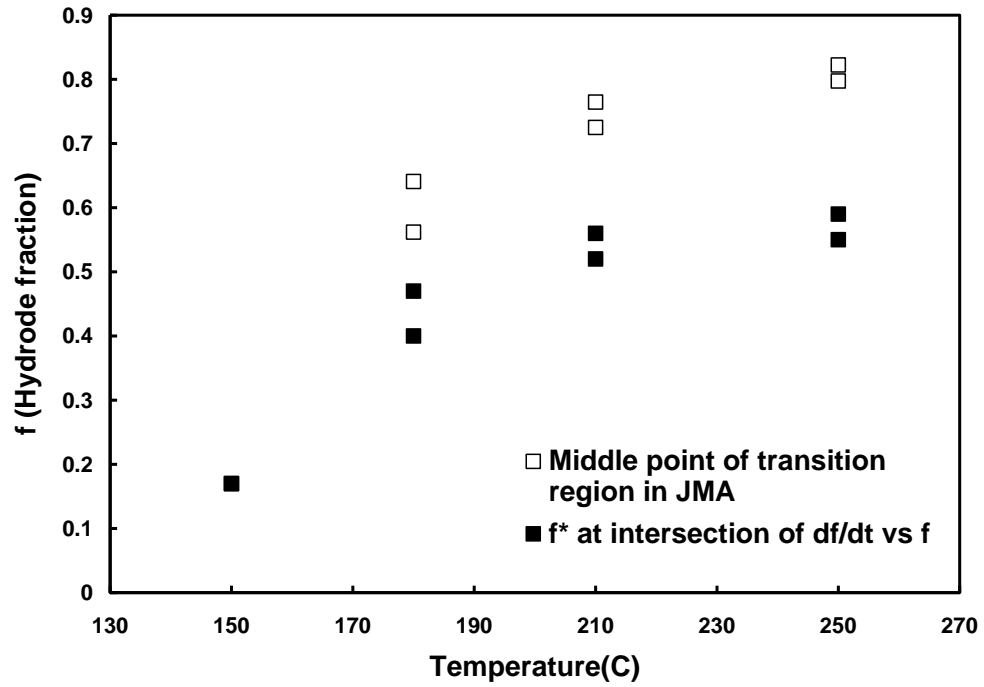


Figure 6-39. A comparison between hydride fraction at impingement analyzed by two different methods (JMA analysis and relationship between hydride fraction and reaction rate).

CHAPTER 7 EFFECT OF POWDER GEOMETRY AND SIZE ON THE HYDROGEN CAPACITY OF MAGNESIUM

7.1 Introductory Remarks

The understanding of hydrogenation kinetics is crucial for energy storage applications. According to the US Department of Energy statistics, the fueling process of a hydrogen vehicle tank by 2010 must not exceed 3 minutes [90]. One of the shortcomings of magnesium powder as a solid hydrogen storage material is its slow reaction rate and low hydrogen capacity. In Chapter 5-3, it was demonstrated that the particle size distribution can significantly affect the kinetics of hydrogen absorption in magnesium powders. In this chapter, the particle geometry as well as the average particle size impact on hydrogenation characteristics under an isothermal and isobaric hydrogenation condition will be investigated.

The effects of particle shape and size on the hydrogenation characteristics of magnesium powder have been studied by only a few researchers. A mathematical model using assumptions from the Core-Shell model for the shape effect on hydrogenation kinetics including sphere, cylinder, and plate of magnesium powders has led to the conclusion that the influences of shape variation and also size distribution of the magnesium particles are not drastic [90]. Mintz et al. reported that the influence is not noticeable for particle shape and size on the hydrogenation of magnesium powders by using single-particle analysis (SPA) [89]. However, interestingly, Jeon et al. have reported that the hydrogen capacity on magnesium flake powders is 4.57 H wt. % at 210°C, but no other shapes of magnesium powders with the same coating procedure were compared in their study [88].

Actually, in the literature no mathematical model and experimental data show what the role of the geometry is on the hydrogen capacity. In this study a vibrating machine called High Speed Orbital Ball Milling (HSOBM) was employed to produce flake shaped magnesium particles from a commercial powder with 300 μm average particle size as described in Chapter 3. The milling creates strong shear and compression stresses and causes the flattening of the powders. The magnesium particles in the as-received powder become thinner and thinner after passing through the gap between the rolling ball and the vessel wall. For Ni coating, a Theta Composer system was not used since the necessary amount of magnesium powder for this method is about 10 gram which is not practical to obtain from HSOBM which produces only 0.1 gram per milling. Both as-received and flake magnesium powders hence were coated by organometallic Ni nanoparticles for the hydrogenation tests. The effect of average particle size was evaluated by comparing the hydrogenation behaviors of as-received commercial 44 and 300 μm powders. A simple mathematical model was developed to explain the observed effects of particle shape and size observed in this study.

7.2 Effect of Particle Shape on Hydrogenation Behavior of Mg Powder

We have shown in Chapter 6 that the nucleation of magnesium hydride controls the hydrogen capacity. It is assumed that the nucleation rate depends on the driving force for nucleation of magnesium hydride, which is a function of temperature and pressure. In this section, an identical hydrogenation condition is employed to as-received 300 μm magnesium nearly sphere and flake powders. Shape change leads to the change of surface to volume ratio (S/V), and it is well-known that a spherical particle has the least surface area compared to any other shape of particles with the same

volume. Figure 7-1 presents the SEM (BSE mode) images for un-milled and milled magnesium particles. Figure 7-1(a) shows that the shape of the as-received 300 μ m magnesium particle is nearly spherical. Figure 7-1(b) displays the external surface image for the HSOBM milled particles, which exhibit a disk-like shape. Based on the finding in Chapter 6, the hydride thickness increases with increasing hydrogenation temperature; therefore, the hydrogenation tests were performed at 300°C to distinguish the differences in the capacity for the as-received magnesium and magnesium flake powders. Figure 7-2 shows the hydrogenation curves of the as-received 300 μ m powder and flake-shaped magnesium powders. The as-received 300 μ m magnesium powder sample reached saturation at about 100 minutes and ended up with a very low hydrogen capacity of only 0.2 H wt. % and then the test was kept recording for 10 hours. On the other hand, magnesium flakes exhibited a much higher capacity at 5.5 H wt. % after 33 hours. As can be seen in Figure 7-2, the initial hydrogenation kinetics of the magnesium flake powders were also much faster than that of the as-received 300 μ m magnesium powder. These findings demonstrate that the shape of the particles in a powder can play an important role in the hydrogenation behavior.

The difference in hydrogen capacity can be explained by examining the microstructure of the hydrogenated powders. Figures 7-3 (a, b) shows the SEM (BSE mode) cross sectional images of the hydrogenated as-received 300 μ m magnesium powder. It is observed that the as-received 300 μ m magnesium particle is covered by a thin nonuniform layer composed of magnesium hydride grains/colonies. In Figure 7-4, when we take a closer look at high magnification of the hydrogenated 300 μ m magnesium spherical particles, the thickest part of hydride layer is about 26 μ m thick

and the thinnest part is about 5 μ m thick. This variation in thickness can partially be attributed to the relative position of the cross-sectioned plane and the hydride colonies as well as any nonuniformity in the hydride nucleation process.

In Figure 7-5, the SEM (BSE mode) cross sectional image shows the hydride distribution in the hydrogenated magnesium flakes. The hydrogenated magnesium flake displays a much larger area fraction of magnesium hydride phase when compared to as-received 300 μ m magnesium particles. However, both of the powder samples demonstrated impingement behavior by a completely covered magnesium hydride layer on the powder surface. It is indicated that that hydrogenated powders had reached saturation in both cases. Figures 7-5 (a, c) shows that there is a metallic magnesium phase left at the center area of the powder and the surface is covered by magnesium hydride phase. From the individual growths of hydride colonies/grains it is predicted the nucleation and growth can best describe the hydrogenation behavior of this magnesium flake particle before the impingement occurs. From now, this hydride layer may not allow further hydrogen to diffuse through and can be treated by the core shell model. Figures 7-5 (b, d) reveal the magnesium flake powders which have nearly completely hydrogenated. The thicknesses of those magnesium flake particles are thinner than the flake particles in Figures 7-5 (a, c). The thinner the flake thickness the less metallic magnesium phase was found in the center area under the same hydrogenation condition. In Figure 7-5 (c), it can be noticed the welding effect from the HSOBM test, where two magnesium flakes stack on each other owing to the high speed rolling process.

The microstructures of the HSOBM milled and the as-received magnesium powders are expected to be identical because the hydrogenation temperature of 300C is anticipated to be sufficient for the re-crystallization of magnesium. Under the same hydrogenation condition, the driving force and thermal energy are equal and the nucleation density is expected to be similar in both sample powders. Moreover, the growth rates are anticipated to be the same since the growth mechanism is a thermally activated diffusion controlled process. Therefore, it is suggested that an identical hydrogenation condition leads to the same area density of nucleation of magnesium hydride on the powder surface as well as equal growth rate prior to the impingement of the hydride colonies/grains. A high surface to volume (S/V) ratio results in a relatively large number of nuclei in magnesium flake particles; therefore, the total volume of the hydride that forms per unit time is larger at the moment of impingement of hydrides. Notice here that the hydrogen capacity increases with increasing S/V ratio. One can consider that if a cube and a sphere have the same surface area, at the same hydrogenation condition, the hydrogenation kinetics is identical in both shapes but the hydrogen capacity will be lower in the spherical particle owing to its lower S/V ratio. Figure 7-6 shows the schematic illustration of the effect of shape on hydrogenation behavior and hydride distribution. Assuming that the hydride grains/colonies have the same size, the model presented in this figure clearly shows the reason why the flake particles have higher hydrogen capacity than spherical particles do. When energy saving is considered, low hydrogenation temperature is favored for the hydrogenation process and thin flake powders are necessary to obtain high hydrogen capacity. Based on the hydride thickness measurement in Chapter 6 at different hydrogenation

temperatures, the lowest temperature, 150°C, leads to an approximate hydride thickness, 2µm. It is suggested that if the flake thickness is thinner than 4µm the hydrogen capacity at 150°C is expected to reach the theoretical value of 7.6 H wt. %.

7.3 Effect of Particle Size on Hydrogen Capacity

Figure 7-7 presents, while the hydrogen capacity after 5 hours of hydrogenation for the as-received 300µm magnesium powder is 0.2 H wt. %, the as-received 44µm magnesium powder displays a much higher capacity of 6.5 H wt. % capacity. Schultz et al. have reported a hydrogen absorption capacity 6.5 H wt. % for a 20µm magnesium powder hydrogenated for 25 minutes [34]. Similar to the particle shape change effect, decreasing the particle size increases the surface to volume ratio, hence increasing the total number of hydride nuclei per unit weight of the material. Consequently, at a given hydride linear growth rate, the amount of hydride formed per unit weight at a given time will be increased resulting in faster observed kinetics. Also, as was demonstrated schematically in Chapter 5, the impingement of the hydride particles is achieved at a higher volume fraction of hydride in the powder with a smaller particle size. Microstructural analysis confirms the hypothesis presented in the schematic shown in Figure 5-10.

Figures 7-8 (a, c) show the SEM (BSE mode) images of magnesium hydride distribution at the cross section of 44µm magnesium particles hydrogenated at 300°C under 1MPa hydrogen pressure for 10 hours. It can be seen that almost all the magnesium phase has transformed to magnesium hydride except a small volume of magnesium phase left at the center of the particle. Lots of cracks are also found inside the hydrogenated particles. The hydride distribution is compared with the 300µm hydrogenated particles in Figures 7-8 (b, d). Again a continuous hydride layer indicative

of complete impingement of the hydride colonies/grains is observed, but a relatively large area of un-reacted metallic magnesium phase was observed in the center of the 300 μm hydrogenated particles. The comparison of microstructural analysis suggests that the hydride fraction in 44 μm is much larger than that of 300 μm hydrogenated particles. This phenomenon also manifested as a variation in the volume fraction of the hydride found in the single batch of the 44 μm powder sample as shown in Figure 5-10.

7.4 Mathematical Modeling

In this section we attempt to predict the hydrogen capacity at the point of impingement, i.e. at the transition between Stages 2 and 3 as defined in Chapter 6, for different particle sizes and geometries. It is assumed that at a given temperature, T , and pressure, P , the hydride thickness at impingement is independent of size and geometry. This assumption is justified because the nuclei areal density and the linear hydride growth rate are expected to vary only with temperature and pressure of the hydrogenation.

The shapes of the as-received magnesium powder, which are approximated as prolate spheroid and the magnesium flake as oblate spheroid (disk), are shown schematically in Figure 7-9. In Chapter 4, the aspect ratio (a/b) was reported to be 0.47 and 0.67 for the as-received 44 μm and 300 μm powders, respectively.

Figure 7-9 (a) exhibits the schematic cross sectional image of a prolate spheroid with the labels of the equatorial radius a and polar radius b and 7-9 (b) the cross section of an oblate spheroid with the labels of polar radius a and equatorial radius b axis, respectively. The cross section looks the same but the volume calculations for those two spheroid particles are different. For the prolate, the volume is $4\pi(a^2b)/3$ and for the

disk, the volume is $4\pi(ab^2)/3$. The volume fraction of the hydride at the point of impingement at a given T and P can be calculated by knowing the average thickness of the hydride, h , for the hydrogenation condition. For example for a prolate the hydride fraction, f , is given as:

$$f = [4\pi(a^2b)/3 - 4\pi(a-h)^2(b-h)/3] / [4\pi(a^2b)/3] \quad (7-1)$$

The volume fraction then can be changed to the wt. % of H absorbed by assuming a density of 1.74 and 1.45 (g/cm³) for magnesium hydride and magnesium, respectively, according to the following relationships:

$$\text{Wt. \% of H} = \{1.45f/[1.74(1-f)+1.45f]\} \times 7.6 \quad (7-2)$$

From Figure 7-4, the average hydride thickness is about 17.3 μm for as-received 300 μm magnesium powders hydrogenated at 300°C under 1MPa for 15 hours. The middle thinner part of the hydride grains/colonies has not been taken into account because the cutting plane is not right on the center of the hydride grain/colony. Only the portion of clearly individual nodules was utilized for the thickness measurement. In Figure 7-5(c), the thickness hydride layer is easier to be distinguished in this thicker flake particle than the thinner one in Figure 7-6(d). A measurement of hydride thickness was done at every 30 μm length on those hydrogenated magnesium flakes and an average hydride thickness, 13.3 μm , was obtained. Unlike the way for measuring the hydride thickness in magnesium flakes, for near spherical particles, as- received 44 and 300 μm , the hydride thickness is measured at every 20 degree from the center of the particle, 18 data will be obtained for each particle. Average thicknesses are 12.2 μm and 9.9 μm for as-received hydrogenated 44 and 300 μm magnesium particles, respectively. As the three hydride thicknesses are compared, an average 11.8 μm and standard

deviation 1.73 is calculated from those three hydride thicknesses. It is noticed that the three hydride thickness values are very close and of the same order. It can be concluded that the hydride thickness is similar no matter the size and shape of the particle, and at the same temperature there is a corresponding hydride thickness. The hydride thickness values at 300°C are not comparable with those of 180, 210, 250°C since the Ni coating process is different and hence the nucleation behavior would be dissimilar, which affects the hydrogen capacity dramatically.

Figure 7-10 shows the calculated absorbed hydrogen as a function of the particle aspect ratio (a/b) for $h = 11.8\mu\text{m}$. Here both 44 μm and 300 μm size are considered and the calculation is done for a spherical prolate. The calculation is done as disc shape for magnesium flakes. As the aspect ratio deviates from the spherical shape ($a = b$) the hydrogen capacity for a given hydrogenation condition, i.e. hydride thickness, increases significantly. Similarly, decreasing the volume of the particle, i.e. its size, results in an enhancement of the hydrogen absorbed at the point of impingement. The hydrogen capacity from the experimental data for those three powder samples are compared in Figure 7-10 with the mathematical model. The modeling predicts that 4.32 H wt. % will be obtained for magnesium flake powders at the aspect ratio = 0.05, which is very close to the experimental data, 5.5 H wt. %. It is also expected about 7.1 wt. % hydrogen will be absorbed at $a/b = 0.47$ for the 44 μm prolate powder sample. The predicted value is also close to the experimental capacity 6.5 H wt. %. However, the model does not fit well for the 300 μm prolate powder sample. The divergence may be caused by the deviation from the calculation for the aspect ratio for as-received 300 μm particles or it may come from the error of the measurement during the real time hydrogen absorption.

7.5 Summary and Conclusions

The aim of this chapter is to study the influence of the magnesium powder particle's shape and size on the kinetics of isothermal hydrogenation under a constant hydrogen pressure. It is concluded that the shape does affect the kinetics and hydrogen capacity of magnesium powder particles. The flake-shaped particles show impressively 25 times more hydrogen capacity than the as-received sphere particles. The microstructural analysis reveals that the thinner the flakes the higher hydride fraction for the magnesium flakes. After hydrogenation, most of the flakes were completely hydrogenated at SEM (BSE mode). Some of the thick flake particles still had metal phase magnesium left in the center of the particles since the thickness of the flake is too thick to be completely hydrogenated by a given hydride thickness $\sim 11.8\mu\text{m}$ at a given temperature 300°C and pressure 1MPa . For the effect of size, the hydrogenation behavior of $44\mu\text{m}$ magnesium powders was also compared with the $300\mu\text{m}$ magnesium particles. The result corresponded to the literature research that shows finer magnesium particles display faster kinetics and higher hydrogen capacity. We can say that the surface to volume ratio plays an important role in the hydrogen capacity. At a constant linear growth rate of hydride, the higher the surface to volume ratio the higher the hydrogen capacity. If the total volume of magnesium powders is fixed, larger surface area will result in faster hydrogenation kinetics. It is also concluded that a hydrogenation temperature corresponds to a specific hydride thickness no matter what the size and shape of the magnesium particles are.

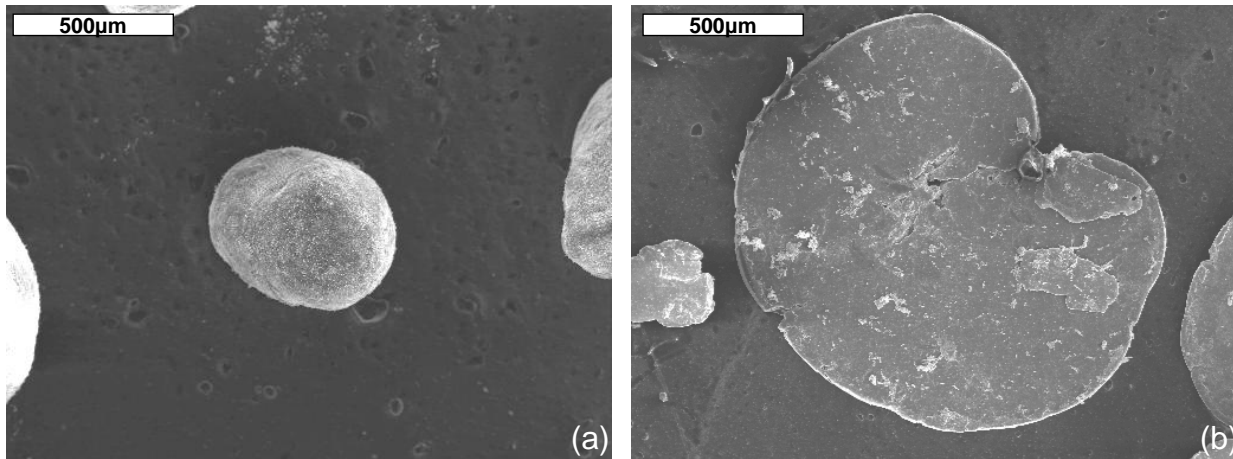


Figure 7-1. External surface images at higher magnification of (a) as-received 300µm magnesium spherical and (b) magnesium flake particles.

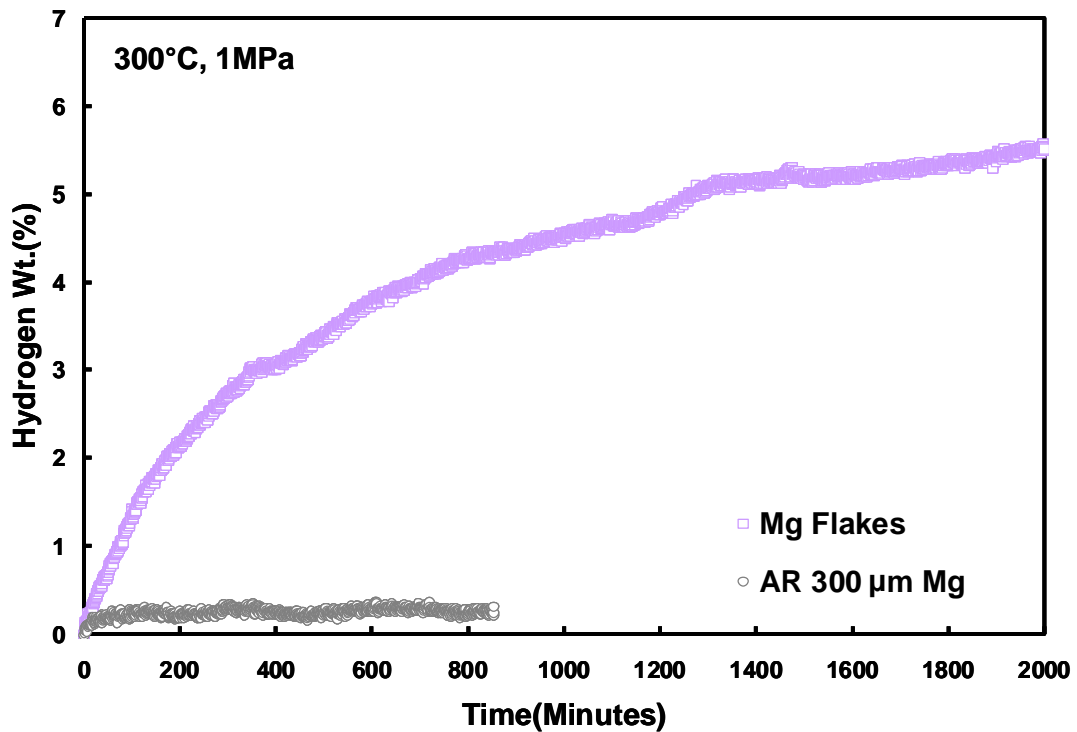


Figure 7-2. The hydrogenation curves of different shapes of particles. The hydrogen capacity of magnesium flakes shows more than 5.5 H wt. % which is much higher than the as-received 300µm magnesium particles with 0.2 H wt. % capacity.

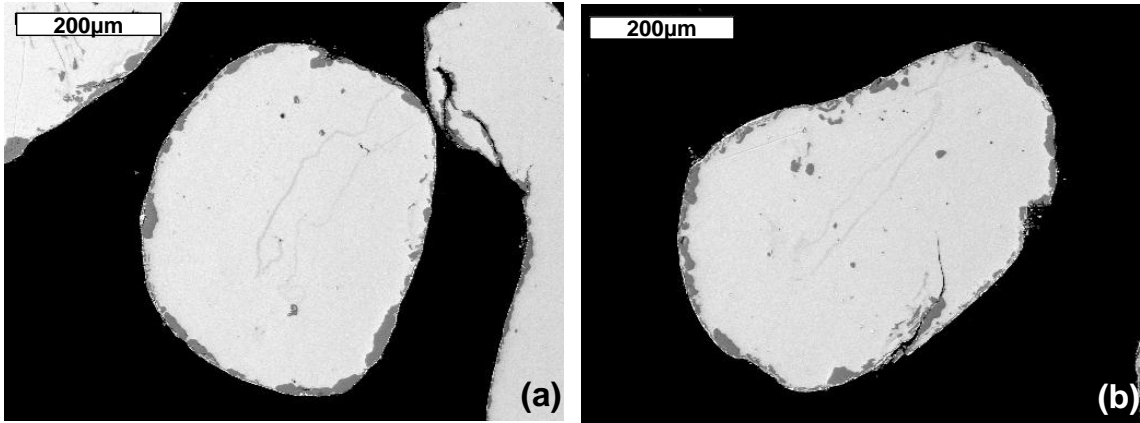


Figure 7-3. The SEM (BSE mode) images of hydrogenated as-received 300µm magnesium particles after hydrogenation at 300°C 1MPa for 15 hours.

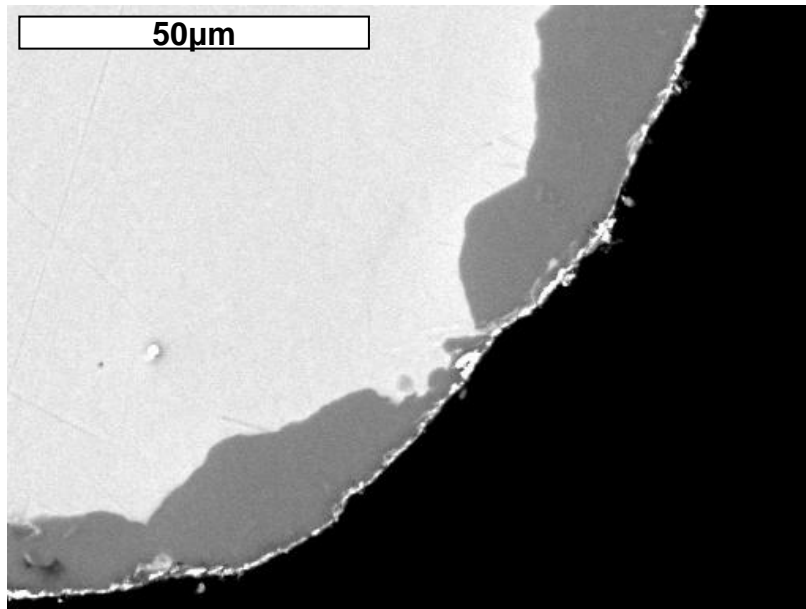


Figure 7-4. The SEM (BSE mode) images for the hydride layer measurement at higher magnification of hydrogenated as-received 300µm magnesium particles after hydrogenation at 300°C 1MPa for 15 hours.

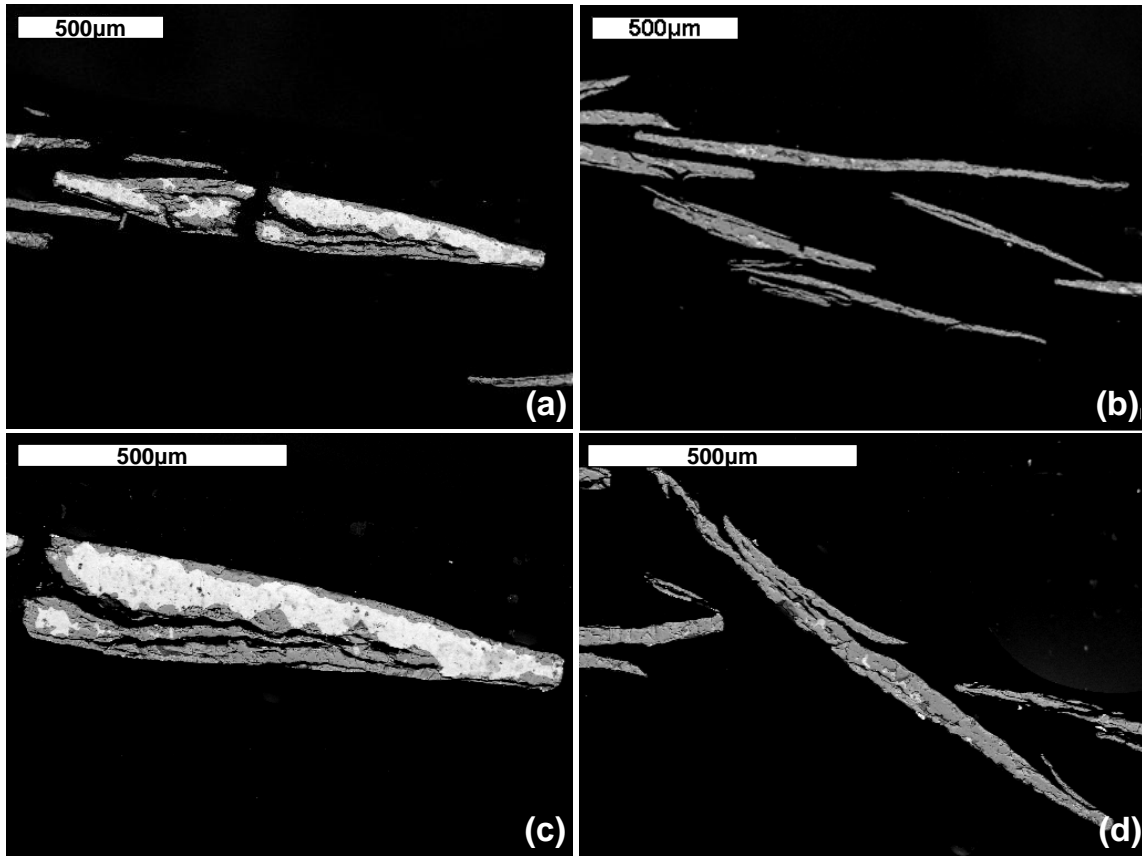


Figure 7-5. The SEM (BSE mode) images of hydrogenated magnesium flake particles after hydrogenation at 300°C 1MPa for 36 hours. (a) Thick flake particles (b) thin flake particles.

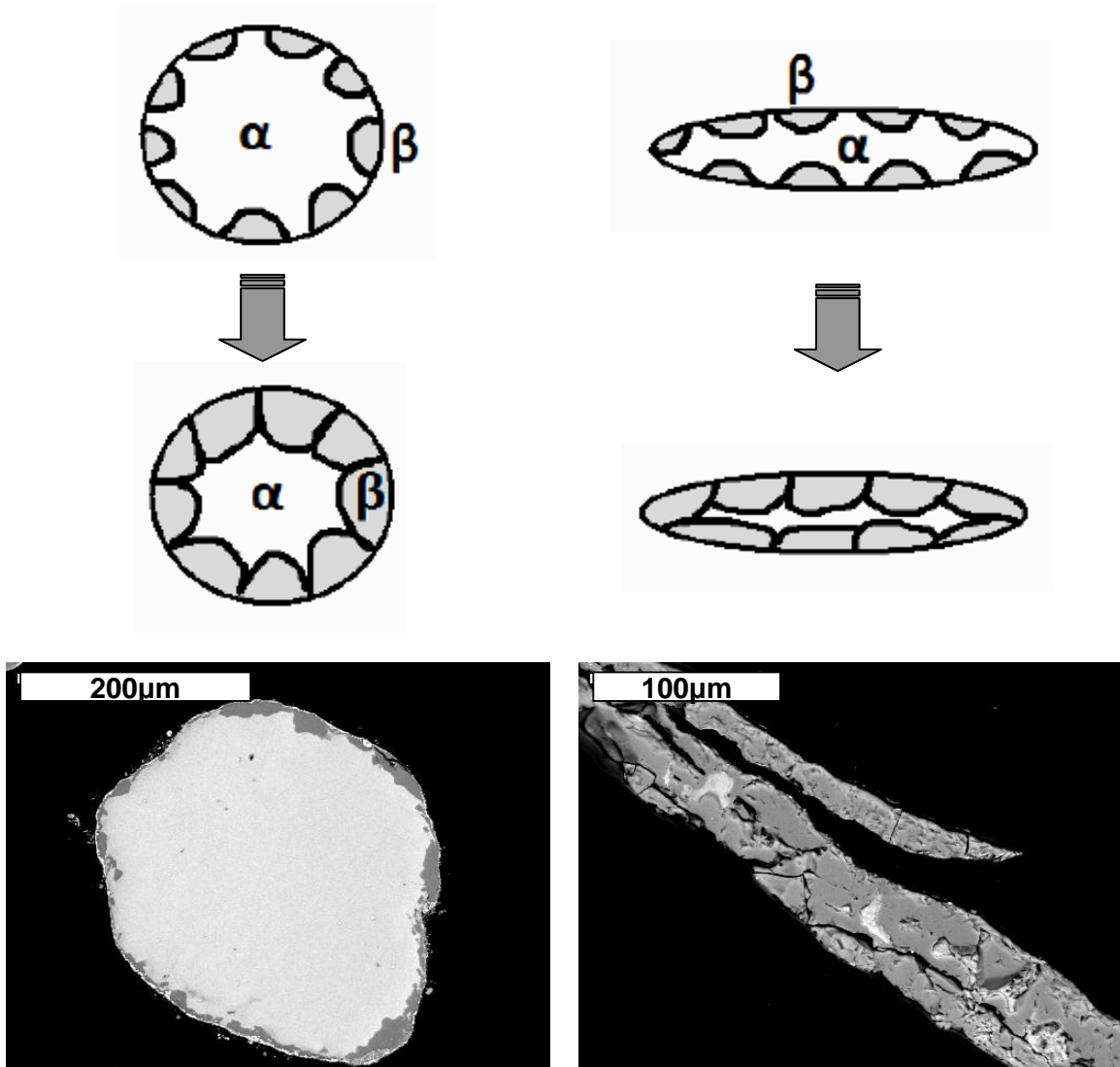


Figure 7-6. The schematics illustration of effect of shape change from sphere to flake on hydrogen capacity of magnesium particles with SEM (BSE mode) images for the comparison.

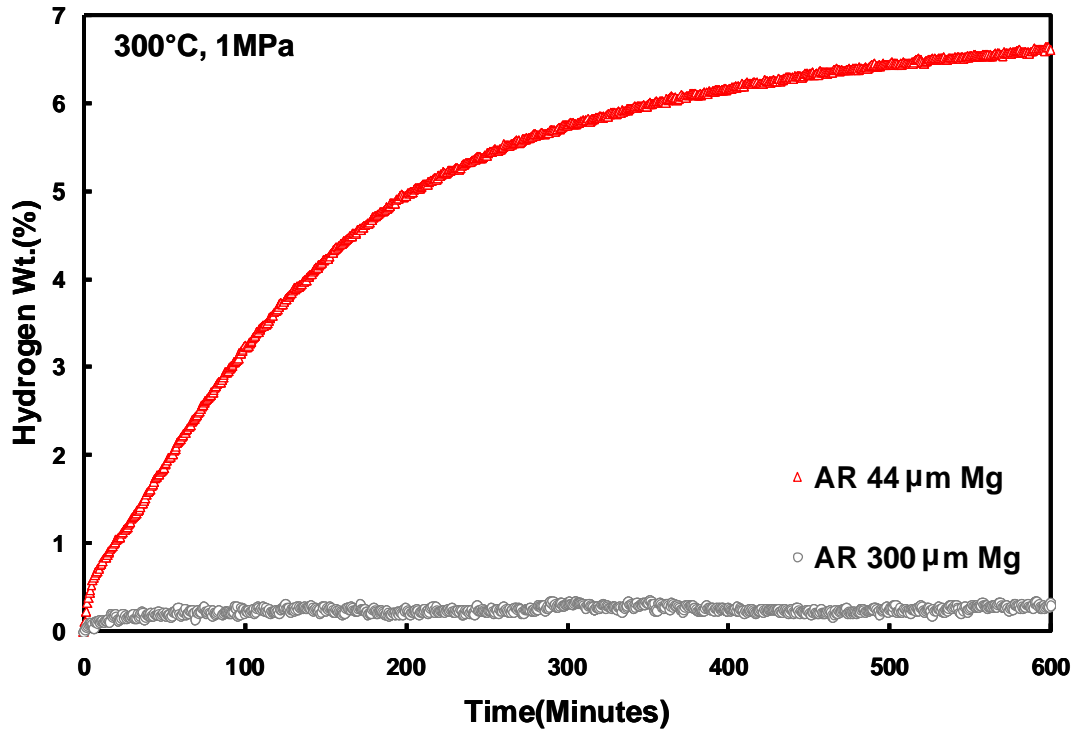


Figure 7-7. The hydrogenation curves of different sizes of particles. The hydrogen capacity of 44 μm magnesium particles shows more than 6.5 H wt. % which is much higher than the 300 μm magnesium spherical particles with 0.2 H wt. % capacity.

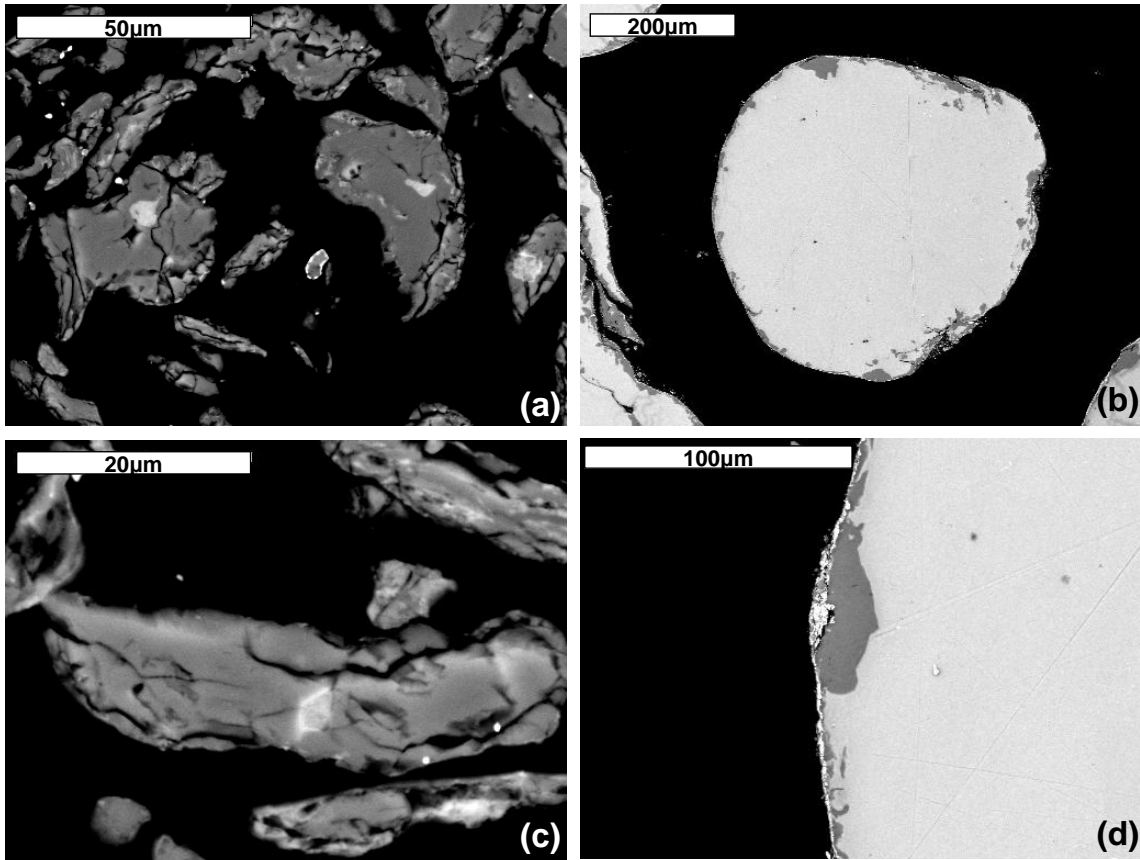


Figure 7-8. (a, c) The SEM (BSE mode) images of hydrogenated 44µm magnesium particles after hydrogenation at 300°C 1MPa for 10 hours compared with the images of (b, d) which show the cross section of hydrogenated as-received 300µm magnesium particles.

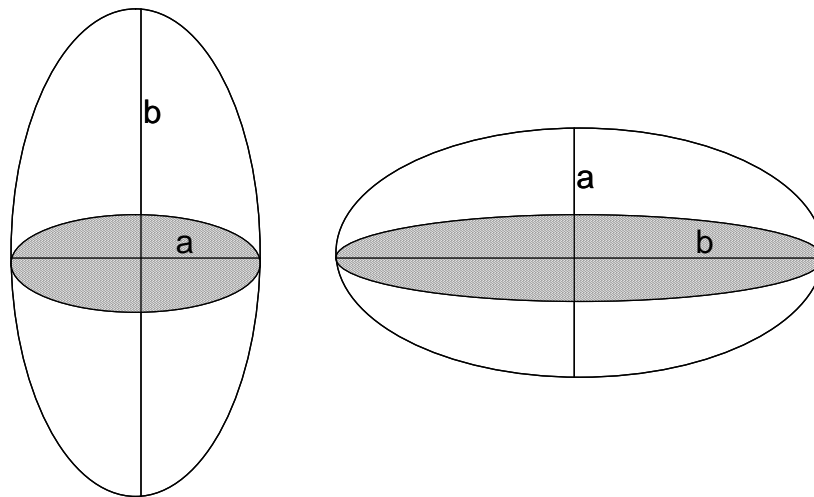


Figure 7-9. (a) Prolate spheroid for AR 44 and 300µm (b) Disk spheroid for flake.

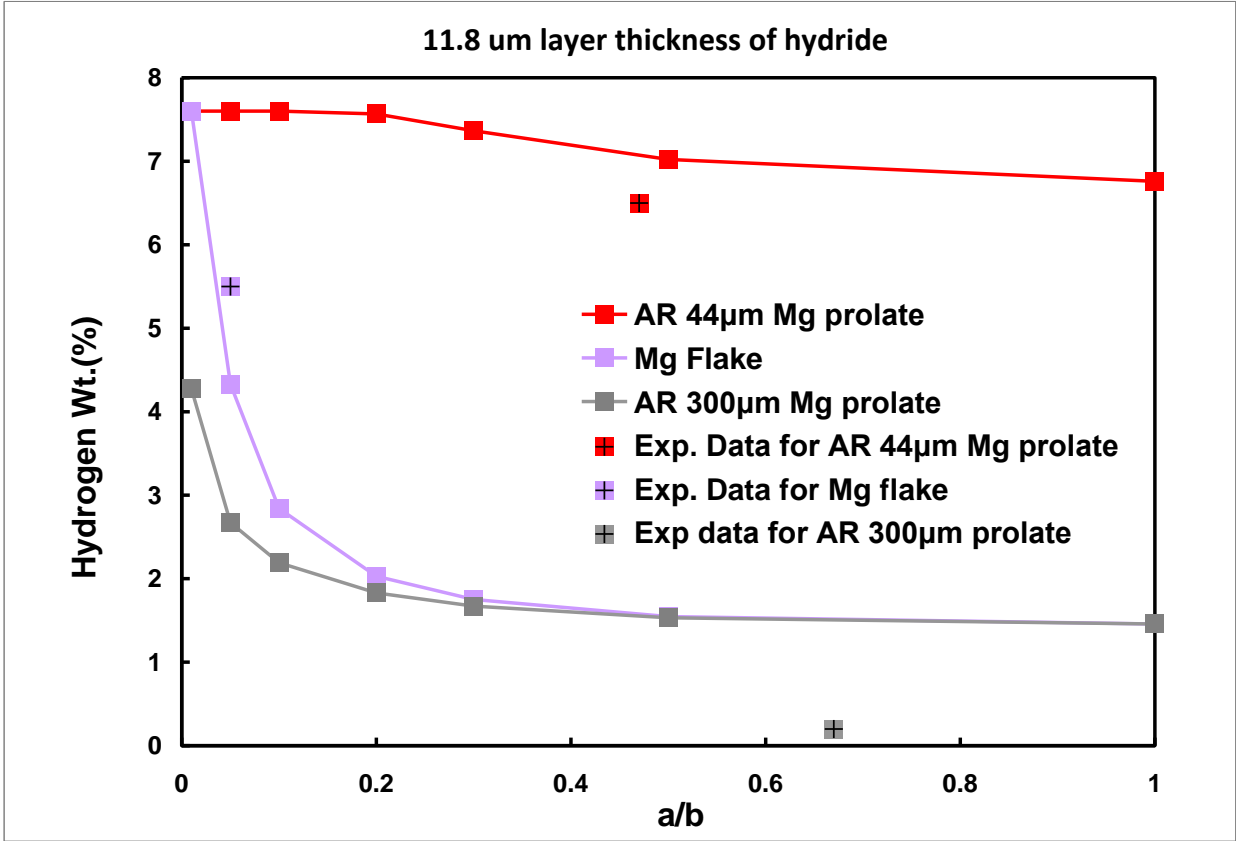


Figure 7-10. The experimental hydrogen capacity compared with theoretical calculation by using 11.8µm thick hydride layer at varying a/b aspect ratio.

CHAPTER 8 DEHYDROGENATION MECHANISM OF MAGNESIUM HYDRIDE

8.1 Introductory Remarks

The industrial application of magnesium hydride as a hydrogen storage medium has been impeded by its high thermodynamic stability, which renders a high hydrogen release temperature and its dawdling kinetics. To date the hydrogen absorption and desorption kinetics can be increased by adding catalyst on powder surface and the thermodynamic properties of magnesium hydride can be modified by the addition of alloying elements to form complex hydride [18, 56]. Generally, the dehydrogenation kinetics increases significantly with increasing the dehydrogenation temperature [31]. In the isothermal and isobaric reaction of hydride formation, $\text{Mg} + \text{H}_2 \rightarrow \text{MgH}_2$, as the hydrogenation temperature is close to the equilibrium temperature ($T_h \approx T_{eq}$, T_h is the hydrogenation temperature and T_{eq} is the equilibrium temperature at a given pressure), it leads to large thermal energy for hydrogen diffusion and interface movement of Mg/MgH_2 in company with a small under-cooling for magnesium hydride nucleation. Furthermore, low nucleation rate and high growth rate are observed at high hydrogenation temperatures. When the difference between applied dehydrogenation temperature and the equilibrium temperature is large ($T_{dh} \gg T_{eq}$, T_{dh} is the desired dehydrogenation temperature), magnesium hydride is easily dissociated and rapid nucleation rate of hcp-Mg with large over-heating occurs upon dehydrogenation[38]. In the kinetics point of view, high dehydrogenation temperature is certainly beneficial to expedite the dehydrogenation process but not favorable to the practical use because the consumption of heat reduces the efficiency of hydrogen-based fuel cells.

In this chapter the effect of hcp-Mg nucleation energy barrier on the dehydrogenation temperature is investigated. To investigate the role of hcp-Mg nucleation on the dehydrogenation temperature, two hydrogenated powder samples were dehydrogenated both in TGA and in the house-build Hydrogenation/Dehydrogenation unit. One partially hydrogenated powder sample contained hcp-Mg on the surface and the other fully hydrogenated one encompassed no hcp-Mg on it. Detailed microstructural analyses were conducted on those powder samples to evaluate the mechanism of nucleation and growth of the hcp-Mg phase. In a different approach dehydrogenation tests were conducted at different temperatures and at constant 0.1MPa pressure to look for the equilibrium temperature by using uncovered hydride particle to avoid the nucleation barrier of hcp-Mg upon dehydrogenation. The results were compared with the reported equilibrium temperature under 0.1MP from the literature.

8.2 Desorption Study by Constant Heating Rate in TGA

The magnesium powder sample was coated with nano-Ni by using organometallic solution for hydrogen absorption and desorption tests. Figure 8-1(a) illustrates the hydrogenation curve of the magnesium powder carried out at 210°C for 5 hours under 1 MPa pressure. After 5 hours of hydrogenation, 6.1 wt. % of hydrogen was absorbed into the powder. As was demonstrated in Chapters 5 and 6 the hydrogen absorption takes place in three stages based on JMA analysis $\ln[-\ln(1-f)]$ vs $\ln t$ is plotted in Figure 8-1(b), which demonstrates the three reaction regimes. To elucidate the effect of the presence of hcp-Mg on the surface on the dehydrogenation behavior, a partial hydrogenation test was designed, in which a powder sample was hydrogenated for 54 minutes, corresponding to point A in Figure 8-1(b). Since this point lies within Stage 2 of

hydrogenation, the powder was expected to be partially covered with hydride. [Figure 8-2](#) shows the SEM (BSE mode) pictures of typical powders after hydrogenation.

Consistently, the microstructure of the powder after 5 hours of hydrogenation, presented in [Figure 8-2\(a\)](#), reveals that the surface of the powders is completely covered with the magnesium hydride phase, while the hydride colonies in powders hydrogenated for 54 minutes did not completely impinge on each other, as demonstrated in [Figure 8-2\(b\)](#).

After the hydrogenation test, the hydrogenated powder sample was weighed 12mg for the TGA analysis. [Figure 8-3](#) illustrates the dehydrogenation curves of the saturated and partially hydrogenated powder samples. The total amount of hydrogen released was consistent with the weight of the hydrogen calculated from the hydrogenation tests ([Figure 8-1](#)). As speculated, a significant difference in the hydrogen release temperature was observed. The onset temperature of hydrogen release from the partially hydrogenated sample (54 minutes) was 219°C, but for the sample hydrogenated to saturation (5 hours), hydrogen was released at 290°C for similar conditions used in the TGA. The hydrogen release rate as indicated by the slope of the weight loss vs temperature curve was found to be slightly higher in the saturated sample, owing to the higher hydrogen release temperature.

The release of hydrogen from the magnesium hydride involves the breakage of the Mg–H bond, the nucleation of the hcp-Mg phase, the diffusion of hydrogen onto the surface and the recombination of H atoms to form a H₂ molecule. When the surface of the powders is completely covered with the hydride phase, the hcp-Mg phase left in the core of the particles can grow upon the dehydrogenation process, but the rate will be extremely slow owing to the low diffusivity of hydrogen through the hydride phase.

Therefore, the observable dehydrogenation process most probably begins by the nucleation of the hcp-Mg on the surface of the hydrogenated powders. To confirm this mechanism, microstructural analysis was carried out on the partially dehydrogenated samples. A powder sample hydrogenated to saturation (5 hours) was partially dehydrogenated in the TGA. This was achieved by heating the powder at the rate of 5°C/minute from room temperature to 310°C, which is just above the onset temperature of hydrogen release room for this powder (see [Fig 8-3](#)), then the sample was cooled down at a much faster rate of 30 °C/minutes in an attempt to retain the microstructure at 310°C. It is anticipated that the rapid cooling reduces the temperature sufficiently fast such that further hydrogen release process was stopped. [Figure 8-4](#) illustrates the microstructure of the partially dehydrogenated powder at different magnifications. At lower magnification in [Figure 8-4\(a\)](#), the hcp-Mg (light contrast) completely covers the surface of the particle. The darker region, which corresponds to magnesium hydride, is observed in the center of the particles. The higher magnification picture, [Figure 8-4\(b\)](#), demonstrates that the light regions extend completely to the surface. The presence of the hcp-Mg on the surface shows that the dehydrogenation started through the nucleation of the hcp-Mg phase on the surface of the powders. This observation is consistent with previously reported studies. Once the hcp-Mg is nucleated on the surface, the dehydrogenation continues to take place at the interface and the hydrogen diffuses through the hcp-Mg phase to the surface, where H₂ molecules form. The above observations suggest that the presence of the hcp-Mg phase on the surface of the partially hydrogenated powders eliminates the nucleation barrier for the formation of the hcp-Mg phase from the magnesium hydride phase. However, powders hydrogenated to

saturation require a higher thermal energy to overcome the nucleation of the hcp-Mg phase; hence it exhibits a higher dehydrogenation temperature.

8.3 Isothermal Dehydrogenation Study of MgH₂

It was demonstrated in the previous chapters that the hydrogenation process of magnesium at 1MPa and in the temperature range of 180 to 300°C can be explained by the nucleation, growth and impingement of the magnesium hydride [99, 100]. Upon the dehydrogenation process, we may perhaps treat the decomposition of magnesium hydride as the nucleation and growth behavior of the hcp-Mg phase. In this study, magnesium powder samples were hydrogenated at 210°C and under 1MPa pressure and then dehydrogenated at 0.1MPa in the same system, as described in Chapter 3, at several temperatures near the reported equilibrium temperature at this pressure [38]. Figure 8-5(a) shows the hydrogenation/dehydrogenation curves. The powder samples were heated at 210°C under 1MPa hydrogen pressure for 5 hours following dehydrogenation tests at varying temperatures. As expected, the hydrogen desorption rate is rapid initially and diminishes afterward due to the reduction of hydride fraction. The increase of the temperature results in fast kinetics and large driving force for hydrogen releasing reaction. At 300°C, 80% of the magnesium hydride is decomposed after 15 minutes. A high dehydrogenation temperature is expected to render a fast hcp-Mg nucleation rate owing to the large driving force for magnesium nucleation and thermal energy for hydrogen diffusion, which results in numerous releasing paths of hydrogen atoms escaping through the hcp-Mg phase. The microstructural evaluation of a partially dehydrogenated sample at 300°C, marked as P on Figure 8-5(a), showed that the dehydrogenation takes place on the surface of particles, where hydrogen can escape easily and the curvature indicates that the movement of hcp-Mg/MgH₂ interface

from the surface into the hydride phase as shown in Figure 8-1(b). At 290°C the amount of hydrogen release was found to be negligible. At 290°C, the driving force for magnesium nucleation is small and the nucleation of hcp-Mg is the rate controlling mechanism. The slow kinetics is attributed to the extraordinarily thick magnesium hydride layer. In this case, the rate limiting step during dehydrogenation is the diffusion of hydrogen atoms through the magnesium hydride layer. If the powder surface is covered by magnesium hydride layer, the hydride fraction remains unchanged which shows the similar hydride distribution with as-hydrogenated powders in Figure 8-5(b). The small amount of hydrogen desorption at 290°C is assumed to issue from the as-hydrogenated powder with very small area of hcp-Mg on the powder surface. Once those powders are entirely dehydrogenated the hydrogen desorption process is brought to an end.

In order to investigate the role of hcp-Mg nucleation on the kinetics of the dehydrogenation process a sample was partially hydrogenated at 210°C and then dehydrogenated at 290°C. The hydrogenation times are different, but dehydrogenation conditions conducted are the same for both hydrogenated samples, at 290°C under 0.1MPa for 5 hours. Figure 8-6 reveals that unlike the dehydrogenation of the saturated powders, the partially hydrogenated powder releases hydrogen easily at 290°C. The desorption rate of powder sample with the existence of hcp-Mg on the surface is much faster than the one without hcp-Mg on the surface. This difference in behavior can be attributed to the availability of hcp-Mg in the latter sample. Figure 8-7 compares the microstructures of partially hydrogenated and saturated powders. The surface of the saturated powder is completely covered with a hydride layer while the partially

hydrogenated powder exhibits exposed hcp-Mg phase. In this case, the energy required during dehydrogenation included the nucleation barrier of the hcp-Mg phase has been reduced and only the growth of magnesium is happening. The availability of hcp-Mg on the surface drastically increases the dehydrogenation kinetics and the nucleation of hcp-Mg plays an important role in the dehydrogenation kinetics of magnesium hydride. These results suggest that for the powders covered by hydride layer, the initial rate limiting step for hydrogen desorption from magnesium hydride is the nucleation of hcp-Mg.

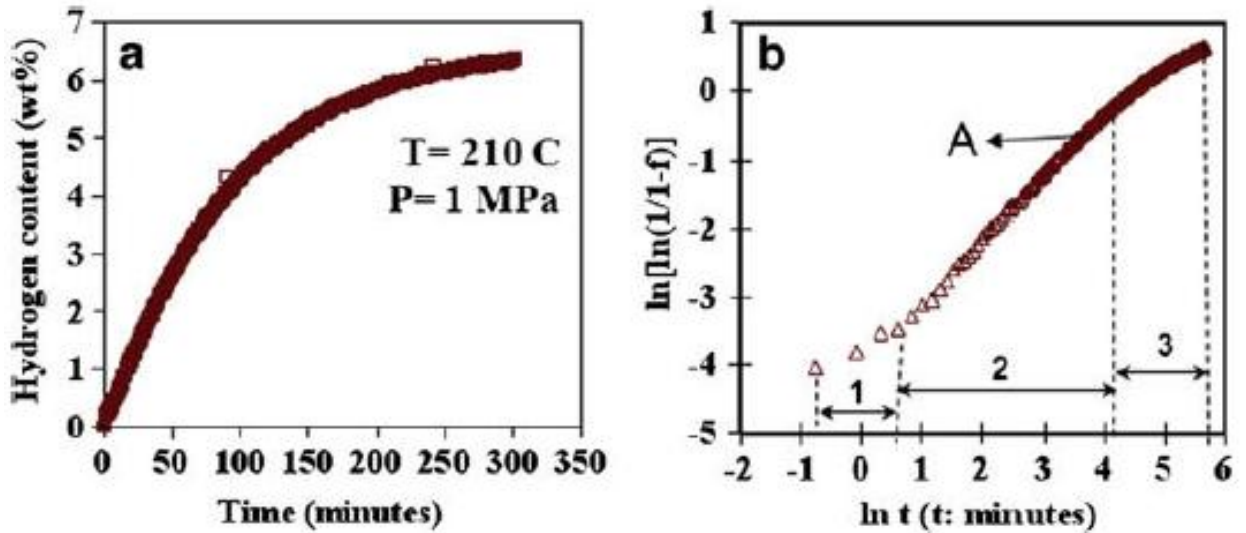
In order to establish the real transformation temperature at 0.1MPa for $\text{MgH}_2 \leftrightarrow \text{hcp-Mg} + \text{H}_2$, partially hydrogenated samples were dehydrogenated at different temperatures. Figure 8-8 illustrates different dehydrogenation temperatures varying from 275°C to 300°C on partially hydrogenated powder samples. The kinetics effect was in the range of 280°C to 300°C, the diffusivity of hydrogen in hcp-Mg increases with increasing the thermal energy hence the kinetics increases with increasing dehydrogenation temperature. As temperature is increased, both the driving force for nucleation of hcp-Mg and the diffusion rate are increased. The rate limiting step is assumed to be the diffusion of hydrogen through the magnesium phase. At 280 °C, the powder sample releases 2.5 H wt. % during dehydrogenation and the dehydrogenation kinetics is very slow. It is assumed that the equilibrium temperature under 0.1MPa is slightly below 280°C. For 275°C curve, thermodynamics mainly controls the dehydrogenation behavior since 275°C is below the equilibrium temperature of 0.1MPa no hydrogen can release at this temperature. Hence it is confirmed that the equilibrium temperature at 0.1MPa is between 275°C and 280°C. As the value is compared with the

equilibrium temperature 287.7°C reported before [38], it is about 8°C lower than it. It is concluded that the reported release temperature usually needs the thermal activation for the nucleation of hcp-Mg. The only reason we obtain lower release temperature than before is because we have been using material without activation barrier required. To the extent that we know the difficulty of achieving equilibrium status, and the parameter for equilibrium reported so far may be a little bit off from the real case due to the unavoidable kinetics effect.

8.4 Summary and Conclusions

In conclusions, we have introduced a logical initiative to enhance the hydrogen desorption kinetics by preserving the hcp-Mg phase on the powder surface. This consideration would expedite the dehydrogenation process via reducing the nucleation barrier of hcp-Mg. The equilibrium temperature of 0.1MPa hydrogen pressure was experimentally tested to be the range of 275°C to 280°C which is about 10°C lower than the equilibrium temperature reported before. Obviously, fully covered hydride powder was used which increases the difficulty of hydrogen release. For the study of computational simulation and phase transformation of Mg-H system, this finding makes a strong point of the importance of careful consideration in kinetics while thermodynamics properties is being measured. From the results of this study, it can be concluded that:

1. Dehydrogenation of magnesium hydride takes place on the surface of the powder.
2. The higher hydrogen release temperature of magnesium hydride in comparison with the equilibrium temperature based on the Mg-H phase diagram can be attributed to the difficulty of hcp-Mg phase nucleation.
3. The presence of hcp-Mg phase in partially hydrogenated powders eliminates the nucleation barrier for formation of the hcp-Mg phase, and thereby reduces the hydrogen release temperature.



4.

Figure 8-1. (a) Hydrogenation curve of hcp-Mg at 210°C under 1MPa pressure. (b) Evaluation of different stages of hydrogenation of magnesium powders based on JMA relationship.

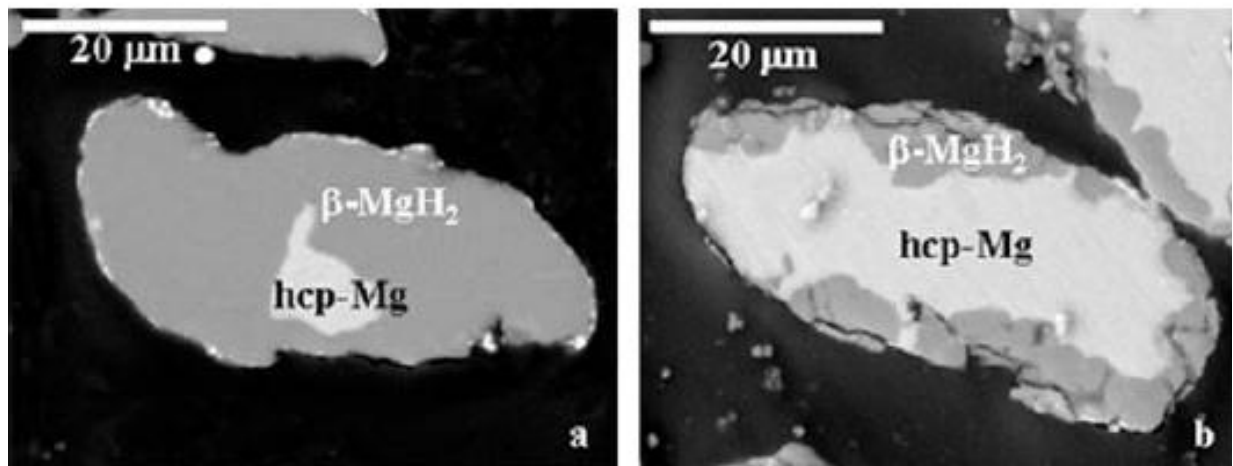


Figure 8-2. SEM (BSE mode) micrographs (a) of the saturated powder revealing the impingement of magnesium hydride grains/colonies and (b) of the partially hydrogenated powder showing the presence of the hcp-Mg phase on the surface.

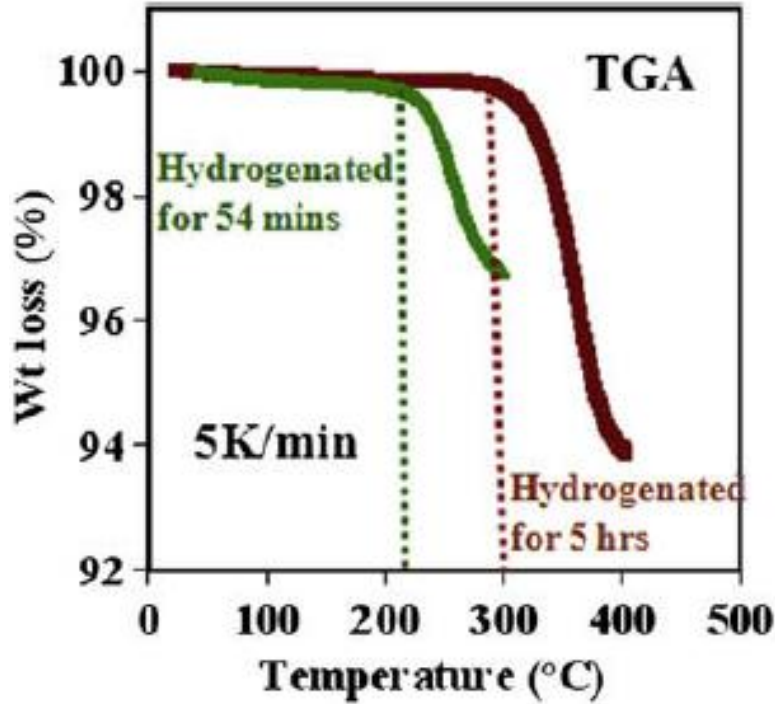


Figure 8-3. Dehydrogenation curves obtained using TGA of the partially and completely hydrogenated powders at 5°C/minute and under He flow, revealing the difference in the hydrogen release temperature between the samples.

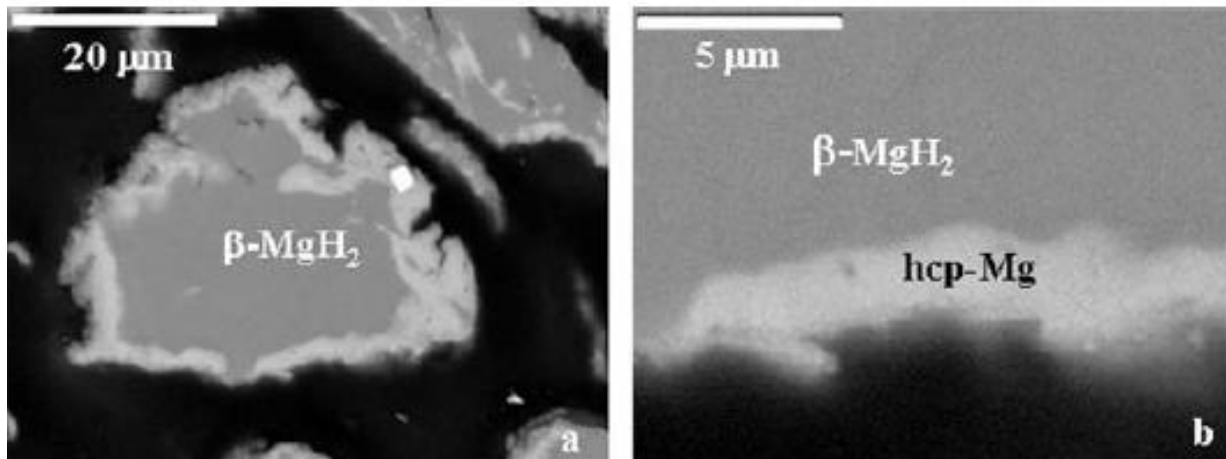


Figure 8-4. SEM (BSE mode) micrographs of the partially dehydrogenated powder. (a) Lowering magnification of the particle showing the release of hydrogenation around the particle with MgH_2 inside the particle. (b) Higher magnification image showing the extension of the hcp-Mg phase to the surface of the particle.

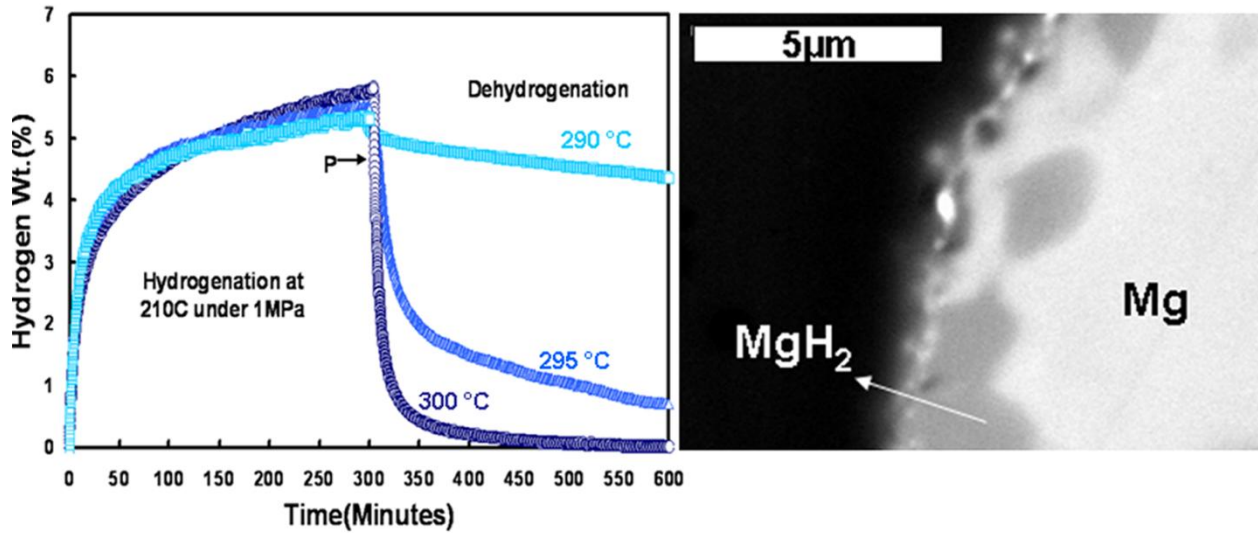


Figure 8-5. (a) Hydrogenation/dehydrogenation curves. The hydrogenation condition is the same for all powder samples (At 210°C under 1 MPa for 5 hours). The dehydrogenation tests were done under 0.1 MPa at 290°C, 295°C, 300°C for 5 hours. The SEM/BSE image at point P is shown in Figure 1(b), in the vicinity near the powder surface of the partial dehydrogenated powders after 5 minutes releasing at 300 °C under 0.1MPa.

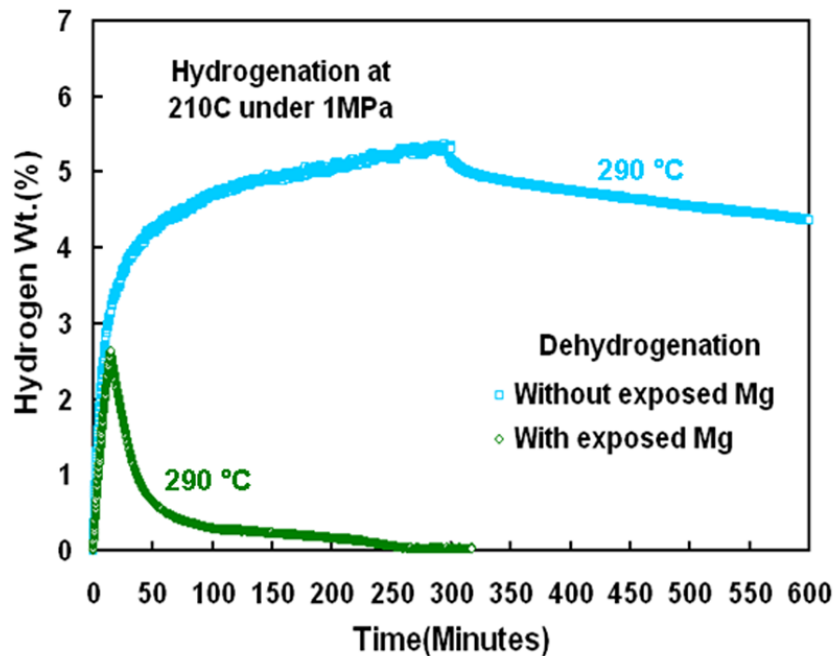


Figure 8-6. Hydrogenation/dehydrogenation curves. The hydrogenation tests are done at 210°C under 1MPa for 15 minutes and 5 hours. The dehydrogenation tests are done under 0.1 MPa at 290°C for 5 hours immediately after hydrogenation tests for both powder samples.

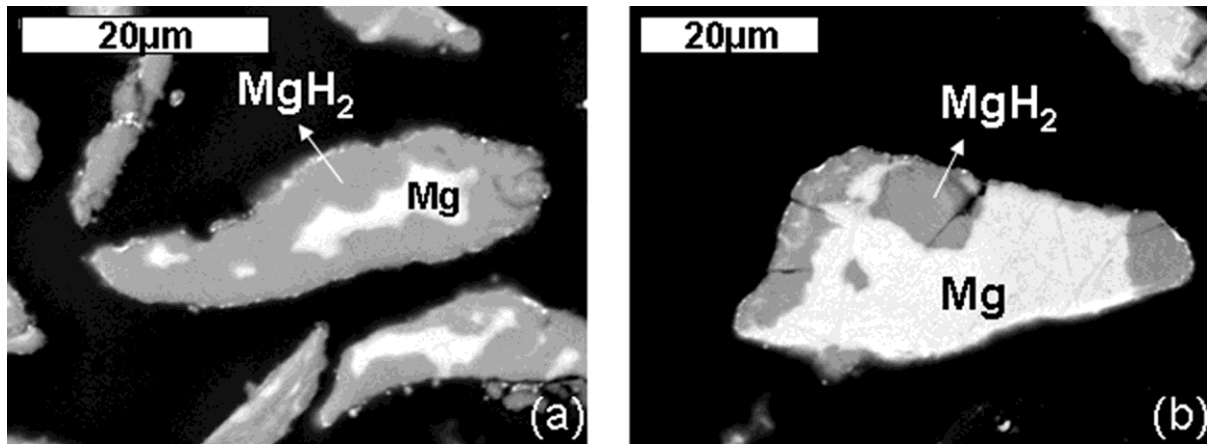


Figure 8-7. The SEM/BSE images of as-hydrogenated powder. In Figure 3(a), SEM/BSE images show the hydride distribution in the hydride powders hydrogenated at 210 °C under 1 MPa for 5 hours. The Sample powder exhibits pseudo-saturation behavior. In Figure 3(b), the SEM/BSE images shows the hydride distribution in the hydride powders hydrogenated at 210°C under 1 MPa for 15 minutes and the sample powder shows unsaturated behavior.

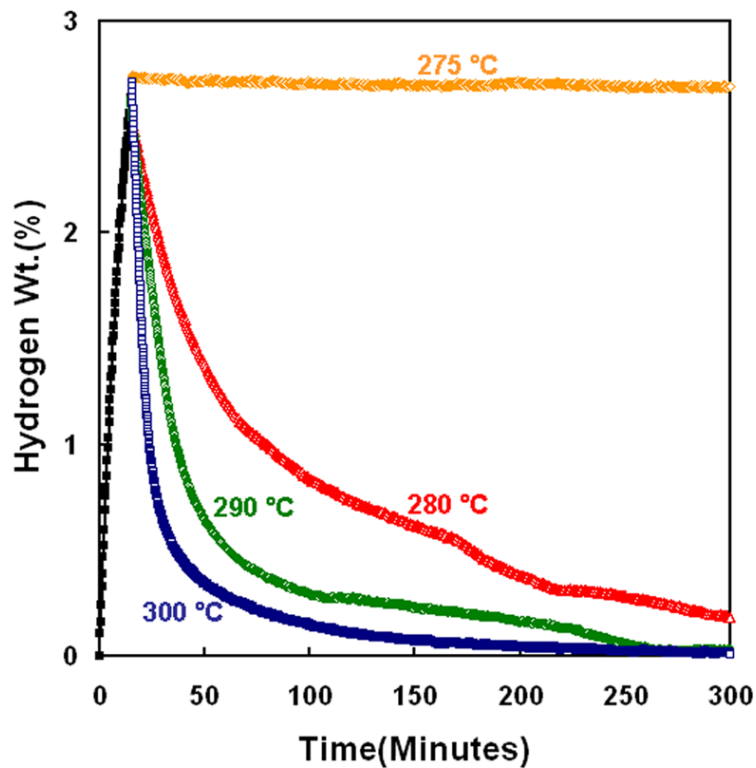


Figure 8-8. Hydrogenation/dehydrogenation curves. The hydrogenation tests are done at 210°C under 1MPa for 15 minutes. The dehydrogenation tests are done under 0.1 MPa at 290°C for 5 hours at 275°C, 280°C, 290°C, and 300°C.

CHAPTER 9 CONCLUSIONS AND FUTURE WORK

Hydrogen is one of the most promising energy sources in the 21st century. In this study, we demonstrated the fundamental hydrogenation behavior of Mg powders. The finding promotes the understanding of hydrogen absorption mechanism using microstructural analysis. At temperature 180 to 250°C, the magnesium hydride formation before impingement is best explained by the impingement model, after impingement the Core-Shell model is applicable for the thickening process of magnesium hydride layer. Pseudo saturation occurred at Stage 3 during the thickening process owing to the very thick hydride layer. At 150°C, it can be treated as Core-Shell model only since a continuous hydride layer immediately formed and the hydride fraction increased with increasing hydride thickness. For a given shape and size of the Mg powders there is an optimum hydrogenation temperature and pressure. By making magnesium flakes for the storage material the hydrogenation energy can be actually lowered to increase the efficiency of the system integration of hydrogen powdered cars. Hydrogenated magnesium powders with magnesium phase on the surface will increase the dehydrogenation kinetics by lowering the nucleation barrier of magnesium phase. The dehydrogenation temperature can be lowered if magnesium phase presents on the hydrogenated powder surface.

Suggested future work: What lack is the effect of hydrogen pressure, because not only temperature affects the capacity also the capacity is a function of pressure. For the hydrogenation, much more work should be emphasized on the effect of pressure. Moreover, the activation energy of hydrogen through magnesium phase was obtained; mass balance can be used to develop a mathematical model based on the hydrogen

flux through magnesium and magnesium hydride phase. The total flux should include the hydrogen flux through both phases. The surface area of magnesium and magnesium hydride can be estimated by the growth rate of magnesium hydride in hemisphere form in Stage 2. A very thin magnesium flake should be made and thickness is suggested to smaller than 4 μm if 150°C is applied for the hydrogenation temperature in order to reach 7.6 H. wt. % capacity. Magnesium coating process is suggested to be applied on the hydrogenated magnesium powder to help to lower the nucleation barrier of magnesium and enhance and dehydrogenation kinetics during hydrogen desorption.

LIST OF REFERENCES

1. MacKenzie, J., *Oil as a finite resource*. Natural Resources Research, 1998. **7**(2): p. 97-100.
2. Bockris, J.O.M., *Will lack of energy lead to the demise of high-technology countries in this century?* International Journal of Hydrogen Energy, 2007. **32**(2): p. 153-158.
3. Hubbert, M.K., *Nuclear Energy and the Fossil Fuels*. Spring Meeting of the Southern District, Division of Production. American Petroleum Institute. San Antonio, Texas: Shell Development Company. , 1956: p. 22-27.
4. Brandt, A.R., *Testing Hubbert*. Energy Policy, 2007. **35**(5): p. 3074-3088.
5. Duncan, R.C., *World Energy Production, Population Growth, and the Road to the Olduvai Gorge*. Population & Environment, 2001. **22**(5): p. 503-522.
6. Schlapbach, L. and A. Zuttel, *Hydrogen-storage materials for mobile applications*. Nature, 2001. **414**(6861): p. 353-358.
7. Chandra, D., J. Reilly, and R. Chellappa, *Metal hydrides for vehicular applications: The state of the art*. JOM Journal of the Minerals, Metals and Materials Society, 2006. **58**(2): p. 26-32.
8. Ritter, J.A., et al., *Implementing a hydrogen economy*. Materials Today, 2003. **6**(9): p. 18-23.
9. Zuttel, A., *Materials for hydrogen storage*. Materials Today, 2003. **6**(9): p. 24-33.
10. Ewan, B.C.R. and R.W.K. Allen, *A figure of merit assessment of the routes to hydrogen*. International Journal of Hydrogen Energy, 2005. **30**(8): p. 809-819.
11. Fichtner, M., *Nanotechnological Aspects in Materials for Hydrogen Storage*. Advanced Engineering Materials, 2005. **7**(6): p. 443-455.
12. Grochala, W. and P.P. Edwards, *Thermal Decomposition of the Non-Interstitial Hydrides for the Storage and Production of Hydrogen*. Chemical Reviews, 2004. **104**(3): p. 1283-1316.
13. Sandrock, G., *A panoramic overview of hydrogen storage alloys from a gas reaction point of view*. Journal of Alloys and Compounds, 1999. **293-295**: p. 877-888.
14. Sandrock, G. and R.C. Bowman, *Gas-based hydride applications: recent progress and future needs*. Journal of Alloys and Compounds, 2003. **356-357**: p. 794-799.
15. De Wit, M.P. and A.P.C. Faaij, *Impact of hydrogen onboard storage technologies on the performance of hydrogen fuelled vehicles: A techno-economic well-to-wheel assessment*. International Journal of Hydrogen Energy, 2007. **32**(18): p. 4859-4870.
16. Kalisvaart W.P., N.P.H.L., *Mechanical alloying and electrochemical hydrogen storage of Mg-based systems*. J. Mater. Res., 2008. **23**: p. 2179.
17. Sakintuna, B., F. Lamari-Darkrim, and M. Hirscher, *Metal hydride materials for solid hydrogen storage: A review*. International Journal of Hydrogen Energy, 2007. **32**(9): p. 1121-1140.
18. Vajo, J.J., et al., *Altering hydrogen storage properties by hydride destabilization through alloy formation: LiH and MgH₂ destabilized with Si*. Journal of Physical Chemistry B, 2004. **108**(37): p. 13977-13983.

19. Steele, B.C.H. and A. Heinzl, *Materials for fuel-cell technologies*. Nature, 2001. **414**(6861): p. 345-352.
20. Steele, B.C.H., *Material science and engineering: The enabling technology for the commercialisation of fuel cell systems*. Journal of Materials Science, 2001. **36**(5): p. 1053-1068.
21. Starz, K.A., et al., *Characteristics of platinum-based electrocatalysts for mobile PEMFC applications*. Journal of Power Sources, 1999. **84**(2): p. 167-172.
22. Jensen, J.O., et al., *100-200[thin space]?C polymer fuel cells for use with NaAlH₄*. Journal of Alloys and Compounds, 2005. **404-406**: p. 653-656.
23. Maddalena, A., et al., *Study of Mg-based materials to be used in a functional solid state hydrogen reservoir for vehicular applications*. International Journal of Hydrogen Energy, 2006. **31**(14): p. 2097-2103.
24. http://www.nrel.gov/basic_sciences/carbon_based_hydrogen_center.cfm.
25. Bouza C., R.S., Satyapal J. and Milliken, *Annual DOE Hydrogen*. Fuel Cell and Infrastructure Technologies Program Review Meeting Philadelphia, May 25, 2004.
26. Zaluska, A., L. Zaluski, and J.O. Strom-Olsen, *Nanocrystalline magnesium for hydrogen storage*. Journal of Alloys and Compounds, 1999. **288**(1-2): p. 217-225.
27. Liang, G., et al., *Catalytic effect of transition metals on hydrogen sorption in nanocrystalline ball milled MgH₂-Tm (Tm=Ti, V, Mn, Fe and Ni) systems*. Journal of Alloys and Compounds, 1999. **292**(1-2): p. 247-252.
28. Vigeholm, B., et al., *Elements of hydride formation mechanisms in nearly spherical magnesium powder particles*. Journal of the Less Common Metals, 1987. **131**(1-2): p. 133-141.
29. Rudman, P.S., *Hydriding and dehydriding kinetics*. Journal of the Less Common Metals, 1983. **89**(1): p. 93-110.
30. Friedlmeier, G. and M. Groll, *Experimental analysis and modelling of the hydriding kinetics of Ni-doped and pure Mg*. Journal of Alloys and Compounds, 1997. **253-254**: p. 550-555.
31. Huot, J., et al., *Structural study and hydrogen sorption kinetics of ball-milled magnesium hydride*. Journal of Alloys and Compounds, 1999. **295**: p. 495-500.
32. Liang, G., *Synthesis and hydrogen storage properties of Mg-based alloys*. Journal of Alloys and Compounds, 2004. **370**(1-2): p. 123-128.
33. Charbonnier, J., et al., *Hydrogenation of transition element additives (Ti, V) during ball milling of magnesium hydride*. Journal of Alloys and Compounds, 2004. **383**(1-2): p. 205-208.
34. Schulz, R., et al., *Recent developments in the applications of nanocrystalline materials to hydrogen technologies*. Materials Science and Engineering A, 1999. **267**(2): p. 240-245.
35. Chou, K.-C., et al., *Kinetics of absorption and desorption of hydrogen in alloy powder*. International Journal of Hydrogen Energy, 2005. **30**(3): p. 301-309.
36. Martin, M., et al., *Absorption and desorption kinetics of hydrogen storage alloys*. Journal of Alloys and Compounds, 1996. **238**(1-2): p. 193-201.
37. Levenspiel, O., *Chemical Reaction Engineering*. 2nd ed. New York: John Wiley, 1999: p. 359-370.

38. Zeng, K., et al., *Critical assessment and thermodynamic modeling of the Mg-H system*. International Journal of Hydrogen Energy, 1999. **24**(10): p. 989-1004.
39. Rudman, P.S., *Hydrogen-diffusion-rate-limited hydriding and dehydriding kinetics*. Journal of Applied Physics, 1979. **50**(11): p. 7195-7199.
40. Bazzanella N., C.R., Miotello A., D'Acapito F., Maurizio C., Barucca G., Majni G., Mengucci P., *Kinetics of hydrogen absorption and desorption in magnesium: role of the structure and of catalysts*". Advanced materials for energy conversion III , Warrendale,2006 TMS annual meeting", San Antonio, Texas, 2006: p. 89-99.
41. Noritake, T., et al., *Chemical bonding of hydrogen in MgH₂*. Applied Physics Letters, 2002. **81**(11): p. 2008-2010.
42. Kelekar, R., et al., *Formation and dissociation of MgH₂ in epitaxial Mg thin films*. Journal of Applied Physics, 2007. **101**(11): p. -.
43. Bérubé, V., et al., *Size effects on the hydrogen storage properties of nanostructured metal hydrides: A review*. 2007, John Wiley & Sons, Ltd. p. 637-663.
44. Palumbo, M., et al., *Thermodynamic and ab initio investigation of the Al-H-Mg system*. Calphad, 2007. **31**(4): p. 457-467.
45. Vajo, J.J. and G.L. Olson, *Hydrogen storage in destabilized chemical systems*. Scripta Materialia, 2007. **56**(10): p. 829-834.
46. Zeng, K.J., et al., *Thermodynamic analysis of the hydriding process of Mg-Ni alloys*. Journal of Alloys and Compounds, 1999. **283**(1-2): p. 213-224.
47. Shao, H.Y., et al., *Hydrogen storage properties of magnesium ultrafine particles prepared by hydrogen plasma-metal reaction*. Materials Science and Engineering B-Solid State Materials for Advanced Technology, 2004. **110**(2): p. 221-226.
48. Zaluska, A., L. Zaluski, and J.O. Strom-Olsen, *Synergy of hydrogen sorption in ball-milled hydrides of Mg and Mg₂Ni*. Journal of Alloys and Compounds, 1999. **289**(1-2): p. 197-206.
49. Bogdanovic, B., et al., *Thermodynamic investigation of the magnesium-hydrogen system*. Journal of Alloys and Compounds, 1999. **282**(1-2): p. 84-92.
50. Andreasen, A., *Hydrogenation properties of Mg-Al alloys*. International Journal of Hydrogen Energy, 2008. **33**(24): p. 7489-7497.
51. Yermakov, A.Y., et al., *Hydrogen reaction kinetics of Mg-based alloys synthesized by mechanical milling*. Journal of Alloys and Compounds, 2006. **425**(1-2): p. 367-372.
52. Baldi, A., et al., *Destabilization of the Mg-H System through Elastic Constraints*. Physical Review Letters, 2009. **102**(22): p. 226102.
53. Zhdanov, V.P., A. Krozer, and B. Kasemo, *Kinetics of first-order phase transitions initiated by diffusion of particles from the surface into the bulk*. Physical Review B, 1993. **47**(17): p. 11044.
54. Fossdal, A., et al., *Determination of the crystal structure of Mg(AlH₄)₂ by combined X-ray and neutron diffraction*. Journal of Alloys and Compounds, 2005. **387**(1-2): p. 47-51.
55. Fichtner, M., O. Fuhr, and O. Kircher, *Magnesium alanate--a material for reversible hydrogen storage?* Journal of Alloys and Compounds, 2003. **356-357**: p. 418-422.

56. Song, Y., Z.X. Guo, and R. Yang, *Influence of selected alloying elements on the stability of magnesium dihydride for hydrogen storage applications: A first-principles investigation*. Physical Review B, 2004. **69**(9): p. 094205.
57. Shang, C.X., et al., *Mechanical alloying and electronic simulations of (MgH₂+M) systems (M=Al, Ti, Fe, Ni, Cu and Nb) for hydrogen storage*. International Journal of Hydrogen Energy, 2004. **29**(1): p. 73-80.
58. Liang, G. and R. Schulz, *The reaction of hydrogen with Mg-Cd alloys prepared by mechanical alloying*. Journal of Materials Science, 2004. **39**(5): p. 1557-1562.
59. Kalisvaart, W.P., R.A.H. Niessen, and P.H.L. Notten, *Electrochemical hydrogen storage in MgSc alloys: A comparative study between thin films and bulk materials*. Journal of Alloys and Compounds, 2006. **417**(1-2): p. 280-291.
60. Tsuda, M., et al., *Mg-H dissociation of magnesium hydride MgH₂ catalyzed by 3d transition metals*. Thin Solid Films, 2006. **509**(1-2): p. 157-159.
61. Stämpfer J.F., H.C.E., Suttle J.F. , *The Magnesium- hydrogen system*. J. Am. Chem. Soc. , 1960. **64**: p. 703-7-4.
62. Vigeholm, B., J. Kjler, and B. Larsen, *Magnesium for hydrogen storage*. Journal of the Less Common Metals, 1980. **74**(2): p. 341-350.
63. Pedersen, A.S., et al., *Magnesium for hydrogen storage*. International Journal of Hydrogen Energy, 1983. **8**(3): p. 205-211.
64. Cermic, J. and L. Krai, *Hydrogen diffusion in Mg-H and Mg-Ni-H alloys*. Acta Materialia, 2008. **56**(12): p. 2677-2686.
65. Evard, E.A., I.E. Gabis, and A.P. Voyt, *Study of the kinetics of hydrogen sorption and desorption from titanium*. Journal of Alloys and Compounds, 2005. **404-406**: p. 335-338.
66. Andreasen, A., T. Vegge, and A.S. Pedersen, *Compensation Effect in the Hydrogenation/Dehydrogenation Kinetics of Metal Hydrides*. The Journal of Physical Chemistry B, 2005. **109**(8): p. 3340-3344.
67. Nishimura, C., M. Komaki, and M. Amano, *Hydrogen permeation through magnesium*. Journal of Alloys and Compounds, 1999. **293-295**: p. 329-333.
68. Fernandez, J.F. and C.R. Sanchez, *Rate determining step in the absorption and desorption of hydrogen by magnesium*. Journal of Alloys and Compounds, 2002. **340**(1-2): p. 189-198.
69. Christian, J.W., *The theory of transformation in metals and alloys- Part I* London: Pergamon Press. 2002: p. 529.
70. Karty, A., J. Grunzweig-Genossar, and P.S. Rudman, *Hydriding and dehydriding kinetics of Mg in a Mg/Mg₂Cu eutectic alloy: Pressure sweep method*. Journal of Applied Physics, 1979. **50**(11): p. 7200-7209.
71. Fernandez, J.F. and C.R. Sanchez, *Rate determining step in the absorption and desorption of hydrogen by magnesium*. Journal of Alloys and Compounds, 2002. **340**(1-2): p. 189-198.
72. Friedrichs, O., et al., *Chemical and microstructural study of the oxygen passivation behaviour of nanocrystalline Mg and MgH₂*. Applied Surface Science, 2006. **252**(6): p. 2334-2345.
73. Schlapbach, L., et al., *Surface effects and the formation of metal hydrides*. Journal of the Less Common Metals, 1980. **73**(1): p. 145-160.

74. Fleisch, T. and R. Abermann, *On the reduction of Ag₂S films by hydrogen spillover under ultra high vacuum conditions*. Journal of Catalysis, 1977. **50**(2): p. 268-278.
75. Charlot, M.-F. and O. Kahn, *Activation de l'hydrogène moléculaire par une petite particule de nickel*. Surface Science, 1979. **81**(1): p. 90-108.
76. Higuchi, K., et al., *Remarkable hydrogen storage properties in three-layered Pd/Mg/Pd thin films*. Journal of Alloys and Compounds, 2002. **330-332**: p. 526-530.
77. Janot, R., et al., *Enhancement of hydrogen storage in MgNi by Pd-coating*. Journal of Alloys and Compounds, 2003. **356-357**: p. 438-441.
78. Gremaud, R., et al., *Ti-catalyzed Mg(AlH₄)₂: A reversible hydrogen storage material*. Journal of Alloys and Compounds, 2005. **404-406**: p. 775-778.
79. Liang, G. and R. Schulz, *Synthesis of Mg-Ti alloy by mechanical alloying*. Journal of Materials Science, 2003. **38**(6): p. 1179-1184.
80. Liang, G., et al., *Hydrogen storage properties of the mechanically milled MgH₂-V nanocomposite*. Journal of Alloys and Compounds, 1999. **291**(1-2): p. 295-299.
81. Xie, L., et al., *Superior hydrogen storage kinetics of MgH₂ nanoparticles doped with TiF₃*. Acta Materialia, 2007. **55**(13): p. 4585-4591.
82. Aguey-Zinsou, K.F., et al., *Effect of Nb₂O₅ on MgH₂ properties during mechanical milling*. International Journal of Hydrogen Energy, 2007. **32**(13): p. 2400-2407.
83. Oelerich, W., T. Klassen, and R. Bormann, *Comparison of the catalytic effects of V, V₂O₅, VN, and VC on the hydrogen sorption of nanocrystalline Mg*. Journal of Alloys and Compounds, 2001. **322**(1-2): p. L5-L9.
84. Barkhordarian, G., T. Klassen, and R. Bormann, *Fast hydrogen sorption kinetics of nanocrystalline Mg using Nb₂O₅ as catalyst*. Scripta Materialia, 2003. **49**(3): p. 213-217.
85. Friedrichs, O., et al., *Hydrogen sorption improvement of nanocrystalline MgH₂ by Nb₂O₅ nanoparticles*. Scripta Materialia, 2006. **54**(7): p. 1293-1297.
86. Friedrichs, O., et al., *MgH₂ with Nb₂O₅ as additive, for hydrogen storage: Chemical, structural and kinetic behavior with heating*. Acta Materialia, 2006. **54**(1): p. 105-110.
87. Bogdanovic, B., et al., *Ni-doped versus undoped Mg-MgH₂ materials for high temperature heat or hydrogen storage*. Journal of Alloys and Compounds, 1999. **292**(1-2): p. 57-71.
88. Jeon, K.-J., A. Theodore, and C.-Y. Wu, *Enhanced hydrogen absorption kinetics for hydrogen storage using Mg flakes as compared to conventional spherical powders*. Journal of Power Sources, 2008. **183**(2): p. 693-700.
89. Mintz, M.H. and Y. Zeiri, *Hydriding kinetics of powders*. Journal of Alloys and Compounds, 1995. **216**(2): p. 159-175.
90. Chernov, I., et al., *Influence of metal powder particle's shape on the kinetics of hydriding*. International Journal of Hydrogen Energy. **35**(1): p. 253-258.
91. Cermak, J. and L. Kral, *Hydrogen diffusion in Mg-H and Mg-Ni-H alloys*. Acta Materialia, 2008. **56**(12): p. 2677-2686.
92. Vittori Antisari, M., et al., *On the nucleation step in the Mg-MgH₂ phase transformation*. Scripta Materialia, 2009. **61**(11): p. 1064-1067.

93. Montone, A., et al., *On the barriers limiting the reaction kinetics between catalysed Mg and hydrogen*. **63**(4): p. 456-459.
94. Oguchi, H., et al., *In-situ infrared imaging methodology for measuring heterogeneous growth process of a hydride phase*. International Journal of Hydrogen Energy. **35**(3): p. 1296-1299.
95. Baldi, A., et al., *Mg-Ti-H thin films as switchable solar absorbers*. International Journal of Hydrogen Energy, 2008. **33**(12): p. 3188-3192.
96. Baldi, A., et al., *Nanoscale composition modulations in Mg_yTi_{1-y}H_x thin film alloys for hydrogen storage*. International Journal of Hydrogen Energy, 2009. **34**(3): p. 1450-1457.
97. Voort, G.V., *Metallography and Microstructures*. ASM Handbook, 2004. **9**: p. 1184.
98. Ebrahimi F, T.M., Tatiparti S, Tien H.Y., Jeon K.J., Wu C.Y. , *A study of hydrogen absorption and desorption in magnesium*. MRS Fall, 2007(Symposium S: MAterial and technology for hydrogen storage).
99. Tien, H.-Y., et al., *Mechanism of hydrogen capacity dependence on the hydrogenation temperature*. Scripta Materialia. **62**(5): p. 274-277.
100. Tien, H.-Y., et al., *Effect of hydride nucleation rate on the hydrogen capacity of Mg*. International Journal of Hydrogen Energy, 2009. **34**(15): p. 6343-6349.

BIOGRAPHICAL SKETCH

Hung-Yu Tien was born in 1979, in Taitung City, Taitung, Taiwan. He did his bachelor's and master's degrees in the Materials Science and Engineering Department of National Tsing-Hua University in Hsin-Chu, Taiwan. The research in his master's study is bulk metallic glass (BMG). He has one year working experience as a 4G Flash integrate engineer in a semiconductor company, Power-Chip Semiconductor Corporation in Hsin-Chu, Taiwan. He join Dr.Ebrahimi's group at University of Florida Materials Science and Engineering Department in summer 2007.